

NATIONAL CENTRE FOR NUCLEAR RESEARCH

DOCTORAL THESIS

---

# Dark matter as a laboratory for new ideas in physics beyond the Standard Model

---

Author

**Krzysztof  
Jodłowski** 

Supervisor

**Prof. Dr. Hab.  
Leszek Roszkowski** 

Co-supervisor

**Dr. Sebastian  
Trojanowski** 

*A thesis submitted in fulfillment of the requirements  
for the degree of Doctor of Philosophy  
in the*

*Department of Fundamental Research*



**Narodowe Centrum Badań Jądrowych**  
**National Centre for Nuclear Research**  
**ŚWIERK**

Warsaw, March 2022



# Declaration of Authorship

I, Krzysztof Jodłowski, declare that this thesis titled, “Dark matter as a laboratory for new ideas in physics beyond the Standard Model” and the work presented in it are my own. I confirm that:

- This work was done wholly or mainly while in candidature for a research degree at the National Centre for Nuclear Research.
- Where any part of this thesis has previously been submitted for a degree or any other qualification at the National Centre for Nuclear Research or any other institution, this has been clearly stated.
- Where I have consulted the published work of others, this is always clearly attributed.
- Where I have quoted from the work of others, the source is always given. With the exception of such quotations, this thesis is entirely my own work.
- I have acknowledged all main sources of help.
- Where the thesis is based on work done by myself jointly with others, I have made clear exactly what was done by others and what I have contributed myself.

Signed:

---

Date:

---



## *Abstract*

### **Dark matter as a laboratory for new ideas in physics beyond the Standard Model**

Krzysztof Jodłowski

One of the most puzzling features of our Universe is that for each unit of mass of ordinary matter, there are five units that are invisible. The nature of this so-called dark matter (DM) remains mysterious and efforts to detect it have been one of the most intense lines of research in physics. This thesis is dedicated to studying popular candidates for particle DM, focusing on models that can be related to other puzzles of the Standard Model (SM) and that will be tested in experiments in the near future.

The underlying cosmological framework is the Standard Cosmological Model ( $\Lambda$ CDM), and we introduce the DM problem as a part of this successful theory. We discuss the mechanism of DM thermal production, which applies to a broad class of DM candidates often predicted by well-motivated extensions of the SM, including most of the DM candidates discussed in this thesis. We also discuss the well-developed experimental program devoted to the searches for such particles, among them the celebrated Weakly Interacting Massive Particles (WIMPs) which could be naturally related to the electroweak scale of the SM, as shown by the numerical coincidence called WIMP miracle. However, current searches for electroweak scale WIMPs have so far yielded null results, which motivates exploring other possibilities.

Among the other possibilities are beyond the SM scenarios involving new light, sub-GeV particles which naturally extend the WIMP miracle scenario and can also be related to some other puzzles of the SM. In particular, realistic models of this type often include unstable particles, which - due to small values of their masses and coupling constants - are generally long-lived. Such particles are of particular interest and, due to their unique properties, they are often present in cosmology and particle physics. Therefore, it is desirable that beyond-the-SM scenarios predicting long-lived states (and DM) should be thoroughly probed, preferably from complementary angles of experimental testing, as in the case of WIMPs. In this thesis, we describe efforts in this direction based on a variety of searches: the emerging forward physics experiments, such as FASER that will soon take data at the LHC; indirect searches for cosmic rays produced in DM annihilations near the Galactic Center and surveys of CMB radiation, among others. While the search for generic WIMP DM and long-lived particles in the simplest SM extensions has been largely explored in the literature, we illustrate a number of interesting phenomenological effects that appear in more elaborate dark sector scenarios which can be studied experimentally in the coming years. Taking into account such effects can have important implications for the physics case of both current and proposed future experiments.



*Streszczenie***Ciemna materia jako laboratorium nowych idei  
w poszukiwaniach fizyki spoza Modelu Standardowego**

Krzysztof Jodłowski

Jedną z najbardziej zagadkowych cech naszego Wszechświata jest fakt, że na każdy atom zwykłej materii przypada pięć innych, które są niewidoczne. Natura tej tak zwanej ciemnej materii (CM) pozostaje tajemnicza, a próby jej wykrycia są jednym z najbardziej intensywnych kierunków badań w fizyce. Niniejsza rozprawa poświęcona jest badaniom popularnych kandydatek do bycia cząstką CM, skupiając się na modelach, które mogą być powiązane także z innymi problemami Modelu Standardowego (MS) i które będą wkrótce testowane w eksperymentach.

Współczesna kosmologia opisana jest poprzez Standardowy Model Kosmologiczny ( $\Lambda$ CDM) i w ramach tej udanej teorii wprowadzamy problem CM. Omawiamy mechanizm produkcji termicznej CM, który dotyczy szerokiej klasy kandydatek na cząstkę CM, które są często przewidywane przez dobrze umotywowane rozszerzenia MS, w tym większości kandydatek na cząstkę CM omawianych w tej pracy. Omawiamy również dobrze rozwinięty program eksperymentalny poświęcony poszukiwaniom takich cząstek, wśród nich masywnych słabo oddziałujących cząstek (WIMP), które mogą być naturalnie związane ze skalą oddziaływań elektroślabych MS, jak pokazuje numeryczna koincydencja zwana *WIMP miracle*. Jednak dotychczasowe poszukiwania WIMP-ów w skali elektroślabej nie przyniosły rozstrzygających rezultatów, co skłania do rozważania innych możliwości.

Wśród innych możliwości są scenariusze fizyki wykraczające poza MS, w których występują nowe lekkie cząstki o masach poniżej 1 GeV, co w naturalny sposób rozszerza mechanizm *WIMP miracle* i może być związane z innymi zagadkami MS. W szczególności, realistyczne modele tego typu często zawierają cząstki niestabilne, które - ze względu na małe wartości ich mas i stałych sprzężenia - są na ogół długożyciowe. Takie cząstki są szczególnie interesujące i ze względu na swoje unikalne własności są często obecne w kosmologii i fizyce cząstek elementarnych. Dlatego pożądane jest, aby scenariusze fizyki spoza MS przewidujące stany długożyciowe (i CM) były dokładnie zbadane, najlepiej pod komplementarnymi kątaami badań eksperymentalnych, tak jak w przypadku WIMP-ów. W niniejszej rozprawie opisujemy wysiłki w tym kierunku, oparte na różnych poszukiwaniach: rozwijających się eksperymentach umieszczonych wzdłuż osi wiązki zderzaczy cząstek, tzw. fizyka "do przodu", takich jak detektor FASER, które wkrótce będą zbierać dane w LHC; pośrednich poszukiwaniach promieniowania kosmicznego wytworzonego w anihilacjach CM zachodzących w pobliżu Centrum Galaktyki, oraz badaniach promieniowania CMB, między innymi. Podczas gdy badanie podstawowych scenariuszy CM typu WIMP i cząstek długożyciowych w najprostszych rozszerzeniach MS zostało w dużej mierze omówione w literaturze, w niniejszej rozprawie przedstawiamy szereg interesujących efektów fenomenologicznych pojawiających się w bardziej rozbudowanych scenariuszach ciemnego sektora, które mogą być zbadane eksperymentalnie w najbliższych latach. Uwzględnienie tych efektów może mieć istotne implikacje dla zakresu badań zarówno obecnych, jak i planowanych w przyszłości eksperymentów.



*For my family*



## Acknowledgments

First and foremost, I want to thank my family for their continuous support. I am thankful to my supervisor, Prof. Leszek Roszkowski for the opportunity to conduct studies and perform research in his group and to Dr. Sebastian Trojanowski for being my co-advisor, and helping me in many ways, especially at the early stage of my PhD studies which helped me getting started with conducting research. Among many people I interacted with while doing research, I am especially thankful to Dr. Andrzej Hryczuk with whom I had many productive discussions during the work on our joint projects. I also want to thank the rest of my collaborators: Dr. Felix Kling, Prof. Emmanuel Moulin, Dr. Lucia Rinchuso, and Dr. Hab. Enrico Maria Sessolo, for their invaluable input. This work has been supported by the National Science Centre (NCN) research grant No. 2015/18/A/ST2/00748. The use of the CIŚ computer cluster at the National Centre for Nuclear Research is gratefully acknowledged.



# Contents

Acknowledgments . . . . .	xi
List of publications on which this thesis is based . . . . .	xvii
List of Figures . . . . .	xix
List of Tables . . . . .	xxvii
List of Acronyms . . . . .	xxix
<b>1 Introduction</b>	<b>1</b>
<b>2 Standard Cosmological Model and the dark matter problem</b>	<b>5</b>
2.1 Background Universe . . . . .	5
2.2 $\Lambda$ CDM model . . . . .	7
2.3 Evidence for the existence of DM . . . . .	9
2.3.1 Astrophysical evidence . . . . .	9
2.3.2 Cosmological evidence . . . . .	12
2.3.3 DM candidates . . . . .	15
<b>3 Thermal dark matter</b>	<b>21</b>
3.1 Relic density of thermal DM candidate . . . . .	21
3.2 Detection methods . . . . .	27
<b>4 Looking for long-lived particles using secondary production</b>	<b>35</b>
4.1 Introduction . . . . .	35
4.1.1 Renormalizable portals . . . . .	36
4.1.2 Intensity frontier searches for light long-lived particles . . . . .	37
4.1.3 Secondary LLP production . . . . .	40
4.2 Models . . . . .	41
4.2.1 Dark bremsstrahlung . . . . .	42
4.2.2 Inelastic DM . . . . .	42
4.2.3 Dark photon with secluded dark Higgs boson . . . . .	44
4.3 Details of modeling . . . . .	45
4.3.1 Primary production of LLPs . . . . .	45
4.3.2 Signatures involving secondary production of LLPs . . . . .	46
4.3.3 Event rate . . . . .	47
4.4 Results for scattering with nuclei . . . . .	48
4.4.1 Sensitivity reach of future experiments . . . . .	49
4.5 Scattering with electrons in SND at SHiP . . . . .	51
4.6 Conclusions . . . . .	53

<b>5</b>	<b>FASER as neutrino beam-dump experiment at the LHC</b>	<b>55</b>
5.1	Introduction . . . . .	55
5.2	New physics from neutrino scatterings in FASER $\nu$ . . . . .	56
5.2.1	Motivation . . . . .	56
5.2.2	FASER $\nu$ experiment . . . . .	57
5.2.3	Neutrino flux and BSM particle production . . . . .	57
5.2.4	Experimental signatures of new physics . . . . .	58
5.3	Selected BSM scenarios . . . . .	60
5.3.1	Neutrino dipole portal . . . . .	61
5.3.2	Dark gauge boson portal . . . . .	62
5.4	Results . . . . .	63
5.4.1	Turning neutrinos into light with neutrino dipole portal . . . . .	64
5.4.2	Bi-modal $e^+e^-$ spectrum in searches of HNLs and dark gauge bosons . . . . .	66
5.4.3	Probing light HNL in electron scattering . . . . .	68
5.5	Conclusions . . . . .	70
<b>6</b>	<b>Testing supersymmetric dark matter in CTA</b>	<b>71</b>
6.1	Introduction . . . . .	71
6.2	MSSM . . . . .	72
6.3	Neutralino DM . . . . .	73
6.4	Indirect detection of WIMPs . . . . .	75
6.5	Observation of the Galactic Center . . . . .	78
6.6	Bayesian scan for neutralino DM . . . . .	80
6.6.1	The p9MSSM . . . . .	81
6.6.2	Scanning setup and constraints . . . . .	81
6.7	Results . . . . .	83
6.7.1	Neutralino DM . . . . .	83
6.7.2	Underabundant neutralinos . . . . .	86
6.8	Conclusions . . . . .	87
<b>7</b>	<b>Indirect detection of long-lived particles</b>	<b>89</b>
7.1	Introduction . . . . .	89
7.2	Motivation . . . . .	90
7.3	Non-local effects in $\gamma$ -ray DM ID searches . . . . .	91
7.4	Model . . . . .	95
7.5	Relic density . . . . .	99
7.6	Current and future constraints from astrophysics, cosmology and colliders . . . . .	101
7.6.1	Current bounds . . . . .	102
7.6.2	Intensity frontier searches for light dark Higgs boson . . . . .	103
7.6.3	Dark matter detection . . . . .	103
7.6.4	Future Cosmic Microwave Background surveys . . . . .	104
7.7	Results . . . . .	104
7.8	Conclusions . . . . .	108

<b>8</b>	<b>Self-interacting dark matter and the Hubble tension</b>	<b>111</b>
8.1	Introduction . . . . .	111
8.2	Hubble tension and other selected problems in the $\Lambda$ CDM model and astroparticle physics . . . . .	112
8.3	Dark matter self-interactions . . . . .	116
8.4	The mechanism . . . . .	119
8.5	Phenomenology . . . . .	121
8.5.1	Thermal history . . . . .	121
8.5.2	Late time decays . . . . .	122
8.5.3	Impact of late decays on the $H_0$ tension and structure for- mation . . . . .	124
8.6	Results . . . . .	127
8.6.1	The SIDM regime (A) . . . . .	127
8.6.2	The SIDM from late decays regime (B) . . . . .	128
8.6.3	The ultra SIDM regime (C) . . . . .	129
8.7	Conclusions . . . . .	130
<b>9</b>	<b>Conclusions</b>	<b>131</b>
<b>A</b>	<b>Frequently used cosmology and particle physics formulae</b>	<b>135</b>
A.1	Units . . . . .	135
A.2	Phase space . . . . .	135
A.3	Decay width and cross section definitions . . . . .	136
A.4	Bremsstrahlung . . . . .	136
A.5	Non-relativistic thermally averaged cross section . . . . .	138
<b>B</b>	<b>Appendix for Chapter 4</b>	<b>139</b>
B.1	Decay branching ratios, $(g - 2)_\mu$ and all that . . . . .	139
B.1.1	$(g - 2)_\mu$ contribution from $A'$ . . . . .	139
B.1.2	Primary production of LLPs . . . . .	139
B.1.3	LLPs decays . . . . .	141
B.2	Scattering cross sections for secondary LLP production . . . . .	142
B.2.1	$2 \rightarrow 2$ scatterings . . . . .	142
<b>C</b>	<b>Appendix for Chapter 5</b>	<b>145</b>
C.1	HNL production in neutrino interactions . . . . .	145
C.1.1	Coherent scatterings with nuclei . . . . .	145
C.1.2	Elastic incoherent scatterings off individual nucleons . . . . .	146
C.1.3	Scattering off electrons . . . . .	147
C.2	Decays widths . . . . .	147
<b>D</b>	<b>Appendix for Chapter 6</b>	<b>151</b>
D.1	Superalgebra and superspace . . . . .	151
D.2	Constructing SUSY Lagrangian . . . . .	153

<b>E</b>	<b>Appendix for Chapter 7</b>	<b>155</b>
E.1	Particle physics formulae . . . . .	155
E.1.1	Decay widths . . . . .	155
E.1.2	Annihilation cross sections . . . . .	156
E.2	Spectrum of gamma rays induced by DM cascade . . . . .	159

## List of publications on which this thesis is based

This thesis contains results which were published in the following papers:

**Paper I** A. Hryczuk, K. Jodłowski, E. Moulin, L. Rinchuso, L. Roszkowski, E. M. Sessolo et al., *Testing dark matter with Cherenkov light - prospects of H.E.S.S. and CTA for exploring minimal supersymmetry*, *JHEP* **10** (2019) 043, [[1905.00315](#)]

**Paper II** K. Jodłowski, F. Kling, L. Roszkowski and S. Trojanowski, *Extending the reach of FASER, MATHUSLA, and SHiP towards smaller lifetimes using secondary particle production*, *Phys. Rev. D* **101** (2020) 095020, [[1911.11346](#)]

**Paper III** A. Hryczuk and K. Jodłowski, *Self-interacting dark matter from late decays and the  $H_0$  tension*, *Phys. Rev. D* **102** (2020) 043024, [[2006.16139](#)]

**Paper IV** K. Jodłowski and S. Trojanowski, *Neutrino beam-dump experiment with FASER at the LHC*, *JHEP* **05** (2021) 191, [[2011.04751](#)]

and the preprint:

**Paper V** K. Jodłowski, L. Roszkowski and S. Trojanowski, *Indirect detection of long-lived particles in a rich dark sector with a dark Higgs boson portal*, [2112.11993](#)

Work during my PhD also resulted in the following preprint and a conference proceeding:

**Paper VI** L. A. Anchordoqui et al., *The Forward Physics Facility: Sites, Experiments, and Physics Potential*, [2109.10905](#)

**Paper VII** K. Jodłowski, *Self-interacting dark matter from late decays and the  $H_0$  tension*, [2110.11622](#)



# List of Figures

1.1	Cartoon showing the SM and a dark (hidden) sector connected by a portal mediator. . . . .	2
1.2	Tag cloud of topics covered in this thesis. . . . .	3
2.1	Temperature power spectrum of the CMB measured by <i>Planck</i> [20]. The best-fit within the $\Lambda$ CDM model is plotted in light blue on the top, while residuals are shown on the bottom. . . . .	8
2.2	Preferred regions in the $(\Omega_m, \Omega_\Lambda)$ plane obtained as a $\Lambda$ CDM fit to various cosmological observations (assuming the Universe is flat). Note significant reduction in error regions and improvement of overlap of best-fit regions achieved in the last decade - compare data from 2011 [21] (left) and from 2020 [22] (right). . . . .	9
2.3	Rotation curve for the Messier 33 galaxy. The expected shape of the curve is indicated by the gray dashed line, while the solid line corresponds to the scenario where the DM halo surrounds the galaxy. The yellow and blue dots denote the observational data. Taken from [35]. . . . .	10
2.4	Cluster of galaxies Abell2029. On the left, the distribution of X-ray gas is shown, while the distribution of galaxies is on the right. Credit: X-ray: NASA/CXC/UCI/A.Lewis et al.; Optical: Pal.Obs.DSS. . . . .	11
2.5	Left: duplicated images of the galaxy marked in light blue which were produced by gravitational lensing of the foreground 0024+1654 cluster (yellow, at the center). Right: Mass reconstruction of the lens which shows peaks of baryonic matter embedded in a smooth background of non-luminous matter. Taken from [36] and <a href="#">Hubble Space Telescope website</a> . . . . .	12
2.6	Optical, X-ray (pink), and weak gravitational lensing (blue) image of the Bullet Cluster (1E 0657-558). Taken from <a href="#">the Chandra X-Ray Observatory website</a> . . . . .	13
2.7	Left: comparison of observations and simulations of N-body simulations of structure formation [37]. Right: the cosmic web obtained in <a href="#">The Millennium Simulation</a> . Taken from [30]. . . . .	14
2.8	A cartoon of particle and composite DM candidates as a function of their mass. Also shown are the general constraints for each class of candidates. Figure credit: Sophia Andalaro. . . . .	16

2.9	Multiple particle DM candidates complementary to those shown in Fig. 2.8 as a function of their mass. Taken from [87]. . . . .	16
3.1	Evolution of the comoving yield of thermal relic of mass $m_1 = 150$ GeV as a function of the dimensionless inverse temperature $x$ . Three lines are shown, indicating from the top: solid line - the observed relic density obtained for the canonical annihilation cross sections, dashed line - a magnitude smaller relic density resulting from equally larger annihilation cross sections, and dotted - equilibrium yield. Freeze-out happens around $x \sim 25$ . . . . .	25
3.2	Sommerfeld enhancement for wino DM annihilating into photons - see Chapter 6 for discussion of this effect which significantly influences DM ID signal. Taken from [177]. . . . .	26
3.3	Complementary program of three main search strategies for WIMPs: collider searches (bottom), direct detection (left), and indirect detection searches (top). Moreover, astrophysical observations, <i>e.g.</i> , the Bullet Cluster can constrain internal interactions within the DS, like DM self-interactions. Modified figure taken from [188]. . . . .	28
3.4	Current exclusion limits for spin-independent WIMP scattering cross section with SM nuclei in direct detection experiments. The limits shown are from current (region filled in green) and near future observations. Note the gold dashed line denoting the irreducible neutrino floor which we discuss in the text. Taken from the recent APPEC Committee Report [87]. . . . .	29
3.5	Plot summarizing upper bounds on the DM annihilation cross section as a function of the DM mass for different SM channels using state-of-the art observations. Conservative bounds were chosen when few were available. The benchmark value of the thermal annihilation cross section is indicated by the dashed gray line. Updated plot taken from [211]. . . . .	30
3.6	Comparison of exclusion limits for spin-dependent WIMP scattering cross section with SM particles obtained in direct detection and collider searches (LHC and Tevatron). Taken from [227]. . . . .	31
4.1	Schematic structure of the detectors considered. From top to bottom, clockwise: FASER (taken from [274]), MATHUSLA (taken from [275]), and SHiP (taken from [258]). . . . .	38

4.2	Schematic illustrations of LLP secondary production that occurs upstream of the detector, allowing intensity frontier searches (this is a broad class of searches that look for light and very weakly-interacting particles that may have escaped detection so far due to lack of sufficient luminosity) to also probe shorter lifetime regime. Top: primary (blue line) and the secondary production (right line) of the light long-lived particle $LLP_2$ , followed by its decays in the decay vessel. Bottom: signatures related to LLP scattering with electrons inside neutrino emulsion detectors, here shown for the SND detector at SHiP, while a similar, more extended analysis dedicated to the study of neutrino non-standard interactions is described in the next chapter for the FASER $\nu$ detector. See also Fig. 4.1. . . .	39
4.3	Results for the model with a single dark matter particle and a dark photon produced by dark bremsstrahlung, as discussed in Section 4.2.1. The sensitivity corresponding to secondary LLP production is shown by colored shaded regions (left) and lines with numbers of events resulting from secondary production (right). . .	49
4.4	The same as Fig. 4.3, but for the model with iDM discussed in Section 4.2.2. On the right, the projected numbers of events in FASER 2 are indicated by blue lines. . . . .	49
4.5	The same as Fig. 4.3, but for a model with a secluded dark Higgs boson discussed in Section 4.2.3. . . . .	50
4.6	Results corresponding to additional signatures employing LLP electron scattering in the SND obtained for the model with inelastic DM (left) and the model with dark photon and secluded dark Higgs boson (right). . . . .	53
5.1	Main results for the dipole portal models: left) universal coupling to all of the neutrino flavors, right) $\nu_\tau$ -specific coupling. The green lines indicate the expected number of the signal events in FASER $\nu$ 2 involving high-energy photons appearing inside the decay vessel. The red lines correspond to such photons appearing in the emulsion detector. The yellow line represents the expected exclusion limit from the search for electron scattering events. The blue shaded area corresponds to scenarios with an increased number of relativistic degrees of freedom in the early Universe. . . . .	65
5.2	Results for the model with universal coupling $\mu_N$ dipole portal: left) energy spectrum of photons coming from HNL decays for the benchmark scenarios, as indicated in the plots, and right) three-body HNL decay branching ratio $N \rightarrow \nu(\gamma^* \rightarrow \ell\ell)$ where $\ell = e$ (solid black line) or $\mu$ (dashed black), as a function of the HNL mass $m_N$ . . . . .	66

5.3	<p><i>Left:</i> FASER 2 sensitivity reach in the model with dark gauge boson connecting the HNL and SM particles. Green line indicates the sensitivity based on detection of the <math>e^+e^-</math> pair in a sequential process <math>\nu Z \rightarrow Z(N \rightarrow \nu Z_D)</math> with subsequent <math>Z_D \rightarrow e^+e^-</math> decay. The yellow line corresponds to the expected sensitivity based on the electron scattering signature. <i>Right:</i> Energy spectrum of <math>e^+e^-</math> pairs from <math>Z_D</math> decays. . . . .</p>	67
5.4	<p>Results for the model with dark gauge boson heavier than HNL, <math>m_{Z_D} = 8m_N</math>, and with the dominant third generation neutrino mixing, <math>U_{\tau N}</math>. <i>Left:</i> Sensitivity of FASER 2 and SHiP in the <math>(m_N, U_{\tau N})</math> plane. The additional FASER 2 sensitivity resulting from secondary HNL production is shown as the green line while the red line corresponds to the additional FASER 2 coverage due to HNL production in the <math>Z_D \rightarrow NN</math> decays. The yellow solid line is the expected reach in the inelastic and elastic scatterings off electrons. <i>Right:</i> The expected number of elastic scattering events in the CHARM-II (blue solid line) and FASER 2 (red solid line). . . . .</p>	69
6.1	<p>Main annihilation channels of the lightest neutralino depending on its composition. Shown from left to right are the bino and wino. The center panel illustrates the funnel annihilation - which takes place also for other neutralino compositions, while the last two panels present the coannihilations of the lightest higgsino with a heavier neutralino and chargino, respectively. Taken from [409, 416]. . . . .</p>	75
6.2	<p>A sketch of the imaging atmospheric Cherenkov technique used by, <i>e.g.</i>, H.E.S.S., and CTA. Taken from [417]. . . . .</p>	76
6.3	<p>Comparison of the most common DM density profiles studied in the literature [418] together with their corresponding parameters. Taken from [419]. . . . .</p>	77
6.4	<p>Photon spectra resulting from annihilation of a <math>m_{\text{DM}} = 100</math> GeV non-relativistic WIMP, as a function of the fraction of photon kinetic energy to the WIMP mass <math>x = E_\gamma/m_{\text{DM}}</math>. Based on the tabulated PPPC spectra [420]. . . . .</p>	78
6.5	<p>Schematic illustration of ID observations in the Milky Way. On the left and bottom right, galactic coordinates are shown, where the Sun is the origin, <math>l</math> is the galactic longitude, and <math>b</math> is the galactic latitude. The figure is based on several illustrations taken from [421]. . . . .</p>	79
6.6	<p>The projected sensitivities of CTA to the annihilation cross section as a function of DM mass <math>m_\chi</math>, derived from 500 hour observations of the inner Galactic halo. Three halo profiles were considered: Cored Einasto (dashed double-dotted), NFW (dotted) and Einasto (dashed lines). Annihilation of DM (a) to the specific SM final states, and (b) to two monochromatic photons. The solid line represents the limit from H.E.S.S. [431]. . . . .</p>	80

6.7	Result of numerical p9MSSM scan shown in $(m_\chi, \sigma v_0)$ plane. Color coding reflects the composition of the lightest neutralino according to the legend. The predicted CTA sensitivity is shown as a thick (Einasto), or thin (Cored Einasto) dashed double-dotted line. To emphasize the complementarity between continuous and monochromatic photon searches, we mark with dark gray triangles the points whose $\sigma v_{\gamma\gamma}$ is in the range of CTA. . . . .	84
6.8	Same as in Fig. 6.7, but shown in the $(m_\chi, \sigma_p^{\text{SI}})$ plane (left), and in the $(\sigma_p^{\text{SI}}, \sigma v_0)$ plane (right). . . . .	85
6.9	Result of numerical p9MSSM scan which only implements the relic density constraint as an upper bound (underabundant neutralinos), shown in (a) $(m_\chi, (\Omega_\chi h^2/0.12)^2 \times \sigma v_0)$ plane, and (b) in $(m_\chi, \sigma v_0)$ plane. Legend is the same as in Fig. 6.7. . . . .	86
7.1	Cartoon of indirect detection of light long-lived particles in observations of the GC region of the Milky Way. We illustrate the region of interest in the analysis as a cone with the aperture angle $2\psi_0$ . A key feature of such a scenario is the galactic-scale separation between the position of DM annihilations near the Galactic Center (LLP production, marked in red) and the LLP decays (blue). It introduces non-locality, which we discuss in detail in the text. We also show typical distance scales relevant for this analysis. . . . .	92
7.2	Left: The ratio of the integrated photon fluxes obtained for increasing decay length $d$ of the mediator and in the standard regime of prompt decays shown with the horizontal black solid line. The results are shown for the toy model with the ratio between the DM and mediator particles masses $m_{\text{DM}}/m_{\text{med}} = 10$ . The mediator decays dominantly into two photons, $\text{med} \rightarrow \gamma\gamma$ . Right: The CTA sensitivity for the secluded WIMP DM scenario shown in the $(m_{\text{DM}}, \langle\sigma v\rangle)$ plane. The solid black line corresponds to the standard reach assuming the mediator promptly decays into light quarks, cf. [474]. The red lines are obtained by taking into account the non-local effects for two different regions of interest, as indicated in the plot. See the text for more details. . . . .	94
7.3	Cartoon of the model in which the DS is connected to the SM via a light dark Higgs boson portal ( $h_D$ ). It mixes with the SM Higgs particle ( $H$ ) by the mixing angle $\theta_{h_D H}$ . The SM gauge symmetry is extended by the $U(1)'$ and $U(1)''$ groups, leading to new gauge bosons, $A'$ and $A''$ , respectively. The fields charged under the first of those groups are colored green and those charged under the second are colored blue. The DM consists almost entirely of the heavy complex scalar $\chi$ , which interacts directly only with the lighter DM particle, $\eta$ , through an exchange of the auxiliary scalar field $\phi$ . . . . .	96
7.4	Left: a schematic illustration of the DS particle mass hierarchy. The unstable mediators are denoted in dark-red, while the two stable DM species - in black. Right: processes leading to DM indirect detection signatures. . . . .	98

7.5	Left: Comoving energy densities, $(mY)_i$ , for two-component DM and the unstable dark vector undergoing thermal freeze-out obtained by solving the Boltzmann equations Eq. (7.5.1). Right: A schematic plot of the unstable dark vector yield, $(mY)_{A'}$ , as a function of the dark coupling constant $g_D$ shown with the black dashed line. The regions constrained by the BBN and CMB bounds on very long-lived $A'$ , and by a perturbativity bound are gray-shaded. The dominant DM yield, $(mY)_\chi$ , is also indicated with the horizontal black dotted line on top of the figure. This yield is not constrained by the BBN bounds. The expected signal rates in DM indirect detection searches grow with increasing $g_D$ as marked with blue color. . . . .	102
7.6	Left: Excluded parameter space of our model (gray) and sensitivity projections of the future experiments (colored dotted lines); shown in the $(m_{A'}, g_D)$ plane. We fixed the other parameters as follows: $m_{h_D} = 500$ MeV, $m_\eta = 150$ GeV, $m_\chi = 1.5$ TeV, $\lambda_{h_D\eta} = 4 \times 10^{-6}$ , and $\tilde{\epsilon} = 10^{-6}$ . For all points in the plot we require that $\Omega_\chi h^2 \simeq 0.12$ . The black dash-dotted lines correspond to fixed values of the $A'$ lifetime, $\tau_{A'}$ . Right: Magnification of the region marked with gray rectangle on the left, showing the impact of non-local effects on the expected sensitivity of CTA. . . . .	105
7.7	Same as the left panel of Fig. 7.6 but for different values of the fixed parameters: $m_{h_D} = 20$ MeV, $\lambda_{h_D\eta} = 4 \times 10^{-7}$ (left) and $m_{h_D} = 250$ MeV, $\lambda_{h_D\eta} = 4 \times 10^{-5}$ (right). . . . .	107
8.1	Combined results of experiments determining $H_0$ . Note the significant discrepancy between the values obtained by the late-Universe observations ( <i>e.g.</i> , SHOES [512]) indicated by cyan vertical band and the early-Universe (pre-recombination) observations ( <i>e.g.</i> , <i>Planck</i> [18]) indicated by the light pink vertical band. All values were determined under the assumption of the Lambda Cold Dark Matter (Standard Cosmological Model) ( $\Lambda$ CDM) model. Taken from [511], where one can find an extensive discussion and a list of the relevant references.	113
8.2	A DM particle in the central region of the DM halo is ejected from it due to the scattering with an energetic outer DM particle. Such dark matter self-interactions result in a core-like DM density profile near the center of the halo, as favored by observations (“cusp vs. core” problem). Taken from [541]. . . . .	116
8.3	A simplified illustration of the model in which the proposed mechanism is implemented. The SM is connected to the DS via a Higgs portal mediator field $S$ . We also introduce a Dirac fermion field $\chi$ charged under spontaneously broken $U(1)_{\text{dark}}$ (this symmetry breaking may, but does not have to be associated with the $Z_2$ breaking), resulting in a massive vector $A^\mu$ . . . . .	120

8.4	Thermal history of the model: evolution of the energy densities of $S$ (blue), $\chi$ (black) and $A^\mu$ (orange) as a function of $x = m_\chi/T$ . Representative parameters were chosen, which lead to early (regime A, solid lines), late (regime B, dashed) and very late (regime C, dotted) decays of $S$ . . . . .	121
8.5	Constraints on the cosmological parameters for the B (blue) and C (red) regimes of DCDM and $\Lambda$ CDM. Both DCDM regimes lead to slightly better values of $H_0$ and $\sigma_8$ ( $\Omega_{\text{matter}}/0.27$ ) <sup>0.3</sup> than $\Lambda$ CDM. . . . .	126
8.6	Results of the analysis relevant for the SIDM regime (A) in the $m_A$ - $m_\chi$ plane. We show with the colorful shading the region in the parameter space of the model for which the self-interaction cross section $\sigma_{\text{tr}}/m_\chi$ is in the range preferred by the small-scale problems of the $\Lambda$ CDM model, i.e., between 0.1 and 10 cm <sup>2</sup> /g. The green-shaded and gray-shaded areas indicate too weak and too strong DM self-interactions, respectively. The results are presented for two representative values of the coupling constant $\alpha_\chi = 0.0001$ (left) and $\alpha_\chi = 0.1$ (right). . . . .	127
8.7	Results of the numerical scans performed for the regime B - the SIDM regime in which late $S$ decays take place. Color coding indicates the value of the coupling $g$ leading to $\sigma_{\text{tr}}/m_\chi \sim (1 \pm 10\%)$ cm <sup>2</sup> /g. In addition, the dark green shading marks the region at $1\sigma$ level around the mean values of DCDM parameters that relax the $H_0$ tension. . . . .	129
8.8	Results of regime C, where the Hubble tension is mildly relaxed (light blue region) and self-interactions are strong enough to accelerate SMBHs formation rates (green and light blue regions). . . . .	130
B.1	Main channels of dark photon primary production as a function of its mass. Taken from [311]. . . . .	140
E.1	Left: The lifetime of $A'$ decaying into $h_D$ and $A''$ as a function of $m_\eta$ (particle flowing in the loop). Right: Dotted black line denotes the $\langle\sigma v\rangle$ for $\chi\bar{\chi} \rightarrow \eta\bar{\eta}A'$ which is relevant for $\chi$ ID, as a function of $m_{A'}$ , while the solid black line corresponds to the $\langle\sigma v\rangle$ yielding $\Omega_\chi h^2 \sim 0.1$ . . . . .	156
E.2	Heavy DM annihilation processes contributing to the $\chi$ relic density.	157
E.3	Feynman diagrams for the $\eta$ annihilation processes into a pair of dark vectors. . . . .	157
E.4	Feynman diagrams for the $\eta$ annihilation processes into a pair of dark Higgs bosons. . . . .	158
E.5	Feynman diagrams for the dark vector annihilations into light dark Higgs bosons. . . . .	158

E.6 Differential flux of photons produced in the DM cascade, shown as a function of the photon energy. The result for the standard scenario is indicated by the black solid line. The black dash-dotted, red dotted, and blue dashed lines correspond to the long-lived regime where the relevant typical decay length of boosted  $A$ 's equal to 0.1, 3, and 30 kpc, respectively. . . . . 159

# List of Tables

6.1	MSSM fields before spontaneous electroweak symmetry breaking. . .	73
6.3	Parameters of DM density profiles we considered: Einasto, NFW, and Cored Einasto. . . . .	75
6.2	A table beside a figure . . . . .	77
6.4	The p9MSSM parameter ranges used in our scans. All masses and trilinear couplings are expressed in units of TeV. . . . .	82
8.1	Results of the Monte Carlo Markov Chain scan - we show the con- straints on cosmological parameters. The uncertainties on the mean values are given at the $1\sigma$ (68%) level. The values of $\Gamma$ and $H_0$ are given in units of km/s/Mpc. . . . .	126



## List of Acronyms

ALP	axion-like particle . . . . .	18
BAO	Baryon Acoustic Oscillations . . . . .	12
BBN	Big Bang Nucleosynthesis . . . . .	15
BG	background . . . . .	38
BSM	beyond the Standard Model . . . . .	1
CDM	cold dark matter . . . . .	8
CMB	Cosmic Microwave Background . . . . .	5
CoM	center of mass . . . . .	56
CTA	Cherenkov Telescope Array . . . . .	3
DCDM	decaying dark matter . . . . .	114
DD	direct detection . . . . .	3
DH	dark Higgs . . . . .	36
DM	dark matter . . . . .	1
DS	dark sector . . . . .	2
EFT	effective field theory . . . . .	31
FLRW	Friedmann–Lemaître–Robertson–Walker . . . . .	5
GC	Galactic Center . . . . .	30
GUT	Grand Unified Theory . . . . .	20
HNL	heavy neutral lepton . . . . .	37
ID	indirect detection . . . . .	3
iDM	inelastic dark matter . . . . .	43
IP	interaction point . . . . .	42
$\Lambda$ CDM	Lambda Cold Dark Matter (Standard Cosmological Model)	xxiv
LHC	Large Hadron Collider . . . . .	3
LLP	long-lived particle . . . . .	3
MACHO	Massive Compact Halo Object . . . . .	15
MC	Monte Carlo . . . . .	45
MOND	Modified Newtonian Dynamics . . . . .	12
MSSM	Minimal Supersymmetric Standard Model . . . . .	3
PBH	primordial black hole . . . . .	15
QCD	Quantum Chromodynamics . . . . .	17
RoI	region of interest . . . . .	62
SE	Sommerfeld enhancement . . . . .	3
SIDM	self-interacting dark matter . . . . .	4

SM	Standard Model . . . . .	1
SMBH	supermassive black hole . . . . .	78
SND	Scattering and Neutrino Detector . . . . .	40
SUSY	supersymmetry . . . . .	2
UV	ultraviolet . . . . .	2
WIMP	Weakly Interacting Massive Particle . . . . .	3

# Chapter 1

## Introduction

The Universe has fascinated human beings since the beginning of our existence, but modern scientific efforts did not begin until five hundred years ago with the formulation of the scientific method by Galileo Galilei, while detailed studies devoted to the fundamental nature of the Universe did not begin until about 1-2 centuries ago. Research conducted since then has allowed scientists to formulate and extensively test theories of very small scales that describe interactions of elementary particles - the Standard Model (SM), and very large scales, like those characteristic of the entire Universe - the  $\Lambda$ CDM. Although both of these theories agree very well with almost all observational data, it is widely believed that they are not a definitive description of the Universe valid up to arbitrarily high energies and to the earliest moments of our Universe's history.

One of the greatest puzzles is the fact that invisible dark matter (DM) outweighs ordinary matter by a ratio of five to one, while its nature is not yet known. The research described in this thesis is motivated by this problem and focuses on scenarios beyond the Standard Model (BSM) and phenomena that: (i) are well motivated, *e.g.*, they also address other problems of the SM and (ii) can be tested in near-future experiments.

The phenomenological aspects of DM are particularly important because any realistic BSM theory should provide a DM candidate, along with its production mechanism and possible means of detection. Although all unambiguous evidence for the existence of DM is gravitational, it does not follow that a DM particle (assuming it is a particle) has to interact only gravitationally, with no connection to the SM particles. Such gravitationally secluded DM would be a highly undesirable scenario because it would render any hope of direct or indirect DM detection unsuccessful. These detection strategies are based on DM scatterings with SM nuclei in deep underground detectors and DM annihilations into SM particles taking place near the center of DM galactic halo, respectively. However, a generic BSM theory, on top of explaining the nature of DM, is expected to preserve the successes of the SM while providing a solution to at least some of its other problems, such as: (i) the hierarchy problem, (ii) the CP-problem, and (iii) the neutrino mass problem - which requires the introduction of some form of connection with the SM. In the following we briefly review the main extensions of the SM that are discussed in more detail further in the thesis.

We start with the most simplified approaches, *e.g.*, those in which one

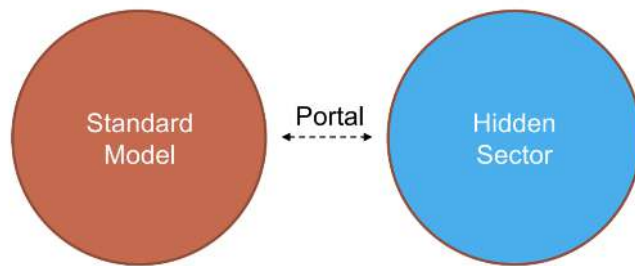


Figure 1.1: Cartoon showing the SM and a dark (hidden) sector connected by a portal mediator.

introduces a mediator (portal) particle connecting the SM particles to a hypothetical set of yet unobserved particles, a so-called dark sector (DS), as shown in Fig. 1.1. The phenomenology of BSM scenarios of this type is easier to analyze because of their relative simplicity, but still illustrates the most important effects. Moreover, such portals may be an effective description - or low-energy limit - of some ultraviolet (UV)-complete BSM theory that is defined at energies higher than those currently achievable experimentally, such as the grand unification energy scale,  $\sim 10^{16}$  GeV, or even the Planck energy scale,  $10^{19}$  GeV. We discuss an example of such a theory - supersymmetry (SUSY) - in Chapter 6.

It turns out that the minimal portal scenarios can be realized in only 3 ways,<sup>1</sup> assuming that the operators are renormalizable<sup>2</sup> and gauge invariant. Although such minimal DM models are too simplistic to constitute a viable BSM theory, they are useful because: (i) they can capture important aspects of complex physics connected to DM, (ii) they can be viewed as toy models in which the structure of the theory is clear and calculations become feasible, and (iii) they provide important benchmarks for detection capabilities in direct, indirect and collider experiments. In fact, such most simplified scenarios have already been thoroughly discussed in the literature - both from the theoretical and experimental sides. However, it is understood that simplified models must eventually be replaced by more fundamental approaches.

In light of this, while the research described in this thesis is largely motivated by simplified models of this type, we actually focus on less simplified models that introduce more degrees of freedom. Such models can lead to *additional experimental signatures* - making them an interesting frontier for the upcoming searches for new physics - and provide a description that is correct up to very high energies. In particular, we will highlight such new effects in the following, as the detection of any associated signature of this type would indicate the existence of a richer dark sector than is often assumed.

In this context, we devote a large part of the thesis to light so-called new physics - which consists of BSM species connected to the SM - as illustrated in Fig. 1.2. We explore the impact of such light new physics models from the perspective

---

<sup>1</sup>We discuss them in detail in Chapter 4.

<sup>2</sup>It means that their mass dimension is 4. In this thesis we work in natural units, cf. Appendix A.1, therefore every dimensional quantity will be expressed in appropriate powers of mass.



Figure 1.2: Tag cloud of topics covered in this thesis.

of both particle physics and cosmology. We introduce basic aspects of modern cosmology and astroparticle physics related to DM studies in Chapters 2 and 3. We then discuss new experimental effects expected in rich dark sector scenarios with long-lived particles (LLPs) in Chapters 4 and 5. We put a particular emphasis on the relevant collider searches at the Large Hadron Collider (LHC), including its far-forward region and in proposed future experiments.

We also discuss a UV-complete model - the Minimal Supersymmetric Standard Model (MSSM) where we explore the prospects for indirect detection (ID)<sup>3</sup> of the lightest neutralino (electrically neutral, fermionic particles made from the mixing of the supersymmetric partners of the  $Z$  boson, photon and the Higgs boson) DM, as discussed in Chapter 6. Although searches at the LHC and direct detection (DD) have largely limited the possibilities for this DM candidate, we have found excellent prospects for a  $\sim 1$  TeV scale DM particle which we project to be largely within reach of the Cherenkov Telescope Array (CTA). ID experiments may be particularly suited for searches for heavy, multi-TeV Weakly Interacting Massive Particles (WIMPs) due to the Sommerfeld enhancement (SE) effect<sup>4</sup> and the formation of bound states that can dramatically amplify the signal coming from annihilations of WIMPs. In the mass regime we consider, the first effect dominates and we fully take it into account in our analysis by dedicated numerical procedures, improving over previous studies.

In Chapter 7 we discuss a rich BSM scenario with heavy WIMPs, long-lived particles, and a light scalar mediator. There, we focus on the interplay between searches for light new physics done at colliders, future CBM surveys constraining late energy injections, and ID searches for heavy DM annihilating into LLPs - unstable particles characterized by a significant decay length; here compared to galactic scales. Among other things, we found distinctive signatures in ID searches

<sup>3</sup>Such searches look for cosmic rays produced by annihilation of DM particles in the galactic halo.

<sup>4</sup>See discussion in Section 3.1.

arising from the effective long-lived nature of the WIMP annihilations that proceed through a cascade with an intermediate LLP. As a result, there are non-local ID effects that have been largely unexplored in previous studies, and which strongly distinguish such a scenario from ordinary WIMPs.

Finally, in Chapter 8 we explore another BSM scenario consisting of both light and heavy new species which could lead to novel phenomenological effects. Specifically, we focus on cosmological impact of self-interacting dark matter (SIDM) which is produced by late decays taking place after the recombination. We find several interesting regimes for such a scenario, including one that could simultaneously resolve the small-scale problems of  $\Lambda$ CDM<sup>5</sup> and the recently uncovered anomaly in the early and late Universe measurements of the present-day rate of the expansion of the Universe (the Hubble tension).

We provide our conclusions in Chapter 9, while Appendices A to E contain results that are complementary to the main discussion.

The thesis is organized as follows. We present:

- the  $\Lambda$ CDM model, focusing on DM in Chapter 2,
- thermal production of WIMP DM in Chapter 3,
- secondary production of LLPs in less-simplified scalar and vector portals in Chapter 4,
- probing non-standard neutrino interactions in the far-forward region of the LHC in Chapter 5,
- supersymmetric DM candidate - the lightest neutralino - detection at CTA in Chapter 6,
- ID of LLPs in a less-simplified scalar portal model in Chapter 7,
- new production mechanism of SIDM connected to the Hubble tension in Chapter 8,
- finally, our conclusions are in Chapter 9.

---

<sup>5</sup>See Section 2.3.2 for brief discussion of these problems.

# Chapter 2

## Standard Cosmological Model and the dark matter problem

### 2.1 Background Universe

Modern cosmology<sup>1</sup> is based on Einstein’s Theory of General Relativity and the assumptions of homogeneity and isotropy at large scales of the Universe. This is the basis of the so-called “Cosmological Principle”. An example of the validity of this principle is the Cosmic Microwave Background (CMB) where deviations from ideal blackbody radiation due to anisotropy occur only at a relative level of  $\sim 0.01\%$ . We discuss the CMB in some detail in Section 2.3.2. Under these assumptions, one can derive the unique solution to Einstein’s equations, called the Friedmann–Lemaître–Robertson–Walker (FLRW) metric [10–12]

$$ds^2 = dt^2 - a^2(t) \left( \frac{dr^2}{1 - \kappa r^2} + r^2 d\Omega^2 \right), \quad (2.1.1)$$

where  $\kappa \in \{-1, 0, 1\}$  is a discrete parameter that corresponds to open, flat and closed universe, respectively, and  $d\Omega = d\phi d\cos\theta$  is the angular volume element in spherical coordinates. Due to assumptions of isotropy and homogeneity, the scale factor  $a$  depends only on time  $t$ . Using it, one introduces the Hubble parameter

$$H = \frac{\dot{a}}{a}, \quad (2.1.2)$$

where the dot denotes the derivative with respect to time. Experimentally, it is more convenient to parametrize the scale factor by a redshift  $z$

$$a = \frac{a_0}{1 + z} = \frac{1}{1 + z}, \quad (2.1.3)$$

where we use the convention that the scale factor now, denoted  $a_0$ , is equal to 1.

Since the *Wilkinson Microwave Anisotropy Probe*<sup>2</sup> (*WMAP*) observations [13], the expanding flat Universe model is better reconciled with the data which

---

<sup>1</sup>Extensive discussion of the topic can be found in the textbooks [8, 9].

<sup>2</sup>It was a NASA probe which operated from 2001 to 2010 and measured the anisotropy in the CMB with exquisite precision.

simplifies the metric to the following form:

$$ds^2 = dt^2 - a^2(t) (dr^2 + r^2 d\Omega^2). \quad (2.1.4)$$

The flat geometry of the Universe is also favored because it is one of the predictions of the theory of inflation, a leading theory of the origin of cosmological perturbations, see recent review [14].

The dynamics of any metric tensor  $g_{\mu\nu}$  is governed by Einstein's equations,

$$R_{\mu\nu} = 8\pi G_N \left( T_{\mu\nu} - \frac{1}{2} T g_{\mu\nu} \right), \quad (2.1.5)$$

where  $G_N$  is Newton's gravitational constant,  $R_{\mu\nu}$  is Ricci's tensor, and  $T_{\mu\nu}$  is the energy-momentum tensor which trace is  $T$ :  $T_{\mu\nu} g^{\mu\nu} = T$ . See, *e.g.*, textbook [15] for detailed exposition of General Relativity.

The matter content of the Universe can be modeled as a perfect fluid, whose energy-momentum tensor has the following form, due to the assumptions of isotropy and homogeneity

$$T_v^\mu = \text{diag}(-\rho, p, p, p), \quad (2.1.6)$$

where  $\rho$  is the fluid's energy density, while  $p$  is its pressure.

For  $g_{\mu\nu}$  given by Eq. (2.1.4), Einstein's equations lead to the following equations, first derived by Friedmann [10]:

$$\begin{cases} H^2 = \frac{8\pi G}{3} \rho, \\ \dot{H} + H^2 = -\frac{4\pi G}{3} (\rho + 3p), \\ \dot{\rho} = -3H(\rho + p). \end{cases} \quad (2.1.7)$$

Assuming that the fluids obey an equation of state (a relation between thermodynamic state variables) which takes the following form

$$p = w\rho, \quad (2.1.8)$$

where  $w$  is a constant, allows one to find an analytic solution of the last equation of Eq. (2.1.7) which is equivalent to the conservation of energy condition. Its solution is of the form

$$\rho \propto a^{-3(1+w)}. \quad (2.1.9)$$

Some special cases are:

- non-relativistic matter (dust):  $w = 0$ ,  $p = 0$ , and  $\rho_m \propto a^{-3}$ . Cold DM and non-relativistic SM particles are described by this equation of state.
- Relativistic particles (radiation):  $w = 1/3$ ,  $p = \rho/3$ , and  $\rho_m \propto a^{-4}$ . Describes photons and any other relativistic components of the Universe (*e.g.*, neutrinos in the early Universe).
- Dark energy:  $w = -1$ ,  $p = -\rho$ , and  $\rho_m \propto a^0 = \text{const}$ . It is also known as vacuum energy density which is believed to cause an accelerating expansion of the Universe at late times, cf. recent review [16].

- Kination:  $w = 1$ ,  $p = \rho$ , and  $\rho_m \propto a^{-6}$ . Describes the hypothetical period in the early Universe after inflation ends, in which the energy density is dominated by the kinetic energy of the inflaton [17].

For further discussion, it is useful to introduce the following dimensionless energy density parameter – often called abundance – of species  $i$ :

$$\Omega_i \equiv \frac{\rho_i}{\rho_c} = \frac{8\pi G \rho_i}{3H^2}, \quad (2.1.10)$$

where  $\rho_c = 3H^2/(8\pi G)$  is the critical density of the Universe which corresponds to the total energy density of the flat Universe, and

$$\sum_i \Omega_i = 1, \quad (2.1.11)$$

where we sum over all the contributions to the energy density of the Universe. At present, the biggest components are: dark energy ( $\sim 78\%$ ), dark matter ( $\sim 27\%$ ), and ordinary, baryonic matter ( $\sim 5\%$ ), while the radiation (all relativistic degrees of freedom) contribution is negligible [18].

We are now ready to rewrite the Eq. (2.1.7) into a simple form describing the redshift evolution of the Hubble parameter

$$H^2(z) = H_0^2 (\Omega_r(1+z)^4 + \Omega_m(1+z)^3 + \Omega_\Lambda). \quad (2.1.12)$$

It describes the Universe filled with radiation  $\Omega_r$ , non-relativistic matter  $\Omega_m$  and dark energy  $\Omega_\Lambda$ . In particular, at present ( $z = 0$ ) the measured value of the present-day Hubble rate<sup>3</sup> is  $H_0 \simeq 67 \text{ km/s/Mpc}$  [18]. We also introduce the reduced (dimensionless) Hubble parameter  $h = H_0/(100 \text{ km/s/Mpc}) \simeq 0.7$ .

## 2.2 $\Lambda$ CDM model

The Standard Cosmological Model, also known as the Concordance Model or  $\Lambda$ CDM model is the leading theory describing the main fundamental components and the evolution of the Universe. It is based on the ‘‘Cosmological Principle’’, Friedmann’s equations, Eq. (2.1.7), and a set of just six parameters. Despite its simplicity, it is remarkably successful and provides an impressive agreement with various observations. Although several serious discrepancies between the predictions of the concordance model and observations have recently been identified, cf. [19, 23–26] for recent reviews, the consistency of the model is not (yet) in question.

The aforementioned six free parameters are determined by a fit to the observational data. In the literature, one can find multiple equivalent parameterizations with different sets of parameters. However, the most common

---

<sup>3</sup>Its determination from various cosmological observations has recently reached astonishing precision, revealing a potentially serious tension in the  $\Lambda$ CDM model [19]. We discuss this problem in Section 8.1 of Chapter 8 where we study a SIDM model that could address this, so-called, Hubble tension.

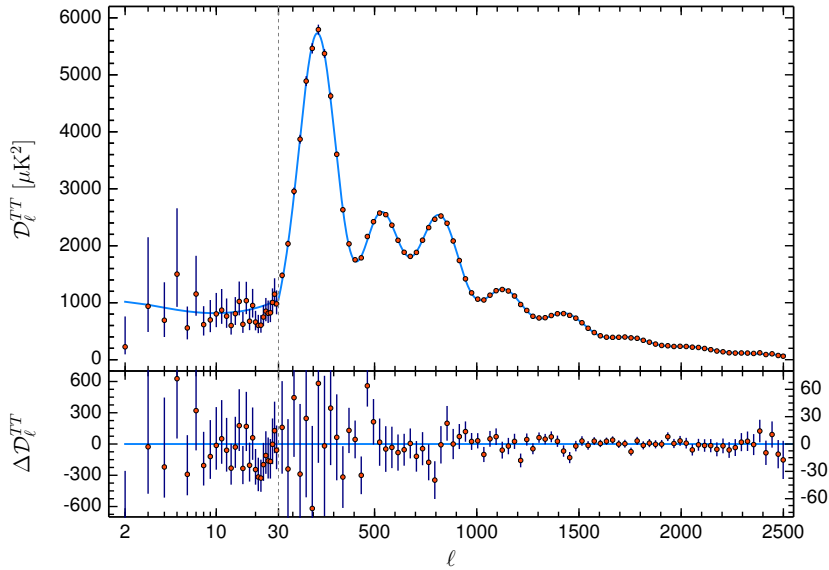


Figure 2.1: Temperature power spectrum of the CMB measured by *Planck* [20]. The best-fit within the  $\Lambda$ CDM model is plotted in light blue on the top, while residuals are shown on the bottom.

- used by, *e.g.*, the *Planck* collaboration [20] - is the following: the baryon energy density  $\Omega_b h^2$ , the cold dark matter (CDM) energy density  $\Omega_c h^2$ , approximate angular size of the sound horizon  $\theta_{\text{MC}}$ , the reionization optical depth  $\tau$ , the logarithm of amplitude of primordial scalar curvature perturbations  $\ln(10^{10} A_s)$ , and the scalar spectral index  $n_s$ .

Put simply, the first two parameters determine the amount of the dominant components of the Universe at present, as one can determine the energy density of dark energy at present using the relation  $\Omega_\Lambda = 1 - \Omega_b - \Omega_c$ . We used the fact that the Universe is flat and that due to faster than matter redshift,  $\rho_r \propto 1/a^4$ , radiation energy density is negligible at present. The parameter  $\theta_{\text{MC}}$  determines the geometry of the Universe, while  $\tau$  indicates the degree of reionization experienced by the Universe due to the formation of the first stars. The last two parameters describe the power spectrum of primordial fluctuations which are the origin of structure in the Universe.

The latest *Planck* [20] fit to the CMB acoustic peaks - shown in Fig. 2.1 - result in the following best-fit values:

$$\begin{aligned} \Omega_b h^2 = 0.02254, \quad \Omega_{\text{DM}} h^2 = 0.119, \quad 100 \theta_{\text{MC}} = 1.042 \\ \tau = 0.0578, \quad \ln(10^{10} A_s) = 3.0479, \quad n_s = 0.9705. \end{aligned} \quad (2.2.1)$$

Finally, let us note that in spite of the aforementioned possible discrepancies between the observational data and the  $\Lambda$ CDM, its main assumptions, such as: (i) the existence of DM which outweighs the baryonic matter by roughly 5:1 and (ii) the accelerating expansion of the Universe, have only been strengthened in the last decade [23]. This impressive improvement in observational cosmology is shown in

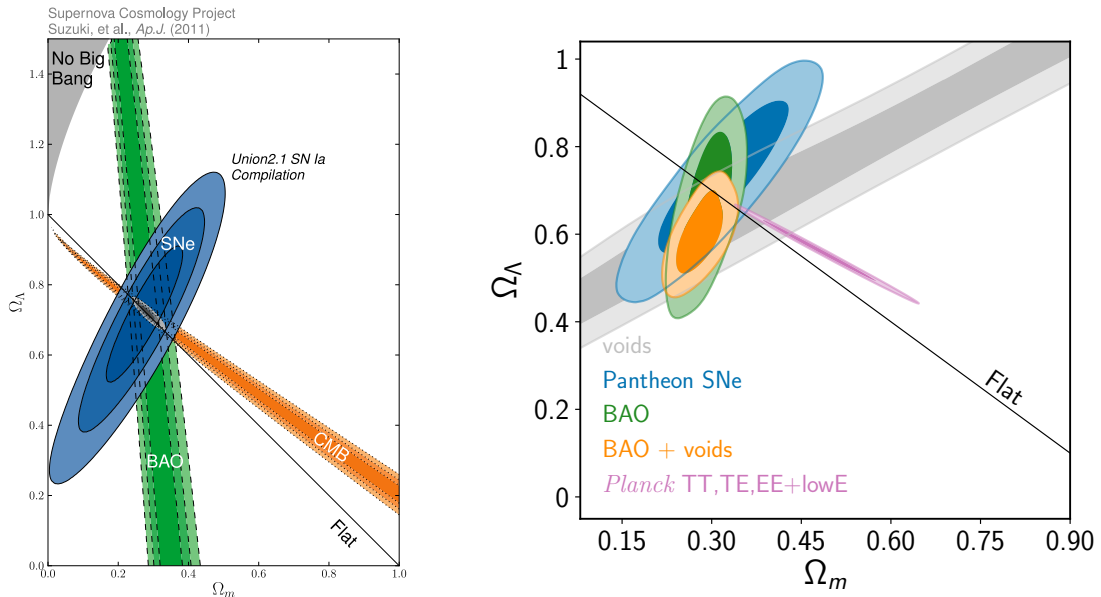


Figure 2.2: Preferred regions in the  $(\Omega_m, \Omega_\Lambda)$  plane obtained as a  $\Lambda$ CDM fit to various cosmological observations (assuming the Universe is flat). Note significant reduction in error regions and improvement of overlap of best-fit regions achieved in the last decade - compare data from 2011 [21] (left) and from 2020 [22] (right).

Fig. 2.2 where the  $\Lambda$ CDM fit is shown in the  $(\Omega_m, \Omega_\Lambda)$  using data from the past (left) and present (right).

In the rest of this chapter, we focus more specifically on the DM sector of the Universe and the observational implications of its existence.

## 2.3 Evidence for the existence of DM

### 2.3.1 Astrophysical evidence

**Galaxy dynamics evidence** The first hints that non-luminous matter exists and is abundant in the Universe, came from astrophysical observations made in the 1920s. One of the first papers to suggest the existence of dark, non-luminous objects was<sup>4</sup> [31], in which James Jeans analyzed data on the vertical motion of stars in the galactic plane collected by Jacobus Kapteyn and concluded that there should be at least “two dark stars for every bright star” to provide enough gravitational pull for high stellar velocities.

Next, in 1933 Fritz Zwicky noted that by applying the virial theorem to the **dynamics of the Coma cluster**, one obtains an estimate of its mass that is roughly one hundred times greater than the sum of the masses of all the luminous matter contained in the cluster [32]. His conclusion was that there is a form of matter that manifests itself only through gravitational interaction which he called dark matter (“Dunkle Materie”).

Despite those works, interest in DM was limited until the 1970s when Vera

<sup>4</sup>Based on the history of DM reviewed in [27]; see also other reviews [28–30].

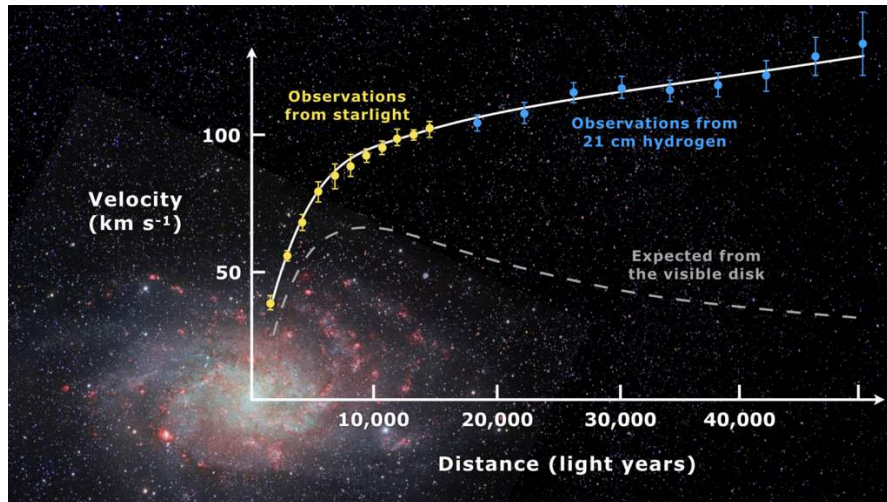


Figure 2.3: Rotation curve for the Messier 33 galaxy. The expected shape of the curve is indicated by the gray dashed line, while the solid line corresponds to the scenario where the DM halo surrounds the galaxy. The yellow and blue dots denote the observational data. Taken from [35].

Rubin and Kent Ford showed that the dependence of the **rotation velocity** on distance from the galactic center in spiral galaxies does not follow the expected Newtonian relation  $v \propto 1/\sqrt{r}$  at large radii, but instead it saturates to a constant [33, 34], as shown in Fig. 2.3. It was quickly realized that such a dependence can be easily explained if the visible galaxies are embedded in much larger DM halos that provide additional gravitational pull.

**Galaxy clusters evidence** Evidence for DM can also be found at much larger scales. For example, large gravitationally bound objects like galaxy clusters contain large amounts of baryonic matter that does not emit light in the visible wavelength range. Interstellar gas is a common example of such matter and is often found in deep gravitational potential wells which causes the gas to heat up to high temperatures, leading to X-rays emission that can be easily detected. An example of a cluster of galaxies - Abell2029 - is shown in Fig. 2.4.

**X-ray observations** allow one to reconstruct the gas temperature which in turn permits reconstructing the total mass profile of the cluster by using the following formula [38]:

$$M(r) = \frac{k_B T r}{G_N m_{\text{proton}}} \left( -\frac{d \ln \rho}{d \ln r} - \frac{d \ln T}{d \ln r} \right), \quad (2.3.1)$$

where  $T(r)$  and  $\rho(r)$  are the temperature and density profiles of the cluster, respectively.

It turns out [39, 40] that the total mass of the clusters determined by this method is roughly 20 times larger than the mass of baryonic matter - hot interstellar gas and galaxies. Moreover, at large distances from the galactic cluster center the mass comes primarily from the non-luminous matter - without which the hot gas would evaporate - consistent with, *e.g.*, the galactic rotation curves.

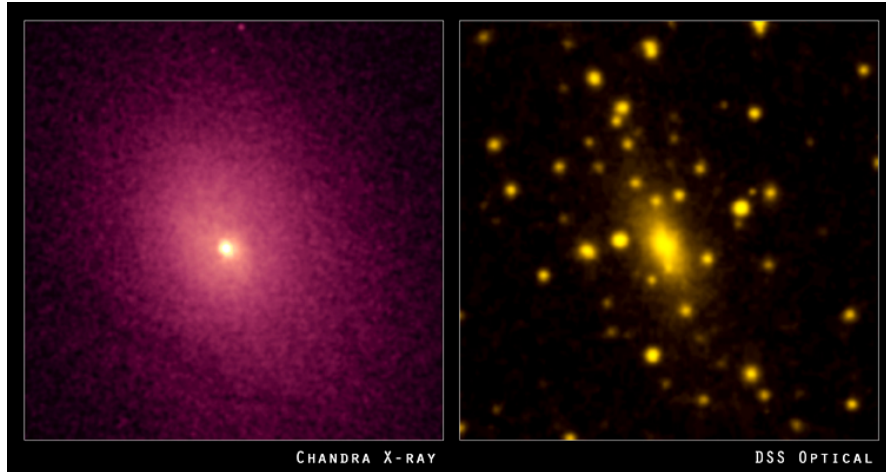


Figure 2.4: Cluster of galaxies Abell2029. On the left, the distribution of X-ray gas is shown, while the distribution of galaxies is on the right. **Credit:** X-ray: NASA/CXC/UCI/A.Lewis et al.; Optical: Pal.Obs. DSS.

Additional evidence comes from **gravitational lensing** where light is deflected by large masses between the observer and the source that emitted the light. This effect was one of the spectacular predictions of the general theory of relativity, and its first detection due to a solar eclipse in 1919 [41] contributed to the widespread acceptance of Einstein’s theory. In 1937 Fritz Zwicky proposed [42] that galaxy clusters will act as gravitational lenses, and the first observation using this so-called strong gravitational lensing effect was made in 1979 [43]. Another particularly spectacular example of this effect is shown on the left side of Fig. 2.5. As reviewed in [44], the strong lensing effect crucially depends on the total mass of the heavy object, and thus it can be reconstructed, as shown on the right side of Fig. 2.5. In this observation, [36], the ratio of the total mass to the visible mass was found to be roughly 200, and furthermore the reconstructed DM distribution was found to be relatively smooth, in contrast to much less regular, peaky, distribution of the visible matter - precisely as expected in the  $\Lambda$ CDM model.

In addition, a similar weak gravitational lensing effect (cf. [44]) allowed one to directly map the spatial distribution of DM in galaxy clusters [45, 46] which was also found to be consistent with the  $\Lambda$ CDM model.

Another spectacular piece of evidence comes from observations of the **Bullet Cluster**,<sup>5</sup> [50–52], shown in Fig. 2.6 where two galaxy clusters collided. After the collision, shock wave cones formed by the hot gas of baryonic matter present in both clusters (red) which formed due to electromagnetic interactions. On the other hand, the collisionless matter of the clusters (blue) passed by each other unaffected. As a result, the luminous and non-luminous parts of the cluster became separated from each other. Moreover, the total mass of the cluster was reconstructed by

<sup>5</sup>Some years ago doubts were raised about the DM interpretation of the Bullet Cluster dynamics [47] due to the expectation that Bullet Cluster like systems are too rare in the  $\Lambda$ CDM model to be observed. However, subsequent works [48, 49] showed that the probability is actually much higher and the existence of the Bullet Cluster does not pose a challenge to the  $\Lambda$ CDM.

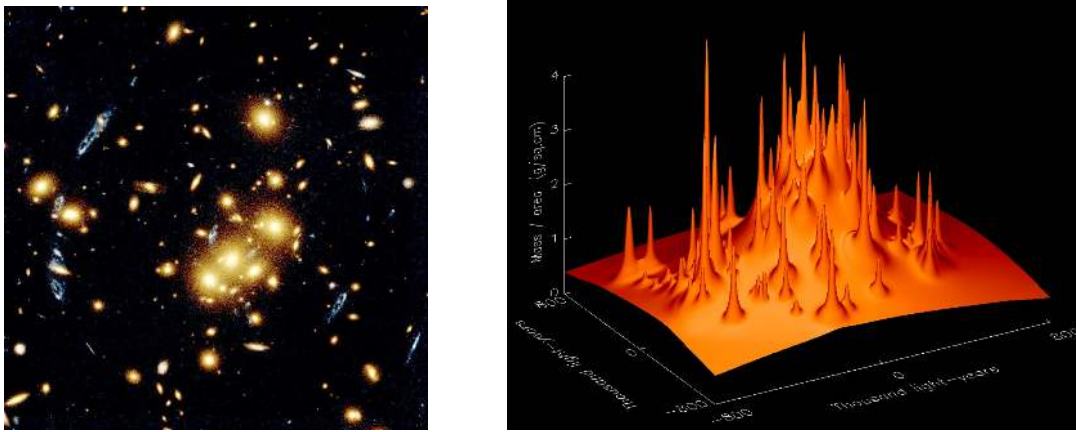


Figure 2.5: Left: duplicated images of the galaxy marked in light blue which were produced by gravitational lensing of the foreground 0024+1654 cluster (yellow, at the center). Right: Mass reconstruction of the lens which shows peaks of baryonic matter embedded in a smooth background of non-luminous matter. Taken from [36] and [Hubble Space Telescope website](#).

gravitational lensing and it mostly follows the collisionless part of the clusters, not the hot baryonic gas which means that most of the cluster’s mass is in the form of invisible matter.

Such an astonishing spatial separation of total and visible masses has been observed in many more cases [53]. This is consistent with the idea of a large DM abundance that outnumbers the visible matter, and poses a challenge to alternative proposals such as modified gravity theories like Modified Newtonian Dynamics (MOND) [54].

### 2.3.2 Cosmological evidence

**Cosmic Microwave Background** In the early universe, baryons and photons were tightly coupled due to electromagnetic interactions, causing them to behave as a single fluid - for a review of the physics, history and significance of the CMB, see [9, 55–57]. The pressure exerted by this fluid opposes gravity and prevents the growth of matter perturbations, but causes them to oscillate, an effect that is called *Baryon Acoustic Oscillations (BAO)*.

About 370 thousand years after the Big Bang photons stopped scattering efficiently with electrons and protons because they became bounded into electrically neutral atoms, causing the photons to decouple from the plasma. This effect is called recombination. Photons that were the last to scatter and form the last scattering surface were accidentally first detected in 1965 by Penzias and Wilson [58], who used a horn antenna to detect the electromagnetic radiation reflected from the Echo balloon satellites. This required the removal of all other signals which they successfully did by considering all known sources, but a thermal noise with  $T \sim 3K$  persisted. The significance of this discovery was soon understood by Dicke’s cosmology group [59] as a remnant of the early Universe, predicted by the hot Big Bang theory.

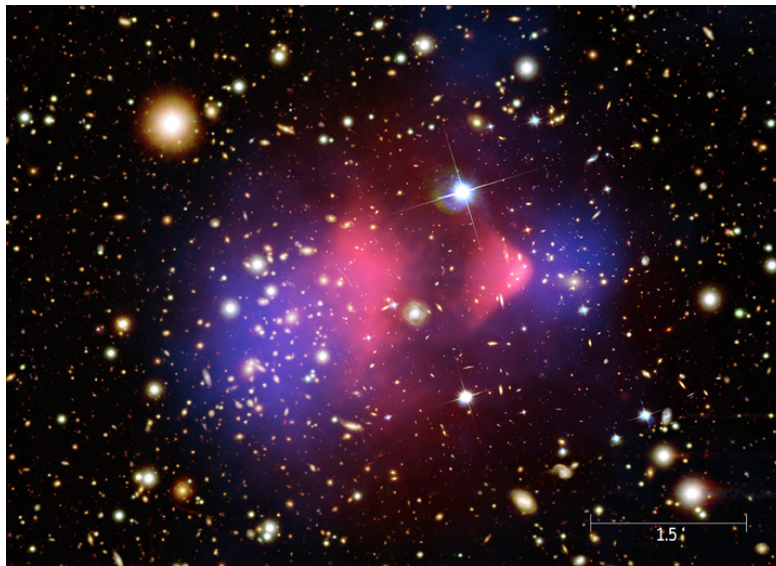


Figure 2.6: Optical, X-ray (pink), and weak gravitational lensing (blue) image of the Bullet Cluster (1E 0657-558). Taken from [the Chandra X-Ray Observatory website](#).

Around the same time, theoretical work on the CMB spectrum was conducted and it was realized by Sakharov [60], Peebles [61], Zeldovich [62], and Silk [63] that the deviations from the blackbody spectrum (anisotropies) also must have formed due to the oscillation of photons in the photon-baryon plasma. An important feature of the CMB is that, although by that time DM has already decoupled from the plasma, it provided a significant gravitational pull, affecting the photon spectrum. Indeed, the plasma was embedded in the gravity well formed by DM, leading to gravitational clustering of baryons. In regions where the baryons were more dense than average, called overdensities, electromagnetic interactions were very efficient, resulting in a repulsive pressure. The interplay between gravitational attraction and repulsive pressure resulted in oscillations in the temperature power spectrum, as overdense regions became cold spots in the CMB map, while underdense regions became hot spots. Since these oscillations are similar in nature to ordinary sound waves, they are called acoustic oscillations.

The anisotropies were first detected by the *Cosmic Background Explorer* (*COBE*) satellite in 1992 [64]. It was found that they occur only at the relative level of  $\sim 10^{-4}$ , as predicted by, *e.g.*, Peebles [65]. The shape of the temperature power spectrum coming from the latest measurement done by *Planck* in 2018 [20] is shown in Fig. 2.1. One can clearly see the series of the acoustic peaks. The location of the first peak determines the geometry of the Universe [9], and the *Planck* measurement points towards the flat Universe.

The relative amplitudes of the second and third peaks are determined by the relative abundances of baryons and DM, since these two matter components are out of phase. This causes DM to enhance odd peaks and suppress even ones. The *Planck* measurement determined the visible matter abundance to be  $\Omega_b h^2 = 0.02254$  and the DM abundance to be  $\Omega_{\text{DM}} h^2 = 0.119$ .

The precise measurement of the CMB is one of the pillars of modern cosmology,

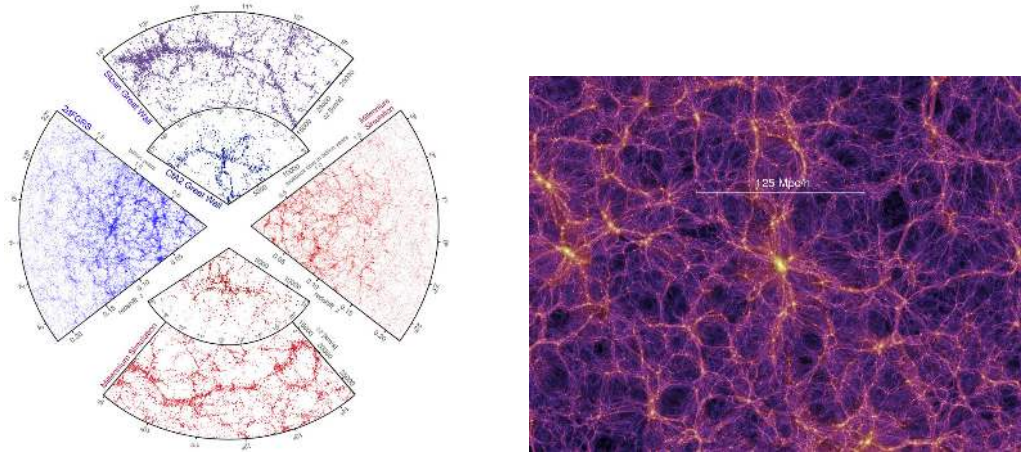


Figure 2.7: Left: comparison of observations and simulations of N-body simulations of structure formation [37]. Right: the cosmic web obtained in [The Millennium Simulation](#). Taken from [30].

as it provided a snapshot of the early Universe, and its understanding contributed to the development of the  $\Lambda$ CDM model. It is an interesting exercise to determine what the shape of the CMB spectrum would look like in a universe of a different composition. One can use online CMB power-spectrum plotters [Powerspectrum](#) and [LAMBDA](#), for a quick check.

Similarly to the BAO found in the CMB spectrum (which describes the directional dependence of temperature fluctuations in the sky), one also finds those oscillations in the matter power spectrum - which represent the matter density contrast of the Universe - [66] in the form of overdense and underdense regions. The characteristic BAO scale allows for the determination of the combined baryon and DM density,  $\Omega_m = \Omega_b + \Omega_{\text{DM}}$ , called matter density. Numerous observations [67–70] are in remarkable agreement with the values obtained through CMB - cf. Fig. 2.2.

**Structure formation** The formation of structure in the Universe depends critically on the total abundance of matter. A simple intuitive argument that modified theories of gravity are not satisfactory and at least a small fraction of invisible matter is necessary comes from a qualitative description of the growth of perturbations [38]. It is well known that in a universe with no DM perturbations of ordinary matter grow only linearly with the scale factor. There was not enough time for the growth of the observed structures in our Universe, which indicates the need for nonlinear perturbations. Moreover, for the theory of structure formation to fit the data, one must introduce, *e.g.*, gravitational potential wells deeper than those produced by baryons before the recombination. Non-baryonic matter which does not interact with either baryons or photons, decouples from the baryon-photon fluid much earlier than the time of recombination and produces the desired effect. Moreover, it reproduces the oscillatory pattern (BAO) found in the matter density spectrum which is a challenge to MOND theories [71].

A qualitative description of structure formation requires numerical N-body

simulations. The large-scale structures of galaxies and clusters are thought to arise from initial over-densities that grew by clustering in gravitational wells created by DM. Consequently, simulations are performed assuming that gravity is the only interaction between particles. Such, “DM-only” simulations, *e.g.*, [72–74] show excellent agreement with large-scale observations from the galaxy surveys [75, 76] - see Fig. 2.7.

It is worth noting that, despite the great success of simulations in fitting to data at large scales, they seem to fail at smaller, galactic scales – for a recent review see [77]. At those scales, the “DM-only” simulations predict much richer structure than has been observed – *e.g.*, a “*missing satellite*” [78] and a “*too-big-to-fail*” [79] problems. Moreover, the DM density profiles predicted from simulations of cold, non-interacting DM appear not to match observations - “*cusp vs. core*” [80, 81], and “*diversity*” [82] problems.

However, it is not clear whether these discrepancies are indeed a problem for the  $\Lambda$ CDM model or whether they are due, for example, to the lack of proper modeling of non-linear baryon interactions in the simulations. It has been shown that, *e.g.*, supernova feedback can transform cuspy DM density profile into cored one [83, 84], and simulations that include baryonic feedback, *e.g.*, [85, 86], indeed seem to predict less structure but simulations including such effects fully are yet to be done.

### 2.3.3 DM candidates

In this section, DM candidates will be discussed. Several major classes of them are shown in Figs. 2.8 and 2.9.

**Composite objects** One of the simplest scenarios for DM is that it consists of **Massive Compact Halo Objects (MACHOs)** - small, massive objects made of baryonic matter which do not glow. Examples include black holes, neutron stars, free-floating planets, brown dwarfs, and possibly any other such objects that drift unbound through the interstellar space and escape direct observation.

Explaining the nature of DM solely with MACHOs, however, is not possible. It has been known since the 1980s [88, 89] that large amounts of baryonic MACHOs are in tension with Big Bang Nucleosynthesis (BBN), as they would point toward different relative abundance of light elements. Moreover, precise CMB observations by *WMAP* [13] have completely ruled out such a scenario. MACHOs made of non-baryonic matter have also been strongly constrained by the MACHO [90] and EROS [91, 92] projects which used the microlensing effect proposed by Bohdan Paczyński [93]. This phenomenon is based on gravitational lensing of background stars’ light which would be enhanced if a MACHO object passed through the line of sight. Roughly a decade of observations and the lack of such signal determined that MACHOs may represent only a small fraction of the total DM abundance.

A way to circumvent the BBN constraints is to form a compact object before the initial nucleosynthesis has occurred. Carr and Hawking showed [94] that primordial density fluctuations in the early Universe may have gravitationally collapsed and formed **primordial black holes (PBHs)**. If they were massive enough, they

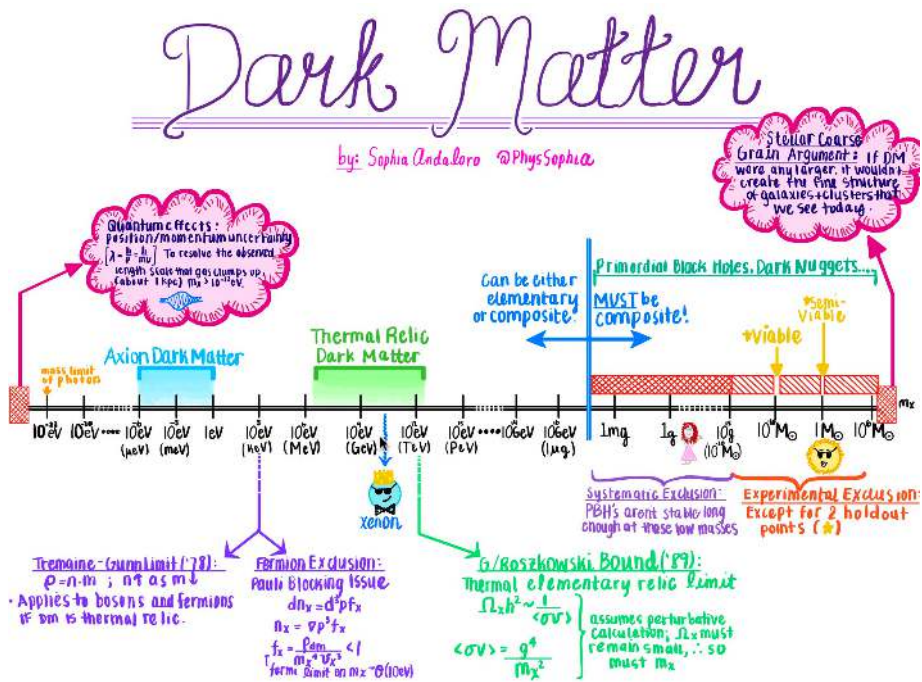


Figure 2.8: A cartoon of particle and composite DM candidates as a function of their mass. Also shown are the general constraints for each class of candidates. Figure credit: Sophia Andaloro.

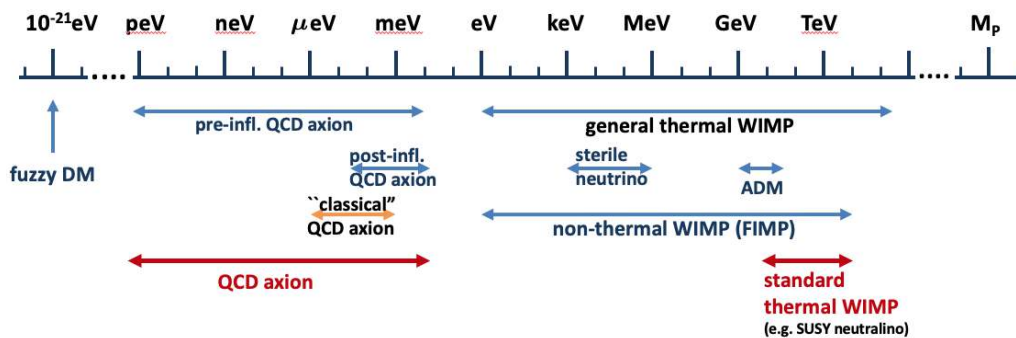


Figure 2.9: Multiple particle DM candidates complementary to those shown in Fig. 2.8 as a function of their mass. Taken from [87].

would have survived till present, accreting more mass, all without the need to invoke a new form of matter. A recent LIGO discovery of gravitational waves from black hole mergers (possibly of primordial origin) [95] has initiated a second wave of interest in those objects as DM candidate. As a result, the constraints on PBHs have been re-evaluated and such objects appear to be a viable option [96], especially in the multi-component DM scenarios. However, even such scenarios are subject to stringent constraints, *e.g.*, in a mixed WIMP-PBH DM scenario, the WIMPs would form spiky density profiles around the PBH, leading to their very efficient annihilation into SM products which is not observed, and thus imposes severe bounds on such a scenario, see [97–100] for recent works on the topic.

**Particle candidates** Before discussing some well-motivated particle DM candidates, let us list some general properties that such a particle must have - cf. also [101] for a ten-point test.

DM particles must be:

- Non-baryonic - observations of the Bullet Cluster, BAO in both CMB and matter power spectrum, and BBN imply that DM cannot be made of baryons.
- Stable - the lifetime of an unstable DM particle must greatly exceed the present age of the Universe [102].
- Electrically neutral - CMB, DD and astrophysical constraints imply that DM can only be millicharged [103].
- Non-relativistic - the main part of DM has to be non-relativistic at the time of structure formation, otherwise DM would free-stream and erase the structure [104].
- Produced in sufficient quantity in the early Universe - CMB, BBN and other observations are all consistent with the DM abundance of  $\Omega_{\text{DM}} h^2 = 0.119$  - see Fig. 2.2.

An important classification of DM particles is based on the velocity they had when they reached their relic density: hot (relativistic), warm (semi-relativistic), and cold (non-relativistic) DM. Since the determination of matter power spectrum, hot DM has been excluded [105] and can only correspond to a small fraction of the total DM relic density,  $\Omega_{\text{DM}}^{\text{hot}} < 0.00245$  [106], while both warm and cold DM are possible scenarios. In fact, warm DM scenario is among the proposed solutions to the small-scale structure problems of  $\Lambda$ CDM [107].

A list of possible particle DM candidates that have proposed in the literature is very long, and still growing. In the following we present candidates and classes of candidates which have attracted much attention over many years.

**Axions** The strong CP problem of Quantum Chromodynamics (QCD) is based on the observation that the symmetries of the theory allow for the CP violating term in the Lagrangian

$$\mathcal{L}_{\text{QCD}} \supset \frac{\theta}{32\pi^2} \text{Tr} \left[ G^{\mu\nu} \tilde{G}_{\mu\nu} \right], \quad (2.3.2)$$

where  $G^{\mu\nu}$  is the field strength tensor of QCD and  $\tilde{G}_{\mu\nu}$  is its dual. This term leads to CP-violating interactions in QCD that are not observed, leading to the bound  $\theta < 10^{-10}$ . Such an unnatural suppression can be explained by introducing a new global  $U(1)$  symmetry that is spontaneously broken by a complex scalar field [108–111]. The resulting naturally light pseudo-Nambu-Goldstone boson is called an axion.

In addition to solving the CP problem of QCD, the axion can also be a good candidate for non-thermal<sup>6</sup> DM [112]. Searches for axions and, more generally, a class of particles featuring axionic interactions – called axion-like particles (ALPs) – are extensively discussed in [113].

**Wave dark matter** Axions and ALPs belong to a general class of very light DM candidates, called wave dark matter, which are characterized by large de Broglie wavelength,

$$\lambda_{\text{dB}} \equiv \frac{2\pi}{m_{\text{DM}}v} = 0.48\text{kpc} \left( \frac{10^{-22}\text{eV}}{m_{\text{DM}}} \right) \left( \frac{250\text{ km/s}}{v} \right), \quad (2.3.3)$$

where we assumed a standard DM velocity from the Standard Halo Model [114]. Wave DM, although composed of single particles, is not described by a single particle equation, but instead behaves effectively as a collective wave for  $m_{\text{DM}} \lesssim 30\text{ eV}$ .<sup>7</sup> On the other hand, observation of small DM halos leads to a lower bound, expressing the simple observation that the wave DM must fit into the halo [38]

$$\lambda_{\text{DB}} = 0.3\text{ cm} \left( \frac{1\text{eV}}{\text{m}} \right) < 3 \times 10^{21}\text{ cm}, \quad (2.3.4)$$

leading to  $m_{\text{DM}} \gtrsim 10^{-22}\text{ eV}$ .

The ultra-light DM in the lower end of the wave DM range is called fuzzy DM which was introduced to solve small-scale structure problems of the  $\Lambda$ CDM model by wave properties of the DM stabilizing the gravitational collapse responsible for DM halo formation [115]. For an extensive discussion, see recent reviews of fuzzy and wave DM [116, 117], and more generally, ultra-light DM [118].

**Sterile Neutrinos** Neutrino flavor oscillations, predicted by Pontecorvo [119] and observed for the first time in the Homestake experiment [120], definitely proved that neutrinos are not massless but have small masses, a property that is missing in the SM description. A simple way to resolve this problem is to introduce a heavy sterile neutrino which explains the small mass values of SM neutrinos through the seesaw mechanism [121]. As mentioned in Chapter 1, the heavy neutrino is called “sterile” due to the fact that it has only a right-handed component and thus is uncharged under the SM gauge groups.

Moreover, a heavy neutrino could be a DM candidate when it is produced via a non-thermal Dodelson–Widrow mechanism [122, 123]. We will sketch this mechanism, for simplicity assuming that the sterile neutrino  $N_1$  mixes only with

---

<sup>6</sup>We discuss thermodynamics of the early Universe, including DM production, in Section 3.1.

<sup>7</sup>Defined as the mass for which the de Broglie wavelength exceeds the average inter-particle separation in the DM halo.

the electron SM neutrino flavor  $\nu_e$ . The mass eigenstates of the sterile and light neutrinos are  $\nu_1, \nu_2$ , respectively, and they are related to the flavor eigenstates by

$$\begin{aligned} |v_1\rangle &= \cos\theta |v_e\rangle - \sin\theta |N_1\rangle \\ |v_2\rangle &= \sin\theta |v_e\rangle + \cos\theta |N_1\rangle, \end{aligned} \quad (2.3.5)$$

where  $\theta \ll 1$ . Sterile neutrinos are produced out of equilibrium due to their small coupling to the thermal bath and their abundance gets accumulated over time, with the production rate given by

$$\Gamma_{v_2} \sim (G_F^2 T^2) \theta^2(T) \cdot T^3. \quad (2.3.6)$$

Because the mixing angle depends on the temperature, calculating the total relic abundance requires numerical methods. It turns out that the peak production occurs near the QCD phase transition,  $T_{\text{peak}} \sim 170 \left(\frac{m}{1\text{keV}}\right)^{1/4} \text{MeV}$ , and the approximate relic density of sterile neutrinos obtained by oscillations is [124]

$$\Omega_{v_1} h^2 \sim 0.1 \left(\frac{\theta^2}{3 \times 10^{-9}}\right) \left(\frac{m_1}{3\text{keV}}\right)^{1.8}. \quad (2.3.7)$$

In recent years, there has been much interest in sterile neutrinos due to the  $\sim 3.5 \text{keV}$  line discovered in XMM-Newton observations of galaxy clusters [125, 126] which could be naturally explained by the decay of a sterile neutrino with a mass of  $\sim 7 \text{keV}$ . However, such mass values could be in tension with the Lyman- $\alpha$  forest data [127]. More details on sterile neutrinos can be found in recent reviews [128–130].

**WIMPs** A particularly important class of DM candidates is a WIMP which is a particle that was in thermal equilibrium with the SM plasma in the early Universe. The WIMP obtains its relic density from annihilations into SM particles - which is the celebrated freeze-out mechanism - first studied in [131–133].

Due to the thermal nature of the DM production, the relic density of WIMPs,  $\Omega_{\text{WIMP}}$ , depends only on the strength of the thermally averaged annihilation cross section,  $\langle\sigma v\rangle$ , (defined in Eq. (3.1.12)) which in turn depends only on particle physics parameters, such as interaction strength couplings and masses, and not on cosmological parameters. Neglecting order-one factors, one can estimate (view recent review [134] for an extensive discussion of WIMP freeze-out, as well as other DM production mechanisms that are beyond the scope of this thesis)

$$\frac{\Omega_{\text{WIMP}}}{0.24} \sim \frac{10^{-9} \text{GeV}^{-2}}{\langle\sigma v\rangle} \sim \frac{10^{-9} \text{GeV}^{-2}}{\frac{g_{\text{WIMP}}^4}{m_{\text{WIMP}}^2}}, \quad (2.3.8)$$

which is remarkably close to the observed value,  $\Omega_{\text{WIMP}} \approx 0.24$ , for  $m_{\text{WIMP}} \sim m_{\text{weak}} \sim 100 \text{GeV}$  and  $g_{\text{WIMP}} \sim g_{\text{weak}} \simeq 0.65$ . This remarkable numerical coincidence is often called a WIMP miracle because it seems to point towards new interactions around the electroweak scale which are in any case also expected due to, *e.g.*, the hierarchy problem. The fascinating (open) question is whether this phenomenon is just a coincidence or whether it is part of an explanation of

the origin of the electroweak scale which is otherwise quite mysterious, given it is so much smaller than the Planck scale.

Due to the importance of WIMPs, we describe their main properties in detail in the next chapter where in particular we discuss extensions of the WIMP paradigm to other scenarios - which will be needed in later chapters - in Section 3.1.

The most prominent class of WIMPs models is based on supersymmetry which we introduce in the next paragraph and then extensively study in Chapter 6. A thorough discussion of WIMPs can also be found in recent reviews [135, 136].

**SUSY** Supersymmetry was introduced in the 1970's as a new type of symmetry relating fermions and bosons [137, 138] but with time it became strongly motivated by, among other things, unification of fundamental interactions at high energies, string theory, and the hierarchy problem.

Evolution of gauge couplings with energy scales of interactions which is governed by renormalization group equations, does not lead to a unification of gauge interactions<sup>8</sup> in the SM [139]. By adding new, heavy degrees of freedom, in SUSY the situation improves, and under generic assumptions this leads to the unification occurring at the  $\sim 10^{16}$  GeV scale [140, 141].

One can promote supersymmetry to a local symmetry which unifies all gauge interactions with gravity [142, 143]. Such a theory is called supergravity and at some point was considered a viable “theory of everything”.<sup>9</sup> Supergravity introduces a supersymmetric partner of the graviton (spin 2 particle responsible for gravity interactions), called gravitino [145] which is a natural DM candidate, and it can obtain its relic density in both thermal [146] and non-thermal ways [147].

There are also well-motivated supersymmetric models of axions which naturally provide a non-thermal DM candidate - the axino [148–150].

Since no supersymmetric particles (called sparticles) have been found so far, it is clear that SUSY is not an exact symmetry and must be broken at some high energy. From a phenomenological point of view, an important step was a formulation of the low-energy supersymmetric version of the SM which was named the Minimal Supersymmetric Standard Model [151]. It doubles the number of SM particles, and solves the DM and proton stability problems by introducing a discrete symmetry, called R-parity.<sup>10</sup> A comprehensive review starting from the SUSY algebra and ending with the MSSM can be found in [152].

The MSSM provides more than one thermal DM candidate that can naturally obtain the correct relic density - see an early SUSY WIMP DM review [153]. One of the most well-motivated candidates is the lightest neutralino [154, 155] which obtains its relic density via thermal freeze-out. In Chapter 6 we discuss in detail the prospects of this important DM candidate.

For extensive discussion of SUSY DM candidates, see recent reviews [135, 147] which discuss the experimental status of the DM candidates we mentioned above.

---

<sup>8</sup>A theory providing such an unified framework is called a Grand Unified Theory (GUT).

<sup>9</sup>In fact, while the developments in supergravity has shown that the theory does not appear to be a complete description of nature [144], it has led to further development of similar ideas in string theories, also based on supersymmetry which appear to be a more promising path.

<sup>10</sup>In generic SUSY theory, one would expect sizable interactions leading to efficient proton decay which is not observed.

# Chapter 3

## Thermal dark matter

A particularly important class of cold, thermal DM candidates is the WIMP which we introduced in the previous chapter. Because of its importance - and the fact that *all the BSM scenarios discussed in this thesis involves WIMPs or other thermal DM particles* - we devote this chapter to their thermal history and detection methods employed in WIMP searches.

Thermal DM is a particle that was in thermodynamic - chemical and kinetic - equilibrium with the thermal plasma in the early Universe. It means that the DS and the SM share the same chemical potential and temperature, due to the presence of efficient number and energy exchanging processes.

Thermal DM is a particularly motivated and developed class of DM candidates because: (i) it's relic density does not depend on initial conditions of the early Universe before the radiation domination era,<sup>1</sup> (ii) it can be naturally implemented in many BSM scenarios, while also seemingly pointing towards new physics near the electroweak scale, as the numerical coincidence, Eq. (2.3.8), indicates, and (iii) because of the fundamental assumption of thermal equilibrium - which requires efficient annihilations of WIMPs into SM particles - similar processes like scattering of WIMPs with SM particles or production of WIMPs in high-energy collisions of SM particles, can be detectable; this leads to the well-developed and complementary program of WIMP detection searches.

### 3.1 Relic density of thermal DM candidate

In the previous chapter we discussed the gravitational influence of the DM on the evolution of the Universe, but in fact DM interactions within the DS and with the SM may be much richer. In this section we start the discussion of such interactions of thermal DM by discussing the thermodynamics of the early Universe.

---

<sup>1</sup>This is the case in the standard cosmological history of the  $\Lambda$ CDM model which assumes that the Universe went through a rapid period of inflation ending with the high-temperature reheating process, which initiated the radiation era. On the other hand, modifications introduced to this scenario, *e.g.*, due to low-temperature reheating [156–158] or the kination period present in the early evolution of the Universe [159], can impact the predicted value of the DM relic density. However, this does not change the main mechanism, which is based on the decoupling of DM from a thermalized plasma in the early Universe.

**Equilibrium thermodynamics** Given the phase-space distribution function  $f_i(\vec{r}, \vec{p}, t)$  of the species denoted with index  $i$ , its number density is given by<sup>2</sup>

$$n_i(\vec{r}, t) = g_i \int \frac{d^3p}{(2\pi)^3} f_i(\vec{r}, \vec{p}, t), \quad (3.1.1)$$

where the factor  $g_i$  denotes the degeneracy for the  $i$  DM species. For example  $g = 1$  for real scalar or Majorana fermion DM.

The equilibrium distribution for bosons/fermions is

$$f(E, \vec{p}) = f(E) = \frac{1}{\exp\left(\frac{E-\mu}{T}\right) \pm 1}, \quad (3.1.2)$$

while for classical particles it is given by the Boltzmann-Maxwell distribution,  $f(E, \vec{p}) = f(E) = \exp\left(\frac{-E+\mu}{T}\right)$ .

Given Eq. (3.1.2), one can asymptotically compute Eq. (3.1.1)

$$n_{\text{eq},i} \simeq \begin{cases} \frac{g_i T^3}{\pi^2}, & \text{when } T \gg m_i \text{ (relativistic limit),} \\ g_i \left(\frac{m_i T}{2\pi}\right)^{3/2} e^{-m_i/T}, & \text{when } T \ll m_i \text{ (non-relativistic limit).} \end{cases} \quad (3.1.3)$$

**Time evolution** of the phase-space distribution function is given by the Liouville equation:

$$\frac{df_i}{dt} = \left( p^\mu \frac{\partial}{\partial x^\mu} - \Gamma_{\nu\rho}^\mu p^\nu p^\rho \frac{\partial}{\partial p^\mu} \right) f_i = C[f_i], \quad (3.1.4)$$

where the Christoffel symbol is given by

$$\Gamma_{\nu\rho}^\mu = g^{\alpha\mu} (g_{\alpha\nu,\rho} + g_{\alpha\rho,\nu} - g_{\nu\rho,\alpha}) / 2, \quad (3.1.5)$$

and the quantity on the right hand side,  $C[f_i]$ , is the collision term which takes into account the scatterings and annihilations of  $i$  DM species with other particles.

For  $\Lambda$ CDM metric given by Eq. (2.1.4), Eq. (3.1.4) takes the following form, called the Boltzmann equation,

$$\frac{df_i}{dt} = E \frac{\partial f_i}{\partial t} - \frac{\dot{a}}{a} |\vec{p}|^2 \frac{\partial f_i}{\partial E} = C[f_i], \quad (3.1.6)$$

where  $E = \sqrt{|\vec{p}|^2 + m^2}$ .

Multiplying Eq. (3.1.6) by  $\frac{1}{E} \frac{g_i}{(2\pi)^3}$  and integrating over the momentum  $d^3p_i$ ,<sup>3</sup> results in

$$\dot{n}_i - H \frac{g_i}{(2\pi)^3} \int \frac{|\vec{p}_i|^2}{E_i} \partial_E f d^3p_i = \dot{n}_i + 3H n_i = \frac{g_i}{(2\pi)^3} \int \frac{\hat{C}f}{E_i} d^3p_i, \quad (3.1.7)$$

where in the first equality we integrated the second term by parts.

---

<sup>2</sup>This section is based on the textbook [8] and Refs. [160, 161].

<sup>3</sup>Formally, this is the zero'th moment of Eq. (3.1.6). Full phase space solution of the Boltzmann equation requires dedicated numerical computations [162]. Those are necessary, for example, when the kinetic decoupling happens before the chemical one [163], however, they are not needed in the generic case we discuss.

The right hand side of Eq. (3.1.7) is the collision term which for the process  $1 + 2 \rightleftharpoons 3 + 4$  takes the following form [161]:

$$\int \cdots \int \prod_{j=1}^4 \left( \frac{d^4 p_j}{(2\pi)^3} \delta(p_j^2 - m_j^2) \theta(p_j^2 - m_j^2) \right) (2\pi)^4 \delta^4(p_1 + p_2 - p_3 - p_4) \sum_{\text{spins}} |\mathcal{M}|^2 \times (f_3 f_4 (1 \pm f_1) (1 \pm f_2) - f_1 f_2 (1 \pm f_3) (1 \pm f_4)). \quad (3.1.8)$$

In the absence of a quantum degeneracy,<sup>4</sup> the second line can be rewritten as

$$f_3 f_4 (1 \pm f_1) (1 \pm f_2) - f_1 f_2 (1 \pm f_3) (1 \pm f_4) \approx f_3 f_4 - f_1 f_2 = e^{-(E_1+E_2)/T} \left[ e^{(\mu_3+\mu_4)/T} - e^{(\mu_1+\mu_2)/T} \right]. \quad (3.1.9)$$

Introducing the number density in the absence of the chemical potential,

$$n_j^{(0)} = e^{-\mu_j/T} n_j, \quad (3.1.10)$$

allows us to put Eq. (3.1.7) to the common form used by numerical packages, such as, *e.g.*, micromegas [164, 165] and DarkSUSY [166, 167],

$$\dot{n}_i + 3Hn_i = -\langle \sigma v \rangle n_1^{(0)} n_2^{(0)} \left[ \frac{n_1 n_2}{n_1^{(0)} n_2^{(0)}} - \frac{n_3 n_4}{n_3^{(0)} n_4^{(0)}} \right], \quad (3.1.11)$$

where the thermally averaged annihilation cross section  $\langle \sigma v \rangle$  is given by

$$\langle \sigma v \rangle = \frac{1}{n_1^{(0)} n_2^{(0)}} \int \frac{d^3 p_1}{(2\pi)^3 2E_1} \int \frac{d^3 p_2}{(2\pi)^3 2E_2} \int \frac{d^3 p_3}{(2\pi)^3 2E_3} \int \frac{d^3 p_4}{(2\pi)^3 2E_4} e^{-(E_1+E_2)/T} \times (2\pi)^4 \delta^3(p_1 + p_2 - p_3 - p_4) \delta(E_1 + E_2 - E_3 - E_4) |\mathcal{M}|^2. \quad (3.1.12)$$

Restricting the general case to the identical initial and final states,  $\chi + \chi \rightleftharpoons \text{SM} + \text{SM}$ , leads to

$$\dot{n}_i + 3Hn_i = -\langle \sigma v \rangle \left[ n_\chi^2 - (n_\chi^{(0)})^2 \right]. \quad (3.1.13)$$

The thermally averaged annihilation cross section can be expressed as one dimensional integral [168]

$$\langle \sigma v \rangle = \frac{2\pi^2 T \int_{4m_\chi^2}^{\infty} ds \sigma(s - 4m_\chi^2) \sqrt{s} K_1\left(\frac{\sqrt{s}}{T}\right)}{\left(4\pi m_\chi^2 T K_2\left(\frac{m_\chi}{T}\right)\right)^2}, \quad (3.1.14)$$

where  $K_1$ ,  $K_2$  are the modified Bessel functions of the second kind [169].

In the non-relativistic regime, one can perform this integral analytically - the formulae are recapitulated in Appendix A.5.

<sup>4</sup>Which holds when, *e.g.*, a gas of particles is very dilute, which we assume.

**Freeze-out** In the early universe, the entropy defined as

$$s = \frac{2\pi^2}{45} g_{*s} T^3 \quad (3.1.15)$$

is conserved,

$$\frac{ds}{dt} + 3Hs = 0. \quad (3.1.16)$$

It is convenient to use this fact and recast Eq. (3.1.13) into

$$\frac{dY}{dx} = \frac{\langle\sigma v\rangle}{3H} \frac{ds}{dx} (Y^2 - Y_{\text{eq}}^2), \quad (3.1.17)$$

where  $Y = n/s$  is the comoving yield and  $x = m/T$  is the dimensionless inverse temperature.

In the very early universe and for large enough couplings between the DM and the SM,  $\chi$  was in thermal equilibrium with the plasma, *i.e.*,  $Y = Y_{\text{eq}}$ . After some time, when the annihilation rate, defined as  $\Gamma_{\text{ann}} = n \langle\sigma v\rangle$ , dropped below the Hubble rate,  $\Gamma_{\text{ann}} \lesssim H$ , the yield  $Y$  almost stopped changing and saturated at a value  $Y_{\text{fr}}$ . This process is referred to as freeze-out (also known as the chemical decoupling). Notably, in the radiation dominated epoch, the Hubble rate is given by  $H = \sqrt{\frac{8\pi^3}{90} g_\epsilon T^2 / M_{\text{Pl}}}$ , where  $g_\epsilon$  denotes relativistic energy degrees of freedom and  $M_{\text{Pl}} = 1.22 \times 10^{19}$  GeV is the Planck mass. The freeze-out process typically takes place when  $x = m_\chi / T \approx 20 - 25$ , almost independent of the WIMP mass  $m_\chi$ .<sup>5</sup> Example evolution of  $Y$  as a function of the  $x$  parameter is shown in Fig. 3.1.

Because both the entropy density and comoving yield are conserved, it is easy to relate the present  $\chi$  energy density to  $Y_{\text{fr}}$ ,

$$\rho_\chi^0 = m_\chi n_\chi^0 = m_\chi s_0 Y_0 = m_\chi s_0 Y_{\text{fr}}, \quad (3.1.18)$$

where  $s_0 = 2970 \text{ cm}^{-3}$  is the present entropy density.

Using the relation defining the decoupling,  $\Gamma_{\text{ann}} \sim H$  gives us the estimate of  $Y_{\text{fr}}$  [170]

$$Y_{\text{fr}} \simeq \frac{\sqrt{\frac{8\pi^3}{90} g_\rho T^2 / M_{\text{Pl}} \langle\sigma v\rangle}}{\frac{2\pi^2}{45} g_s T^3} \simeq 0.4 \frac{1}{M_{\text{Pl}} \langle\sigma v\rangle T_{\text{fr}}}. \quad (3.1.19)$$

Finally, the present-day relic density reads

$$\Omega_\chi^0 = \frac{\rho_\chi^0}{\rho_{\text{cr}}} = \frac{s_0 Y_{\text{fr}} M}{3H_0^2 / 8\pi G} = \frac{688 \pi^3 T_0^3 Y_{\text{fr}} M}{1485 M_{\text{Pl}}^2 H_0^2} \approx 0.2 \frac{2.2 \times 10^{-26} \text{ cm}^3 / s}{\langle\sigma v\rangle}. \quad (3.1.20)$$

Coincidentally, a particle  $\chi$  which interacts with SM via weak gauge boson would naturally lead to such annihilation cross section

$$\langle\sigma v\rangle \simeq \left(\frac{g}{0.1}\right)^4 \left(\frac{100 \text{ GeV}}{m_\chi}\right)^2 2.2 \times 10^{-26} \text{ cm}^3 / s, \quad (3.1.21)$$

---

<sup>5</sup>In fact, the corrections to the relation  $x \approx 20 - 25$  depend on the mass  $m_\chi$  logarithmically.

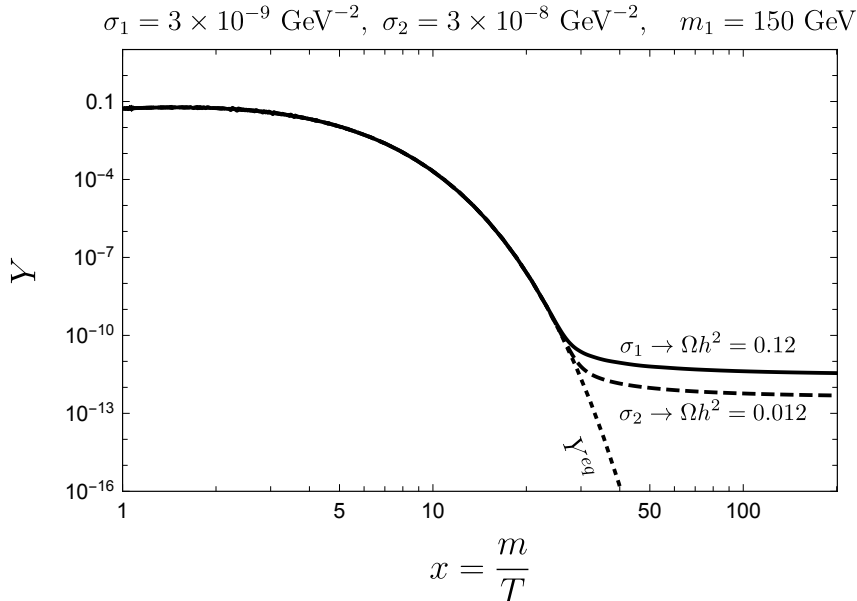


Figure 3.1: Evolution of the comoving yield of thermal relic of mass  $m_1 = 150 \text{ GeV}$  as a function of the dimensionless inverse temperature  $x$ . Three lines are shown, indicating from the top: solid line - the observed relic density obtained for the canonical annihilation cross sections, dashed line - a magnitude smaller relic density resulting from equally larger annihilation cross sections, and dotted - equilibrium yield. Freeze-out happens around  $x \sim 25$ .

where  $2.2 \times 10^{-26} \text{ cm}^3/\text{s} = 1.88 \times 10^{-9} \text{ GeV}^{-2}$ . This is an expression of the WIMP miracle, introduced in Section 2.3.3. As can be seen in Fig. 3.1, larger values of annihilation cross section lead to suppressed thermal DM relic density.

It should be noted that the canonical value of the thermally averaged annihilation cross section  $\langle \sigma v \rangle = 2.2 \times 10^{-26} \text{ cm}^3/\text{s}$  can be also obtained for masses and couplings much smaller or larger than the electroweak ones. We describe below some examples of such generalized WIMPs.

**Variations on the theme** So far we have discussed the basic mechanism of freeze-out, however, in specific implementations several important departures occur, first noted by [171]. While these effects introduce changes to the WIMP paradigm, they also mean that thermal freeze-out can be extended in a number of ways, broadening the scope of thermal DM production mechanisms. We briefly discuss those effects below:

- **Resonant production** Whenever the WIMP mass is close to half the mass of the s-channel mediator, the annihilation cross section is resonantly enhanced, which means that the observed DM relic density is obtained for much smaller couplings than the electroweak scale. This results in suppressed DD and collider signals, making DM detection even more difficult. A common example is the Higgs funnel region where  $m_{\text{WIMP}} \approx m_H/2 = 125/2 \text{ GeV} = 62.5 \text{ GeV}$  [106], which will be discussed in Chapter 6.
- **Sommerfeld enhancement** Another enhancement of the annihilation

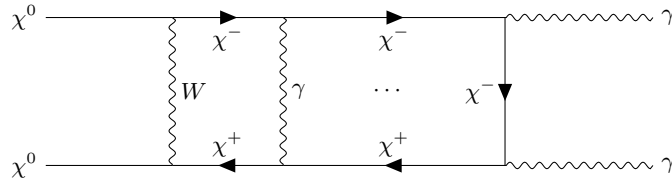


Figure 3.2: Sommerfeld enhancement for wino DM annihilating into photons - see Chapter 6 for discussion of this effect which significantly influences DM ID signal. Taken from [177].

cross section comes from the exchange of light mediators, which effectively leads to a long-range force of significant strength for slow-moving DM particles [172–175].<sup>6</sup> It will be discussed in Chapter 6 in the context of heavy neutralino DM,  $m_{\text{WIMP}} \sim 2 \text{ TeV}$ . In the case when the neutralino is mostly composed of heavy superpartner of the neutral weak gauge boson (wino), there are sizable couplings of neutralino to much lighter SM gauge bosons, leading to formation of “ladder” diagrams shown in Fig. 3.2. A resummation of such diagrams leads to the Sommerfeld enhancement.

- **Coannihilation** If there are many particles in the dark sector that survive until DM freeze-out and their masses are similar to the lightest one, their contributions to the annihilation cross section Eq. (3.1.14) must also be taken into account. It requires the use of  $\langle \sigma v \rangle_{\text{eff}}$  in Eq. (3.1.13),

$$\langle \sigma v \rangle_{\text{eff}} = \sum_{i,j} \frac{n_i^{\text{eq}} n_j^{\text{eq}}}{(n_{\text{eq}})^2} \langle \sigma_{ij} v \rangle, \quad (3.1.22)$$

where  $i, j$  are the indices of the coannihilating particles. Coannihilations often occur in models with a compressed spectrum, *e.g.*, SUSY and may even be the main mechanism for DM production. For example, in models with dominant inelastic coupling between two dark sector states where only the lighter one is stable and constitutes the DM - so-called inelastic DM [178] - coannihilation naturally leads to the observed relic density, while avoiding the stringent CMB constraints on the energy injection from DM annihilation that heats the photon-baryon plasma.

- **Forbidden dark matter**<sup>7</sup> In discussing freeze-out we assumed that DM annihilates into lighter particles in the thermal plasma because the DM is non-relativistic when decoupling. One can also consider the inverse mass hierarchy,  $m_{\text{DM}} < m_{\text{SM}}$ , in which case the DM particles are very light. By the principle of detailed balance, we can relate the “forbidden” annihilation cross section of two such light DM particles into the SM species,  $\langle \sigma v \rangle_{\text{DMDM}}$ ,

<sup>6</sup>A similar effect also potentially significantly increasing the DM annihilation cross section is based on DM bound-states formation. It is expected to take place efficiently for heavy, multi-TeV DM - see [176] and references therein for thorough discussion.

<sup>7</sup>It was first introduced in [171] under the name of “threshold effect”, while a detailed discussion and the name of “forbidden dark matter” comes from [179].

to the one relevant for the “allowed” inverse process,  $\langle\sigma v\rangle_{\text{SMSM}}$

$$\begin{aligned}\langle\sigma v\rangle_{\text{DMDM}} &= \langle\sigma v\rangle_{\text{SMSM}} \left(\frac{n_{\text{SM}}^{\text{eq}}}{n_{\text{DM}}^{\text{eq}}}\right)^2 \sim \langle\sigma v\rangle_{\text{SMSM}} e^{-2(m_{\text{SM}}-m_{\text{DM}})/T} \\ &\sim \frac{\alpha_D^2}{m_{\text{DM}}^2} e^{-2(m_{\text{SM}}-m_{\text{DM}})/T},\end{aligned}\tag{3.1.23}$$

where in the last step we estimated the thermal annihilation cross section assuming DM particles annihilate into a pair of SM species. As can be seen, the velocity-averaged cross section for the forbidden annihilation channel is exponentially suppressed which follows from the conservation of energy. Annihilation into heavier particles is only allowed for fast-moving DM particles that correspond to the tail of the non-relativistic Maxwell-Boltzmann distribution. Comparing Eq. (3.1.23) to the WIMP estimate,  $\langle\sigma v\rangle_{\text{DMDM}} \sim 10^{-9} \text{ GeV}^{-2}$ , one can obtain the DM mass for which the correct relic density is obtained in the forbidden regime [134, 180]

$$m_{\text{DM}} \sim \frac{e^{-(m_{\text{SM}}-m_{\text{DM}})/T_f} \alpha_D}{\sqrt{10^{-9} \text{ GeV}^{-2}}} \ll \text{TeV},\tag{3.1.24}$$

where  $T_f$  is the temperature of freeze-out. Note that such DM mass ranges are exponentially smaller than the mass ranges of WIMPs.

- **WIMPless miracle** Although Eq. (2.3.8) is naturally satisfied for a WIMP with mass at the electroweak scale, many other values of the  $(m_{\text{DM}}, g_{\text{DM}})$  parameters also lead to the correct relic density *beyond the weak-scale mass or weak interaction ranges* [181]. This is particularly true for SUSY models with gauge-mediated supersymmetry breaking, where  $m_{\text{WIMP}} \sim g_{\text{WIMP}}^2$  [182, 183], and also for light DM candidates - with mass in the range  $\sim 10 \text{ MeV} - 10 \text{ GeV}$  - where we lower both the DM mass  $m_{\text{DM}}$  and the coupling  $g_{\text{DM}}$  [184, 185].

We discuss scenarios where the DM production is directly based on this mechanism in Chapters 4 and 5.

**Non-thermal production mechanisms** Although in this thesis we focus on thermal DM candidates, it should be noted that alternative, non-thermal production mechanisms have been proposed and investigated, including notably: asymmetric production [186], freeze-in [187], the misalignment [112], and Dodelson-Widrow [122] mechanisms. A thorough discussion can be found in recent reviews on the topic [134, 147].

## 3.2 Detection methods

As we discussed in the previous section, thermal DM would be efficiently produced in the early Universe if there are sizable interactions between the DS and the SM. Interestingly, the processes that are responsible for DM thermal freeze-out also lead to sizable interactions with the SM particles taking place at present. It allows for a complementary programme of experimental searches, shown in Fig. 3.3. Below, we

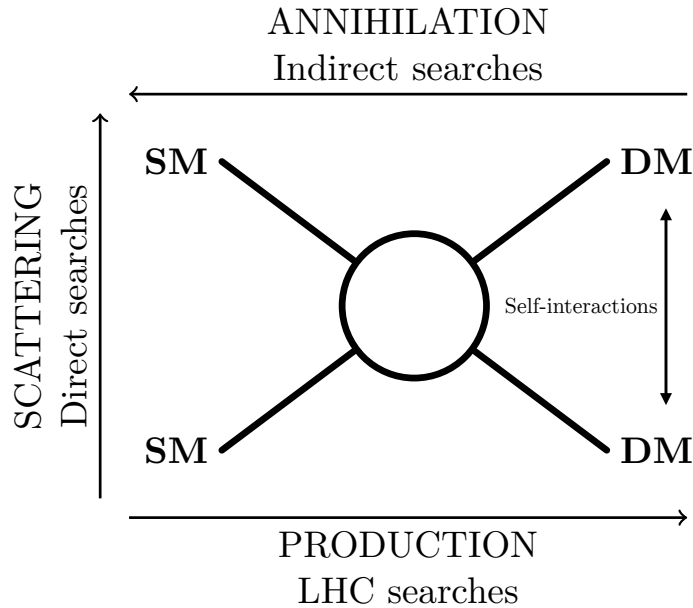


Figure 3.3: Complementary program of three main search strategies for WIMPs: collider searches (bottom), direct detection (left), and indirect detection searches (top). Moreover, astrophysical observations, *e.g.*, the Bullet Cluster can constrain internal interactions within the DS, like DM self-interactions. Modified figure taken from [188].

describe them in some detail, while we also note that, given weaker experimental bounds in the DS, DM can scatter with itself quite efficiently [189] and such DM self-interactions lead to interesting modifications of the  $\Lambda$ CDM model, which we discuss in Chapter 8.

**Direct detection (DD) searches** In the early 1980s it was realized that there was a viable route to direct detection of neutrinos through coherent scattering off nuclei [190]. This had first been theoretically proposed a decade earlier [191]. It was soon realized that a similar method could be used to search for DM via nuclear recoils [192, 193]. Scattering of a WIMP of mass  $\sim 100$  GeV in liquid noble gas detectors will result in recoil energy of the SM target nucleus in the range 10–100 keV. This is at least an order of magnitude smaller than the corresponding signal of the coherent neutrinos scattering off nuclei which in 2017 was detected for the first time by the COHERENT experiment [194]. This illustrates both the promise and difficulty of such DM searches. For a more detailed discussion of the development of DM DD searches, see, *e.g.*, the recent review [87].

Despite great progress in DD experiments, there is no conclusive direct signal of DM to date.<sup>8</sup> Instead, exclusion limits were derived, as shown in Fig. 3.4, which presents spin-independent WIMP scattering cross section with SM nuclei.

<sup>8</sup>Over the years, there have been several claims of DM direct detection. The most notable of which came from the DAMA/LIBRA collaboration [195] which claimed to observe an annual signal modulation, due to the Earth’s orbital motion around the Sun (first discussed in [193]). However, other experiments, *e.g.*, the COSINE-100 collaboration [196] have not observed this modulation, calling into question its putative origin from DM.

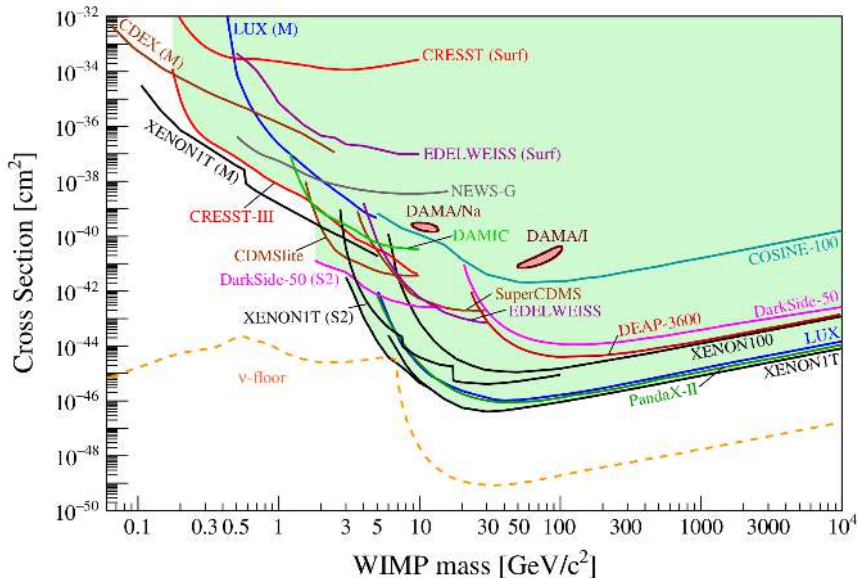


Figure 3.4: Current exclusion limits for spin-independent WIMP scattering cross section with SM nuclei in direct detection experiments. The limits shown are from current (region filled in green) and near future observations. Note the gold dashed line denoting the irreducible neutrino floor which we discuss in the text. Taken from the recent APPEC Committee Report [87].

Important features of DD shown in this plot are: (i) coverage of the  $\sim 5$  GeV WIMP region has already reached the irreducible neutrino floor [197]<sup>9</sup> and (ii) experiments lose sensitivity to the low DM mass range due to insufficient nuclear recoil.

To address that problem, many new detection methods were proposed, which are based, *e.g.*, on scattering off electrons in atoms or crystals - resulting in atomic ionization [199] and Migdal effect [200] - inelastic nuclear recoils [201], and collective excitations (phonons) of the atoms in the medium which DM scatters off [202]. For extensive discussion, cf. recent reviews [203, 204], which - in addition to the above methods - also discuss proposals involving Dirac materials [205], semiconductors [206], superfluid helium [207], and many others.

**Indirect detection (ID) searches** ID searches are based on observations of primary or secondary gamma and cosmic rays or neutrinos produced by the annihilation or decay of DM particles [208–210]. Current limits on present-day annihilation cross sections obtained in such a way are shown in Fig. 3.5.

DM ID processes: (i) may be related to the DM freeze-out, meaning that ID is naturally suited to study such DM production mechanism and (ii) should lead to distinctive signatures that could not be easily mimicked by ordinary astrophysical

<sup>9</sup>The neutrino floor is expected to be caused by a large flux of solar and atmospheric neutrinos interacting with detector nuclei. For  $\sim 5$  GeV WIMP mass scattering off nucleus with the same mass, the solar neutrino with incident energy of  $E \sim 2$  MeV is expected to produce the same recoil, mimicking the DM signal. The gold line shown in Fig. 3.4 marks the region where the WIMP DM signal is expected to be buried in the neutrino signal - but also see [198] and references therein for a discussion how this limit can be overcome.

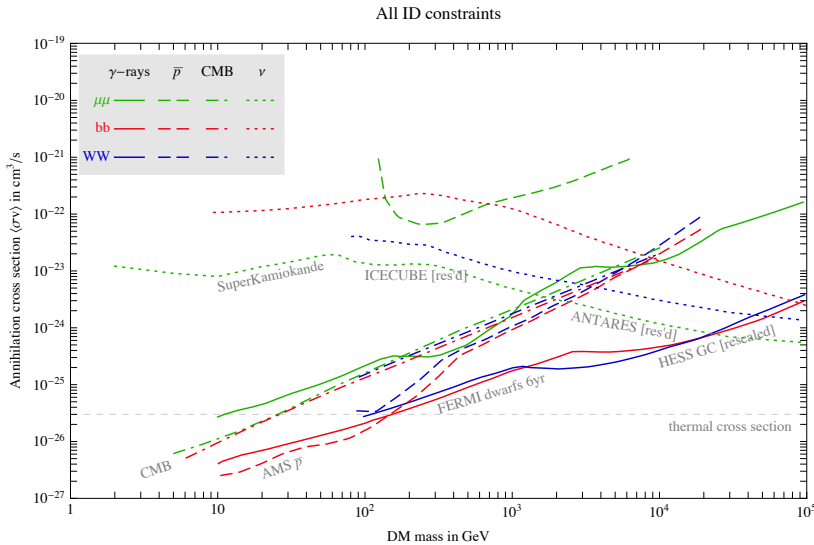


Figure 3.5: Plot summarizing upper bounds on the DM annihilation cross section as a function of the DM mass for different SM channels using state-of-the-art observations. Conservative bounds were chosen when few were available. The benchmark value of the thermal annihilation cross section is indicated by the dashed gray line. Updated plot taken from [211].

processes. Therefore, the targets of ID searches are regions in the sky with high DM density and well-understood astrophysical background. These are, *e.g.*, the selected regions around the Galactic Center (GC) [212, 213], and less bright dwarf spheroidal galaxies [214, 215], which involve much smaller background than the GC.

However, even in the presence of significant astrophysical background, we can search for signals of DM also based on non-standard features in the spectrum induced by DM annihilations. This is, *e.g.*, employed in searches for DM-induced antimatter cosmic rays, which - as can be seen in Fig. 3.5 (the AMS  $\bar{p}$  line) - can be strong enough to exclude light  $\sim 10 - 100$  GeV WIMPs with the thermal annihilation cross section [216, 217]; see also corresponding analysis using positrons [218]. Lighter DM can be further constrained by the DM annihilations and decays into SM particles, which would significantly modify the CMB spectrum. Other methods of DM ID involve searches for DM-induced neutrinos [219], X-rays [220, 221], and 21-cm hydrogen line observations [222].

Similarly to the DD searches, several anomalies potentially involving DM were identified, *e.g.*, the Galactic Center excess [223], cf. also recent review [224], where leading explanations involve either annihilation of DM or milli-second pulsars. For extensive discussion of DM ID anomalies cf. [208, 210].

From Fig. 3.5, one can see that the benchmark value of the thermal annihilation cross section for the WIMP with the mass  $m \lesssim 10$  GeV is covered by CMB observations, assuming *s*-wave (velocity independent) annihilation cross section. In addition, the  $\sim 10 - 100$  GeV range is also covered by Fermi-LAT [225] observations of dwarf galaxies and AMS [226]  $\bar{p}$  observations. In addition, the corresponding searches towards the GC can constrain thermal DM up to mass of the order of several hundred GeV - Fermi-LAT  $\gamma$ -ray [213], and AMS [226] positron search.

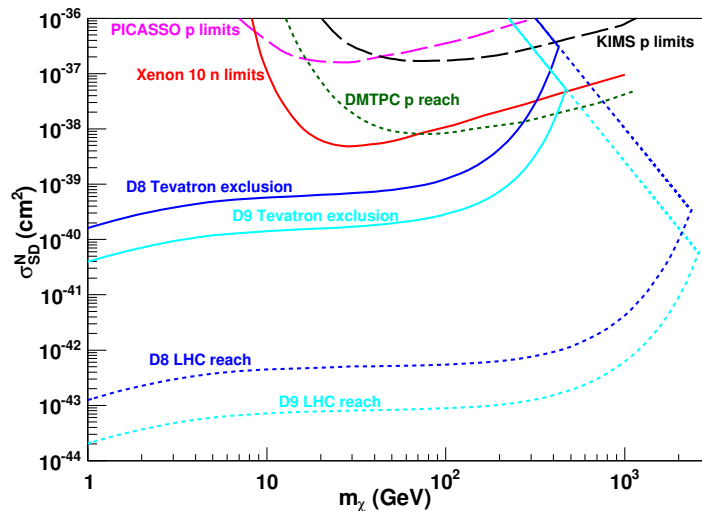


Figure 3.6: Comparison of exclusion limits for spin-dependent WIMP scattering cross section with SM particles obtained in direct detection and collider searches (LHC and Tevatron). Taken from [227].

Those limits, however, depend on less well understood quantities, such as the DM halo density profile and also potentially numerous astrophysical background, which could relax them.

Furthermore, it should be emphasized that, with the exception of CMB observations, ID experiments can only constrain present-day DM annihilations, and not the DM annihilations occurring during the freeze-out process unless the DM annihilates dominantly via the  $s$ -wave process with the velocity-independent annihilation cross section. If the DM relic density is obtained, *e.g.*, thanks to  $p$ -wave annihilations or coannihilations, they do not directly constrain such scenarios.

**Missing energy searches at colliders and beyond** Collisions at high energies are expected to copiously produce BSM states, which may also be related to the DM problem. One major signature is the search for events with missing transverse energy where the background for such signatures involves SM scattering and decay processes producing neutrinos. In light of that, detailed analyses are necessary to account for the background and isolate the DM signal.

At present, no unambiguous DM signal has been observed, and model-dependent limits were obtained. In Fig. 3.6 we show a comparison of the sensitivity of collider (Tevatron and LHC) and DD searches (DMTPC [228], KIMS [229], PICASSO [230], and XENON [231]) within the effective field theory (EFT) approach to DM-SM particles scattering following [227]. The results shown for illustration correspond to the axial current dimension-6 operator (labeled D8) between quarks and DM. As one can see, the collider searches can be used to obtain stringent limits, especially for the smaller DM mass below the TeV scale. As we do not discuss standard collider DM searches in further chapters, for extensive discussion of such searches we refer to the recent reviews [232, 233].

Missing energy or momentum searches are also employed to search for sub-

GeV, very weakly interacting DM at lower energies, as a part of the rapidly developing program of intensity frontier searches for new physics [234–236]. Among the current and proposed such experiments are: BaBar [237, 238], Belle-II [239], LDMX [240], M<sup>3</sup> [241], and NA64 [242].

**Direct DM accelerator-based searches** DM, possibly along with other DS particles, can also be directly studied via their scatterings off SM particles in dedicated detectors after being produced in beam-dump, neutrino, or collider experiments. These include recent neutrino experiments, *e.g.*, MiniBooNE [243], as well as direct detection type detectors, *e.g.*, the proposed BDX [244], FLArE [245], SND@SHiP [246], and SND@LHC [247] detectors; cf. recent community review [244] for details.

The strategy employed by these observations differs from both the missing energy collider searches and the DD searches because it relies on detecting boosted DM scatterings, which occur in the relativistic regime. Let us also note that the results of past experiments have been reinterpreted in this way, *e.g.*, [248, 249].

**Astrophysical probes** Finally, DM can be probed by astrophysical observations (i) in which DM gravitational imprint can be constrained, using, *e.g.*, astrometry like the Gaia space mission [114] - cf. recent review [250] and (ii) also self-interactions within the DS can be constrained.

The constraints on the DM self-interactions are expressed as a bound on the transfer cross section defined as

$$\sigma_{\text{tr}} = \int d\Omega (1 - \cos\theta) \frac{d\sigma}{d\Omega}, \quad (3.2.1)$$

where  $d\Omega = d\cos\theta d\phi$ , and  $(1 - \cos\theta)$  is the weight factor corresponding to the forward momentum transfer in each of the scattering events [189].<sup>10</sup> Observations put stringent bounds on DM self-interactions

$$\sigma_{\text{tr}}/m_{\text{SIDM}} \lesssim 0.13 \text{ cm}^2/\text{g}, \quad (3.2.2)$$

which is determined from observation of the Bullet Cluster [251], other cluster mergers [53], data from strong lensing of clusters [252], and observed halo surface densities of DM halos [253].

Interestingly, a similar range of self-interactions,  $0.10 \text{ cm}^2/\text{g} \lesssim \sigma_{\text{tr}}/m_{\text{SIDM}} \lesssim 10 \text{ cm}^2/\text{g}$ , is invoked as one of the leading solutions to the small-scale problems of the  $\Lambda$ CDM [189]. Solving the small structure problems while avoiding galaxy cluster bounds might require velocity-dependent self-interaction cross section which becomes suppressed for the increasing DM velocity. We note that typical DM velocities in dwarf galaxies correspond to  $v \sim 30 \text{ km/s}$ , Milky-way-size galaxies to  $v \sim 200 \text{ km/s}$ , and in clusters of galaxies to  $v \sim 1000 \text{ km/s}$  [189]. Finally, we also note that there are additional constraints on SIDM models from structure formation [254] and model building [255] perspectives.

---

<sup>10</sup>This quantity is commonly used in the literature and simulations, but alternative choices are also adapted [189].

Although the thermal DM production mechanism discussed in this chapter is robust and far from being excluded even at the GeV scale [256], experiments to date - such as the LHC - have not found any clear signs of a  $\sim 100$  GeV WIMP. This motivates the search for lighter and even weaker interacting particles than WIMPs, which we study in the next few chapters.



# Chapter 4

## Looking for long-lived particles using secondary production

### 4.1 Introduction

After a detailed introduction to the DM problem, we devote this and the next chapter to the study of models with light DM or other sub-GeV dark sector particles. We focus on both the most simplified models and scenarios that extend them. The motivations for such studies are multiple: (i) the lack of experimental confirmation of DM WIMPs at the electroweak scale,<sup>1</sup> (ii) the fact that straightforward generalization of the WIMP DM miracle to the WIMPless one - introduced in Section 3.1 - takes place for much lighter and sub-weakly interacting particles, and (iii) the existence of a general class of BSM scenarios, *e.g.*, the “Hidden Valley” scenario [257] - see also reviews [235, 258] - which predicts at least one LLP within a low mass dark (hidden) sector.

If the light new physics particles exist in nature and are coupled to the SM, they might be the most convenient sector of the full BSM model to be probed experimentally. This is first due to their relative accessibility even in low-energy searches, but it is also driven by a possible simplicity in their theoretical description. The simplest but effective way to study BSM scenarios predicting LLPs is through the EFTs. There, one generically expects a decoupling of the heavier fields from the dynamics occurring at low-energy scales. In result, only the light degrees of freedom remain, which in turn can be described by the simplified models. Such bottom-up theoretical considerations are both simple and universal, see, *e.g.*, [259], as they considerably simplify the analysis while being easily extended to various UV-complete theories. Let us also note that due to the interest of the high-energy community in such BSM scenarios, extensive experimental efforts in probing new light physics [234, 235, 244] has been developed.

---

The contents of this chapter is based on: K. Jodłowski, F. Kling, L. Roszkowski and S. Trojanowski, *Extending the reach of FASER, MATHUSLA, and SHiP towards smaller lifetimes using secondary particle production*, *Phys. Rev. D* **101** (2020) 095020, [1911.11346].

<sup>1</sup>Let us note that while general electroweak scale WIMPs are hardly excluded, as we discuss in Chapter 6, the most optimistic such theories, *e.g.*, those based on naturalness or those postulating grand unification of interactions, are disfavored, if not completely ruled out [135].

### 4.1.1 Renormalizable portals

In this section, we introduce the simplified models of new physics that rely on renormalizable and gauge invariant portals connecting the SM and a DS, as illustrated in Fig. 1.1. It turns out that while there are only a few such possibilities, they can lead to quite rich physics. Moreover, the DS within them can be naturally extended, leading to further interesting phenomena.

**Vector portal** In particular, BSM physics models often extend the gauge symmetry group of the SM to larger ones. In the simplest scenarios, an additional  $U(1)$  gauge symmetry with a corresponding gauge boson,  $A'$  - which is typically called dark photon described by the field strength tensor  $F'_{\mu\nu} = \partial_\mu A'_\nu - \partial_\nu A'_\mu$  - is postulated; cf. recent reviews on the topic [260–262].

The dark photon can be connected to the SM  $A_\mu$  gauge boson,<sup>2</sup> described by ordinary electromagnetism theory with the field strength tensor  $F_{\mu\nu} = \partial_\mu A_\nu - \partial_\nu A_\mu$ , by the kinetic mixing operator

$$\mathcal{L}_{\text{vector portal}} = -\frac{\epsilon}{2} F'_{\mu\nu} F^{\mu\nu}. \quad (4.1.1)$$

The kinetic mixing parameter,  $\epsilon$ , is generically generated at the loop level in many theories BSM [263, 264], which leads to decays of the dark photon into kinematically allowed SM states, see also recent review [265],

$$\epsilon \sim \frac{g_1 g_2}{16\pi^2} \ln \left( \frac{M^2}{\mu^2} \right), \quad (4.1.2)$$

where  $g_1, g_2$  are the gauge couplings of the SM and the additional  $U(1)$  groups,  $M$  is the mass of the particle flowing in the loop, and  $\mu$  is a renormalization scale. This typically leads to  $\epsilon \lesssim 10^{-4}$ . As a result, the relevant unstable dark vector particle can have a sizable lifetime, see Eq. (4.2.2).

We discuss a few DS models based on the vector portal in later sections of this chapter.

**Scalar portal** introduces the following coupling between a new gauge singlet scalar  $S$  and the SM Higgs doublet  $H$ :

$$\mathcal{L}_{\text{scalar portal}} = \alpha_1 S H^\dagger H + \alpha S^2 H^\dagger H, \quad (4.1.3)$$

see recent reviews [258, 266, 267]. The coupling  $\alpha_1$  leads to mixing of the dark Higgs (DH)  $S$  and the SM Higgs boson  $H$ , parametrized by the mixing angle  $\theta \approx (\alpha_1 v_{SM})/m_H^2$ , where  $v_{SM} = 246$  GeV and  $m_H = 125$  GeV [106]. This expression assumes that the DH is much lighter than ordinary Higgs boson.

We discuss an extended realization of such a scenario in Chapters 7 and 8.

---

<sup>2</sup>One can also consider connection to the SM  $Z_\mu$  gauge boson, which is typically considered for dark photon heavier than the  $Z_\mu$  gauge boson.

**Neutrino portal** couples the new gauge singlet fermion  $N$  to the  $\epsilon_{ab}\bar{L}_a H_b$  term<sup>3</sup>

$$\mathcal{L}_{\text{neutrino portal}} = F_\ell (\epsilon_{ab}\bar{L}_{\ell,a} H_b) N, \quad (4.1.4)$$

where  $L_a$  is the  $SU(2)$  lepton doublet and  $\epsilon_{ab}$  is absolutely antisymmetric tensor in 2 dimensions; cf. recent reviews [128, 268]. The name ‘‘sterile neutrino’’ comes from the fact that neutrino portal interactions fixes  $N$  to be uncharged under the SM gauge groups, as only the right-handed part of  $N$  interacts with the active neutrinos from the SM. As a result, sterile neutrinos are also often called right-handed neutrinos.

We discuss a particular realization of such a scenario in Chapter 5.

**Dark matter within the renormalizable portals** can naturally be produced in the early Universe with the correct amount in scenarios with a light DM particle and a light mediator thanks to the WIMPless mechanism introduced in Section 3.1.

For example, a scalar DM with mass  $m_{\text{DM}} < m_{A'}$  coupled to the dark photon can efficiently annihilate into SM fermions through an exchange of an off-shell dark photon,  $\chi\chi^* \rightarrow A'^* \rightarrow f\bar{f}$

$$\sigma v \sim v^2 \frac{\alpha \epsilon^2 g_D m_{\text{DM}}^2}{m_{A'}^4}, \quad (4.1.5)$$

where  $\alpha$  is the SM fine structure constant. Notably, this annihilation cross section is  $p$ -wave suppressed, as it depends on the square of the velocity partial wave expansion - see Appendix A.5 - which allows it to evade stringent CMB bounds [269, 270].

For opposite mass hierarchy,  $m_{\text{DM}} > m_{A'}$  - called the secluded DM [185, 271] - the dominant annihilation channel is  $\chi\chi^* \rightarrow A'A'$ . The relevant annihilation cross section has the following form:

$$\sigma v \sim \alpha_D^2 \frac{m_{\text{DM}}^2}{m_{A'}^4}, \quad (4.1.6)$$

*i.e.*, it depends only on the dark gauge coupling constant  $g_D$  and the masses of the DM particle and the dark vector. It is worth noting that for a GeV-scale DM mass and for sub-GeV dark vector, the correct relic density is obtained for  $\alpha_D \sim 10^{-5}$  which leads to negligible scattering rates in DD searches as well as negligible present-day annihilation cross section, also making ID searches not possible.

Further details and other related scenarios are discussed in, *e.g.*, [272]. For fermionic DM - either Majorana or pseudo-Dirac fermion - a similar thermal freeze-out mechanism can also take place with suitably modified annihilation cross sections.

### 4.1.2 Intensity frontier searches for light long-lived particles

In recent years, there have been dedicated experimental, *e.g.*, [234–236] and theoretical, *e.g.*, [244, 273] efforts in this direction which lead to, among other

<sup>3</sup>The fermion  $N$  is also known as heavy neutral lepton (HNL) or sterile neutrino.

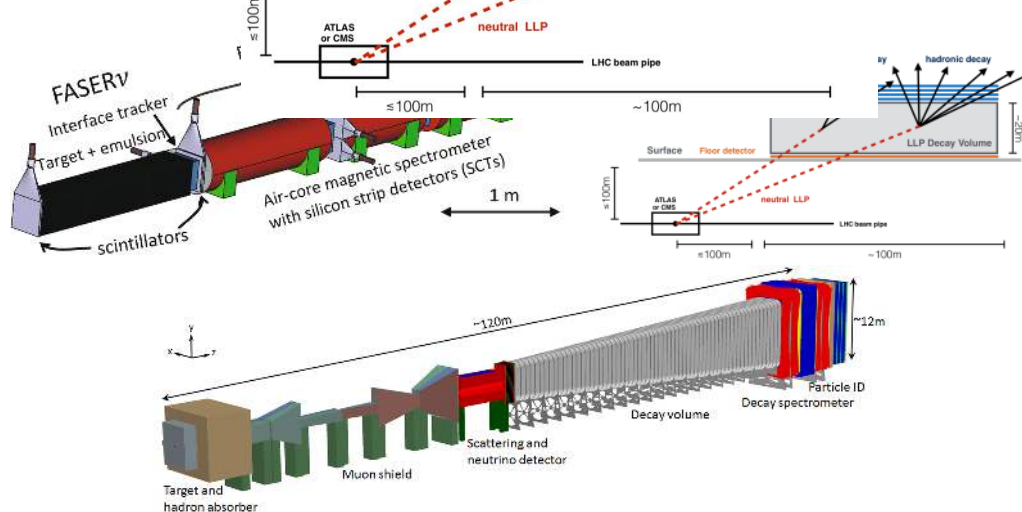


Figure 4.1: Schematic structure of the detectors considered. From top to bottom, clockwise: FASER (taken from [274]), MATHUSLA (taken from [275]), and SHiP (taken from [258]).

things, recasting of limits from previous experiments into the LLP models, and many proposals of new-generation detectors (see Fig. 4.1 containing a few of the CERN based ones relevant to our discussion), including those that would take data at the LHC - see the aforementioned reviews [234–236, 244, 273] and the [LHC Long-lived Particles Working Group](#) initiative.

A promising and well-motivated signature involves highly displaced LLPs decays in distant detectors that are (i) spatially separated from the primary interaction point and (ii) well shielded from the SM background (BG). Such separation makes this search a very promising avenue to potentially uncover BSM physics, as the observation of only a few such events would be sufficient.

Among the experiments that have been proposed to employ such strategy are the LHC experiments, FASER and MATHUSLA, as well as the CERN-based beam-dump experiment SHiP which we illustrate in Fig. 4.1. We will focus on them, as they will probe the strongly boosted light and long-lived particles in different, complementary regimes in the near future. We also note that there are other experiments whose goal is to search for such particles: neutrino experiments like Super-Kamiokande [276], B factories like Belle-II [277, 278], and experiments using  $e^+e^-$  collisions, *e.g.*, BaBar [279].

#### 4.1.2.1 FASER

The FASER experiment was proposed [280] to search for LLPs abundantly produced in the forward direction of the LHC and then decay in the distant detector [280–284]. The experiment was approved to collect data during LHC Run 3, while a larger version of the detector, named FASER 2, was also proposed [284] that could collect data during the HL-LHC era. This could be hosted in the future Forward Physics Facility at CERN [6] which would also contain many other detectors dedicated to searches for light new physics. In what follows, we present results for both FASER and FASER 2 experiments, as well as for the small version

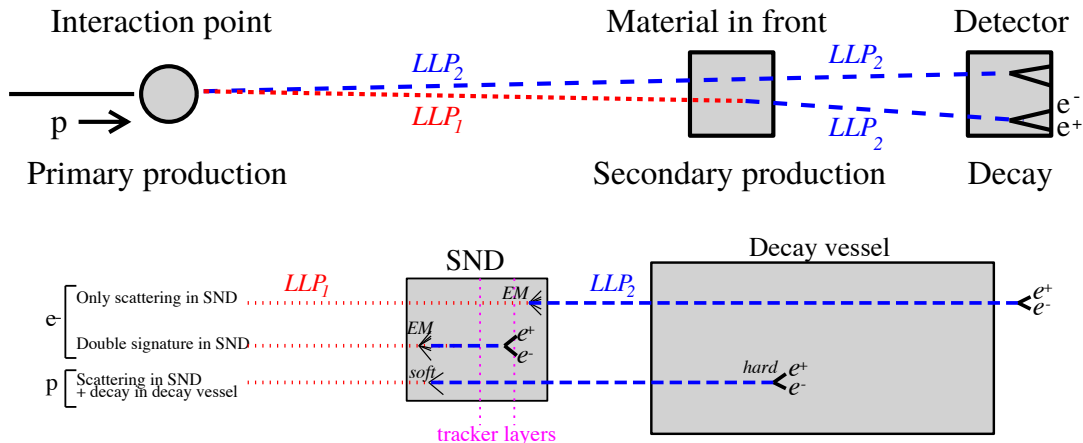


Figure 4.2: Schematic illustrations of LLP secondary production that occurs upstream of the detector, allowing intensity frontier searches (this is a broad class of searches that look for light and very weakly-interacting particles that may have escaped detection so far due to lack of sufficient luminosity) to also probe shorter lifetime regime. Top: primary (blue line) and the secondary production (right line) of the light long-lived particle  $LLP_2$ , followed by its decays in the decay vessel. Bottom: signatures related to LLP scattering with electrons inside neutrino emulsion detectors, here shown for the SND detector at SHiP, while a similar, more extended analysis dedicated to the study of neutrino non-standard interactions is described in the next chapter for the FASER $\nu$  detector. See also Fig. 4.1.

of FASER left for the entire HL-LHC era.

The FASER detector consists of a decay vessel in the shape of a cylinder with length  $\Delta$  and radius  $R$ , followed by a spectrometer and calorimeter. The muon-induced BG is vetoed by the layer in front of the detector. The detector is located at the LHC TI12 tunnel about  $L = 480$  m from the ATLAS IP along the axis of the beam. Moreover, it is shielded from the ATLAS IP by 10 m of concrete and about 90 m of rocks, on top of various LHC infrastructure elements. The detector geometries and integrated luminosities corresponding to all three versions of the FASER experiment are as follows:

- **FASER**  $\Delta = 1.5$  m,  $R = 10$  cm,  $\mathcal{L} = 150$  fb $^{-1}$ ,
- **FASER (HL)**  $\Delta = 1.5$  m,  $R = 10$  cm,  $\mathcal{L} = 3$  ab $^{-1}$ ,
- **FASER 2**  $\Delta = 5$  m,  $R = 1$  m,  $\mathcal{L} = 3$  ab $^{-1}$ .

In addition to the main FASER detector, an additional detector will be taking data during LHC Run 3 [285], named FASER $\nu$ ,<sup>4</sup> which is an emulsion detector made of about a thousand 1-mm-thick tungsten layers interleaved with emulsion films. It will be placed in front of the main detector with the main role of studying high-energy neutrino interactions.

<sup>4</sup>In fact, a prototype of this detector has recently observed first neutrino candidate events [286], which is the first such measurement at the LHC or any other particle collider.

### 4.1.2.2 MATHUSLA

Like FASER, the MATHUSLA experiment has been proposed [287, 288] to exploit the potential abundant production of LLPs at the LHC that could have avoided detection so far. It will use a large-scale hodoscope detector placed above the CMS IP to take data during the HL-LHC era.

We use the proposed MATHUSLA100 design [289]. The main part of MATHUSLA is a decay volume of  $20 \text{ m} \times 100 \text{ m} \times 100 \text{ m}$  size followed by a tracking system covering the entire detector. In addition, layers of scintillators are placed at the bottom and sides of the decay volume to veto charged particles entering the detector. The geometry of the decay volume that we use is

$$80 \text{ m} < x < 100 \text{ m}, -50 \text{ m} < y < 50 \text{ m}, 68 \text{ m} < z < 168 \text{ m}, \quad (4.1.7)$$

where we set the origin of the coordinate system at the CMS IP,  $x$  denotes the upward direction, while  $z$  is the direction along the LHC beam pipe.

### 4.1.2.3 SHiP

The proposed SHiP detector [258, 290] is a beam dump experiment that will use a beam of 400 GeV protons incident on a target made of titanium-zirconium doped molybdenum alloy and tungsten. As the expected number of protons on target is  $N_{\text{POT}} = 2 \times 10^{20}$ , a large number of LLPs could be produced.

The most important part of SHiP from the point of view of secondary LLPs is the Scattering and Neutrino Detector (SND), its surrounding magnet, and a 50 m long decay vessel.<sup>5</sup> The scattering processes occurring at SND can lead to LLP production just a few meters in front of the decay vessel. The SND consists of an emulsion detector followed by the SND muon system. The latter can partially act as a veto for the decay vessel, thus we exclude all scattering events occurring in the material lying in its close vicinity, within  $3 \lambda_{\text{hadronic,interactions}}$ .

## 4.1.3 Secondary LLP production

The presented searches for light and long-lived particles are limited by the lifetimes of the LLPs which must travel the entire distance from the production point to the detector. Importantly, however, LLPs with smaller lifetimes driven by larger couplings to the SM are often interesting targets for new physics searches. This is both due to their larger production rates and the fact they might also more easily be related to various experimental anomalies that can be attributed to such BSM particles.

In realistic BSM scenarios, we actually expect there to be more than just a single new particle, in particular there can be more light new species (which, however, do not need to be long-lived). Furthermore, in less simplified models with particle spectrum containing at least two LLPs, coupling between the BSM species naturally leads to additional production modes in the BSM interactions in the material surrounding the detector. Below, we provide specific examples of such scenarios. If such *secondary LLP production* occurs much closer to the decay vessel

---

<sup>5</sup>For detailed discussion of SHiP detector - and its many updates - see [2, 291].

than primary production, then one can also probe LLP lifetimes much smaller than usual, while still searching at essentially zero BG. We illustrate this in Fig. 4.2, where we also show the main signatures of new physics considered by us: the displaced decay of LLPs inside the decay vessel and LLP scattering with electrons in neutrino emulsion detectors.

In the following sections, we analyze the prospects for such searches in the complementary experiments, we have already introduced, *i.e.*, FASER, MATHUSLA, and SHiP which could naturally employ the secondary production mechanism to increase their discovery potential. FASER will collect data during the upcoming Run 3 of the LHC. It is planned to be extended (FASER 2) to a larger decay vessel toward the high luminosity (HL) LHC phase. Around this time, MATHUSLA, and SHiP are also planned to start taking data.

## 4.2 Models

We study popular extensions of the massive, light dark vector portal associated with the kinetic mixing, Eq. (4.1.1), between the SM hypercharge gauge boson and the dark vector  $A'$  associated with the new  $U(1)_D$  symmetry group. The mass term and the interactions between the dark vector and the SM fermions  $f$  after removing the non-diagonal kinetic mixing term by the field redefinition are as follows:

$$\mathcal{L} \supset \frac{1}{2} m_{A'}^2 A'^2 - \epsilon e \sum_f q_f \bar{f} A' f, \quad (4.2.1)$$

where  $q_f$  are the electromagnetic charges of the corresponding fermions in the units of elementary charge  $e$ .

We focus on the mass range  $m_{A'} \lesssim \text{MeV} - \text{GeV}$  and the kinetic mixing parameter  $\epsilon \sim 10^{-3}$  that are one of the main targets of intensity frontier searches and lie below current bounds on this scenario [234–236].

After such dark photons are produced, they decay mainly into SM particles with the corresponding decay length given in Eq. (B.1.9) which leads to the following decay length:

$$(c\tau\beta\gamma)_{A'} \sim 1 \text{ m} \times \left[ \frac{10^{-4}}{\epsilon} \right]^2 \left[ \frac{E_{A'}}{100 \text{ GeV}} \right] \left[ \frac{30 \text{ MeV}}{m_{A'}} \right]^2, \quad (4.2.2)$$

where  $E_{A'}$  is the energy of the dark photon. As one can see, this regime indeed leads to a boosted  $A'$  with lifetimes that can be probed in intensity frontier detectors if the dark photon is produced right in front of the detector at a close distance to the decay vessel of the order of 1 m.

More LLPs with similar masses arise in models with light DM, or in connection with the generation of  $A'$  mass through the spontaneous symmetry breaking of the  $U(1)_D$  by a Higgs-like scalar - the so-called dark Higgs mechanism. In turn, in such scenarios, dark photons decay either into SM or into DS particles, depending on the exact mass hierarchy of the species. We briefly discuss several such scenarios.

### 4.2.1 Dark bremsstrahlung

New light sub-weakly coupled particles may play an important role in cosmology and astrophysics, acting as mediators between the SM and DM (see Section 4.1.1 and, *e.g.*, [244]). In particular, a light dark photon is an example of such a portal that naturally leads to the correct relic density of thermal DM by either the generalized WIMP miracle [181, 184] or a secluded WIMP scenario [185, 271]. Moreover, depending on the hierarchy between the masses of DM and dark photon, one can easily introduce DM self-interactions.<sup>6</sup>

We focus on the model extending the dark photon portal described by Eqs. (4.1.1) and (4.2.1) with the fermionic DM  $\chi$

$$\mathcal{L} \supset \bar{\chi} (i \not{D} - m_\chi) \chi, \quad (4.2.3)$$

where  $D_\mu = \partial_\mu - i g_D A'_\mu$ ,  $m_\chi$  is the DM mass, and  $g_D$  is the  $U(1)_D$  gauge coupling constant. In result, there are four free parameters in this model:  $m_{A'}$ ,  $m_\chi$ ,  $\epsilon$  and  $\alpha_D = g_D^2/(4\pi)$ . It is worth noting that the dark fermion  $\chi$  remains electrically neutral after the gauge field transformations involving massive dark photon are applied [292].

In further discussion, we fix  $\alpha_D = 0.1$ , which is often used as a benchmark in the literature [234], as it is within the perturbativity limits but still large enough for the  $\alpha_D$ -dependent secondary LLP production to become significant. We also fix the mass ratio  $m_\chi : m_{A'} = 0.6 : 1$  that corresponds to a particularly interesting mass regime in which  $m_\chi < m_{A'} < 2 m_\chi$ . In this case, dark photons decay visibly into SM particles, while the DM relic density is set by a freeze-out due to the  $\chi\bar{\chi}$  annihilations into SM particles via intermediate  $A'$  [293]. Therefore, only two parameters of the model remain free:  $m_{A'}$  and  $\epsilon$ .

While the DM particles  $\chi$  are stable, spectacular signatures can come from visible decays of the dark photons inside the detector. Significantly, in addition to the  $A'$ s produced at the pp interaction point (IP), further dark photons can come from the dark bremsstrahlung process,  $\chi T \rightarrow \chi T A'$  occurring in the material in front of the detector. In this case,  $\chi$  scatters with the target  $T$  (electron or proton/nucleus) in the material in front of the detector and emits a dark photon (see, *e.g.*, [294–296]). Furthermore, one can study DM particle scattering signature on electrons,  $\chi e^- \rightarrow \chi e^-$ , which can lead to an excess of high-energy EM showers at the detector without significant nuclear recoil over expected neutrino-induced BG [245, 297–301].

### 4.2.2 Inelastic DM

One can generalize the above scenario by considering a pair of Weyl (dark) fermions  $\chi_L$  and  $\chi_R$  that share the same charge under the dark gauge group  $U(1)_D$ ; see, *e.g.*, [302, 303]. After the  $U(1)_D$  spontaneous symmetry breaking, Majorana mass terms can be generated in addition to the Dirac mass. The corresponding

---

<sup>6</sup>We discuss how self-interactions can solve the small-scale  $\Lambda$ CDM problems in Chapter 8. There we also discuss a concrete SIDM model based on scalar-vector portal, similar to the models discussed in this chapter.

Lagrangian is

$$\mathcal{L} \supset (\Psi^T C M \Psi + \text{h.c.}), \quad (4.2.4)$$

where  $\Psi^T = (\chi_L, \chi_R^c)$  and the real mass matrix

$$M = \begin{pmatrix} m_L & M_\chi \\ M_\chi & -m_R \end{pmatrix}, \quad (4.2.5)$$

where  $m_L$  and  $m_R$  are the Majorana masses, while  $M_\chi$  is the Dirac mass. After changing to the eigenbasis, two dark fermion appear with the following masses:

$$m_{\chi_{1,2}} = \left| \frac{1}{2} \left( m_L + m_R \mp \sqrt{(m_L - m_R)^2 + 4 M_\chi^2} \right) \right|. \quad (4.2.6)$$

The effective Lagrangian is

$$\mathcal{L} \supset \sum_{i=1,2} g_{ii} \bar{\chi}_i \gamma^\mu \chi_i A'_\mu + (g_{12} \bar{\chi}_2 \gamma^\mu \chi_1 A'_\mu + \text{h.c.}), \quad (4.2.7)$$

where we focus on the case with  $g_{ii} \ll g_{12}$  and the coupling between the dark photon and the SM from Eq. (4.2.1). The couplings between dark fermions depend on their mixing angle  $\theta$ . The diagonal coupling is proportional to  $\cos 2\theta$ , while the non-diagonal coupling - to  $\sin 2\theta$ . The mixing angle  $2\theta$  is defined as  $\tan 2\theta = 2 M_\chi / (m_L + m_R)$ .

Whenever  $M_\chi \gg m_L, m_R$ , the diagonal couplings are suppressed and the two dark fermion states have masses that differ by only a small amount. This corresponds to a well-known scenario of inelastic dark matter (iDM), introduced in the context of the DAMA anomaly in DM DD searches [304] Such model has recently received new attention due to possible interesting signatures in intensity frontier searches and other experiments, coming from displaced decays of the heavier fermion,  $\chi_2 \rightarrow \chi_1 e^+ e^-$ , see [272, 305–312].

A similar suppression of the diagonal couplings is achieved even for larger Majorana masses by requiring  $m_L \approx -m_R$ . This leads to a larger mass splitting between  $\chi_1$  and  $\chi_2$

$$\Delta_\chi = \frac{m_{\chi_2} - m_{\chi_1}}{m_{\chi_1}} \simeq \frac{2 \min \{M_\chi, m_L\}}{|m_L - M_\chi|}, \quad (4.2.8)$$

while the mass eigenvalues are  $m_{\chi_{1,2}} \simeq |m_L \mp M_\chi|$ . In order for  $\chi_1$  to be a cold DM candidate, we require that  $m_{\chi_1}$  is not too suppressed. This can be achieved, for example, by assuming  $m_L \simeq -m_R \simeq 2 M_\chi$ , which leads to  $m_{\chi_2} \simeq 3 M_\chi \simeq 3 m_{\chi_1}$ . In this case, as the masses of dark fermions increase, other decay channels appear in addition to the dominant channel of decay to the electron-positron pair. These include, *e.g.*,  $\chi_2 \rightarrow \chi_1 \mu^+ \mu^-$  and decays with hadronic particles in the final state.

Because of the suppression of the diagonal couplings, the lighter dark fermions produce a heavier state while scattering with an electron or proton target,  $\chi_1 T \rightarrow \chi_2 T$  (provided the process is kinematically allowed). If such upscattering occurs in front of the detector, subsequent  $\chi_2$  decays lead to a spectacular signature inside

the detector. For a large mass splitting between both the two dark fermions, the approximate decay length of the boosted  $\chi_2$  is

$$(c\tau\beta\gamma)_{\chi_2} \sim 1 \text{ m} \\ \times \left[ \frac{0.1}{\alpha_D} \right] \left[ \frac{5 \times 10^{-4}}{\epsilon} \right]^2 \left[ \frac{E_{\chi_2}}{100 \text{ GeV}} \right] \left[ \frac{100 \text{ MeV}}{m_{\chi_1}} \right]^5 \left[ \frac{300 \text{ MeV}}{m_{\chi_2}} \right] \left[ \frac{m_{A'}}{400 \text{ MeV}} \right]^4 \left[ \frac{2}{\Delta_\chi} \right]^5, \quad (4.2.9)$$

where  $E_{\chi_2}$  is the energy of the decaying  $\chi_2$ , while a full expression for the decay length is given in Eq. (B.1.10).

When presenting the results in Section 4.4, we use the following mass scaling mentioned above:  $m_{\chi_2} \sim 3 m_{\chi_1}$ . We also put both masses in the MeV – GeV range, which is chosen for illustrative purposes. Since the upscattering cross section decreases with the increasing dark photon mass, we additionally focus on the case where  $m_{A'}$  saturates the minimal value required for on-shell invisible  $A'$  decays into a  $\chi_1\chi_2$  pair - we assume  $m_{\chi_1} : m_{\chi_2} : m_{A'} \sim 1 : 3 : 4$ . In addition, as in Section 4.2.1, we assume  $\alpha_D = g_{12}^2/(4\pi) = 0.1$ . As in the previous model, there remain two free parameters:  $m_{\chi_1}$  and  $\epsilon$ .

### 4.2.3 Dark photon with secluded dark Higgs boson

A natural way to introduce a non-zero dark photon mass is to use the dark Higgs mechanism. The  $m_{A'}$  is obtained thanks to the vacuum expectation value (vev),  $v_S$ , of a new SM-singlet complex scalar field  $S$  added to the model. Moreover, as the dark species are expected to have small masses, we assume  $v_S \ll v_{\text{SM}} = 246 \text{ GeV}$ . The new dark scalar is called the dark Higgs boson. It can have non-negligible couplings to the SM fermions that arise due to mixing between  $S$  and the SM Higgs boson  $H$  or appear at a loop level with the intermediate  $A'$  exchange. The relevant Lagrangian terms are [271, 297]

$$\mathcal{L} \supset |D_\mu S|^2 + \mu_S |S|^2 - \frac{\lambda_S}{2} |S|^4 - \frac{\lambda_{SH}}{2} |S|^2 |H|^2, \quad (4.2.10)$$

where  $D_\mu = \partial_\mu - i g_D A'_\mu$ , while the coupling of dark photon to the SM is given by Eq. (4.2.1). The phenomenology of such new BSM light scalars in connection to intensity frontier searches is widely studied; see, *e.g.*, [234, 258, 281, 313, 314].

Assuming small mixing,  $\lambda_{SH} \ll \lambda_S$ , and solving the tadpole equations, one rewrites the dark scalar mass in terms of  $v_S$  as:  $m_S^2 = 2\mu_S^2 - \lambda_{SH} v_h^2 = 2\lambda_S v_S^2$ . The dark photon mass is induced by the vev of  $S$ :  $m_{A'}^2 \simeq g_D^2 v_S^2$ , so  $m_S^2 \sim m_{A'}^2 \times \lambda_S/(2\pi\alpha_D)$ , i.e., masses of both dark bosons are naturally of the same order. In what follows, we require the mixing term to be very small,  $\lambda_{SH} \sim (m_S^2/v_h^2) \lesssim 10^{-6}$ , which results in highly suppressed mixing angle values between the dark and SM Higgs bosons. It then plays a negligible role in our phenomenological analysis.

In fact, the dominant couplings of the secluded  $S$  to the SM fermions arise through both the dark photon portal and the unsuppressed coupling between  $S$  and  $A'$  that appears after spontaneous breaking of the  $U(1)_D$  symmetry,  $\mathcal{L} \supset g_D m_{A'} S A'^\mu A'_\mu$ . This typically leads to an efficient coproduction of light scalars in any process leading to the production of  $A'$  where  $S$  can be emitted from the vector

final state. This can result in a flux of dark scalars going towards the detector along with the dark photons produced in the original IP.

Importantly, unlike the dark photons which can decay promptly depending on the value of the kinetic mixing parameter  $\epsilon$ , the dark Higgs bosons in such a scenario are usually very long-lived, provided  $m_S < m_{A'}$ . The reason for such long lifetime is that the dominant  $S$  decay channel,  $S \rightarrow e^+e^-$ , occurs at the one loop level with intermediate vector states, leading to the following lifetime:

$$\tau_S \sim 0.1 \text{ s} \times \left[ \frac{0.1}{\alpha_D} \right] \left[ \frac{10^{-3}}{\epsilon} \right]^4 \left[ \frac{20 \text{ MeV}}{m_S} \right] \left[ \frac{m_{A'}}{30 \text{ MeV}} \right]^2. \quad (4.2.11)$$

Similar to previous cases, we fix  $m_S = (3/4) m_{A'}$  and  $\alpha_D = 0.1$ , leading to only two free parameters of the model:  $m_{A'}$  and  $\epsilon$ .

Eq. (4.2.11) shows that  $S$  is effectively stable on particle collider scales. Consequently, in this model there is no displaced vertex signature coming from the dark Higgs bosons. Instead,  $S$  scatters with nuclei and electrons upstream of the detector, which produces the secondary dark photons,  $ST \rightarrow A'T$  with a much smaller lifetime, cf. Eq. (4.2.2). Such dark photons can then visibly decay inside the decay vessel, allowing the study of the small dark photon lifetime regime.

## 4.3 Details of modeling

As shown in Fig. 4.2, in models with more than one LLP, the production of BSM species can occur in both initial  $pp$ ,  $pN$  interactions at the LHC or in the target material and in scattering processes taking place in the vicinity of the decay vessel. Recall that we refer to the former as primary and to the latter as secondary production.

The initial production of LLPs at the IP is associated mainly with rare decays of mesons originating from  $pp$  and  $pN$  collisions. Other processes are also possible, as we discuss below, while further details, including the expressions relevant for both modes of production (branching ratios, decay widths and scattering cross sections) are given in Appendices B.1 and B.2.

### 4.3.1 Primary production of LLPs

Light new physics particles can be produced in high-energy interactions by a variety of processes. We list here the main ones for all species invoked by the models described in Section 4.2.

**Dark photons** In the MeV – GeV mass range, the dominant production processes are:

**Meson decays** We use Monte Carlo (MC) event generators EPOS-LHC [315] and the CRMC [316] package to simulate the distribution of mesons produced in  $pp$  collisions at the LHC and  $pN$  collisions with the molybdenum target at SHiP. We consider rare BSM decays of pions,  $\eta$  and  $\eta'$  mesons, and vector mesons  $\rho$  and  $\omega$ , where the dominant decay channels are  $\pi^0, \eta, \eta' \rightarrow \gamma A'$  and  $\rho, \omega \rightarrow \pi A'$ .

**Proton bremsstrahlung of  $A'$**   $A'$  heavier than the threshold for production in rare pion and  $\eta$  meson decays can be copiously produced by bremsstrahlung in coherent proton scatterings. We model it following the Fermi-Weizsacker-Williams approximation, where we also account for an additional off-shell mixing with vector mesons  $\rho$  and  $\omega$  [280, 299, 317, 318]. This mixing increases the production rate for  $m_{A'} \sim 775$  MeV, noticeable on the results plots, see Fig. 4.4.

**Hard processes** For dark photons with masses  $m_{A'} \gtrsim 1.5$  GeV, the Drell-Yan process starts to dominate. We model this contribution, although it applies to only a small part of the parameter space of the iDM model.

For the primary production of other LLPs, intermediate meson spectra or  $A'$ s are generated by the procedure described above.

Below, we describe the relevant processes leading to the flux of these LLPs traveling from the IP toward the detector, for each of the models described in Sections 4.2.1 to 4.2.3.

**Dark bremsstrahlung** In the benchmark scenario described in Section 4.2.1, the flux of  $\chi$  DM particles heading towards the detector comes primarily from the following 3-body decays of light pseudoscalar mesons,  $\pi^0, \eta \rightarrow \gamma A'^* \rightarrow \gamma \chi \chi$  [296].

**Inelastic dark matter** Our benchmark model discussed in Section 4.2.2 is characterized by the fact that the dark photon mass exceeds the masses of the two dark fermions,  $m_{A'} > m_{\chi_1} + m_{\chi_2}$ . In this case, dominant 2-body on-shell decays of dark photons to a  $\chi_1 \chi_2$  pair become possible. The flux of the parent dark photons is then governed by one of the production processes discussed above, depending on the mass of  $A'$ . The heavier LLP,  $\chi_2$ , is not stable and it decays into  $\chi_1$  and, typically, an electron-positron pair. These decays allow the detection of  $\chi_2$ , if they occur inside the decay vessel. On the other hand, for  $\chi_2$  decays taking place before reaching the decay vessel, the resulting lighter fermions further contribute to the  $\chi_1$  flux, which can be relevant for secondary production discussed below, thus we take it into account in our simulations.

**Secluded dark Higgs boson** As discussed in Section 4.2.3, the secluded dark Higgs boson coupled to the SM sector via the dark photon, can be efficiently co-produced in any of the  $A'$  production mechanisms described above. In particular, in the mass range of our interest, the most important contribution to the production comes from 3-body meson decays,  $\pi^0, \eta \rightarrow \gamma A'^* \rightarrow \gamma A' S$ , and 2-body decays of vector mesons such as  $\rho \rightarrow S A'$ .

### 4.3.2 Signatures involving secondary production of LLPs

In addition to the LLP particles produced in the vicinity of the primary IP, secondary production scatterings are also possible in models of our interest. They can occur on both electrons and nuclei. The dominant contribution to secondary production comes from  $Z^2$ -enhanced coherent scatterings with nuclei.

They are characterized by low momentum transfer to the nuclear target,  $p_{\text{recoil}} \sim \mathcal{O}(100 \text{ MeV})$ ,<sup>7</sup> therefore they do not activate the front veto and such events are not rejected in the experimental analysis. In addition, in order to minimize the chance of vetoing the events, we exclude from the analysis all scattering events occurring in the last three hadronic interaction lengths,  $3 \lambda_{\text{hadronic,interactions}}$ , of the material lying in the closest vicinity of the veto layers. It is also worth noting that since the incoming LLP particle is highly boosted, the resulting momentum of the outgoing LLP is highly collimated, *i.e.*,  $\vec{p}_{\text{LLP}_1} \approx \vec{p}_{\text{LLP}_2}$ , which simplifies the corresponding scattering cross sections given in Appendix B.2.

To illustrate the impact of LLP secondary production, we examine the expected sensitivity for three representative experiments introduced in Section 4.1.2, while we note that the same idea can be applied to other existing, or planned, experiments. We note that our choice is dictated by the fact that (i) they all cover strongly boosted particles - for which the impact of secondary production is more pronounced - and (ii) due to the design and geometry of the detectors, they will probe different regimes of transverse momenta of the LLPs produced at IP. Next, we describe the basics of the main signature employed by the experiments, while a detailed exposition of the physics cuts applied to signal events in each experiment can be found in [2].

#### 4.3.2.1 LLP decay signature in the decay vessel

**FASER** The expected BG in the search for LLP decays in FASER (2) can be brought down to negligible levels by applying the following simple procedure: (i) a high-energy cut on the visible energy,  $E_{\text{visible}} > 100 \text{ GeV}$  and (ii) the pointing and timing information can be used to associate the two charged tracks originating from LLP decay with  $pp$  collisions happening at the ATLAS IP [319, 320].

**MATHUSLA** We consider all LLP decays inside the decay volume of MATHUSLA that produce two charged SM tracks. We assume ideal, 100% efficiency of detection and we demand the momenta of each of the daughter tracks to satisfy  $p_{\text{daughter}} > 1 \text{ GeV}$ . Thanks to the position and timing information about the tracks, the BG can be greatly reduced and we assume in the following that such search can be performed with zero BG.

**SHiP** We apply a simplified acceptance procedure that relies on the momentum of visible tracks from LLP decays. We require each visible track to have  $p \gtrsim 1 \text{ GeV}$ . We assume that SHiP can probe BSM interactions in zero SM BG environment, and we also assume perfect signal detection capabilities - see [291] for discussion about BG in SHiP and [321] for more realistic studies of the efficiency.

#### 4.3.3 Event rate

The number of expected signal events associated with decays of LLPs, produced by either primary or secondary production, depends on both the relevant production

<sup>7</sup>We always require that  $p_{\text{recoil}} < 1 \text{ GeV}$  for the recoil momentum, which is a sufficient cut, while we found that the typical recoil momentum is roughly an order of magnitude smaller.

rates, and on the probability of decay inside the detector volume. The latter contains the acceptance factor  $\mathcal{A}$  that depends on the geometry of the detector, as well as on the efficiency to generate and detect visible charged tracks that meet the experimental criteria. We carry out fully numerical MC simulations that take into account kinematics of the interactions and geometry of each detector we consider.

Consider the probability  $\mathcal{P}_{\text{prim.}}$  of primary production of  $\text{LLP}_2$  followed by the signal (*e.g.*,  $\text{LLP}_2$  decay) in the detector, and the corresponding probability  $\mathcal{P}_{\text{sec.}}$  for the secondary production of  $\text{LLP}_2$ . The probability in the first case is

$$\mathcal{P}_{\text{prim.}}(\vec{p}) = e^{-L/d} (1 - e^{-\Delta/d}) \mathcal{A}(\theta, \phi), \quad (4.3.1)$$

where  $\vec{p}$  is the momentum of both LLPs,  $L$  is the distance from the production point to the beginning of the decay vessel, and  $\Delta$  is the length of the decay vessel. The decay length of the LLP in the ultrarelativistic regime is  $d = c\tau\beta\gamma \simeq c\tau E/m$ , where  $\tau$  is the  $\text{LLP}_2$  lifetime,  $m$  is its mass, and  $E$  - its energy.  $\mathcal{A}$  denotes acceptance factors that vary with each detector and signature.

The probability in the second case (secondary production) is

$$\mathcal{P}_{\text{sec.}}(\vec{p}) = \int_{x_{\min}}^{x_{\max}} \frac{dx}{\ell_{\text{int.}}} e^{-x/d} (1 - e^{-\Delta/d}) \mathcal{A}(\theta, \phi), \quad (4.3.2)$$

which is the convolution of the scattering rate with the signal probability. Limits of integration are  $x_{\min}$  and  $x_{\max}$ , which correspond to the distance to the decay vessel and depend on the geometry of the detector and the surrounding material, as well as by the veto requirements discussed above. The interaction length is given by the formula  $\ell_{\text{int.}}^{-1} = \sigma(E) \times (\rho/m_T)$ , where  $\sigma$  is the secondary production scattering cross section per nucleus,  $\rho$  is the density of material,  $m_T$  is the mass of the target and in Eq. (4.3.2) we assumed that  $\ell_{\text{int.}} \gg (x_{\max} - x_{\min})$ , which is always the case for the scenarios of our interest. The contributions associated with the various detector components are then added together to obtain the total event rate.

As is clear from  $\ell_{\text{int.}} \gg (x_{\max} - x_{\min})$  and Eq. (4.3.2), the secondary production processes tend to be subdominant to primary production due to additional suppression from the small scattering cross section. However, since secondary production can occur much closer to the detector,  $x_{\min} \ll L$ , it allows the study of the much smaller lifetime regime, where the contribution from primary production is already suppressed by the exponential factor in Eq. (4.3.1),  $\exp(-L/d) \ll 1$ .

## 4.4 Results for scattering with nuclei

To illustrate the interplay between the primary and secondary production mechanisms, we examined the sensitivity reach for the selected LLP models in the FASER, MATHUSLA, and SHiP detectors. The corresponding results are shown in Fig. 4.3 for the model with dark bremsstrahlung, in Fig. 4.4 for the model with iDM, and in Fig. 4.5 for the model with a secluded dark Higgs boson which we described in Sections 4.2.1 to 4.2.3, respectively.

All the models we study are constrained by various observations, and in our result plots we mark the excluded parts of the parameter space with gray shading.



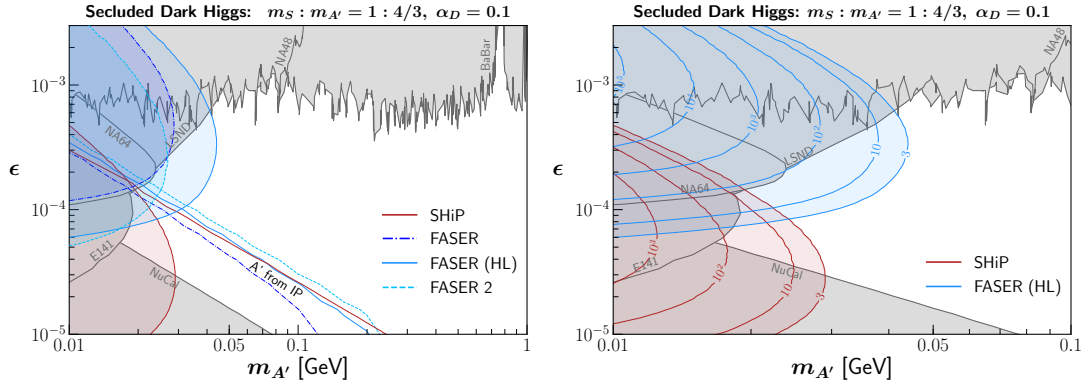


Figure 4.5: The same as Fig. 4.3, but for a model with a secluded dark Higgs boson discussed in Section 4.2.3.

could affect the interpretation of experimental results.

This can be clearly seen in the right panels of Figs. 4.3 to 4.5, where we present a series of contours denoting the number of events originating from secondary production. Depending on the model and experiment, we can typically expect  $\mathcal{O}(10^3)$  such events, with a maximum value of  $\sim 10^6$  in certain scenarios for the SHiP experiment.

#### 4.4.1.1 FASER (Run 3, HL-LHC) and FASER 2

For all benchmark models and iterations of the FASER experiment, the secondary production mechanism extends the sensitivity towards smaller LLP lifetimes, or larger values of the couplings. For iDM, even the vanilla FASER detector, which will operate during LHC run 3, could probe a large region of the currently unbounded parameter space.

It is worth noting that even though the FASER detector has a smaller size than FASER 2, its reach is larger, extending further to a larger coupling. This is caused by the additional dense material in the tungsten-based neutrino detector, FASER $\nu$ , placed in front of the FASER decay volume, which we did not assume for FASER 2.<sup>8</sup>

A particularly interesting aspect of secondary production in FASER is that it opens up coverage of the parameter space that can be related to outstanding problems of particle physics: (i) in the case of iDM, FASER can probe the currently unconstrained region of parameter space that yields the correct value of the DM relic density by coannihilations of  $\chi_1$  and  $\chi_2$  (which allows to evade CMB constraints), as discussed in [303, 305, 311]; (ii) the secondary production also opens up the possibility of probing an otherwise unconstrained region of the iDM parameter space which corresponds to the long-standing discrepancy between measurements and SM predictions of the muon anomalous magnetic moment [324, 325] - see Appendix B.1.1 for the relevant formula in the context of dark photon explanation. Recently, this discrepancy was also observed in the results of the Fermilab-based Muon g-2 experiment [326], which further motivates

<sup>8</sup>In fact, after publication of the results of this chapter, FASER $\nu$ 2 was proposed, see [6, 323] for extensive discussion.

coverage of this region.

It is worth noting that these special regions of the parameter space can already be explored during the LHC Run 3 whereas this would not be the case if only primary LLP production at the IP were considered.

#### 4.4.1.2 MATHUSLA

The MATHUSLA detector is to be placed off the LHC beam collision axis and probe the complementary region of the new light particles produced at IP with sizable transverse momentum  $p_T$  (in contrast to FASER which covers  $p_T \approx 0$ ). Thus, it is not surprising that MATHUSLA has no reach in the allowed region of parameter space of the models discussed with  $m_{A'} \lesssim \text{GeV}$  decays in the detector. However, in the iDM model shown in Fig. 4.4, MATHUSLA can have some reach for both primary and secondary LLP production. This is due to the larger angular distribution in the DM flux produced with one additional decay of dark photon,  $A' \rightarrow \chi_1 \chi_2$ , when compared to the LLP flux produced directly by meson decays. Additionally, the primary production and subsequent detection of even less boosted heavier dark fermions benefits from the relatively large  $\chi_2$  lifetime in some regions of the parameter space of the model. In result, MATHUSLA will cover two disconnected regions of the parameter space, The one on top of Fig. 4.4, corresponding to the secondary production, partially covers the region with the correct DM relic density and the aforementioned  $(g - 2)_\mu$  anomaly.

#### 4.4.1.3 SHiP

Secondary production in the SHiP experiment not only leads to better discovery prospects, cf Figs. 4.3 and 4.5, but also to a very large number of such events, as shown in Fig. 4.4 for the iDM model. When obtaining the results, we used a conservative approach to exclude all the secondary processes occurring in the SHiP detector closer than  $\sim 2.5$  m away from the decay vessel, as described in Section 4.3.2.1. Weakening these cuts lead to an increase in SHiP sensitivity, with a further increase in the relative contribution of the secondary production.

Interestingly, in addition to the interplay between secondary and primary LLP production, for SHiP experiment, additional signatures can arise through LLP scatterings with electrons, see the bottom panel of Fig. 4.2. We discuss them in more detail in the section below.

## 4.5 Scattering with electrons in SND at SHiP

The SND emulsion sub-detector of the SHiP experiment contains electronic tracker layers that may prove to be advantageous for BSM searches compared to the experiments containing only a decay vessel. Depending on the time resolution of an emulsion detector, they could time-label scattering events by detecting the recoil products. Such events can then be analyzed either separately or in combination with subsequent LLP decay. LLP interactions with electrons typically generate large recoil energy of  $e^-$ , as discussed in Appendix B.2. This leads to a pronounced EM cascade with no hadronic counterpart, for which the expected BG

is strongly reduced. Although the actual capabilities of the SHiP experiment for such signatures will depend on the final detector design, we briefly discuss two such search strategies using electron scatterings in the SND with secondary production of LLPs.

**(Only) Electron scattering signature** The search for light DS particles scattering with electrons is one of the goals of the SND [321]. The expected number of BG events was reported to be  $\sim 800$  [291]. These events are mostly produced by electron neutrino and anti-neutrino charged current quasi-elastic interactions with nuclei.

A similar scattering signature is possible in some of the models considered by us, in particular for scenarios when the subsequent LLP decay takes place outside the detector. We follow [301, 321] to apply cuts on the recoil energy,  $1 \text{ GeV} < E_e < 20 \text{ GeV}$ , and on the recoiled electron angle,  $10 \text{ mrad} < \theta_e < 20 \text{ mrad}$ .

**“Double” signature inside the SND** Another spectacular signature is related to the simultaneous generation of two resolvable collinear EM showers with no hadronic recoil counterpart inside the emulsion detector. These may be associated with the secondary production followed by a prompt decay of the LLP.

We require that both EM showers satisfy the cuts relevant for the pure scattering signature, and that both showers are initiated not too close to each other in the emulsion detector - we choose a minimum distance of 10 cm. This allows each shower to be detected by different tracking layers as these are spaced approximately every 8 cm, while a distance of 10 cm corresponds to more than 15 radiation lengths in lead. This greatly reduces any possible overlap between the showers.

Figs. 4.6a and 4.6b show the results of such searches for the iDM, as well as for the bremsstrahlung and secluded dark Higgs boson models, respectively. In these plots, the area above the dot-dashed green lines corresponds to at least three electron scattering events in the SND. These lines denote the absolute lower limit on  $\epsilon$  as a function of the relevant mass which could be probed by any signature based on LLP scattering with electrons in the SND, assuming zero BG. One can compare this line with the reach from the standard decay in the volume signature discussed previously. The corresponding results for both primary and secondary LLP production are shown as solid red and solid blue lines in Fig. 4.6, respectively.

The results corresponding to the scattering “only” search are shown for the iDM model in Fig. 4.6a as dotted purple lines with a fixed number of expected events:  $N = 3, 30, 300, 3000$ . The number of events in the allowed region of the parameter space in this case can reach up to  $\mathcal{O}(1000)$  which is to be compared with  $\sim 100$  events needed to exceed the expected level of BG by  $5\sigma$  (assuming only statistical uncertainty). These events are related to the  $\chi_1$  upscattering into  $\chi_2$  occurring in the SND, while  $\chi_2$  survives long enough to decay outside the decay vessel.

Complementary searches can be performed using the “double” signature of both upscattering and decay occurring inside the SND with at least 10 cm gap

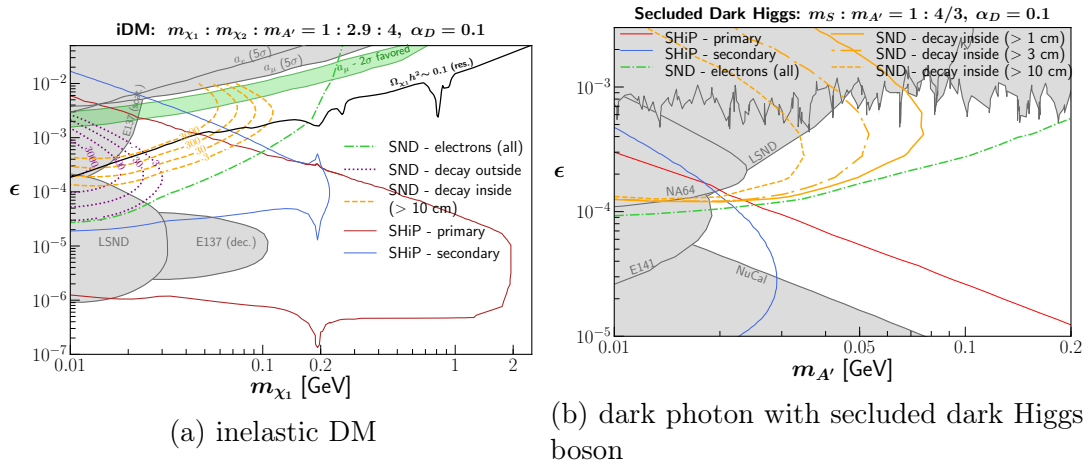


Figure 4.6: Results corresponding to additional signatures employing LLP electron scattering in the SND obtained for the model with inelastic DM (left) and the model with dark photon and secluded dark Higgs boson (right).

between them. Such searches allow one to probe a regime of an even smaller  $\chi_2$  lifetime as the heavier fermion is no longer required to travel until it can reach the decay vessel. We assume the aforementioned 10 cm of a minimal separation to guarantee that both EM showers can be reconstructed and detected in different tracker layers of SND. As a result, the corresponding dashed gold lines with the following consecutive number of events:  $N_{\text{ev}} = 3, 30, 300 \dots$ , cover the region in the parameter space with large values of  $\epsilon$ . As can be seen in Fig. 4.6a, a combination of different search strategies using both the SND and the decay spectrometer, could further shed light on the nature and lifetime of LLPs.

A slightly different scenario is shown in Fig. 4.6b for the model with the secluded dark Higgs boson. In this case, the LLP produced by secondary production processes in the SND is a very short-lived dark photon that quickly decays to an electron-positron pair. Consequently, no events with  $A'$  traveling outside the detector are expected. In fact, even a 10 cm distance between the two showers in the SND may be too large as dark photons will typically decay very quickly. We show several lines corresponding to 3 double signature events with varying minimal distance between the scattering and decay vertices, ranging from 1 cm to 10 cm. As expected, the smaller the allowed distance, the better the reach. On the other hand, for distances much smaller than  $\sim 1$  cm, the two showers could no longer be effectively resolved. In such a case, we would re-enter the regime of an effectively pure scattering signature with a much larger expected BG.

## 4.6 Conclusions

Light new physics is currently one of the most important theoretical and experimental frontiers in physics BSM. In the simplest scenarios, unstable light and very weakly-interacting particles are long lived, so they can be adequately probed in the intensity frontier searches. However, going beyond such simple models, interactions in DS can occur quite efficiently, so smaller lifetimes of unstable LLPs

are to be expected. Moreover, such a regime is also invoked with respect to the DM problem, or various experimental anomalies. The secondary production of LLPs is an important contribution in this direction which extends the sensitivity of the intensity frontier searches towards a regime of smaller LLP lifetimes. We have also shown great promise of the signatures associated with LLP scattering with electrons in emulsion neutrino detectors. In the next chapter, we extend the ideas developed here to BSM neutrino interactions.

# Chapter 5

## FASER as neutrino beam-dump experiment at the LHC

### 5.1 Introduction

In this chapter, we continue to study the secondary production of new, light BSM states that are present in non-minimal scenarios based on renormalizable portals, cf. Eqs. (4.1.1), (4.1.3) and (4.1.4), and typically at least some of them are long lived.

In Chapter 4 we extensively discussed how secondary production extends the reach of intensity frontier detectors at the LHC to a smaller lifetime regime in BSM scenarios based on scalar or vector portals with additional DM candidates, while here we focus on the remaining portal which involves sterile neutrinos [121, 327–330]. Within this framework, we also probe extended models featuring non-standard neutrino interactions, such as the neutrino dipole and the dark neutrino portals - see [331–333] and references in [4].

Since the discovery of neutrino oscillations [334–336] is currently one of the few certain clues of BSM physics, a multifaceted dedicated approach to probing neutrinos has been developed. Low-energy neutrinos with energies  $\sim$  tens of GeV have already been extensively studied experimentally and will be further precisely measured in the future in particular at DUNE [337] and HyperKamiokande [338], see recent reviews [339, 340] for thorough discussion.

At higher energies, probing neutrino interactions remains more challenging and it will be probed as a part of the multi-messenger astronomy [341]. It involves, *e.g.*, observations at the IceCube [342] neutrino telescope, which has already observed an extremely energetic flux of neutrinos with astrophysical origin with  $E_\nu \sim$  PeV [343]. However, at lower, TeV-scale energies, measuring the neutrino cross section in the large-scale neutrino telescopes suffers from substantial uncertainties from the determination of the atmospheric neutrino flux and spectrum [344, 345]. Besides, detailed characteristics of these events are very challenging to probe due to limited detector capabilities.

The recently approved FASER $\nu$  experiment [285, 346] and the SND@LHC

---

The contents of this chapter is based on: K. Jodłowski and S. Trojanowski, *Neutrino beam-dump experiment with FASER at the LHC*, *JHEP* **05** (2021) 191, [2011.04751].

experiment [347] at the LHC aims to fill this gap starting with the LHC Run 3. Since the mean expected energy of these neutrinos interacting in the distant detector is of order several hundred GeV [285], FASER $\nu$  is particularly suited to look for signatures of neutrinos taking place at such relatively pristine range of energies. Importantly, the expected excellent spatial and energy resolution of the detectors will allow detailed measurements of the products of relevant neutrino scattering processes. This will therefore usher in a new era of precision neutrino physics at the TeV scale and open the way to study possible BSM neutrino interactions in this regime.

## 5.2 New physics from neutrino scatterings in FASER $\nu$

### 5.2.1 Motivation

Neutrinos are abundantly produced in decays of mesons originating from  $pp$  collisions at the LHC. Energetic such neutrinos are preferentially produced in the far-forward region as dictated by the tiny fraction of their parent meson transverse and total momenta,  $p_T/p \ll 1$ , where typical  $p_T$  is of the order of the meson mass. The total flux of neutrinos passing through the FASER detectors during the HL-LHC era is predicted to be  $\sim 2 \times 10^{15}$  neutrinos with an average energy  $E_{av} \sim 250$  GeV [274, 348, 349].

Despite the large number of forward-going neutrinos at the LHC, only a few of them will interact in the detector due to their tiny scattering cross section. In particular, during LHC Run 3 about  $10^4$  neutrino-nucleus scattering events are expected in FASER $\nu$  [285], while this number will increase to  $10^5 - 10^6$  in the high luminosity (HL) LHC phase. Therefore, there is little room for BSM particles to be produced at detectable rates in these processes, especially given their suppressed interaction strength with the SM species characterized by the coupling constant  $g_D \ll 1$ .

However, the event rate becomes significantly larger in the presence of a light mediator particle  $X$  interacting with neutrinos and other SM fermions. In this case, for a low momentum exchange and  $g_D^4/m_X^4 \sim G_F^2$ , where  $G_F \simeq 1.166 \times 10^{-5}$  GeV $^{-2}$  is the Fermi coupling constant [350], the Fermi contact interaction of neutrinos in the SM can be supplemented by a similar BSM contribution to the total cross section. In the following, we will study selected such scenarios and we will make use of signatures involving (i) displaced decays of neutrino-induced BSM particles and (ii) differences in the scattering rates that could be captured with the use of appropriate cuts.

The high-energy and luminosity of the neutrino beam produced at the LHC will lead to further improvements in the sensitivity reach in these models, especially for an increasing mass of the BSM species produced. For TeV-energy neutrino scattering with electron, one obtains the center of mass (CoM) energy in the collision of the order  $\sqrt{s} = \sqrt{2E_\nu m_e} \sim$  GeV, while it increases even more for interactions with nuclei. For larger BSM particles masses, and their decreasing lifetime, larger boost factors at the LHC allows for better reconstruction of their

displaced decay signatures. Another powerful way to constrain these scenarios is by searching for increased rates in the neutrino scattering off electrons [351] or for a similar effect in coherent scattering off nuclei [352].

### 5.2.2 FASER $\nu$ experiment

The FASER $\nu$  detector will be located in the LHC side tunnel, about 480 m away from the ATLAS IP in front of the FASER detector - see the discussion in Section 4.1.2.1. It will be sensitive to the signatures of high-energy neutrino interactions occurring in a 1 m long emulsion detector made of tungsten layers interleaved with emulsion films. The detailed design of the neutrino detector, and the main spectrometer, can be found in [346, 353], the simplified plan of the future FASER 2 detector, which we use, is described in [284], while for the design of FASER $\nu$ 2, we follow [245]; see also [6] for updated discussion.

The emulsion detector in FASER $\nu$  will be placed along the proton beam of the LHC. The transverse size of the tungsten active material in FASER $\nu$  is set to be 10 cm  $\times$  10 cm and its length is equal to 1 m, while for FASER $\nu$ 2 it is planned to be 50 cm  $\times$  50 cm and its length will be equal to 2 m. As discussed in Section 5.2.3, it is also worth considering installing a sweeping magnet along the beam collision axis in front of the detector, and interleave the emulsion films with layers of the electronic detectors, as such modifications would help suppressing the muon-induced BG.

We also note that alternative detector designs, which would use liquid-argon time projection chamber, have also been discussed in the literature [245]. They would also remain sensitive to BSM neutrino interactions discussed below.

### 5.2.3 Neutrino flux and BSM particle production

**Neutrino flux** The flux and spectrum of high-energy neutrinos passing the far-forward region of the LHC have been simulated by the FASER collaboration [285] and by the CERN STI group [354]. Due to ease of use, we follow the first results, as we estimated that the uncertainties in modeling of the neutrino spectrum at the FASER have only a mild impact on our results. For the HL-LHC phase, we simply rescale said flux by an appropriate factor which takes into account the increased luminosity and larger detector transverse size.

**Primary and secondary LLP production** High-energy BSM particles with masses of the order of GeV can be abundantly produced at the LHC, especially in the forward direction, provided that the corresponding coupling constant  $g_D$  to the SM is not too suppressed. However, too large  $g_D$  leads to too quick decays of the dark states to travel near the FASER detector, unless efficient secondary production just in front of the detector takes place. In the latter case, the LLP can be produced near the detector and leave a visible signature by decaying in the decay vessel, similar to the signatures discussed in Chapter 4, in particular in Section 4.3.2. In turn, here we focus on such secondary production occurring in BSM neutrino interactions.

**Secondary LLP production in neutrino interactions** We use dedicated MC simulations within the framework developed in Chapter 4 where in our analysis we follow the experimental cuts based on Section 4.3.2.1.

The neutrino interactions leading to secondary production of new particles can occur in any material in between the IP and the FASER detector. However, it occurs most effectively in close proximity to the FASER detector, particularly in the dense tungsten target material of the FASER $\nu$  subdetector. Then, such produced particles travel  $\mathcal{O}(1\text{m})$  distance and decay into SM particles inside the decay vessel, depositing significant energy. The dominant contribution to the secondary production mode comes from coherent neutrino scatterings off nuclei defined by a small momentum exchange,  $|Q^2| < (100 \text{ MeV})^2$ . In turn, the incoherent contributions are subdominant or even negligible for all models considered below except for the massive vector mediator, as discussed below. All the relevant formulae for the scattering cross sections and decay widths can be found in Appendix C.1.

Note also that we also consider the primary production of BSM particles due to light mesons decays. We obtain the meson spectra with the CRMC simulation package [316] and the MC event generator EPOS-LHC [315]. LLPs can also be produced as a result of dark bremsstrahlung, which we model with the use of the Fermi-Weizsacker-Williams approximation according to [280, 299, 318].<sup>1</sup>

## 5.2.4 Experimental signatures of new physics

Before discussing example models of BSM neutrino interactions, we first briefly introduce the standard and novel experimental signatures of our interest

### 5.2.4.1 LLP decays inside the FASER decay vessel

**Signal** The fundamental signature of a LLP in FASER is its decay into a pair of high-energy and oppositely charged tracks, *e.g.*, an  $e^+e^-$  pair. Such pairs are detected mainly in the spectrometer, but they can also deposit energy in the calorimeter. A second class of signatures that FASER will also be sensitive to are photon-induced electromagnetic showers arising from LLP decays.

**Background** The threshold energy of the visible particles produced in such events that we employ in our analysis is  $E_{\text{vis}} > 100 \text{ GeV}$  [353, 355]. Such large value guarantees vetoing virtually all the background processes, leading to very sensitive probing of new physics. In particular, in searches for single high-energy photons appearing in the decay vessel, one can minimize the neutrino-induced BGs by using a dedicated preshower detector. It allows to reject BG events arising from charged current electron neutrino scatterings taking place sufficiently deep inside the calorimeter, while the BG from muon-induced photons would be vetoed due to detection of a time-coincident muon [353]. Therefore, any excess of single photon

---

<sup>1</sup>On the other hand, we neglect the contribution of the deep inelastic scattering, since it would generate conspicuous electromagnetic and hadronic activity inside or in front of the detector which would be promptly vetoed.

events accompanied by no muon will constitute a signal of new physics, especially if they occur only in a limited range of visible energies.

#### 5.2.4.2 LLP decays inside the emulsion detector

**Signal** Following their secondary production, LLPs can also decay promptly inside the emulsion detector. We consider the search for such a signature consisting of very high-energy photons with  $E_\gamma > 1 - 3$  TeV which are not accompanied by any time-associated muon. As such signature could be probed only in the future FASER $\nu$ 2 detector, we focus on it in further discussion.

The interaction vertex of our interest corresponds to a single photon with no hadronic activity inside the emulsion detector. Such condition is satisfied provided that momentum transfer in the scattering process is low,  $|Q|^2 < (100 \text{ MeV})^2$ . This signature has already been studied in [356] where the usage of the proposed scattering and neutrino detector (SND) [357] in the planned SHiP experiment [258, 290] was proposed to constrain other BSM scenarios. We extend this analysis to other models and also by studying other signatures. This allows us to study almost instantaneous LLP decays, which occur for larger masses and LLP coupling constants, extending the sensitivity reach of FASER to the regime of smaller lifetimes. We discuss this signature in the context of the neutrino dipole portal model in Section 5.3.1.

**Background** Since the single photon signature in FASER $\nu$ 2 has been discussed for the first time by us, we briefly discuss the BG arising in this case. First, the emulsion detectors can only collect data integrated over time. Therefore inside them, BG from muon-induced photons can mimic the BSM signal, unless the muons can be vetoed, *e.g.*, using the methods described earlier.

Additional control over that BG can be obtained by increasing the energy threshold of photon-initiated EM showers. In particular, while the total number of passing muons in the HL-LHC phase can be as large as  $N_{\mu, \text{HL-LHC}} \sim 10^{11}$ , it is smaller by one or three orders of magnitude for  $E_\mu > \text{TeV}$  or 3 TeV, respectively. We estimated the production rate of muon-induced high-energy photons,  $E_\gamma > 1 \text{ TeV}$  (3 TeV), inside FASER $\nu$ 2 during the HL-LHC to be  $10^{-3}$  ( $10^{-7}$ ) per a single muon track in the detector. We used the FLUKA code [358, 359], for technical details of this simulation, see [245].

We have also estimated the effect of BG on the search for single photons coming from high-energy deep inelastic scattering of neutrinos and quasi-elastic scattering of electron neutrinos. In the first case, there is a large momentum transfer to the nucleus which generates additional hadronic activity easily vetoed thanks to the interleaved electronic detectors, which should be installed for this purpose in the emulsion detector. In the second case, events involving an electron reconstructed as a photon can occur. We used the GENIE [360, 361] package to determine that several dozen such events could potentially mimic the BSM signal assuming  $E_e > \text{TeV}$ . As will be discussed in Section 5.4, for the models we consider, the number of the BSM-induced high-energy photon signal events can reach even up to  $10^4$  in the detector. Therefore, the BSM signals considered by us will not be overwhelmed by the background. It is also possible that a detailed simulation of BG signatures

at the detector level would lead to, *e.g.*, improved kinematical cuts which would further increase the expected sensitivity of FASER to such BSM scenarios.

### 5.2.4.3 Scatterings off electrons

**Signal** We also consider events originating from new-physics-induced neutrino scattering with the electron producing detectable electron recoils inside the neutrino detector. Here, in order to minimize neutrino-induced BG, we use the appropriate kinematical cuts determined by the dedicated study [245].

As discussed in Section 5.4, the scattering signature can also arise from the interactions of new unstable species, provided that their lifetimes are long enough for them to reach the detector. It will then be very similar to the DM scattering signature described above and will contribute to the total expected neutrino-like event rate.

**Background** A detailed discussion of BG for this experimental signature can be found in [245], while we describe its main elements. In particular, before introducing the angular cuts on the recoiled electron, one can expect several tens of neutrino-induced BG events during HL-LHC, which are characterized by the absence of detectable additional charged tracks coming out of the vertex next to the electron with the recoil energy between 0.3 and 20 GeV. This number falls to  $\mathcal{O}(10)$  after accounting for additional angular cuts. In what follows, we will assume that the BG event rate is dominated by statistical fluctuations. For simplicity, we will consider new physics limits by requiring  $\sim 20$  BSM events over the BG.

## 5.3 Selected BSM scenarios

HNL are BSM fermions and singlets with respect to the SM gauge group that are coupled to the SM particles through the gauge-invariant neutrino portal Eq. (4.1.4).

The motivation for studying such particles come from baryogenesis, DM, neutrino mass problem, and as a possible solution to many experimental anomalies - see recent reviews [128, 268]. Moreover, a simple extension of the SM based on the introduction of three right-handed neutrinos with masses smaller than the electroweak scale - the so-called  $\nu$ MSM [362] - has been proposed to explain the first three problems in a natural way.

In light of that, the study of HNL physics is very important. As the simplest scenarios involving HNLs are subjected to strong bounds, we will study models with a richer structure of their interactions with the SM.

In order to exploit the production of new physics in neutrino scattering in FASER $\nu$ , we will focus on BSM models predicting new GeV-scale HNLs that can be produced in upscatterings of the SM neutrinos, which are significantly enhanced by the presence of a light vector mediator  $X$ .<sup>2</sup> For this purpose, we will assume that  $X$  is either the massless SM photon or a new light dark gauge boson  $A'$ . The

---

<sup>2</sup>Secondary HNL production could also occur due to mixing with active neutrinos induced by the neutrino coupling portal, however, we estimated that such contribution leads to negligible event rate in the allowed parameter space of all models considered.

choice of the following models is also dictated by the unique phenomenological aspects of searches in FASER. We note that extension of the secondary production to other models in other neutrino detectors is possible, *e.g.*, for models with scalar mediators see [363].

### 5.3.1 Neutrino dipole portal

Introduction of right-handed neutrinos leads to the generation of neutrino magnetic moment. Its value is proportional to the neutrino mass [364–368], therefore it does not lead to sizable interactions. However, it is predicted to be much larger, up to a detectable level, in more complex BSM models [333, 369–371], often invoked in the context of beam-dump and neutrino experiments, its cosmological impact on relativistic degrees of freedom at early Universe, and unaccounted signals in DM DD experiments [333, 356, 372–374].

A popular example of such scenario is the neutrino dipole portal to HNLs, which is described by the following effective Lagrangian:

$$\mathcal{L} \supset \mu_N \bar{\nu}_L \sigma_{\mu\nu} N_R F^{\mu\nu} + \text{h.c.}, \quad (5.3.1)$$

where  $\sigma^{\mu\nu} = \frac{i}{2}[\gamma^\mu, \gamma^\nu]$ ,  $F^{\mu\nu}$  is the electromagnetic field strength tensor,  $\nu$  is the SM neutrino and  $N_R$  is the sterile neutrino (we also call it the HNL). The coupling  $\mu_N$  is a dimensional quantity,  $[\text{mass}^{-1}] = -1$ , and present data bounds it to be  $\mu_N \lesssim 10^{-6} \text{ GeV}^{-1}$  for GeV-scale HNLs [333, 356, 373]. We note that although the UV-completion scale for this model can be as large as  $1/\mu$ , at electroweak energies, the dipole interaction in Eq. (5.3.1) must be promoted to dimension-6 operator by insertion of the Higgs boson, so that it is fully gauge invariant. Despite the fact that the interaction of neutrinos of interest to us take place at  $E_\nu \sim \text{TeV}$ , the typical momentum transfer is much smaller than the electroweak scale, hence one can directly use Eq. (5.3.1).

The dipole interactions lead to inelastic upscattering transitions of the active neutrinos into the HNLs,  $\nu Z \rightarrow N Z$  where  $Z$  is a target nucleus.<sup>3</sup> Once produced, the HNLs travel a finite distance and then decay into a single photon and a neutrino,  $N \rightarrow \gamma\nu$ , with the typical decay length

$$\bar{d}_{N,\text{dipole}} \simeq (1 \text{ m}) \left( \frac{E_N}{500 \text{ GeV}} \right) \left( \frac{1 \text{ GeV}}{m_N} \right)^4 \left( \frac{10^{-6} \text{ GeV}^{-1}}{\mu_N} \right)^2. \quad (5.3.2)$$

For given values of model parameters, the typical energy of a decaying HNL is dictated by the reciprocity between the energy-dependent  $\bar{d}_{N,\text{dipole}}(E_N)$  and the distance  $l \sim 1 \text{ m}$  between the tungsten FASER $\nu$  plates where upscattering can occur most efficiently, and the FASER decay vessel. The condition  $\bar{d}_{N,\text{dipole}}(E_N) \sim l$  also determines the energy range of the visible photons - see Section 5.4.1 and also Section 5.4.2 for the discussion concerning the bi-modal  $e^+e^-$  spectrum in the dark vector portal model).

<sup>3</sup>We refer to the coherent superposition of light neutrinos as the active neutrino in a flavor eigenstate. Given the distance  $L \sim 0.5 \text{ km}$  between the production and interaction point, and the energy scales involved, neutrino oscillations play a negligible role in our analysis .

Furthermore, three-body HNL decays, *e.g.*,  $N \rightarrow \nu \ell \ell$ , are also possible, which could generate a signal consisting of two oppositely charged tracks, albeit with a suppressed branching fraction,  $\mathcal{B}(N \rightarrow \nu \ell \ell) \sim 10^{-3}$  to  $10^{-2}$ . We give the corresponding expressions for the scattering cross sections and decay widths in this model in Appendices C.1 and C.2.

The transition between the active and sterile neutrinos due to the magnetic moment have been considered as a possible BSM explanation of the MiniBooNE [331, 375, 376] and LSND [377] anomalies. Recently, the former has been strengthened to the  $4.8\sigma$  level [378]. A pure dipole-portal explanation of both anomalies has been performed in [356], however, further studies has shown [379] that such explanation of MiniBooNE-only region of interest (RoI) is disfavored by the MINER $\nu$ A data [380]. For completeness, while presenting our results, we highlight the MinoBooNE RoI in the sensitivity reach plots.

### 5.3.2 Dark gauge boson portal

Secondary HNL production in neutrino scattering can also be enhanced by light BSM mediators which are coupled to neutrinos. Such vector mediator  $Z_D$  naturally arises due to gauging one of the global anomaly-free symmetries of the SM, although the corresponding couplings are then suppressed, cf. [261, 381]. Furthermore, the upscattering cross section,  $\nu(e/Z) \rightarrow N(e/Z)$ , is additionally suppressed by the active neutrino-HNL mixing,  $U_{\nu N}^2$ , which results in negligible secondary production interaction rates. Instead, the corresponding cross section can be significantly increased when the new dark gauge symmetry couples  $Z_D$  directly, and only, to the HNL [332, 382].

On top of this,  $Z_D$  can also couple to quarks and electrons due to kinetic or mass mixing. However, the latter is suppressed for  $m_{Z_D} \lesssim \text{GeV}$ , while the kinetic mixing allows for higher interaction rates in this region, with upper bounds dictated by the mixing parameter  $\epsilon \lesssim 10^{-3}$ , see [234] for a recent review.

We consider a simplified model that accounts for both the kinetic mixing and the dark coupling of  $Z_D$  to the HNL. It is described by the following Lagrangian [332, 382]:

$$\mathcal{L}_D \supset \frac{m_{Z_D}^2}{2} Z_{D\mu} Z_D^\mu + g_D Z_D^\mu \bar{N} \gamma_\mu N + e\epsilon Z_D^\mu J_\mu^{\text{em}}, \quad (5.3.3)$$

where  $Z_D$  couples to the electromagnetic current  $J_\mu^{\text{em}}$  due to the kinetic mixing. The upscattering cross section of the active neutrinos to HNLs depends on the model parameters as  $g_D^2 U_{\nu N}^2 \alpha \epsilon^2 / m_{Z_D}^4$ , thus it can be significant for the dark gauge boson with masses in the sub-GeV range. We provide the relevant expressions in Appendices C.1 and C.2.

Since the secondary production depends on only a few free parameters, and a detailed scan of the model parameters is not needed to illustrate the impact of the secondary production on the FASER/FASER $\nu$  sensitivity reach, we vary only the HNL mass and the mixing parameter of HNL with the muon neutrino,  $U_{\nu\mu}$ , while we fix all other parameters as follows. We fix  $\alpha_D = 0.25$ ,  $\alpha\epsilon^2 = 2 \times 10^{-10}$ , and  $m_{Z_D} = 30 \text{ MeV}$ , which was the benchmark introduced to fit the MiniBooNE anomaly [332]. For  $m_N > m_{Z_D}$  in such a case the HNL produced in active neutrino

upscattering quickly decays into an on-shell mediator boson,  $N \rightarrow \nu Z_D$ . The latter then decays inside FASER,  $Z_D \rightarrow e^+e^-$ , generating a visible signature of two high-energy, oppositely charged tracks. The typical decay length of such  $Z_D$  is

$$\bar{d}_{Z_D} \simeq (1 \text{ m}) \left( \frac{E_N}{300 \text{ GeV}} \right) \left( \frac{30 \text{ MeV}}{m_{Z_D}} \right)^2 \left( \frac{2 \times 10^{-10}}{\alpha \epsilon^2} \right). \quad (5.3.4)$$

We also consider the case with the dominant mixing with the tau neutrinos and  $m_N < m_{Z_D}$ . Prospects of such a scenario in FASER has recently been discussed in [383]. In this case, HNL undergoes a three-body decay,  $N \rightarrow \nu e^+e^-$ , via an off-shell  $Z_D$  mediator. Such decays can then be detected by observing the  $e^+$  and  $e^-$  tracks in the FASER spectrometer, and the HNL lifetime can easily be large enough so that the dominant contribution to the signal rate in FASER comes from HNLs produced at the ATLAS IP [383].

We extend the previous analysis by examining the prospects of HNL searches with electron scattering signature in FASER $\nu$ 2 in both the inelastic  $\nu_\tau e \rightarrow Ne$  and the elastic  $Ne \rightarrow Ne$  processes. We also consider an additional way of producing HNLs in on-shell decays of the dark gauge boson,  $Z_D \rightarrow NN$ . We note that the elastic scattering cross section is not suppressed by the mixing angle,  $U_{\tau N}^2$ , but this suppression can occur in the  $N$  production rate. We determine it from the tau neutrino production rate which we adjust for the non-zero mass of the HNL following [384]. In result, both elastic and inelastic contributions to the electron scattering signature can play a comparable role in the sensitivity plots. On the other hand, there is no suppression of the  $N$  production rate for a very low mixing angle and small  $m_N$ . In this case, the HNL is mainly produced in the on-shell decays of the dark gauge bosons, and this contribution is independent of  $U_{\tau N}^2$ , provided the HNL is sufficiently long-lived.

Finally, as we mentioned above, models using light vector or scalar BSM mediators also were proposed in connection to the MiniBooNE anomaly where both off-shell [382] and on-shell [332] mediators were studied. However, the former model is in strong tension with the T2K ND280 search [379]. This tension is somewhat less pronounced for the latter scenario, although it is disfavored by the MINER $\nu$ A search [380], the CHARM-II data [385], and by requiring good fit to the angular distribution of the events in MiniBooNE [386]. For illustration, we show the MiniBooNE RoI for the model described by Eq. (5.3.3) following [332].

## 5.4 Results

Below, we discuss the capabilities of the multi-purpose FASER 2 detectors in observing new physics signals arising from neutrino interactions. We present the corresponding sensitivity reach plots using the detector designs introduced in Section 4.3.

### 5.4.1 Turning neutrinos into light with neutrino dipole portal

As mentioned in Section 5.3.1, the secondary production of HNLs in neutrino scatterings from electrons or nuclei through the dipole portal, may lead to many non-standard signatures in FASER. In particular, the following prompt decays,  $N \rightarrow \nu\gamma$ , taking place inside the decay vessel or the emulsion detector, would form a clear excess of EM showers initiated by single photons, following the BG rejection procedure we described above.

**Single photons in the decay vessel** In Fig. 5.1, we show by the green solid lines the results of the analysis done for the single photons appearing in the FASER 2 decay vessel. From bottom to top, the lines correspond to  $N_{\text{ev}} = 3$  and 30 events expected in the HL-LHC phase. Larger values of  $N_{\text{ev}}$  are suppressed for clarity of the plot. In the left panel, the results are shown for the dipole portal model with universal coupling  $\mu_N$  to all the neutrino flavors, while the right panel presents the scenario with the coupling to only a single flavor,  $\mu_{N\tau}$  where larger region of the parameter space is available because the bounds from muon neutrino  $\nu_\mu$  experiments are no longer applicable. While tau neutrinos are much more challenging to probe, at the LHC they are copiously produced in the decays of the charm mesons and tau leptons. We also indicate the expected reach of the SHiP experiment [356] with black dashed line. The gray-shaded area marks the current experimental bounds where the most stringent limits come from null searches in the CHARM-II [387], MiniBooNE [376] and NOMAD [388] experiments, and from the LEP searches for  $\gamma + \cancel{E}_T$  events [389]. Cosmological and astrophysical constraints from the BBN, and observations of Supernova SN1987A are also important, especially for the light and very weakly coupled HNLs. There, we follow [333, 356, 372, 373].

We find that in the model with the universal coupling, up to  $\mathcal{O}(10^3)$  of HNL-induced single photons can be observed in the allowed region of parameter space, and in the  $\nu_\tau$ -specific scenario, about 100 of such events can be expected. The lower luminosity and detector size leads to no more than  $\mathcal{O}(10)$  single photon events are expected in FASER during LHC Run 3. This would allow us to explore only a small region of the model parameter space with the universal coupling  $\mu_N$  in the initial run of the experiment, while further improvement would take place during the HL-LHC.

In Fig. 5.1, we also present the expected sensitivity reach of FASER 2 in the search for an  $e^+e^-$  pair from the three-body decay  $N \rightarrow \nu(\gamma^* \rightarrow \ell\ell)$ , dotted green lines. The branching fraction of this decay is suppressed by 2 to 3 orders of magnitude compared to the dominant two-body decay, as shown in the right panel of Fig. 5.2. In the plot we show both the total, and the “effective” branching fraction which accounts for the lower threshold of the visible energy,  $E_{\text{vis}} > 100 \text{ GeV}$ , and assumes that the energy of the parent HNL is equal to  $E_N = 1 \text{ TeV}$ . Unfortunately, the sensitivity of FASER 2 in these searches will only cover a small region of the model parameter space, and it will not be complementary to the single photon search.

We show a photon energy spectrum for the BSM signal events in the left panel

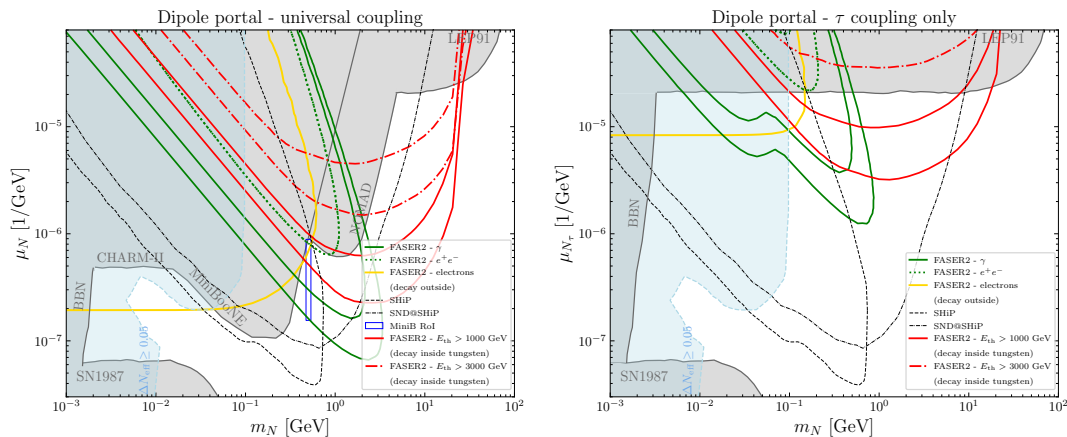


Figure 5.1: Main results for the dipole portal models: left) universal coupling to all of the neutrino flavors, right)  $\nu_\tau$ -specific coupling. The green lines indicate the expected number of the signal events in FASER $\nu$ 2 involving high-energy photons appearing inside the decay vessel. The red lines correspond to such photons appearing in the emulsion detector. The yellow line represents the expected exclusion limit from the search for electron scattering events. The blue shaded area corresponds to scenarios with an increased number of relativistic degrees of freedom in the early Universe.

of Fig. 5.2 for the two benchmark scenarios within the reach of FASER 2. As discussed in Section 5.3.1, the energy spectrum of photons from HNL decays is dictated by both the relevant decay length and the distance the HNLs need to travel between the tungsten plates in the neutrino detector and the decay vessel. In particular, for HNLs with a smaller lifetime this spectrum is shifted towards high energies resulting in larger boost factors. This makes it easier to separate the signal events from the muon-induced BG. The latter should reach maxima at lower energies due to the increasing bremsstrahlung cross section of soft photons [390].

**Single photons in the neutrino emulsion detector** HNL can also decay into a single photon in the FASER $\nu$ 2 emulsion detector. The search for such high-energy photons (with  $E_\gamma > 1$  TeV) may play a complementary role to the signature discussed above based on the same decays but occurring in the decay vessel. This complementarity is especially true for HNLs with small lifetimes, so that they decay promptly after being produced in the neutrino scatterings in the emulsion detector and often before they can reach the decay vessel, cf. Section 4.3 for the discussion about the expected BG in this search. We show the contours at a fixed number of such events,  $N_{\text{ev}} = 3$  and 30, for a 1 TeV (3 TeV) photon energy threshold by the red solid (dash-dotted) lines in Fig. 5.1. They correspond to the FASER $\nu$ 2 experiment taking data during HL-LHC. This search would extend the corresponding reach towards large values of both the HNL mass and the coupling constant. Assuming a threshold of 1 TeV, one can expect up to  $10^4$  and 100 of such events for the scenario with the universal coupling  $\mu_N$  and the  $\nu_\tau$ -specific coupling  $\mu_{N\tau}$ , respectively. It is worth noting that in the former model, several hundred signal events can be expected even for the 3 TeV photon energy threshold,

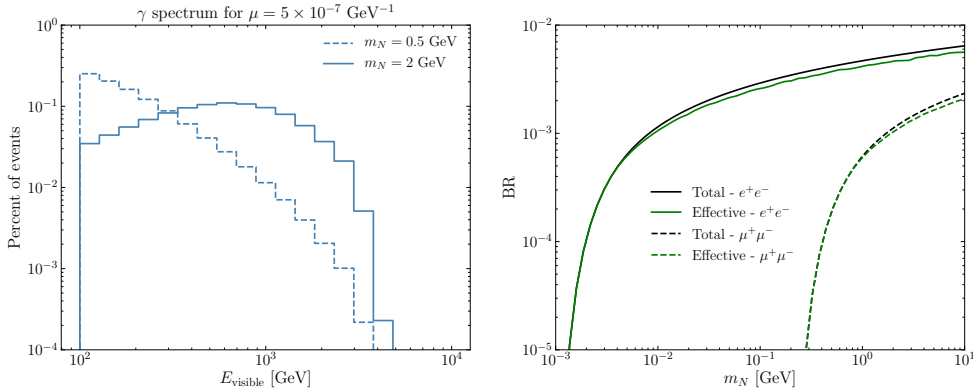


Figure 5.2: Results for the model with universal coupling  $\mu_N$  dipole portal: left) energy spectrum of photons coming from HNL decays for the benchmark scenarios, as indicated in the plots, and right) three-body HNL decay branching ratio  $N \rightarrow \nu(\gamma^* \rightarrow \ell\ell)$  where  $\ell = e$  (solid black line) or  $\mu$  (dashed black), as a function of the HNL mass  $m_N$ .

while one expects a smaller number of muon-induced such background photons. In some cases, detectable event rates are obtained for both the aforementioned single photon search in the decay vessel and for a similar signature in the emulsion detector. This further increases the combined chances of discovering BSM physics in FASER 2.

#### 5.4.2 Bi-modal $e^+e^-$ spectrum in searches of HNLs and dark gauge bosons

While the HNL decay into  $e^+e^-$  is suppressed in the dipole portal, it remains the main signature of HNLs in the dark gauge boson portal, cf. Section 5.3.2, in particular for the  $m_{Z_D} < m_N$  case. The HNLs decay rapidly and primarily to the invisible final state,  $N \rightarrow \nu Z_D$  where the following  $Z_D \rightarrow e^+e^-$  decays lead to visible signatures at FASER with  $E_{e^+e^-} > 100$  GeV,

$$\begin{aligned} \text{mesons} &\rightarrow \nu(\text{IP}) \Rightarrow \nu Z \rightarrow N Z \text{ (rock/FASER}\nu) \\ &\Rightarrow N \rightarrow \nu Z_D \text{ (rock/FASER}\nu) \Rightarrow Z_D \rightarrow e^+e^- \text{ (decay vessel)}. \end{aligned} \quad (5.4.1)$$

In Fig. 5.3, we present the relevant expected sensitivity reach of FASER 2 in the  $(m_N, U_{\mu N})$  plane where  $U_{\mu N}$  is the HNL mixing angle with the active muon neutrino. We set the values of the following parameters of the model:  $m_{Z_D} = 30$  MeV,  $\alpha_D = 0.25$  and  $\alpha\epsilon^2 = 2 \times 10^{-10}$ . This choice is motivated by the proposal to fit the MiniBooNE anomaly, cf. the discussion in Section 5.3.2. The most stringent bounds on the considered model are derived from searches performed by the MINER $\nu$ A [380] and CHARM-II [385] experiments. We implement them following [386]. Additional important constraints are related to rare meson decays, the Michel spectrum for muon decays, and the universality of leptons [391, 392], as discussed in [332]. A recent review and update of constraints on the HNLs can be found in [393]. In particular, the lack of FASER sensitivity and CHARM-II and MINER $\nu$ A constraints of the large values of the mixing angle,  $U_{\mu N}^2 \sim 10^{-3}$ ,

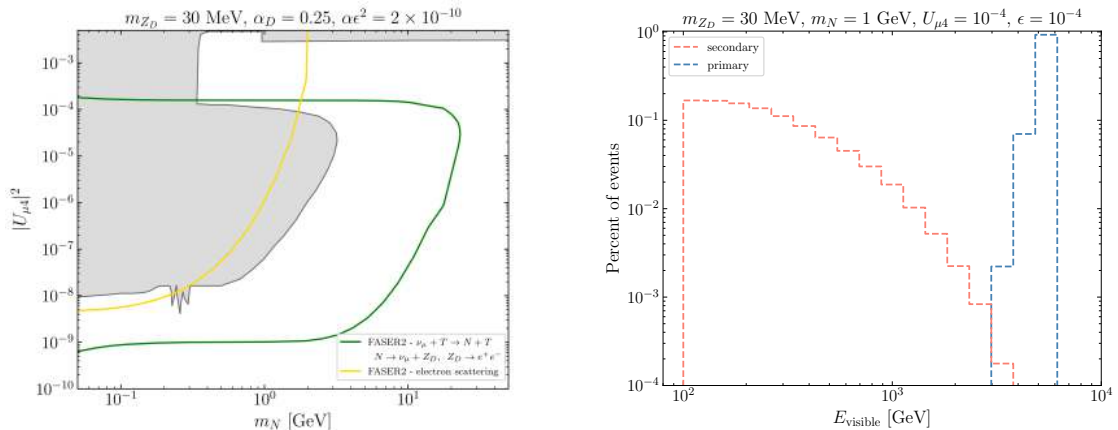


Figure 5.3: *Left*: FASER 2 sensitivity reach in the model with dark gauge boson connecting the HNL and SM particles. Green line indicates the sensitivity based on detection of the  $e^+e^-$  pair in a sequential process  $\nu Z \rightarrow Z(N \rightarrow \nu Z_D)$  with subsequent  $Z_D \rightarrow e^+e^-$  decay. The yellow line corresponds to the expected sensitivity based on the electron scattering signature. *Right*: Energy spectrum of  $e^+e^-$  pairs from  $Z_D$  decays.

is due to the dominant invisible decays of the dark gauge boson,  $Z_D \rightarrow \nu\bar{\nu}$  where the visible  $Z_D$  decay branching fraction is  $\lesssim 10^{-4}$ .

We show the range of FASER 2 coverage corresponding only to the secondary production of HNLs and  $Z_D$ s taking place upstream and inside the detector. As can be seen, FASER 2 will probe currently unexplored regions in the parameter space corresponding to low mixing angle values and increasing HNL mass, up to  $m_N \sim \mathcal{O}(10 \text{ GeV})$ . For light HNLs, FASER 2 will also cover the MiniBooNE RoI, and provide a complementary probe to the NA62 experiment searching for HNLs produced in rare kaon decays [394].

We note that, although we study the regime of a relatively small  $Z_D$  lifetime, a small fraction of these bosons produced in  $pp$  collisions can still contribute to the final signal rates on top of the contribution from the  $Z_D$ s produced in neutrino scatterings. However, the initial production of  $Z_D$  at the ATLAS IP does not depend on the mixing angle  $U_{\mu N}$  and the HNL mass. It then corresponds to a fixed expected number of signal events which should be added to the events shown in the sensitivity plot in the left panel of Fig. 5.3.

The reciprocity between these two production processes is on the one side driven by the exponentially damped decay-in-volume probability for the less long-lived  $Z_D$ s produced in the ATLAS IP. On the other hand, it also depends on the small secondary production cross section relevant for the production in front of the decay vessel. The first attenuation causes the primary production spectrum of  $Z_D$  to peak toward higher energies,  $E_{Z_D} \gtrsim \text{TeV}$ , so that they can reach FASER without decaying. Instead, the dark gauge bosons produced by the secondary production processes near the detector favor the lower energies of the visible signal at the detector. In such a case the energy spectrum of the parent neutrinos has a peak around a few hundred GeV, but only  $\sim 1/2$  of this energy is transferred into  $Z_D$  due to the HNL decay. This suppresses the typical energy of the dark gauge

boson to  $E_{Z_D} \sim 100 - 300$  GeV. In the right panel of Fig. 5.3 we illustrate this effect. One can see a bi-modal energy spectrum of the  $e^+e^-$  pairs detected in FASER 2 where each peak corresponds to the same BSM species but a different  $Z_D$  production process.

### 5.4.3 Probing light HNL in electron scattering

BSM neutrino interactions can also manifest themselves in the FASER $\nu$ 2 detector in the form of enhanced neutrino-electron scattering rate. We discussed the expected BG in this case in Section 4.3, also see [245]. We show the projection of the corresponding exclusion bounds for the dipole and dark gauge boson portals in Figs. 5.1 and 5.3 denoted by the solid yellow lines.

The results presented there correspond to neutrino upscattering events,  $\nu e \rightarrow Ne$ . As the typical incident neutrino energy is on the order of  $\sim 100 - 500$  GeV, the CoM energy in such collisions allows for the production of HNLs of mass  $m_N \lesssim$  GeV. For the dipole portal model, the interplay between electron scattering and both of the aforementioned single photon signatures, allows FASER to study a wide range of the HNL mass,  $1 \text{ MeV} \lesssim m_N \lesssim 10 \text{ GeV}$ . Moreover, the scattering signature alone can cover parameter space corresponding to the increased value of the number of relativistic degrees of freedom in the early Universe,  $0.05 \lesssim \Delta N_{\text{eff}} \lesssim 0.3$ , which is one of the solutions to the cosmological Hubble tension [395, 396]. We present the relevant region in the parameter space as a blue shaded region in Fig. 5.1 following [333].

Interesting phenomenological aspects of the electron scattering signature also appear in the model with the dark gauge boson mediator heavier than the HNL,  $m_N < m_{Z_D}$ . Such scenario has been recently discussed in [383]. We present our results in Fig. 5.4 where we assume, for concreteness,  $m_{Z_D} = 8m_N$  and that the dominant coupling of  $Z_D$  is to the tau neutrinos. We fix the values of the couplings constants  $g_D = 1$  and  $\epsilon = 10^{-3}$ . It is worth noting that this value of the kinetic mixing lies close to the upper limit obtained by the BaBaR search for invisible decays of the dark photon, which constrains the regime where  $Z_D \rightarrow NN$  decays into very long-lived HNL that typically leaves the detector before decaying. Other bounds shown in the plot come from the search for  $\tau$  lepton decays in BaBaR and Belle-II [397], the LEP search for monojets [398], and the beam-dump experiments CHARM-II [384] and NOMAD [399]. We implement them following [383] for all limits except the CHARM-II bound, which we adjust to our scenario by also taking into account the additional HNL flux from the  $Z_D \rightarrow NN$  decays and by including the elastic scattering processes,  $Ne \rightarrow Ne$ , occurring in the detector, as we discuss below.

We note that our benchmark was chosen for illustrative purposes only and a similar number of scattering events is expected in the detector for other values of the model parameters as long as the combination  $g_D^2 U_{\nu N}^2 \alpha \epsilon^2 / m_{Z_D}^4$  is held constant and  $m_{Z_D} > 2m_N$  so that  $Z_D \rightarrow NN$  decays are kinematically allowed.

The sensitivity reach of FASER $\nu$ 2 in the scattering signature in this model is indicated by the yellow line in the left panel in Fig. 5.4. We consider contributions from the inelastic processes,  $\nu e \rightarrow Ne$  and the elastic processes,  $Ne \rightarrow Ne$ . Instead, the contribution from the inelastic processes,  $Ne \rightarrow \nu e$ , is strongly

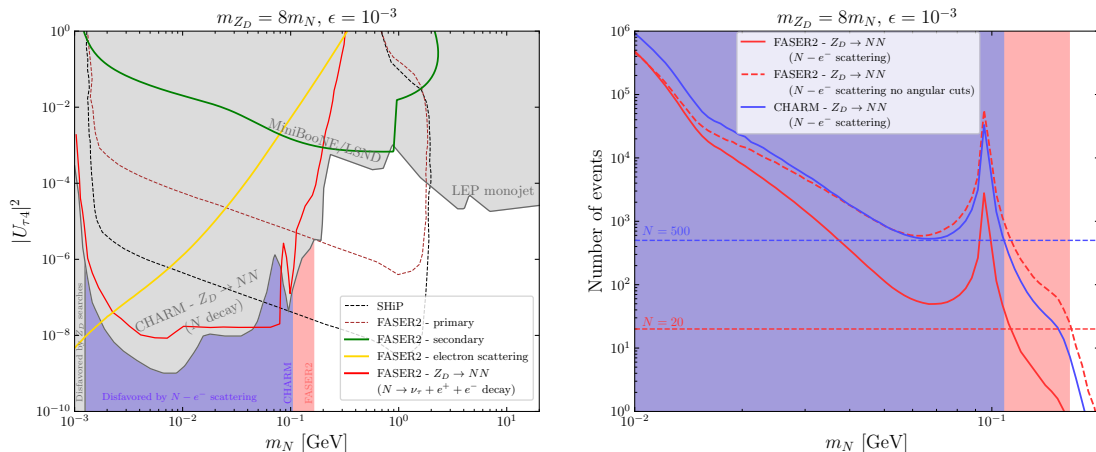


Figure 5.4: Results for the model with dark gauge boson heavier than HNL,  $m_{Z_D} = 8m_N$ , and with the dominant third generation neutrino mixing,  $U_{\tau N}$ . *Left*: Sensitivity of FASER 2 and SHiP in the  $(m_N, U_{\tau N})$  plane. The additional FASER 2 sensitivity resulting from secondary HNL production is shown as the green line while the red line corresponds to the additional FASER 2 coverage due to HNL production in the  $Z_D \rightarrow NN$  decays. The yellow solid line is the expected reach in the inelastic and elastic scatterings off electrons. *Right*: The expected number of elastic scattering events in the CHARM-II (blue solid line) and FASER 2 (red solid line).

suppressed by the square of the mixing angle present in both the production and scattering rates. We consider values of this parameter that are small enough so that the HNL does not decay before reaching the detector.

HNLs can also be produced in decays of on-shell dark gauge bosons, which does not depend on the mixing angle, hence we separately plot the sensitivity obtained in this way in the right panel of Fig. 5.4. We show the projected number of the signal events as a function of the HNL mass for both the CHARM-II and FASER $\nu$ 2 experiments which set the most stringent bounds. The total observed number of  $\nu$  and  $\bar{\nu}$  electron scattering events in CHARM is equal to  $2677 + 2752$  [400]. Based on that fact, and assuming the uncertainty of the neutrino flux of order 5% [401], we predict that a few hundred additional scattering events in CHARM would be a clear BSM effect. Given the cuts on the electron recoil energy and angle used by the CHARM collaboration, which we implement following [386], we determine that scenarios predicting  $N_{\text{ev}} \gtrsim 500$  such events are already ruled out.

Similar cuts designed to efficiently look for new physics effects in electron scattering events in FASER $\nu$ 2 [245] lead to a significantly suppressed number of neutrino-induced BG events,  $N_{\text{ev}} \sim 10$  or  $\mathcal{O}(100)$  where the latter estimate neglects the cuts on the electron recoil angle. This leaves room for better constraints on this scenario based on observations of  $Ne \rightarrow Ne$  events. We show the corresponding number of events as a function of  $m_N = m_{Z_D}/8$  in the right panel of Fig. 5.4. While the resulting HNL spectrum is hard with typical energy  $E_N > 100$  GeV, the spectrum of recoiled electrons is shifted towards lower energies, see [245] for an extensive discussion for light vector mediator DM models. The red shaded region in the plot indicates the expected FASER $\nu$ 2 exclusion limit, which is based on

observation of more than 20 neutrino-like BSM elastic scattering events,  $Ne \rightarrow Ne$ . As can be seen, with FASER $\nu$ 2, the CHARM-II limit, indicated by the blue shaded region, can be improved, covering a larger HNL mass range.

## 5.5 Conclusions

Neutrinos remain one of the least experimentally studied SM species. The recently approved FASER experiment, with its neutrino subdetectors FASER $\nu$  and FASER $\nu$ 2, will pave the way for such an exploration starting from LHC Run 3. We analyzed the discovery potential for new physics particles appearing in high-energy neutrino interactions.

We have shown that such searches could much benefit from the unique properties of the FASER 2 detector, like the possible reciprocity between its spectrometer and the neutrino subdetector. In particular, the latter allows for a very precise reconstruction of the interaction vertices which leads to several novel signatures that can be used to study new physics. In our discussion, we focus on the search for two high-energy oppositely charged tracks, but also on the search for high-energy photons appearing in the detector, and the single-electron scattering signature. These provide complimentary discovery channels where FASER effectively works as the high-energy neutrino beam-dump experiment, and significantly extend its sensitivity reach. We illustrated that in well-motivated BSM scenarios, such as the dipole magnetic portal, and the dark neutrino portal, which have been considered in the literature, *e.g.*, in connection with the persisting MiniBooNE anomaly [376, 378]; also see [402–405] probing new physics interactions of neutrinos can much improve relevant discovery prospects at the LHC.

# Chapter 6

## Testing supersymmetric dark matter in CTA

### 6.1 Introduction

In this chapter, we focus on ID searches for a supersymmetric WIMP - the lightest neutralino in MSSM which, as already mentioned in Section 2.3.3, is one of the most motivated thermal DM candidates. Moreover, it is a DM candidate that fits into a popular and attractive framework that has played an important role in the development of both experimental and theoretical particle physics in the recent decades. While in this chapter we focus on the prototypical heavy DM candidate, in the following chapter we will discuss the possible interesting phenomenological consequences of the connections between light and heavy new physics in DM searches.

Neutralinos as thermal DM candidates have been intensively studied since the 1980's [155, 406–408], when the first experimental tests of supersymmetric phenomenology were performed at the Tevatron and the Large Electron–Positron Collider. A recent review of progress can be found in [135]; see also [409].

One of the primary motivations driving our exploration of the BSM is related to the hierarchy problem. This is a phenomenon in which the mass of a fundamental scalar particle<sup>1</sup> undergoes strong renormalization by the degrees of freedom contributing in the high-energy (ultra-violet) regime. This means that one would expect the mass of the Higgs boson to be large, as it should be driven by the aforementioned corrections taking place at high energies, possibly even near the Planck scale  $M_{\text{Pl}} \sim 10^{19}$  GeV. The LHC measurement revealed that the Higgs boson mass is equal to  $m_H = 125$  GeV which is not at all close to the Planck scale. If there is no new physics between the electroweak scale,  $v = 1/\sqrt{G_F\sqrt{2}} \cong 160$  GeV, and the Planck scale, this would require significant fine tuning of the input parameters in the Lagrangian, see [411] for further discussion and references. If however, there are new degrees of freedom close

---

The contents of this chapter is based on: A. Hryczuk, K. Jodlowski, E. Moulin, L. Rinchuso, L. Roszkowski, E. M. Sessolo et al., *Testing dark matter with Cherenkov light - prospects of H.E.S.S. and CTA for exploring minimal supersymmetry*, *JHEP* **10** (2019) 043, [1905.00315].

<sup>1</sup>There is no such problem for fundamental fermions, as their masses are protected by breaking of the chiral symmetry [410].

to the electroweak scale, the fine tuning can be significantly reduced.

Actually, one of the most thoroughly studied scenarios for such a new physics is low-scale SUSY, introduced in Section 2.3.3. Among other things, SUSY provides an attractive solution to the hierarchy problem thanks to the SUSY non-renormalization theorem [412]. It states that in the limit of exact supersymmetry,<sup>2</sup> there is no renormalization of the mass terms, including the Higgs. One can say that SUSY “protects” the Higgs boson mass from obtaining UV corrections.

## 6.2 MSSM

Below, we introduce the supersymmetric Standard Model, the MSSM, while the basics of SUSY can be found in Appendix D.

Analogous to the fields of the SM, MSSM consists of superfields which are multiplets composed of bosons and fermions; see Table 6.1. The SM fermions and the SM Higgs doublet,  $H_1$ , will be contained in chiral multiplets consisting of chiral Weyl-type fermions and complex scalar fields, while the gauge bosons will be contained in vector multiplets consisting of Majorana-type fermions and real scalar fields.

Recall that in the SM a single Higgs doublet  $H$  is sufficient to give masses to both up and down quarks, since one can use both  $H$  and  $H^\dagger$  in the Lagrangian. However, going from fields to superfields, the same procedure is not allowed because a supersymmetric Lagrangian must be holomorphic<sup>3</sup> and the term with complex conjugated SM Higgs simply has to vanish. A simple solution is to introduce an additional Higgs doublet,  $H_2$  which is used to give masses to up quarks, while  $H_1$  gives the masses to down quarks.

What is more, the introduction of a second Higgs doublet leads to the cancellation of chiral anomalies which would occur for a MSSM with only one Higgs doublet. In such a model, in addition to all the SM fields for which the anomaly cancellation criterion,

$$\text{Tr}(Y_f) = \text{Tr}(Q_f) = 0, \quad (6.2.1)$$

is satisfied, there would be an extra nonvanishing contribution coming from a charged spin-1/2 particle - a higgsino. By introducing the second Higgs doublet with the opposite hypercharge, a second higgsino restores the anomaly cancellation.

The MSSM Lagrangian is

$$\mathcal{L}_{MSSM} = \mathcal{L}_{kin+int} + \mathcal{L}_{soft} - V_Y - V_F - V_D, \quad (6.2.2)$$

where  $\mathcal{L}_{kin+int}$  contains the kinetic terms and interactions with gauge bosons,  $\mathcal{L}_{soft}$  corresponds to soft SUSY breaking<sup>4</sup> by mass terms, and  $V_Y, V_F, V_D$  describe: Yukawa interactions,  $F$ , and  $D$  terms, respectively. The resulting Feynman rules,

---

<sup>2</sup>SUSY must be broken, otherwise the superpartners would have the same masses as their SM counterparts which follows from the relation  $[Q_\alpha, P^2] = 0$ .

<sup>3</sup>For a complex function  $f(z)$  to be holomorphic, it needs to satisfy  $\frac{df}{d\bar{z}} = 0$ , where  $\bar{z}$  is a complex conjugate of a complex variable  $z$ .

<sup>4</sup>Soft SUSY breaking makes sparticles heavier than their SM counterparts, but in a way that

Superfield	Particle	Spin	$SU(3)_C \times SU(2)_W \times U(1)_Y$	Superparticle	Spin
$\hat{V}_1$	$B_\mu$	1	(1, 1, 0)	$\tilde{B}$	$\frac{1}{2}$
$\hat{V}_2$	$W_\mu^i$	1	(1, 3, 0)	$\tilde{W}^i$	$\frac{1}{2}$
$\hat{V}_3$	$G_\mu^a$	1	(8, 1, 0)	$\tilde{g}^a$	$\frac{1}{2}$
$\hat{Q}$	$Q = (u_L, d_L)$	$\frac{1}{2}$	$(3, 2, \frac{1}{3})$	$\tilde{Q} = (\tilde{u}_L, \tilde{d}_L)$	0
$\hat{U}^c$	$U^c = \bar{u}_R$	$\frac{1}{2}$	$(3^*, 1, -\frac{4}{3})$	$\tilde{U}^c = \bar{\tilde{u}}_R^*$	0
$\hat{D}^c$	$D^c = \bar{d}_R$	$\frac{1}{2}$	$(3^*, 1, \frac{2}{3})$	$\tilde{D}^c = \bar{\tilde{d}}_R^*$	0
$\hat{L}$	$L = (\nu_L, e_L)$	$\frac{1}{2}$	(1, 2, -1)	$\tilde{L} = (\tilde{\nu}_L, \tilde{e}_L)$	0
$\hat{E}^c$	$E^c = \bar{e}_R$	$\frac{1}{2}$	(1, 1, 2)	$\tilde{E}^c = \bar{\tilde{e}}_R^*$	0
$\hat{H}_1$	$H_1 = (H_1^0, H_1^-)$	0	(1, 2, -1)	$\tilde{H}_1 = (\tilde{H}_1^0, \tilde{H}_1^-)$	$\frac{1}{2}$
$\hat{H}_2$	$H_2 = (H_2^+, H_2^0)$	0	(1, 2, 1)	$\tilde{H}_2 = (\tilde{H}_2^+, \tilde{H}_2^0)$	$\frac{1}{2}$

Table 6.1: MSSM fields before spontaneous electroweak symmetry breaking.

needed for perturbative computations, and explicit  $\mathcal{L}_{MSSM}$  can be found in, *e.g.*, [413].

Although a detailed discussion of the MSSM is beyond the scope of this thesis, let us discuss the possible DM candidates in MSSM. While more extended SUSY theories provide many of them - cf. Section 2.3.3 - the vanilla MSSM provides only a few.

Neutrinos, sneutrinos, and neutralinos are the only electrically and color-neutral particles in the MSSM. The former cannot be DM, since they would be hot DM, incompatible with large-scale structure formation in the Universe - discussed in Chapter 3. Sneutrinos were viable WIMP DM candidates, but severe constraints on them were obtained, mainly by DD searches, through efficient  $Z$ -mediated scatterings with liquid noble gasses [414], excluding such a scenario. Finally, the lightest of 4 neutralinos is a prominent thermal DM candidate which we discuss next.

## 6.3 Neutralino DM

Simply put, neutralinos are fermions introduced as superpartners of SM gauge bosons and the Higgs boson.

Before the (super)symmetry breaking, the gauge bosons and their SUSY states (so-called bino  $\tilde{B}$  for the hypercharge  $B$  boson, and wino  $\tilde{W}$  for the  $SU(2)$   $W_3$  boson) are massless, so each of them must have 2 degrees of freedom. It means that the gauginos must be their own antiparticles, *i.e.*, they are Majorana fermions. In addition to bino and wino, there are two other neutral gauginos  $\tilde{H}_1, \tilde{H}_2$  - called higgsinos - related to the Higgs sector, and together they mix to form 4 neutralinos. Due to SUSY breaking, the gauginos get mass terms:  $M_1$  for bino,  $M_2$  for wino, and  $\mu$  is also introduced which is a mass parameter of the Higgs doublet superfields.

---

does not reintroduce a quadratic UV sensitivity to the masses of the Higgs bosons (there are 5 physical fundamental scalars in MSSM). Also, soft terms must be gauge invariant, renormalizable, and R-parity invariant.

In result, the neutralino mass matrix has the following form:

$$M = \begin{pmatrix} M_1 & 0 & -m_Z s_w \cos \beta & m_Z s_w \sin \beta \\ 0 & M_2 & m_Z c_w \cos \beta & -m_Z c_w \sin \beta \\ -m_Z s_w \cos \beta & m_Z c_w \cos \beta & 0 & -\mu \\ m_Z s_w \sin \beta & -m_Z c_w \sin \beta & -\mu & 0 \end{pmatrix}, \quad (6.3.1)$$

where  $s_w = \sqrt{1 - c_w^2}$  is a sinus of the Weinberg angle,  $m_Z$  is the mass of the  $Z$  boson, and  $\tan \beta = v_2/v_1$  is a ratio of vacuum expectation values of the two Higgs doublets  $H_1$ , and  $H_2$ .

The physical degrees of freedom are obtained as eigenvectors of this matrix, with masses equal to the eigenvalues. The mass matrix is symmetric, therefore it can be diagonalized by the orthogonal rotation matrix  $N$

$$N\mathcal{M}N^{-1} = \text{diag} \left( m_{\tilde{\chi}_j^0} \right), \quad j = 1, \dots, 4. \quad (6.3.2)$$

Then, the lightest neutralino (denoted further as  $\chi$ ) is the mixture of the gauge eigenstates:

$$\tilde{\chi}_1 = N_{11}\tilde{B} + N_{12}\tilde{W} + N_{13}\tilde{H}_1 + N_{14}\tilde{H}_2.$$

There are 3 limiting cases that will be of our main interest below. These also determine the main annihilation channels contributing to the DM relic density, illustrated in Fig. 6.1. We define the composition of the lightest neutralino as:  $f_{\text{bino fraction}} = |N_{11}|^2$ ,  $f_{\text{wino fraction}} = |N_{22}|^2$ , and  $f_{\text{higgsino fraction}} = |N_{13}|^2 + |N_{14}|^2$ . They allow to identify the phenomenologically distinct cases

- Pure bino (defined as  $f_{\text{bino fraction}} > 0.9$ ): Characterized by the following hierarchy between the mass parameters  $M_1 \ll M_2, \mu$ , where  $\chi \approx \tilde{B}$  mainly annihilates into SM fermions through t-channel sfermion exchange. Unless the sfermions are not much heavier than the lightest neutralino, this typically leads to overabundance of bino DM.
- Pure wino ( $f_{\text{wino fraction}} > 0.9$ ):  $M_2 \ll M_1, \mu$ , where  $\chi \approx \tilde{W}$  annihilates efficiently to  $W$  bosons, leading to the correct abundance of wino DM for the mass  $m_\chi \sim 2.2$  TeV.
- Pure higgsino ( $f_{\text{higgsino fraction}} > 0.9$ ):  $\mu \ll M_1, M_2$ , where  $\chi \approx (\tilde{H}_1 + \tilde{H}_2)/\sqrt{2}$  can annihilate efficiently into fermions,  $W$ , and  $Z$  bosons, leading to the correct higgsino DM thermal relic density for  $m_\chi \sim 1$  TeV.
- Mixed higgsinos are non-pure neutralinos defined as those, where the sum of two compositions is greater than 0.9. They typically rely on coannihilations or other mechanisms to obtain the correct relic density.

If the neutralino is a pure  $SU(2)$  multiplet - higgsino or wino - then gauge interactions essentially fix the thermal freezeout in the following way, cf. [415].

Higgsinos come as a pair of almost degenerate neutralinos and there is also a slightly heavier chargino at a mass scale  $\sim \mu$ . All of these species contribute to  $\langle \sigma v \rangle_{\text{eff}}$  (cf. Eq. (3.1.22) and the following discussion), where the main SM final states are  $W^+W^-$  and  $ZZ$  - see last two panels of Fig. 6.1. The correct value of

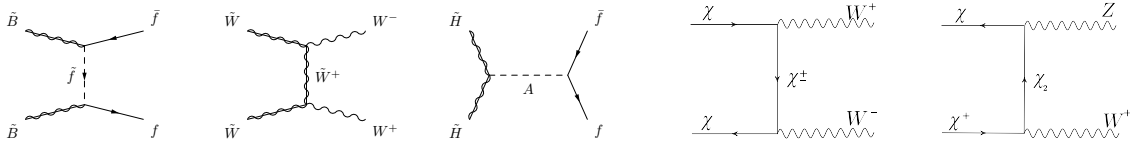


Figure 6.1: Main annihilation channels of the lightest neutralino depending on its composition. Shown from left to right are the bino and wino. The center panel illustrates the funnel annihilation - which takes place also for other neutralino compositions, while the last two panels present the coannihilations of the lightest higgsino with a heavier neutralino and chargino, respectively. Taken from [409, 416].

Profiles	Einasto (E)	NFW	Cored Einasto (CE)
$\rho_s$ ( $\text{GeVcm}^{-3}$ )	0.079	0.307	0.079
$r_s$ (kpc)	20.0	21.0	20.0
$\alpha_s$	0.17	—	0.17
$r_c$ (kpc)	—	—	3.0

Table 6.3: Parameters of DM density profiles we considered: Einasto, NFW, and Cored Einasto.

the relic density emerges naturally for  $m_\chi \sim 1$  TeV, and coannihilations become even more important for higgsinos heavier than about 1.3 TeV.

In the case of winos, the lightest neutralino is almost degenerate with the lightest chargino, and both have mass close to  $M_2$ . Again, coannihilations - mainly into  $W^+W^-$  - play an important role. The correct relic density occurs for  $m_\chi \sim 2.2 - 3$  TeV.

Neutralinos with significant bino contribution - which do not couple to gauge or Higgs bosons - usually are characterized by very weak annihilation cross sections at freeze-out. As a result, there is typically an overabundance of bino-like neutralino DM, unless there is another mechanism to increase the  $\langle\sigma v\rangle_{\text{eff}}$ , *e.g.*, coannihilations with sfermions, or resonant  $s$ -channel annihilations mediated by one of the Higgs bosons (the so-called *funnels*, illustrated at the center panel of Fig. 6.1). As a result, bino neutralinos tend to have a lower present-day annihilation cross section, therefore ID of them will be quite challenging.

## 6.4 Indirect detection of WIMPs

As discussed in Section 3.2, the process of annihilation of WIMPs into SM particles which contributes to the DM freeze-out taking place in the early Universe, should also occur quite efficiently today, provided there is significant abundance of DM particles and the relevant annihilation cross sections is not too much suppressed. In light of that, we will present the basics of ID searches for WIMP DM within our Milky Way galaxy which will be used later when discussing the sensitivity of the proposed observatory CTA to neutralino DM.

In Section 2.3.1 we reviewed substantial evidence that each visible galaxies,

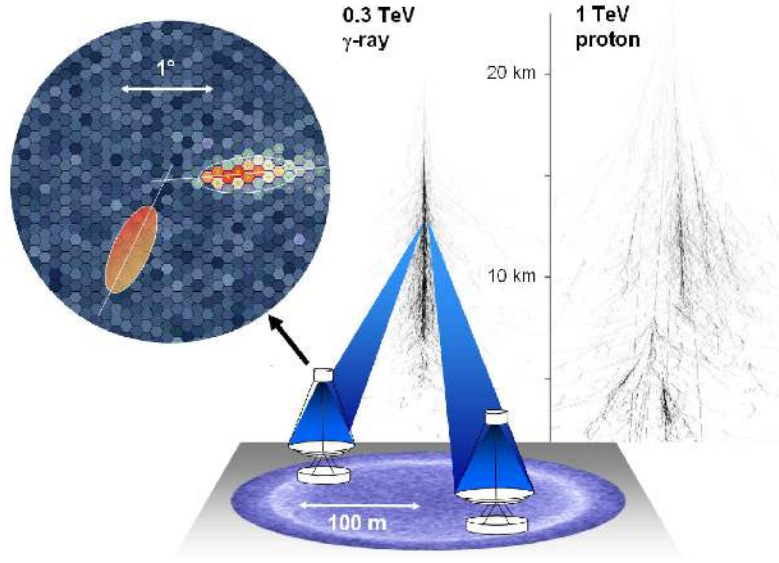


Figure 6.2: A sketch of the imaging atmospheric Cherenkov technique used by, *e.g.*, H.E.S.S., and CTA. Taken from [417].

such as the Milky Way, is gravitationally embedded in a much larger, spherically symmetric DM halo. Such distribution of DM is generally expected from N-body simulations and astrometric surveys like Gaia [422, 423], and many DM density profiles have been proposed in the literature. We illustrate the most popular ones in Fig. 6.3, where it can be seen that the differences between them occur in the region close to the center of the DM halo,  $r \lesssim 8$  kpc, where  $r$  is the distance from the GC and the point of DM annihilations.

The exact DM profile is not known near the center of the Galaxy. In the following, we will focus on cuspy profiles that are favored by extensive numerical studies of DM haloes and lead to the most promising discovery prospects in DM ID searches. In particular, we will show our results for the Einasto [424] and the Navarro-Frenk-White (NFW) [425] profiles that are parametrized as follows:

$$\rho_E(r) = \rho_s \exp \left\{ -\frac{2}{\alpha_s} \left[ \left( \frac{r}{r_s} \right)^{\alpha_s} - 1 \right] \right\} \quad \text{and} \quad \rho_{\text{NFW}}(r) = \rho_s \left[ \frac{r}{r_s} \left( 1 + \frac{r}{r_s} \right) \right]^{-2}, \quad (6.4.1)$$

where  $r_s$  is the scale radius,  $\rho_s = \rho(r_s)$  is the normalization factor, and  $\alpha_s$  is the power index (only for Einasto). The values of these parameters are given in Table 6.3. We take the local DM density to be  $\rho_\odot = \rho(r_\odot) = 0.39 \text{ GeV cm}^{-3}$  [426], where  $r_\odot = 8.5$  kpc is the distance between the Sun and the GC. To illustrate the effects of such a choice (which leads to an enhanced signal) we additionally compare our results with those obtained for a cored profile, called Cored Einasto. It matches the aforementioned Einasto profile at large distances:  $\rho_{\text{CE}}(r \geq r_c) = \rho_E(r)$ , while at small ones it assumes a constant, cored profile  $\rho_{\text{CE}}(r < r_c) = \rho_E(r_c)$ , where  $r_c = 3$  kpc.

We note that in addition to a smooth halo, DM can also form small-scale, clumpy structures [427] that can significantly enhance the ID rates. An estimate

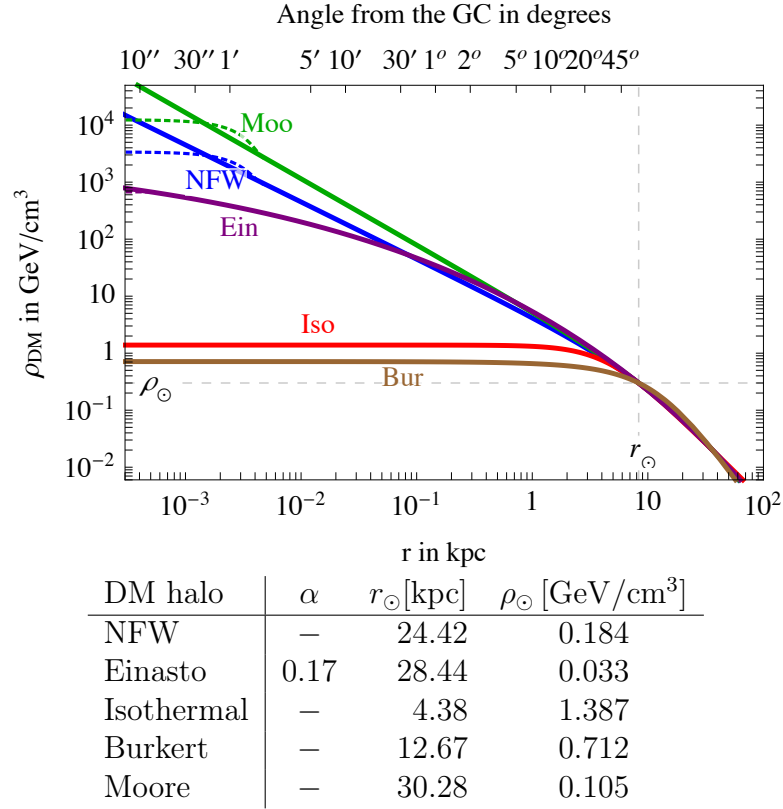


Figure 6.3 & Table 6.2: Comparison of the most common DM density profiles studied in the literature [418] together with their corresponding parameters. Taken from [419].

of this effect is captured by the ratio

$$B = \langle \rho^2 \rangle / \langle \rho \rangle^2, \quad (6.4.2)$$

called the boost factor, where  $\langle \rangle$  denote averaging over a stochastic distribution of DM clumps within the Galaxy, see [203] for an extensive discussion. However, the impact of substructures is expected to be negligible for searches near the GC, see [428] and references therein, thus we do not include them in further analysis.

The differential flux of photons coming from pair-annihilation of WIMPs is the following integral of the annihilation rate performed over the solid angle observed  $\Delta\Omega$  and the line of sight

$$\frac{d\Phi_\gamma^{\text{DM}}}{dE}(\Delta\Omega, E) = \left( \frac{\sigma v_0}{8\pi m_{\text{DM}}^2} \frac{dN_\gamma(E)}{dE} \right) \times J(\Delta\Omega), \quad (6.4.3)$$

- see [208, 210] - where  $\sigma v_0$  is the total present day annihilation cross section,  $dN_\gamma(E)/dE$  is the photon spectrum per annihilation which we take from PPPC [420], see Fig. 6.4, and

$$J(\Delta\Omega) = \int_{\Delta\Omega} d\cos\theta d\phi \int_0^\infty ds \rho_{\text{DM}}(r(s, \theta))^2, \quad (6.4.4)$$

where  $s$  is the distance between the place of WIMP annihilations and the GC,<sup>5</sup>

<sup>5</sup>The integral over  $s$  is convergent because  $\rho_{\text{DM}}$  has a finite support as a DM halo is finite.

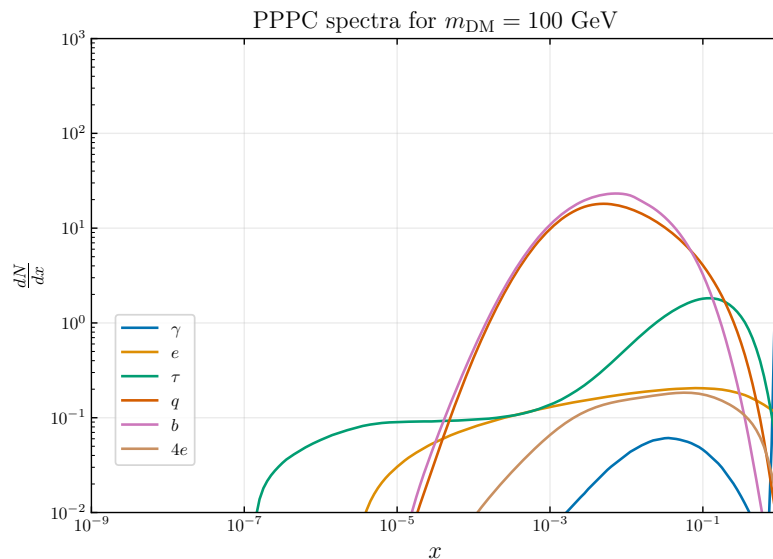


Figure 6.4: Photon spectra resulting from annihilation of a  $m_{\text{DM}} = 100$  GeV non-relativistic WIMP, as a function of the fraction of photon kinetic energy to the WIMP mass  $x = E_{\gamma}/m_{\text{DM}}$ . Based on the tabulated PPPC spectra [420].

is the so-called J-factor. It depends only on the DM distribution profile and the region of observations, while it does not depend on particle physics parameters of a particular WIMP model - hence Eq. (6.4.3) conveniently factorizes. From Fig. 6.5 we see that

$$r = \sqrt{s^2 + r_{\odot}^2 - 2r_{\odot}s \cos \psi} = \sqrt{s^2 + r_{\odot}^2 - 2r_{\odot}s \cos l \cos b}, \quad (6.4.5)$$

where we expressed  $\psi$ , the polar angle between the direction of observation and the GC, in the galactic reference frame using  $\cos \psi = \cos l \cos b$ .

## 6.5 Observation of the Galactic Center

Due to the high density of DM, the Galactic Center is the brightest source of DM-induced  $\gamma$  rays available for the observations at Earth [429], and is therefore one of the most important regions of interest for ID searches. Among them, the most prominent experiments are based on imaging atmospheric Cherenkov technique - for illustration see Fig. 6.2 - used by arrays of telescopes, such as The High Energy Stereoscopic System (H.E.S.S.) [430, 431] and the upcoming Cherenkov Telescope Array (CTA) [432, 433].

These telescopes can look for both continuum and monochromatic  $\gamma$ -ray signals originating from DM annihilations, provided the background is under control. There are numerous astrophysical sources emitting high energy photons and cosmic rays in the vicinity of the GC, among them the supermassive black hole (SMBH) Sagittarius A\* [434], and a diffuse emission along the Galactic plane [435, 436].

H.E.S.S. observations of the inner  $1^{\circ}$  of the GC have been performed with 10 years of data, and effective 250 hour of exposure.<sup>6</sup> The null results of this search

<sup>6</sup>Some regions have been excluded from observations, as, *e.g.*, close to the SMBH, background

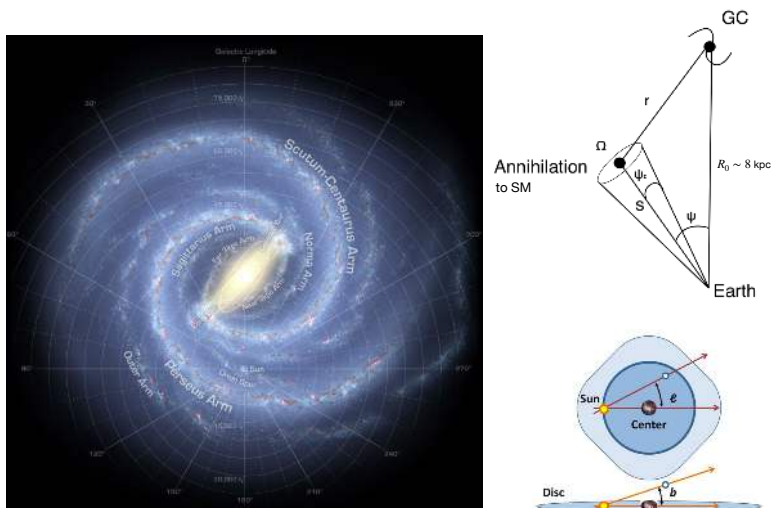


Figure 6.5: Schematic illustration of ID observations in the Milky Way. On the left and bottom right, galactic coordinates are shown, where the Sun is the origin,  $l$  is the galactic longitude, and  $b$  is the galactic latitude. The figure is based on several illustrations taken from [421].

allowed the collaboration to set one of the most stringent limits on the annihilation cross section of heavy WIMP DM, almost touching the thermal benchmark of  $\sigma v_0 = 2.2 \times 10^{-26} \text{ cm}^3/\text{s}$  for WIMPs heavier than  $\sim 1 \text{ TeV}$  and the assumed Einasto DM profile towards the GC - see Fig. 6.7 which we discuss in detail in Section 6.7.

It is imperative to test the thermal WIMP paradigm, therefore a new-generation array of telescopes, CTA, has been proposed and intensively developed which could further strengthen these bounds. The network is expected to start collecting data in the coming few years, while prototype detectors recorded the first light in 2019. A dedicated, multi-year DM detection programme with 500 hours of exposure is one of the main goals of CTA, described in detail in [433]. We refer to that reference for technical details of the experimental aspects of neutralino ID, while our discussion will be brief.

A dedicated 3-dimensional likelihood ratio test statistics technique will be adapted by CTA for DM searches, to exploit the spectral and spatial features of the expected signal. Spatial pixels are defined as squares of  $0.5^\circ$  size between  $|b|, |l| < 5^\circ$ . In addition to that, 20 energy bins are logarithmically distributed from 10 GeV to 100 TeV. The likelihood function quantifies the amount of excess events over the expected astrophysical background in each such bin. It is defined as the product of the Poisson probabilities of counting event in the signal and background regions in the  $i$ -th energy bin,  $j$ -th Galactic longitude bin, and  $k$ -th Galactic latitude bin

$$\mathcal{L} = \prod_{i,j,k} \mathcal{L}_{ijk}, \quad (6.5.1)$$

---

overwhelming the signal is expected; for details, see [1].

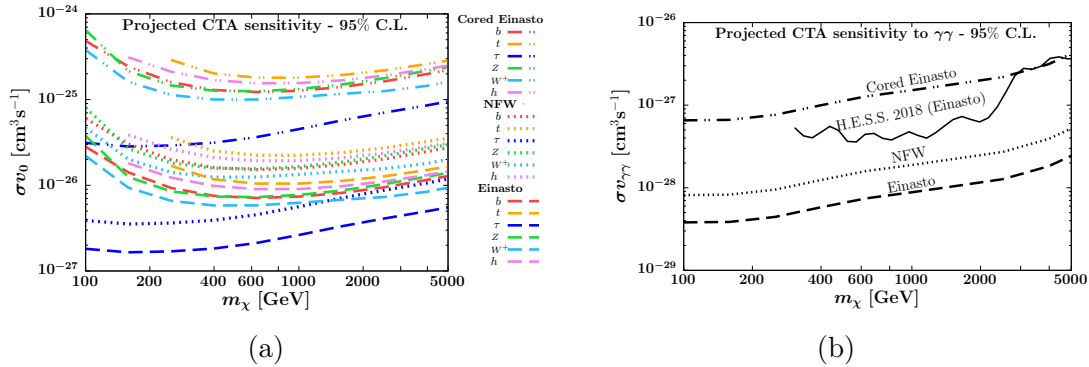


Figure 6.6: The projected sensitivities of CTA to the annihilation cross section as a function of DM mass  $m_\chi$ , derived from 500 hour observations of the inner Galactic halo. Three halo profiles were considered: Cored Einasto (dashed double-dotted), NFW (dotted) and Einasto (dashed lines). Annihilation of DM (a) to the specific SM final states, and (b) to two monochromatic photons. The solid line represents the limit from H.E.S.S. [431].

where

$$\mathcal{L}_{ijk}(s_{ijk}, b_{ijk}) = \text{Pois}(s_{ijk} + b_{ijk}, m_{ijk}) \text{Pois}(\alpha_{jk} b_{ijk}, n_{ijk}). \quad (6.5.2)$$

The  $s_{ijk}$  and  $b_{ijk}$  are the number of expected signal and background events measured in the signal region, respectively, while  $\alpha_{jk}$  corresponds to the ratio of the size of the solid angle of the background over the signal regions. Finally,  $m_{ijk}$  and  $n_{ijk}$  are the measured counts in the signal and background regions, respectively.<sup>7</sup>

A log-likelihood ratio test statistic is calculated for each WIMP mass  $m_\chi$  and a one-sided upper 95% C.L. exclusion bound on  $\sigma v_0$  is then presented. The exclusion lines computed for three DM density profiles: Einasto, NFW and Cored Einasto are shown in Fig. 6.6a. The DM particle is assumed to annihilate into SM final states with 100% branching fraction, as specified in the plot. In addition, in Fig. 6.6b we show the corresponding sensitivity for DM annihilating directly into monochromatic  $\gamma$  rays.

## 6.6 Bayesian scan for neutralino DM

One of the most thoroughly explored scenarios for new physics at the electroweak scale is supersymmetry, as described in detail in the previous sections of this chapter. Despite the lack of a definitive signal of new physics, SUSY remains attractive, especially in light of the discovery of the Higgs boson at the LHC, where its mass was measured to be not much larger than that of the  $Z$  boson. Indeed, experimental data have so far ruled out only models based on optimistic expectations, based on theoretical or aesthetic arguments, *e.g.*, the naturalness.

<sup>7</sup>Exact formulae for each quantity can be found in [1].

### 6.6.1 The p9MSSM

The MSSM introduced in Section 6.2 has over 100 free soft-breaking parameters [413], thus it is challenging to study the most general parameterization of the MSSM. However, it is also not absolutely necessary, as two commonly used approaches show. One can study more constraining models that assume a high-scale SUSY breaking mechanism (*e.g.*, CMSSM/mSUGRA) or consider a p(henomenological)MSSM which is well suited to low-energy phenomenological analysis we are interested in, therefore we follow it.

The pMSSM is defined by restricting MSSM to satisfy [437, 438]: (i) CP conservation, (ii) Minimal Flavor Violation at the electroweak scale, and predict (iii) degenerate first two generations of sfermion soft-mass parameters, and (iv) negligible Yukawa couplings and trilinear couplings ( $A$ -terms) in the first two matter generations.

In our numerical scan, we consider a 9 free parameters parametrization, the p9MSSM, where in addition to the above assumptions, we set the gluino mass, the third-generation down-type right soft squark mass, and the first two generations of soft slepton masses to 20 TeV. Such high masses mean that these species are decoupled and do not influence the electroweak dynamics. See Table 6.4 for details of the model parameters and their ranges used in our analysis. Such a restricted parameter space is both large enough and sufficient to capture the most essential aspects of neutralino DM phenomenology because the remaining free parameters are precisely the ones that determine the DM properties of the CP and R-parity symmetric MSSM. As we shall see, this also allows for rich electroweak scale phenomenology without loss of generality.

### 6.6.2 Scanning setup and constraints

We follow the methodology described in Sec. 6.5, and apply the predicted CTA sensitivity to annihilation of WIMPs, to the case of neutralino DM. We use the nested sampling algorithm implemented in the `Multinest_v.2.7` [439, 440] package to efficiently scan over the parameters listed in Table 6.4. To this end, we use flat priors and 20000 randomly-chosen (according to the prior functions) live points which initiate the operation of the sampling algorithm.

The spectrum of p9MSSM is obtained thanks to `SPheno v4.0.3` [441, 442]. We also scan over negative values of the bino mass  $M_1$  and the  $\mu$  parameter in order to study blind spots in DM DD [443, 444]. We require that the remaining gaugino mass parameter satisfies the condition  $M_2 > 100$  GeV, as determined by the LEP bounds on charginos. The masses of third-generation sfermions can take a wide range of values. For small values, the sfermions participate in efficient coannihilations, leading to the correct bino relic abundance. In contrast, for large values of the squarks masses the characteristic SUSY scale is increased which allows for obtaining the correct mass of the SM-like Higgs boson. The remaining sfermions masses and the gluino mass  $M_3$  do not play a significant role in the following discussion, so their values are fixed at 20 TeV.

The mass parameters are defined at the SUSY scale determined by the geometrical average of the stops masses,  $M_{\text{SUSY}} = (m_{\tilde{t}_1} m_{\tilde{t}_2})^{1/2}$ . Other parameters,

Parameter	Range
bino mass	$-10 < M_1 < 10$
wino mass	$0.1 < M_2 < 10$
gluino mass	$M_3 = 20$
trilinear couplings	$-30 < A_t = A_b = A_\tau < 30$
pseudoscalar mass	$0.1 < m_A < 10$
$\mu$ parameter	$-10 < \mu < 10$
3rd gen. left soft squark mass	$0.1 < m_{\tilde{Q}_3} < 30$
3rd gen. right up soft squark mass	$0.1 < m_{\tilde{t}_R} < 30$
3rd gen. right down soft squark mass	$m_{\tilde{b}_R} = 20$
1st/2nd gen. soft squarks masses	$m_{\tilde{Q}_{1,2}} = m_{\tilde{d}_R, \tilde{s}_R} = 20$
soft sleptons masses	$0.1 < m_{\tilde{\tau}_R} = m_{\tilde{L}_3} < 10$
soft sleptons masses	$m_{\tilde{e}_R, \tilde{\mu}_R} = m_{\tilde{L}_{1,2}} = 20$
ratio of Higgs doublet VEVs	$1 < \tan \beta < 62$
Nuisance parameter	Central value, error
Top pole mass $m_t$ (GeV)	(173.34, 0.76) [445]

Table 6.4: The p9MSSM parameter ranges used in our scans. All masses and trilinear couplings are expressed in units of TeV.

the top quark pole mass,  $m_t$  (treated as a nuisance parameter in the scan because it is a less precisely known quantity), and  $\tan \beta$  are defined at the electroweak symmetry breaking (EWSB) scale. The scans are driven by a global likelihood function which contains a standard set of constraints described below.

**Dark matter relic density** The constraint that has the strongest impact on our numerical result is related to the DM relic abundance measurement given by *Planck* [20],

$$\Omega_\chi h^2 = 0.120 \pm 0.001. \quad (6.6.1)$$

To calculate the relic density we use `micrOMEGAs v.5.0.6` [446, 447] supplemented with the `DarkSE` [448] code for a numerical implementation of the Sommerfeld enhancement.

We perform the numerical scans in two commonly discussed cases: (i)  $\Omega_\chi h^2 \cong 0.120$  and (ii)  $\Omega_\chi h^2 < 0.120$ . In the first case - corresponding to a single DM component in the Universe with a standard cosmological history - we use a Gaussian likelihood distribution function for the relic density which takes into account the relevant observational uncertainty. In the second case - concerning multi-component DM, or a modified Universe history - we use a half-Gaussian distribution with the relic density constraint imposed only as an upper bound.

**Sommerfeld enhancement and DM ID** As discussed above, the CTA and H.E.S.S. telescope arrays are particularly suited for studying  $\sim 1$  to a several TeV WIMP DM. In the context of neutralino, this often leads to a scenario - described in Section 3.1 and illustrated in Fig. 3.2 - where the SE plays a crucial role. It strongly affects both the calculation of the present-day neutralino annihilation

cross section,  $\sigma v_0$ , and, to a lesser extent, its relic density [172, 449, 450]. An accurate treatment of SE in a theory as complex as the MSSM requires the inclusion of SE contributions from multiple exchanges of all the gauge bosons and of the SM Higgs. Also all coannihilation channels should also be considered, adding to the numerical difficulty. Previous studies, [438, 451–458], took SE into account in a simplified way, whereas our analysis takes this effect, in principle, fully into account. A complete numerical treatment of the SE is very CPU-expensive. Therefore, we use a two-step approach. First, i.e., in the numerical scans of the extensive parameter space of the p9MSSM, we use the simplified approach described in, *e.g.*, [452]. Then the points in the parameter space of the model found this way are post-processed with the accurate SE treatment using the full `DarkSE` code. Sommerfeld enhancement is also included in the computation of  $\sigma v_0$ ,  $\sigma v_{\gamma\gamma}$ , and  $\sigma v_{Z\gamma}$ .

**Other constraints** In addition to the relic density, we use the latest data coming from complementary experimental searches: (i) DM DD, (ii) collider constraints, (iii) Higgs boson and flavor physics, and (iv) DM ID. They have ruled out much of the parameter space, especially thanks to the tremendous progress in DD searches, and the fact that the Higgs boson mass is not much larger than the  $Z$  boson mass. See [1] for details.

## 6.7 Results

Our numerical scan results in a set of points in the multidimensional parameter space of the model with an increasingly improving fit to the constraints that we impose. For each such point in the scan, we calculate the H.E.S.S. and CTA limits for the present-day annihilation cross section. We use the 95% C.L. bounds shown in Fig. 6.6a. We also take into account other bounds discussed above. In the plots below we only present the points which lie within the 95% C.L. region of the global profile-likelihood. In other words, we select the points satisfying the condition  $\Delta\chi^2 \leq 5.99$ , where  $\Delta\chi^2 = -2 \ln(\mathcal{L}/\mathcal{L}_{\max})$  and  $\mathcal{L}$  is the product of the individual likelihood functions for each of the constraints used in the analysis, while  $\mathcal{L}_{\max}$  is the likelihood function of the best fit point obtained in the scan.

### 6.7.1 Neutralino DM

In Fig. 6.7 we show the scan points in the  $(m_\chi, \sigma v_0)$  plane, where we require thermal relic density  $\Omega_\chi h^2 \simeq 0.12$  of neutralinos. The colors of each point denote the dominant gauge composition of the neutralino which by construction in the MSSM is never a 100% pure eigenstate. Following Section 6.3, we define a “pure” state, if the composition of a single gaugino (and a sum for higgsinos) is greater than 90%. We show binos in green, winos in blue, and higgsinos in red. There are also mixed neutralinos, consisting of two gauginos, defined such that the contribution to their composition from the third gaugino must be smaller than 10%. The wino-bino is shown in cyan, and the bino-higgsino in gold.

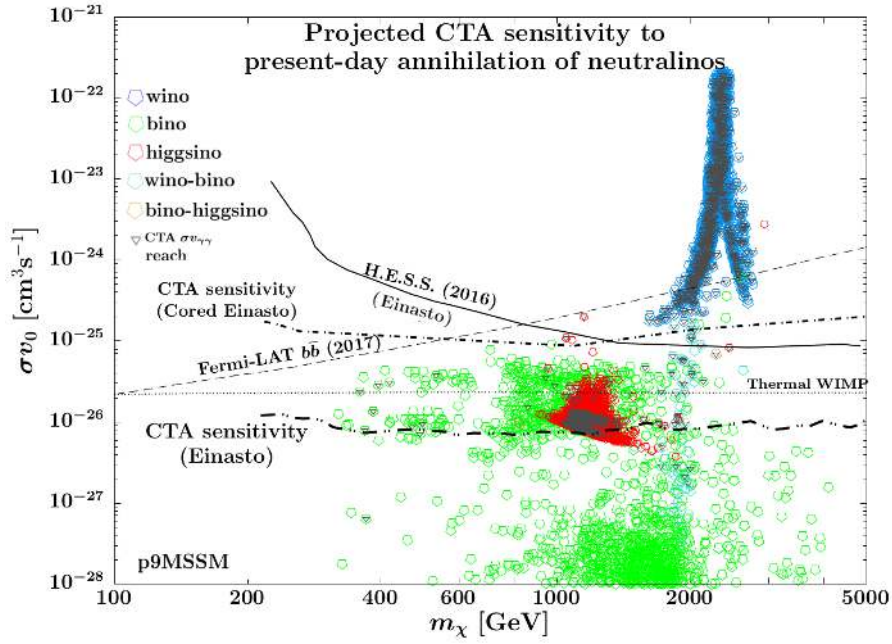


Figure 6.7: Result of numerical p9MSSM scan shown in  $(m_\chi, \sigma v_0)$  plane. Color coding reflects the composition of the lightest neutralino according to the legend. The predicted CTA sensitivity is shown as a thick (Einasto), or thin (Cored Einasto) dashed double-dotted line. To emphasize the complementarity between continuous and monochromatic photon searches, we mark with dark gray triangles the points whose  $\sigma v_{\gamma\gamma}$  is in the range of CTA.

We show with a black dashed line our projection of the CTA sensitivity in searches for the neutralino-induced diffuse photon flux, with 500 hours of observation of the GC and assuming the Einasto DM density profile. It should be noted that the CTA bound derived in our model cannot be represented by a single line due to the number of possible neutralino DM annihilation final states that must be taken into account. We run detailed simulations for selected benchmark points with  $m_\chi \gtrsim 1$  TeV which shown that the approximate limit we present mirrors the true CTA sensitivity. For smaller masses, the line shown in Fig. 6.7 represents a conservative approach, *i.e.*, each point lying above the line will be in range of CTA. In a similar way, we obtain the approximate H.E.S.S. limit shown as a solid line.

Fig. 6.7 clearly shows the *impact of neutralino composition* on the placement in the  $(m_\chi, \sigma v_0)$  plane, consistent with the description of Section 6.3. The predicted CTA sensitivity shown in Fig. 6.7 is obtained for the two cases of Einasto and Cored Einasto DM halo density profiles. As can be seen, the CTA discovery prospects in the search for neutralino DM will strongly depend on this assumption. In particular, the expected future bounds on  $\langle\sigma v\rangle$  differ by about an order of magnitude for the two aforementioned profiles. We have also verified numerically that the results for the NFW profile can be easily obtained by multiplying the predicted Einasto line by a factor of  $\sim 2.5$ .

In particular, one can see the  $m_\chi \sim 1$  TeV higgsino region (red points in the plot), where there is an inverse relation between the neutralino mass and the  $\sigma v_0$ ,

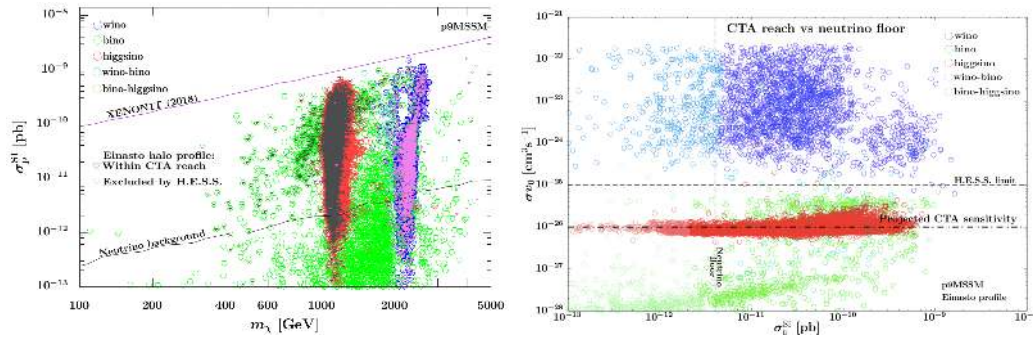


Figure 6.8: Same as in Fig. 6.7, but shown in the  $(m_\chi, \sigma_p^{\text{SI}})$  plane (left), and in the  $(\sigma_p^{\text{SI}}, \sigma_{\nu_0})$  plane (right).

due to the coannihilations being the primary mechanism responsible for thermal freeze-out. In result, the heavier higgsinos,  $m_\chi \gtrsim 1.5$  TeV, partially lie outside the sensitivity of CTA, while lighter ones will be fully covered assuming Einasto DM density profile. Instead, for the cored Einasto, the higgsino region will not be covered at all.

In the case of winos (blue), there is a characteristic resonance peak centered around  $m_\chi \sim 2.2$  TeV which is due to the Sommerfeld enhancement of the present-day annihilation cross section. The enhancement is strong enough that this region is already excluded by H.E.S.S. (confirming the results of previous studies, *e.g.*, [452, 453]), assuming the Einasto profile, while mixed wino-bino neutralinos will be fully probed by CTA, improving over previous limits. It is interesting to note that CTA will be able to fully probe wino DM even assuming the cored Einasto DM density profile.

Other neutralino compositions are characterized by a significant bino contribution (green), where the correct relic density can be obtained thanks to various mechanisms, see Section 6.3, therefore there is no single region around which the bino DM is scattered around. Typically, bino neutralinos are characterized by a lower present-day annihilation cross section than the CTA sensitivity, and it will be challenging to probe a large portion of them by ID searches.

The importance of the *complementarity* of direct and indirect searches can be seen in Fig. 6.8. On the left, we present the points from the scan in the plane of neutralino mass  $m_\chi$  and spin independent proton scattering cross section  $\sigma_p^{\text{SI}}$ . The XENON1T 90% C.L. upper limit [459] is indicated by a solid violet line. Note that the XENON1T results are included in the global likelihood function, excluding the points in the  $\sim 2\sigma$  region of the profile likelihood that lie above the violet line. We denote the points excluded by ID searches for  $\sigma_{\nu_0}$  with triangles - violet for points excluded by H.E.S.S., and black for projected sensitivity of CTA. Note that a large fraction of neutralinos that lie below the XENON1T reach, and to a lesser extent even those lying below the irreducible neutrino background denoted with a black solid line, will be covered by CTA.

This can be seen even more spectacularly on the right side of Fig. 6.8, where we project the p9MSSM points onto the  $(\sigma_p^{\text{SI}}, \sigma_{\nu_0})$  plane. The future reach of DD searches is bound to cover the parameter space from right to left until it reaches

the irreducible neutrino background, shown as a shaded region.<sup>8</sup> For simplicity, we also show a vertical dashed gray line which indicates the irreducible neutrino background  $\sigma_p^{\text{SI}} \approx 4 \times 10^{-12}$  pb taken at  $m_\chi \approx 2$  TeV. Conversely, the reach of ID searches gradually increases from top to bottom, providing a complementary coverage of the parameter space.

### 6.7.2 Underabundant neutralinos

As discussed in Sec. 6.6.2, the lightest neutralino can be a good DM candidate even when its thermally produced relic abundance is less than the total DM relic density in the Universe. In Fig. 6.9, we show the results of the scan looking for such underabundant neutralinos in the  $(m_\chi, \sigma v_0)$  plane. Only the points that belong to the 95% C.L. region of the global profile-likelihood are shown.

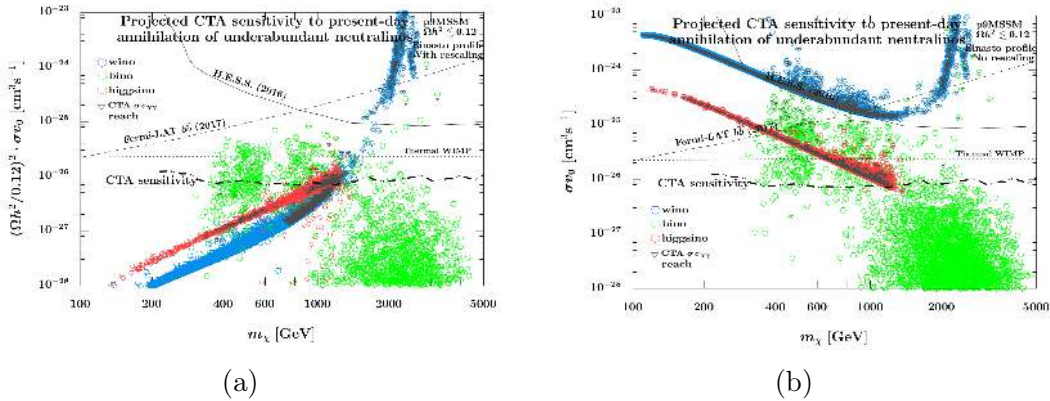


Figure 6.9: Result of numerical p9MSSM scan which only implements the relic density constraint as an upper bound (underabundant neutralinos), shown in (a)  $(m_\chi, (\Omega_\chi h^2/0.12)^2 \times \sigma v_0)$  plane, and (b) in  $(m_\chi, \sigma v_0)$  plane. Legend is the same as in Fig. 6.7.

In Fig. 6.9a, we rescale  $\sigma v_0$  by  $(\Omega_\chi h^2/0.12)^2$  which corresponds to the case, where the neutralino constitutes only a fraction of the total relic density,  $\Omega_\chi h^2 < 0.12$ . We also rescale the DM DD cross section  $\sigma_p^{\text{SI}}$  by  $\Omega_\chi h^2/0.12$  when imposing the relevant constraints. As can be seen, underabundant higgsino-like and wino-like neutralinos with masses of the order of a few hundred GeV usually lie beyond the reach of CTA. However, there are some higgsino-like points that can be probed by the CTA monochromatic photon search. This constrains the combination of the annihilation cross section into the  $\gamma\gamma$  and  $Z\gamma$  final states,  $(\sigma v_{\gamma\gamma} + \frac{1}{2}\sigma v_{\gamma Z})$ , where the latter is rescaled by a factor of a half to take into account that photons induced by  $Z$  boson decays will not reproduce a monochromatic signal. We note that some such points obtained in our scans lie below the predicted CTA sensitivity in searches for DM-induced diffuse photon spectrum (dash-dotted line in the plot) which is due to the relative strength of the search for monochromatic signals. These points are indicated by gray triangles in the plot. The key impact of searching for monochromatic photons is even more pronounced for heavier neutralinos with mass

<sup>8</sup>The value of  $\sigma_p^{\text{SI}}$  characteristic of the neutrino floor depends on the value of the DM mass, hence the shaded region does not form a regular shape.

$m_\chi \approx 1$  TeV. In particular, it is worth noting that, monochromatic-line searches of CTA can probe an underabundant wino-like neutralino DM with  $m_\chi \approx 1$  TeV, while there will be no diffuse spectrum signal. Even heavier, but still insufficiently abundant wino-like neutralinos, may also be probed by the CTA, in both types of searches.

In Fig. 6.9b we show the results corresponding to the scenario in which, even though the predicted thermal neutralino DM abundance is lower than the total observed DM relic density, neutralino is the only DM particle and its production in the early Universe needs to be supplemented by, *e.g.*, some non-thermal contribution. In particular, this allows us to consider significantly larger values of the annihilation cross section that would lead to too low  $\Omega_\chi h^2$  without the non-thermal production component. In this case, CTA may easily discover a few hundred GeV higgsino-like neutralino DM in both diffuse photon and monochromatic-line searches. As can be seen, in such cases the current Fermi-LAT limits from the null DM searches in dwarf galaxies [225] - see also the later analysis [213] which improves the Fermi-LAT bounds further - cover the low mass region of the parameter space, where CTA loses sensitivity - see the dashed line for fixed annihilation into a  $b\bar{b}$  pair. This line also represents the position of the exclusion limit that we would obtain by imposing Fermi-LAT as a constraint in the likelihood function. It's worth noting that this scenario is independently constrained by DD searches which we also take into account in our scanning procedure.

## 6.8 Conclusions

We conducted an updated and improved study of the CTA reach in testing neutralino DM in the pMSSM. Our analysis improved previous studies by: (i) deriving the projected CTA sensitivity by state-of-the-art binned likelihood analysis, (ii) using up-to-date experimental constraints and numerical tools, *e.g.*, full 13 TeV LHC data, and (iii) implementing the SE for all points in the scan, whereas previous works only included its estimate. In particular, for the first time SE in sfermion coannihilations was included in a scanning framework.

These developments allowed us to critically assess the neutralino DM detection prospects in the leading future ID telescope arrays. Assuming the Einasto profile, H.E.S.S. was able to cover the neutralinos with present-day annihilation cross sections within an order of magnitude from the WIMP thermal value, while we project the CTA will go significantly below it. We confirmed that H.E.S.S. is sensitive to most of the wino region, while CTA will also cover much of the 1 TeV higgsino region which is still an excellent thermal DM candidate.

It is worth pointing out that such good detection prospects of neutralino DM can only be obtained assuming cuspy DM density profiles towards the GC, while they will be much more challenging for the core-like profiles. Finally, given those and other astrophysical uncertainties, it remains crucial to continue a broad experimental program targeting neutralino DM and SUSY in various types of searches.



# Chapter 7

## Indirect detection of long-lived particles

### 7.1 Introduction

In this chapter we describe the results of a project that ties together the main goals of my thesis, namely to explore complementarity in searches for LLPs, light DM, and WIMPs. Specifically, we study a heavy secluded WIMP DM candidate coupled to the SM particles via the dark Higgs boson portal and rich dark sector species. The signatures of the light, sub-GeV dark Higgs boson are usually studied in intensity frontier searches, similar to the case described in Chapters 4 and 5. Instead, heavy DM particles with the mass at the TeV scale can more efficiently be probed by other means, including ID searches, as discussed in Chapter 6. In this chapter, we will discuss interesting phenomenological consequences of the presence of both the light and heavy new species that could allow for disentangling between such scenario and vanilla LLP and WIMP DM models.

To this end, we first focus on the complementarity between intensity frontier studies and ID searches for signatures induced by heavy DM, as well as on related observations in next generation CMB surveys. Notably, this complementarity has been largely unexplored, given that scenarios in which it becomes important often lead to stringent cosmological bounds. We show, however, that avoiding such bounds is possible in non-minimal BSM sectors. Interestingly, this can then generate new features in DM ID searches that employ non-local effects. They significantly affect the usual detection strategies and allow one to distinguish such a scenario from the ordinary signatures based on WIMPs or simplified models. In the following, for simplicity, we will refer to this search strategy as *indirect detection of long-lived particles*.

---

The contents of this chapter is based on: K. Jodłowski, L. Roszkowski and S. Trojanowski, *Indirect detection of long-lived particles in a rich dark sector with a dark Higgs boson portal*, [2112.11993](#).

## 7.2 Motivation

As described in Section 3.1, the standard freeze-out mechanism does not require the new physics to occur near the electroweak scale, but can be generalized to a much wider range of DM mass and coupling constants [181]. While overly large values of DM couplings are limited by unitarity, lowering them by even a few orders of magnitude below the electroweak strength can still give the correct relic density, provided that the masses of at least some of the dark sector species lie below the GeV scale. In particular, to provide the connection between the SM and a DM particle with mass in the GeV range, or below, one typically introduces some BSM light mediator particle(s) [184, 185].

Scattering of light DM with SM particles in DD searches kinematically leads to insufficient energy deposit in the detector, requiring introducing novel strategies for DD of light DM that have only recently been explored [87, 244]. In collider-type experiments, probing further signatures of light new physics may be possible, *e.g.*, with searches for decays of unstable mediator species; see [234–236] for recent reviews.

Such studies are usually carried out within a framework of simplified models such as a dark photon or a dark Higgs boson; see discussion in front of Eqs. (4.1.1), (4.1.3) and (4.1.4) and also cf. recent reviews [260, 262, 460]. However, it is understood that further experimental probes are possible in more realistic models that could be made UV complete. This could also provide other, complementary ways to experimentally test such non-minimal scenarios. Given the lack of well-established and non-gravitational DM signal in the observations up to date, it is imperative to explore such non-standard possibilities, especially if they lie at the intersection of two of the most widely discussed topics in current DM searches.

A rich dark sector that is secluded from the SM, with only a weak portal communicating between them, is naturally not strongly constrained by observations. However, there may be additional effects (compared to WIMP-like DM) that would significantly affect them, potentially leading to constraining even such scenarios. These include, *e.g.*, secluded [185, 271] or Sommerfeld-enhanced DM annihilations, cf. discussion in [461], into the DS particles, which significantly influence the prospects for DM ID detection and can also be constrained by CMB radiation measurements. When the coupling constants between the dark species are large and the lifetimes of the decaying particles are smaller, new effects appear also in collider probes, *e.g.*, the secondary production of new BSM species that are produced just in front of the detectors - as we described in Chapters 4 and 5. Therefore, rich dark sector models with LLPs remain an excellent laboratory to propose and study new experimental strategies.

In the main part of the discussion in this chapter, we focus on the dark Higgs boson portal defined by Eq. (4.1.3), which can be introduced as a natural mediator between the SM and even very complicated sectors of BSM physics [462–466]. In particular, such a portal may be naturally associated with the hidden valley scenarios predicting a few LLPs [257]. Motivated by this, we assume that the new scalar particle is very weakly coupled to the SM sector and has a mass smaller than about 1 GeV. The remaining BSM content of our model will contain few particles on broad mass scales between  $\sim 1$  MeV and 10 TeV, including a heavy

secluded DM candidate that may be a target for future ID observations.

Before we discuss the details of this BSM scenario, we first introduce the non-local effects in DM ID that will be present in this model, while also can be found in a more general class of models predicting the existence of extremely long-lived dark mediator species.

### 7.3 Non-local effects in $\gamma$ -ray DM ID searches

Let us begin by discussing the photon flux arising from cascade annihilations or decays involving DM and LLPs which arrive at a detector on Earth. Our goal is to compare a formula for the differential flux of gamma rays in the case when non-local effects in DM ID cannot be neglected with the one obtained for WIMPs annihilating directly into SM particles. The latter is described by Eq. (6.4.3). Further discussion of non-local effects in DM ID can be found in [467–471]. In our analysis, we also follow studies of multi-step WIMP cascade annihilations [472, 473].

The main difference between the ID of WIMPs and the ID in rich dark sector models containing LLPs that we focus on arises when one of the BSM species produced as a result of DM annihilation can travel a large distance of order kpc before generating a visible signal. As a result, there is no longer a one-to-one relationship between the position of the DM annihilation process and the place where the visible SM species are produced. Instead, as illustrated in Fig. 7.1, these points are spatially separated and the flux no longer factorizes into a universal  $J$ -factor and a particle physics part, like in the case of WIMPs. The observationally inferred spatial distribution of DM-induced signal does not have to follow the DM density profile in the Galaxy.<sup>1</sup>

We are interested in the generic scenario, in which the ID of the LLP takes place due to the following cascade of events:

$$\begin{aligned} \text{DM} + \text{DM} &\rightarrow \text{other particles} + \text{LLP} \\ \text{LLP} &\rightarrow \dots \rightarrow \text{the SM}, \end{aligned} \quad (7.3.1)$$

where the initial DM annihilation process produces the very long-lived LLP which can decay after traveling a long distance. In the LLP decay, the dots can indicate another cascade process involving less long-lived particles which ends with the final decay into the SM particles. In the following, we will focus on the  $\gamma$ -ray signatures induced by these SM products of the cascade event.

The final flux of photons originating from such cascade and observed in the

---

<sup>1</sup>In the plot and discussion below, we refer to the very long-lived mediator species as LLPs, even though the analysis of non-local effects that we provide can also be applied to heavier new particles. We note that in our analysis, this mediator species will always be significantly lighter than the heavy DM particle.

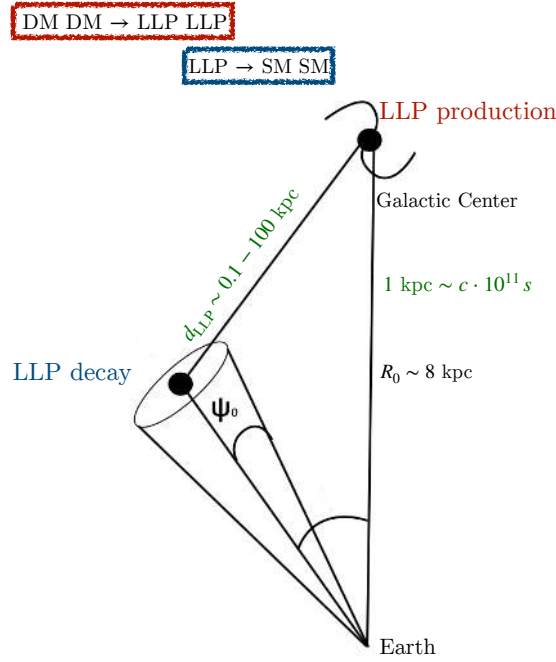


Figure 7.1: Cartoon of indirect detection of light long-lived particles in observations of the GC region of the Milky Way. We illustrate the region of interest in the analysis as a cone with the aperture angle  $2\psi_0$ . A key feature of such a scenario is the galactic-scale separation between the position of DM annihilations near the Galactic Center (LLP production, marked in red) and the LLP decays (blue). It introduces non-locality, which we discuss in detail in the text. We also show typical distance scales relevant for this analysis.

detector on Earth is given by

$$\left. \left( \frac{d\Phi}{dE_\gamma} \right) \right|_{\text{non-local}} = \sum_{\text{bins } E_{\text{LLP}}} \left[ \frac{1}{8\pi} \frac{\langle \sigma v \rangle_{E_{\text{LLP}}}}{m_{\text{DM}}^2} \frac{1}{\bar{d}_{\text{LLP}}} \int_{\Delta\Omega} d\Omega \int_{\text{l.o.s.}} ds \int_{V_{\text{DM}}} d^3\vec{r}_{\text{DM}} \frac{f(\theta)}{4\pi} \times \right. \\ \left. \times \frac{\rho_{\text{DM}}^2(|\vec{r}_{\text{DM}} - \vec{r}_{\text{GC}}|)}{|\vec{r}_{\text{LLP}} - \vec{r}_{\text{DM}}|^2} \exp\left(-\frac{|\vec{r}_{\text{LLP}} - \vec{r}_{\text{DM}}|}{\bar{d}_{\text{LLP}}}\right) \gamma_{\text{LLP}} (1 - \beta_{\text{LLP}} \cos\theta) \left( \frac{dN_\gamma}{dE_\gamma} \right)_{\text{DM}} \right]_{E_{\text{LLP}}}, \quad (7.3.2)$$

where  $\bar{d}_{\text{LLP}} = c\tau_{\text{LLP}}\gamma_{\text{LLP}}\beta_{\text{LLP}}$  is the decay length of the LLP in the Galactic frame,  $\gamma_{\text{LLP}}$  is its boost factor, and the vectors  $\vec{r}_{\text{DM}}$ ,  $\vec{r}_{\text{LLP}}$ ,  $\vec{r}_{\text{GC}}$  correspond to the positions of the  $\chi$  annihilation, the LLP decay, and the GC with respect to the detector on Earth, respectively.

Compared to the standard case, Eq. (6.4.3), in the non-local DM ID there appears an additional integration over the position of the initial  $\chi$  annihilation. This accounts for the fact that the LLP produced in the DM annihilation process at  $\vec{r}_{\text{DM}}$  can travel a long-distance before decaying at the  $\vec{r}_{\text{LLP}}$  position. Specifically, the position  $\vec{r}_{\text{LLP}}$  may lie outside the RoI in a given DM ID analysis and, therefore, this event will not contribute to the measured DM-induced signal rate even though the initial DM annihilation process could occur at  $\vec{r}_{\text{DM}}$  inside the RoI. On the other hand, DM annihilations occurring outside the RoI can have an

impact on the analysis, if the LLP travels inside the RoI before decaying. The probability of mediator decay decreases exponentially with the increasing distance from its production point in the Galaxy,  $|\vec{r}_{\text{LLP}} - \vec{r}_{\text{DM}}|$ . Therefore, although the aforementioned non-local effects impact the analysis, typically only a limited region of the Galaxy around the RoI contributes to the DM-induced photon flux measured on Earth.

In Eq. (7.3.2), we also employ additional anisotropy factors that depend on the angle  $\theta$  defined as the angle between the LLP boost direction and the detector,

$$\cos \theta = \frac{\vec{r}_{\text{LLP}} \cdot (\vec{r}_{\text{DM}} - \vec{r}_{\text{LLP}})}{|\vec{r}_{\text{LLP}}| |\vec{r}_{\text{DM}} - \vec{r}_{\text{LLP}}|}. \quad (7.3.3)$$

The function  $f(\theta)$  is defined as follows:

$$f(\theta) = \frac{d \cos \tilde{\theta}}{d \cos \theta} = \frac{(1 + \tan^2 \theta)^{3/2}}{\tan^2 \theta} \frac{[(\beta_{\text{LLP}}/\tilde{\beta}_{h_D}) + \cos \tilde{\theta}] \sin^2 \tilde{\theta}}{(\beta_{\text{LLP}}/\tilde{\beta}_{h_D}) \cos \tilde{\theta} + 1}. \quad (7.3.4)$$

The relevant angle in the LLP rest frame is  $\tilde{\theta}$ , obtained by the following expression:  $\cos \tilde{\theta} = \cos \tilde{\theta}_+$  for  $\theta \leq \pi/2$  and  $\cos \tilde{\theta} = \cos \tilde{\theta}_-$  otherwise, where

$$\cos \tilde{\theta}_{+,-} = \frac{-\gamma^2 \tan^2 \theta \frac{\beta}{\tilde{\beta}_{h_D}} \pm \sqrt{\gamma^2 \tan^2 \theta \left(1 - \frac{\beta^2}{\tilde{\beta}_{h_D}^2}\right) + 1}}{\gamma^2 \tan^2 \theta + 1}. \quad (7.3.5)$$

The remaining undefined quantity is  $\tilde{\beta}_{h_D} = \sqrt{1 - (2m_{h_D}/m_{\text{LLP}})^2}$ , where  $h_D$  is the less long-lived mediator decaying into SM particles at the last step of the cascade. In the simplest case (irrelevant for our concrete model), in which the LLP mediator decays directly into a pair of photons, one would reproduce a known expression for radiative beaming,  $f(\theta) = \gamma_{\text{LLP}}^2 (\beta_{\text{LLP}} \cos \tilde{\theta} + 1)^2$ . The anisotropy factors arise from the boost of the decaying LLP in the Galactic frame. They affect the final photon flux on Earth because in each region of the Galaxy, the decaying mediators preferentially come from the direction of the GC, where the DM density is the largest. However, in the non-relativistic limit which matches the traditional (local) WIMP DM annihilations, we obtain  $f(\theta) \rightarrow 1$  and there are no anisotropy effects besides the most straightforward dependence of the DM-induced  $\gamma$ -ray flux on the DM density profile towards the GC.

**Non-local effects in  $\gamma$ -ray DM ID** In the left panel of Fig. 7.2 we show the impact of non-local effects on the integrated photon flux in a toy DM model with  $m_{\text{DM}} = 100$  GeV and a long-lived mediator of mass  $m_{\text{med}} = 10$  GeV. For simplicity, we assume that the mediator decays directly into a photon pair. With the red lines we show the ratio between the fluxes obtained for the large and small mediator lifetimes and several different RoIs. A large region around the GC defined by  $|b|, |l| < 12^\circ$  is indicated by the red solid line where we use the Galactic coordinate system with the Galactic longitude  $l$  and latitude  $b$ . Although this is a larger region than in typical CTA analyses, *e.g.*, the one described in Chapter 6, we use it for illustration because it is better suited for highlighting the ID non-local

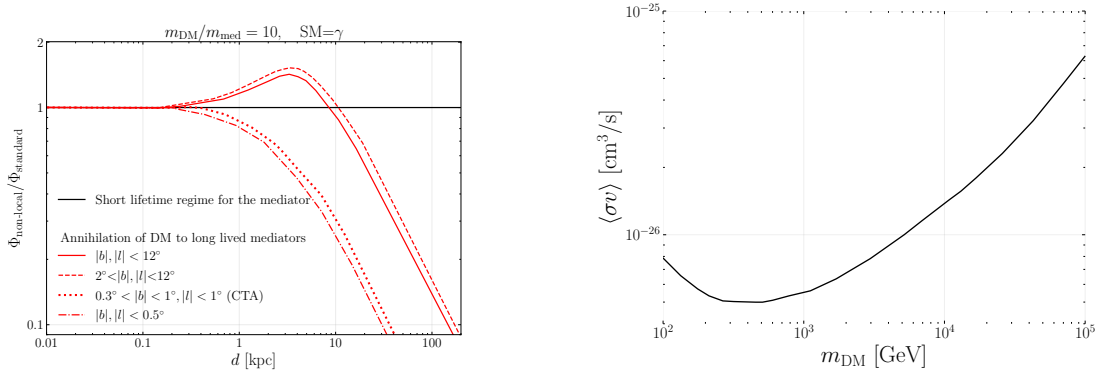


Figure 7.2: Left: The ratio of the integrated photon fluxes obtained for increasing decay length  $d$  of the mediator and in the standard regime of prompt decays shown with the horizontal black solid line. The results are shown for the toy model with the ratio between the DM and mediator particles masses  $m_{\text{DM}}/m_{\text{med}} = 10$ . The mediator decays dominantly into two photons,  $\text{med} \rightarrow \gamma\gamma$ . Right: The CTA sensitivity for the secluded WIMP DM scenario shown in the  $(m_{\text{DM}}, \langle \sigma v \rangle)$  plane. The solid black line corresponds to the standard reach assuming the mediator promptly decays into light quarks, cf. [474]. The red lines are obtained by taking into account the non-local effects for two different regions of interest, as indicated in the plot. See the text for more details.

effects. The large RoI presented by us extends to about  $d_{\text{RoI}} \sim R_0 \sin b \simeq 2.3$  kpc distance from the GC, where the distance between the Earth and the GC is  $R_0 = 9$  kpc.

As shown in the figure, for  $\bar{d}_{\text{med}} \lesssim d_{\text{RoI}}$  the impact of non-local effects on the observed spectrum is very small and the photon spectrum resembles the one obtained in the regime of a small mediator lifetime. We denote the latter by the horizontal black solid line. On the other hand, for very large decay lengths of  $A'$  the expected DM-induced photon flux coming from the RoI falls well below the standard expectations. The decrease of the flux is approximately linear with growing  $\bar{d}_{\text{med}}$ , as one can see from Eq. (7.3.2) in the limit of  $\bar{d}_{\text{med}} \gg |\vec{r}_{\text{med}} - \vec{r}_\chi| \sim d_{\text{RoI}}$ .

The relative increase in photon flux for intermediate values of  $\bar{d}_{\text{med}} \sim d_{\text{RoI}}$  seen in the plot can be understood as follows, see [469] for first discussion of this effect. Most of the mediators produced near the GC decay within the RoI and only a small fraction of them produced in the GC would generate photons traveling towards the detectors. The signal from other mediators would be lost in the standard case, while in the non-local regime this can be partially overcome by dark vectors moving away from the GC before they decay. At these distant positions, they can produce photons moving towards the Earth which would not be seen had they been produced close to the GC. In result, the DM ID signal rates from distant positions within the RoI receive contributions not only from DM annihilations that occur locally, but also from DM annihilations that take place close to the GC. This increase is even more pronounced for the modified RoI around the GC, in which we exclude the innermost region of the size of  $2^\circ$  in the sky. We show this with the dashed red line in the figure, where the photon flux in the non-local

regime is even more strongly enhanced.

In addition, we also show the expected photon fluxes for much smaller RoIs. Here, with the red dotted line we show the results for a small ROI specific to the CTA Galactic center survey, where we have additionally excluded part of the region very close to the GC, *i.e.*, we assume  $0.3^\circ < |b| < 1^\circ$  and  $|l| < 1^\circ$ . Instead, we use the red dash-dotted line to represent the flux for an even smaller region around the GC with  $|b|, |l| < 0.5^\circ$  which represents a typical DM halo size for dwarf galaxies in the Fermi-LAT analyses [214]. For both small RoIs, the relative increase in flux for smaller  $\bar{d}_{\text{med}}$  is difficult to reconstruct, while for the decay length of the order of several kpc the flux is already suppressed.

In the right panel of Fig. 7.2, we illustrate the impact of non-local effects on the DM ID searches for the aforementioned toy model. We compare the expected reach of CTA sensitivity in the secluded WIMP DM scenario presented in [475] with the corresponding reach obtained for a very long-lived mediator with  $\tau_{\text{med}} = 10^9 \text{ s}$  and fixed  $m_{\text{med}} = 10 \text{ GeV}$  where the final decay states are light quarks. Larger values of the mass of the annihilating DM  $m_{\text{DM}}$  imply greater values of the boost factor of the mediator and the corresponding decay length  $\bar{d}_{\text{med}} \simeq (m_{\text{DM}}/1 \text{ TeV})(10 \text{ GeV}/m_{\text{med}}) \times 1 \text{ kpc}$ . This results in an effective suppression of the DM-induced signal from a small ROI around the GC for  $m_{\text{DM}} \gtrsim$  a few hundred GeV, as denoted by the red line. We also present even larger ROI,  $|b|, |l| < 12^\circ$ , denoted by the red dashed line. In this case, we observe a relative improvement of the bound in the intermediate region of  $m_{\text{DM}} \sim$  a few TeV due to the excess photon flux for  $\bar{d}_{\text{med}} \sim d_{\text{ROI}}$ .

## 7.4 Model

In order to illustrate the impact of the non-local effects in DM ID and the complementarity to the intensity frontier searches, we study a fairly rich dark sector model schematically presented in Fig. 7.3. In the model, the DS and the SM are connected by the mixing between a light, sub-GeV dark Higgs boson  $h_D$  and its heavier SM counterpart  $H$ . The DS consists of, *i.a.*, a dark photon  $A'$ , a gauge boson of the secluded  $U(1)'$  group which obtains its mass via the dark Higgs mechanism. The dark Higgs boson, and all fields shown in green, are charged under the  $U(1)'$ . An additional stable complex scalar field  $\eta$  is also introduced which is charged under the  $U(1)'$  group and will comprise a small fraction of the DM. Notably, such a scenario is one of the prototype models with light DM at the MeV-GeV scale which is discussed in intensity frontier studies, see, *e.g.*, [303, 308, 476] for recent analyses.

Our goal is to identify new features that may emerge when such a simple scenario is extended with additional dark species that may be both light and heavy. We introduce a new heavy stable complex scalar field  $\chi$  which will be the dominant DM component. It is coupled to  $\eta$  (subdominant DM component) through a heavy, auxiliary spectator real scalar field  $\phi$  which plays only a marginal role in our discussion.<sup>2</sup> The full DS should also contain some additional degrees of freedom that are not relevant to our analysis. These can be charged under an

<sup>2</sup>Alternatively, the scalars  $\chi$  and  $\eta$  could be coupled by a renormalizable contact operator.

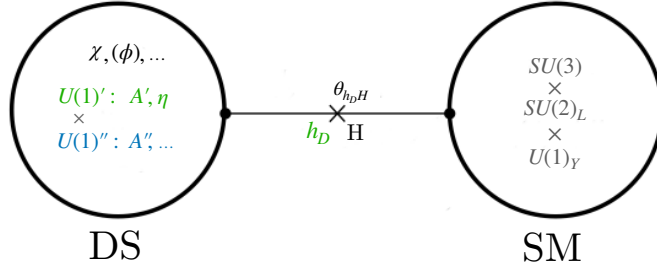


Figure 7.3: Cartoon of the model in which the DS is connected to the SM via a light dark Higgs boson portal ( $h_D$ ). It mixes with the SM Higgs particle ( $H$ ) by the mixing angle  $\theta_{h_D H}$ . The SM gauge symmetry is extended by the  $U(1)'$  and  $U(1)''$  groups, leading to new gauge bosons,  $A'$  and  $A''$ , respectively. The fields charged under the first of those groups are colored green and those charged under the second are colored blue. The DM consists almost entirely of the heavy complex scalar  $\chi$ , which interacts directly only with the lighter DM particle,  $\eta$ , through an exchange of the auxiliary scalar field  $\phi$ .

additional  $U(1)''$  group that adds another light dark gauge boson  $A''$  to the particle spectrum studied by us. As discussed below, we introduce the  $A''$  field to better illustrate the non-local DM ID phenomenological effects. We also assume that the dark Higgs boson  $h_D$  is not charged under  $U(1)''$ .

The model is described by the following Lagrangian

$$\mathcal{L} = \mathcal{L}_{\text{SM}} + \mathcal{L}_{\text{DS}} + \mathcal{L}_{\text{portal}}, \quad (7.4.1)$$

where  $\mathcal{L}_{\text{SM}}$  is the Lagrangian of the SM,  $\mathcal{L}_{\text{DS}}$  corresponds to the DS, and  $\mathcal{L}_{\text{portal}}$  describes the interactions between the SM and the DS as well as between the two parts of the DS charged under the  $U(1)'$  and  $U(1)''$  gauge groups,

$$\mathcal{L}_{\text{portal}} = -\lambda_{Hh_D} |\Phi|^2 |\sigma|^2 - \frac{\epsilon'}{2} F'_{\mu\nu} F^{\mu\nu} - \frac{\epsilon''}{2} F''_{\mu\nu} F^{\mu\nu} - \frac{\tilde{\epsilon}'}{2} F'_{\mu\nu} (F^{\mu\nu})''. \quad (7.4.2)$$

We assume vanishing of the kinetic mixing of both dark vectors with the SM photon,  $\epsilon' = \epsilon'' = 0$ , as we focus on identifying possible new phenomenological aspects of the model – with respect to the usual dark photon signatures – that can arise in the presence of extremely long-lived dark vectors. Such choice is self-consistent, as the kinetic mixing terms with the SM photon are not regenerated perturbatively which will be discussed later. In turn, we assume a non-zero kinetic mixing between the two dark vectors which could be generated by loop processes with some additional heavy fields charged under both dark groups.

In Eq. (7.4.2),  $\Phi$  stands for the SM Higgs doublet, while  $\sigma$  corresponds to the dark Higgs boson singlet. We parametrize both fields after the spontaneous symmetry breaking of both the electroweak and the dark gauge symmetries in the unitary gauge

$$\Phi = \left( 0, (v_{\text{SM}} + h) / \sqrt{2} \right)^T, \quad \sigma = (v_D + H_D) / \sqrt{2}, \quad (7.4.3)$$

where  $v_{\text{SM}} = 246 \text{ GeV}$  is the SM Higgs boson vacuum expectation value, while  $v_D$  is the corresponding quantity for the dark Higgs boson. The portal coupling

$\lambda_{Hh_D}|\Phi|^2|\sigma|^2$  generates a non-diagonal mixing of  $h$  and  $H_D$ . We denote the physical eigenvector states (the mass basis) by  $H$  and  $h_D$ , respectively.

We couple the lighter DM component  $\eta$  to both the dark vector  $A'$  and the dark Higgs boson  $h_D$ , while  $\phi$  connects both DM components  $\chi$  and  $\eta$

$$\begin{aligned} \mathcal{L}_{\text{DS}} \supset & \mu_\chi |\chi|^2 \phi + \mu_\eta |\eta|^2 \phi + (q'_H g_D)^2 A'^\mu A'_\mu |h_D|^2 \\ & + i q'_\eta g_D A'_\mu [\eta^* (\partial^\mu \eta) - (\partial^\mu \eta^*) \eta] + (q'_\eta g_D)^2 A'_\mu A'^\mu |\eta|^2. \end{aligned} \quad (7.4.4)$$

Here  $q'_i$  denotes the charges of the particle  $i$  under the dark gauge group  $U(1)'$ . In the following discussion, we set  $q'_H = q'_\eta = 1$ . As we will discuss below, invoking two component DM allows us to relax the otherwise stringent constraints on heavy WIMP-like scalars coupled to the SM sector via light mediator species, see [477, 478].

The DS Lagrangian also contains the potential of the dark Higgs boson, including the mass terms, the cubic and quartic interactions between the dark Higgs boson and the lighter scalar  $\eta$

$$\begin{aligned} \mathcal{L}_{\text{DS}} \supset & \mu_D^2 |\sigma|^2 - \frac{1}{2} \lambda_D |\sigma|^4 \\ & + m_\chi^2 |\chi|^2 + m_\eta^2 |\eta|^2 \\ & - \lambda_{h_D \eta} h_D^2 |\eta|^2 - (\mu_{h_D \eta} h_D |\eta|^2 + \text{h.c.}). \end{aligned} \quad (7.4.5)$$

Due to the spontaneous breaking of the dark  $U(1)'$  gauge symmetry, the dark bosons  $A'$  and  $h_D$  obtain their masses, given by the formulas  $m_{A'} = g_D v_D$  and  $m_{h_D} = \sqrt{\lambda_D} v_D$ . Moreover, the mixing of the dark Higgs boson with the SM Higgs boson can be parametrized by the angle  $\theta_{hh_D} \simeq \lambda_{Hh_D} v_D v_{\text{SM}} / m_H^2$ . This expression is valid whenever  $m_{h_D} \ll m_H$  which will be the case in the following sections.

Let us note that a similar dark Higgs mechanism (with an additional fundamental scalar) could also occur in the part of the DS charged under the group  $U(1)''$  which would generate a non-zero mass for the corresponding gauge boson  $m_{A''}$ . For simplicity, we assume that  $m_{A''} \ll m_{A'}$  and that this part of the DS remains secluded from the SM, while the presence of additional light dark species, not indicated in the equations below, would render the  $A''$  vector unstable.

The couplings most relevant to our discussion appear after applying the dark vector field redefinition,  $A' \rightarrow A' - \tilde{\epsilon}' \delta A''$ . They are induced by changing the gauge basis into the mass basis which removes the non-canonical kinetic mixing term between the two dark field-strength tensors in Eq. (7.4.2). We emphasize the presence of an additional multiplicative factor  $\delta = (m_{A''}/m_{A'})^2$  which modifies the field shift relative to the case when one of the vector fields is massless [261]. In the following we will denote  $\tilde{\epsilon} = \tilde{\epsilon}' \delta$  and assume  $\tilde{\epsilon} \sim 10^{-6}$ . Therefore,  $m_{A''} \gtrsim 10^{-3} m_{A'}$  and  $m_{A''} \sim \text{MeV} - \text{GeV}$ .

The field redefinition of  $A'$  introduces the following terms

$$\mathcal{L}_{\text{DS}} \supset \frac{1}{2} m_{A''} A''^2 - i \tilde{\epsilon} g_D A''_\mu [\eta^* (\partial^\mu \eta) - (\partial^\mu \eta^*) \eta]. \quad (7.4.6)$$

As can be seen, the lighter DM scalar  $\eta$  obtains a suppressed coupling (by a factor  $\tilde{\epsilon}$ ) to the light dark vector  $A''$ . We note that a similar coupling could be obtained

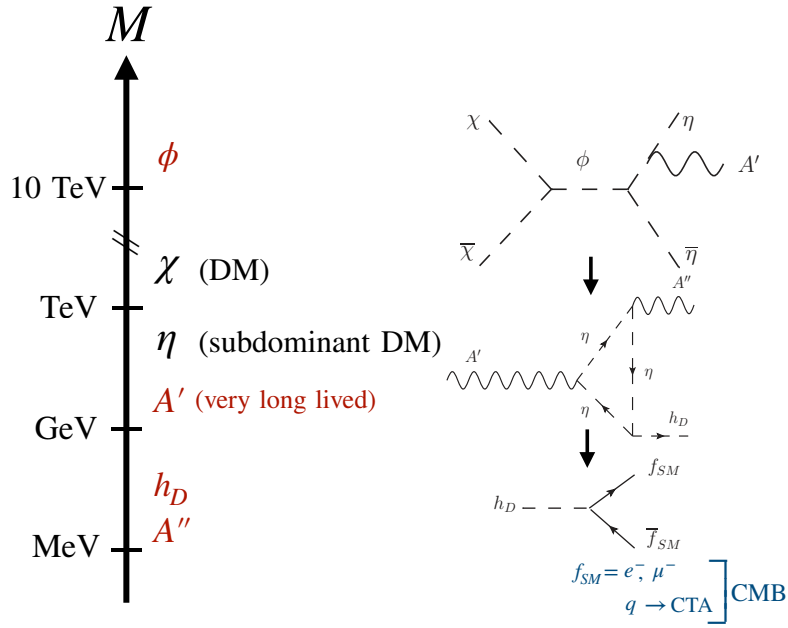


Figure 7.4: Left: a schematic illustration of the DS particle mass hierarchy. The unstable mediators are denoted in dark-red, while the two stable DM species - in black. Right: processes leading to DM indirect detection signatures.

for  $\tilde{\epsilon}' = 0$  by introducing a small (milli)charge to the  $\eta$  field with respect to the  $U(1)''$  group. In this case, the  $A''$  boson could even be much lighter.

The particle spectrum of the DS spans at least several orders of magnitude, as shown on the left side of Fig. 7.4. Even for all the dark charges set to unity - which we assume further for simplicity - the model still features a set of 12 free parameters. To structure our discussion and better illuminate the interesting phenomenological prospects of this scenario, we assume below the following hierarchy of masses in the BSM sector of the model

$$(m_\phi \gg) m_\chi > m_\eta > m_{A'} > m_{h_D} > 2m_f \quad \text{and} \quad m_{A''} \sim m_{h_D}. \quad (7.4.7)$$

Under this assumption, the dominant component of DM is the heavier scalar  $\chi$  which decouples from the thermal plasma earlier than the lighter scalar  $\eta$ . The decoupling of  $\chi$  occurs via annihilations mediated by the intermediate heavy scalar  $\phi$ ,  $\chi\chi \rightarrow (\phi^*) \rightarrow \eta\eta$ . The right side of Fig. 7.4 shows the relevant Feynman diagrams of the key processes leading to indirect signals of DM. In particular,  $2 \rightarrow 3$  annihilations  $\chi\chi \rightarrow (\phi^*) \rightarrow \eta\eta A'$  will play the key role in our discussion of ID observables.

As can be seen, the dark photon produced by the  $2 \rightarrow 3$  process then decays into a dark Higgs boson  $h_D$  and the dark vector,  $A' \rightarrow h_D A''$  which indeed is kinematically allowed; cf Eq. (7.4.7). This decay occurs via a radiative process with exchange of  $\eta$  in the triangle loop.<sup>3</sup> As a result, the decay width is naturally

<sup>3</sup>Note that other loop-induced decays into two lighter dark vectors,  $A' \rightarrow A'' A''$ , or two scalars,  $A' \rightarrow h_D (h_D \text{ or } H)$ , are excluded by the scalar QED analog of the Furry theorem which applies to loop diagrams with an odd number of external vector fields, see Chapter 10 of [479]. The decays of  $A'$  into the SM Higgs boson and the light dark Higgs boson would, either way,

suppressed and  $A'$  can have a very large, astrophysically significant, lifetime

$$c\tau_{A'} \simeq 1 \text{ kpc} \left( \frac{1}{g_D} \right)^2 \left( \frac{10^{-6}}{\tilde{\epsilon}} \right)^2 \left( \frac{4 \times 10^{-6}}{\lambda_{h_D \eta}} \right)^2 \left( \frac{m_\eta}{150 \text{ GeV}} \right)^4 \left( \frac{10 \text{ GeV}}{m_{A'}} \right)^5. \quad (7.4.8)$$

The full expression is given in Eq. (E.1.2), while the above approximation holds assuming  $m_\eta \gg m_{A'} \gg m_{h_D}$ . We give a full list of decay widths and annihilation cross sections relevant for our discussion in Appendix E.1.

As can be seen from Eq. (7.4.8), the dark vector can travel galactic scale distances before decaying and producing visible signals due to subsequent decays of the dark Higgs boson,  $h_D \rightarrow f\bar{f}$ , where  $f\bar{f} = e^+e^-$ ,  $\mu^+\mu^-$ , or hadrons (obtained from quark pairs  $q\bar{q}$ ). We require that  $h_D$  decays before the BBN, *i.e.*,  $\tau_{h_D} \lesssim 0.1$  s. In fact, the  $h_D$  lifetime is often even shorter, lying within the reach of the intensity frontier searches for light new physics.

Before discussing the phenomenological aspects of our scenario, let us go back to the issue of the vanishing of the kinetic mixing terms in Eq. (7.4.2) that are proportional to  $\epsilon'$  and  $\epsilon''$ . In general, even if there is no such kinetic mixing between the hypercharge and the dark photon field-strength tensors at the tree level, it can be generated at the loop level [263, 264] if the charge conjugation symmetry is also broken in the DS [265]. To obtain this symmetry breaking, one can either introduce a new particle (or several new particles) that is charged under both the SM and the dark gauge groups, or introduce interactions in the DS that break this symmetry, analogous to the SM, where weak interactions are responsible for the charge conjugation symmetry breaking. Otherwise, there can be no perturbative generation of a kinetic mixing term [265].

In the model considered here there is no such symmetry breaking and therefore non-zero kinetic mixing can only occur at the tree level. This can also be seen directly because for each loop diagram that a priori could contribute to generation of kinetic mixing, there exists the same diagram but with the particle flow reversed, corresponding to virtual antiparticles, and the contributions of the two diagrams cancel in pairs. Thus, in the following we will assume a negligible kinetic mixing which is not regenerated perturbatively. In this way, we will also be able to avoid stringent terrestrial, astrophysical, and possible BBN constraints on light dark vectors [260, 480].

## 7.5 Relic density

We begin the discussion of the specific features of our model by examining the relic densities of the two DM components, the dominant  $\chi$  and the smaller  $\eta$  – for which we require  $\Omega_\chi h^2 + \Omega_\eta h^2 \simeq 0.12$  [18] – and the abundance of the unstable long-lived dark vector  $A'$ . To this end, we numerically solve a set of Boltzmann equations which extend the well-known assisted freeze-out mechanism introduced

---

correspond to only narrow regions of the parameter space of the model studied in Section 7.7. The similar process involving two identical scalars in the final state, *e.g.*, dark Higgs bosons, is also excluded by angular momentum conservation and Bose symmetry. Such decay would involve the initial state particle with  $J = 1$  and two identical real scalar bosons in the final state that due to Bose statistics must have even  $J$ .

for the coupled two-component DM scenario [481] to compute the relic densities of the three dark species

$$\begin{aligned} \frac{dY_\chi}{dx} &= -\frac{\lambda_\chi}{x^2} \left( Y_\chi^2 - \frac{Y_\eta^2}{(Y_\eta^{\text{eq}})^2} (Y_\chi^{\text{eq}})^2 \right), \\ \frac{dY_\eta}{dx} &= -\frac{\lambda_\eta}{x^2} \left( Y_\eta^2 - (Y_\eta^{\text{eq}})^2 \frac{Y_{A'}^2}{(Y_{A'}^{\text{eq}})^2} \right) + \frac{\lambda_\chi}{x^2} \left( Y_\chi^2 - \frac{Y_\eta^2}{(Y_\eta^{\text{eq}})^2} (Y_\chi^{\text{eq}})^2 \right), \\ \frac{dY_{A'}}{dx} &= \frac{\lambda_\eta}{x^2} \left( Y_\eta^2 - (Y_\eta^{\text{eq}})^2 \frac{Y_{A'}^2}{(Y_{A'}^{\text{eq}})^2} \right) - \frac{\lambda_{A'}}{x^2} \left( Y_{A'}^2 - (Y_{A'}^{\text{eq}})^2 \right), \end{aligned} \quad (7.5.1)$$

where  $Y_i$  is the respective yield,  $i = \chi, \eta, A'$  and  $x = m_\eta/T$ .<sup>4</sup>

We stress again that we assume that the lifetime of the dark Higgs boson  $h_D$  is small enough for it to decay before the BBN era. The calculation of its abundance is therefore not needed in the following analysis.

The parameters  $\lambda_i$  are proportional to the annihilation cross sections of the main processes determining the abundances of species in the DS

$$\begin{aligned} \lambda_\chi &\equiv \frac{s(m_\eta)}{H(m_\eta)} \langle \sigma_{\chi\bar{\chi} \rightarrow \eta\bar{\eta}} v \rangle \simeq \frac{1.32 g_{*s}(m_\eta)}{\sqrt{g_*(m_\eta)}} m_\eta m_{\text{Pl}} \langle \sigma_{\chi\bar{\chi} \rightarrow \eta\bar{\eta}} v \rangle, \\ \lambda_\eta &\equiv \frac{s(m_\eta)}{H(m_\eta)} \langle \sigma_{\eta\bar{\eta} \rightarrow A'A'} v \rangle \simeq \frac{1.32 g_{*s}(m_\eta)}{\sqrt{g_*(m_\eta)}} m_\eta m_{\text{Pl}} \langle \sigma_{\eta\bar{\eta} \rightarrow A'A'} v \rangle, \\ \lambda_{A'} &\equiv \frac{s(m_\eta)}{H(m_\eta)} \langle \sigma_{A'A' \rightarrow h_D h_D} v \rangle \simeq \frac{1.32 g_{*s}(m_\eta)}{\sqrt{g_*(m_\eta)}} m_\eta m_{\text{Pl}} \langle \sigma_{A'A' \rightarrow h_D h_D} v \rangle, \end{aligned} \quad (7.5.2)$$

where  $s \equiv s(T)$  is the entropy density,  $H \equiv H(T)$  is the Hubble rate,  $m_{\text{Pl}} = 2.44 \times 10^{18}$  GeV is the reduced Planck mass, and  $g_{*s}(T)$  and  $g_*(T)$  denote the effective number of relativistic degrees of freedom for the entropy and energy densities of the thermalized SM-DS plasma, respectively. Moreover, we introduced the equilibrium comoving yields

$$Y_i^{\text{eq}}(x) = n_i^{\text{eq}}/s = \frac{g_i}{g_{*s}(x)} \frac{45}{4\pi^4} (r_i x)^2 K_2[r_i x], \quad (7.5.3)$$

where  $r_i = m_i/m_\eta$  and  $g_i$  is the number of internal degrees of freedom of particle  $i$ . The resulting relic density is obtained from the relation  $\Omega_i h^2 = (\rho_i/\rho_{\text{crit}}) h^2 = (s_0 Y_{i,0} m_i/\rho_{\text{crit}}) h^2$ , where  $s_0$  is the current entropy density and  $Y_{i,0}$  is the final yield of the dark species  $i$  after its freeze-out.

For the dominant heavy DM component  $\chi$ , an additional contribution to the total relic density can come from the  $2 \rightarrow 3$  processes  $\chi\bar{\chi} \rightarrow \eta\bar{\eta}A'$ . We take this into account in the results below by tuning the  $\mu_\chi$  and  $\mu_\eta$  parameters in Eq. (7.4.4) accordingly, and by modifying the heavy scalar mass  $m_\phi$ , so that the total pair-annihilation cross section of  $\chi$ s takes the thermal value. In the case of

<sup>4</sup>We solve the Boltzmann equations by doing a partial wave decomposition of the thermally averaged annihilation cross sections for each process,  $\langle \sigma v \rangle$ . Due to the large mass hierarchies between the three species, their thermal freeze-out temperatures are well separated which means that it is not necessary to take into account the full temperature dependence of  $\langle \sigma v \rangle$ .

$\eta$  relic abundance, the possible annihilation modes are into the  $A'A'$ ,  $h_D h_D$ , and  $A'h_D$  final states. As we will discuss below, it turns out that the allowed region of parameter space of the model which we study corresponds to large values of the dark coupling constant  $g_D \gtrsim 0.1$ . In this case the first of the aforementioned annihilation modes dominates. The coupling  $g_D$  must take such large values because it also determines the annihilation rate of dark photons into  $h_D h_D$  pairs. We require  $\langle\sigma v\rangle_{A'A'\rightarrow h_D h_D}$  to be up to a few orders of magnitude larger than the thermal value to suppresses the abundance of  $A'$ . We then avoid the strict limits resulting from the BBN, cf. Section 7.6.1. As a result, in the allowed region of the model parameter space, we typically find

$$\Omega_\chi h^2 \simeq 0.12 \gg \Omega_\eta h^2 \sim \Omega_{A'} h^2 . \quad (7.5.4)$$

We illustrate the evolution of the mass yield  $m_i Y_i$  for all the three dark species as a function of  $x$  on the left side of Fig. 7.5. In the plot, we fixed the masses in the DS as follows:  $m_\chi = 1.5$  TeV,  $m_\eta = 150$  GeV,  $m_{A'} = 20$  GeV,  $m_{h_D} = 250$  MeV, as well as we used the following values of the coupling constants in the Higgs sector:  $\lambda_{hh_D} = 10^{-4}$  and  $\lambda_{h_D\eta} = 4 \times 10^{-7}$ . This choice corresponds to benchmark scenarios discussed in Section 7.7. The remaining mass of the heavy scalar  $\phi$ , and the coupling constants  $\mu_\chi$  and  $\mu_\eta$  are chosen such that the annihilation cross section  $\langle\sigma v\rangle_{\chi\chi\rightarrow\eta\eta}$  achieves the thermal value.

As can be seen in the plot, the heavier DM species  $\chi$  freeze out within the DS almost independently of the evolution of the relic densities of the other two dark particles,  $\eta$  and  $A'$ . The heavy scalar relic density almost saturates the total DM abundance,  $\Omega_\chi h^2 \simeq 0.12$ , which justifies referring to it as secluded DM. Instead, the yield of both  $A'$  and  $\eta$  is much suppressed and it decreases with increasing the dark coupling constant  $g_D$ ,  $Y_{A'} \propto 1/\langle\sigma v\rangle_{A'A'\rightarrow h_D h_D} \propto g_D^{-4}$ , cf. Eq. (E.1.12). We illustrate this in the right panel of Fig. 7.5 which shows  $(mY)$  as a function of  $g_D$ . We also schematically show the BBN bounds which exclude too low values of the coupling constant  $g_D$ . This is because suppressed  $g_D$  leads to both an increased abundance of late decaying  $A'$  and its large lifetime,  $\tau_{A'} \propto 1/g_D^2$ , cf. Eq. (7.4.8). Such late-time decays of  $A'$ , and related energy and entropy injection around the BBN era, might distort successful predictions of light element abundances in the Universe. We defer the discussion of a more precise implementation of the BBN bounds in our analysis to Section 7.6.1. The CMB data constrain even larger lifetimes than BBN, leading to stringent bounds on the  $A'$  yield. As seen in the figure, both cosmological constraints become weaker for larger  $g_D$ . Interestingly, this simultaneously increases the sub-thermal  $2 \rightarrow 3$  annihilation cross section  $\chi\chi \rightarrow \eta\eta A'$  which is responsible for the DM ID signals in our model. Therefore, in this scenario, avoiding cosmological bounds naturally favors regions in model parameter space that can be probed in DM ID searches.

## 7.6 Current and future constraints from astrophysics, cosmology and colliders

While most of the DS species present in our model are secluded from the SM, their indirect couplings to the light dark Higgs boson  $h_D$  still induce interactions with

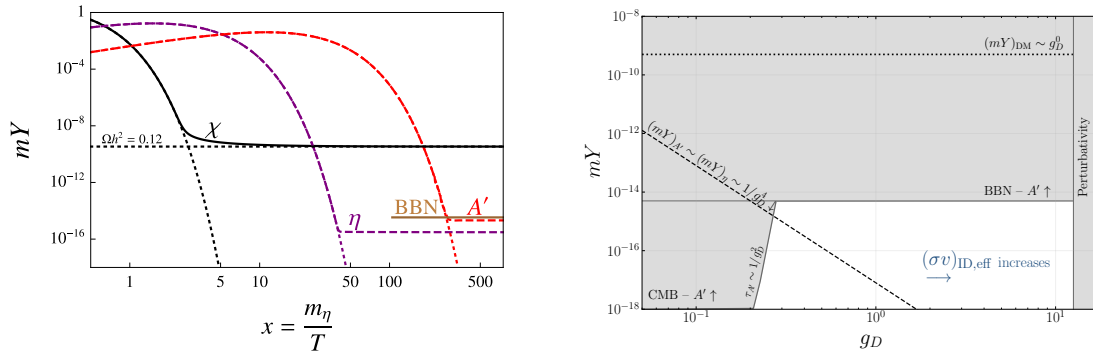


Figure 7.5: Left: Comoving energy densities,  $(mY)_i$ , for two-component DM and the unstable dark vector undergoing thermal freeze-out obtained by solving the Boltzmann equations Eq. (7.5.1). Right: A schematic plot of the unstable dark vector yield,  $(mY)_{A'}$ , as a function of the dark coupling constant  $g_D$  shown with the black dashed line. The regions constrained by the BBN and CMB bounds on very long-lived  $A'$ , and by a perturbativity bound are gray-shaded. The dominant DM yield,  $(mY)_\chi$ , is also indicated with the horizontal black dotted line on top of the figure. This yield is not constrained by the BBN bounds. The expected signal rates in DM indirect detection searches grow with increasing  $g_D$  as marked with blue color.

the visible sector, leading to experimental constraints which we review below.

### 7.6.1 Current bounds

**Accelerator-based searches** Light dark Higgs boson is one of the primary targets of intensity frontier searches for sub-GeV new physics as it corresponds to one of only a few available simple renormalizable portals to the DS. Based on the available data, upper bounds on the mixing angle  $\theta_{h_D H}$  can be put. Particularly relevant for our study are the constraints obtained from the E949 data on rare kaon decays [482] and from rare  $B$  meson decays at the LHCb [483, 484], as well as the results of beam-dump searches in the CHARM [485], MicroBooNE [486], and NA62 [487] experiments. We take them into account following [234, 322, 488–490].

**Astrophysical and cosmological bounds** Constraints on light dark scalars can also be derived from their impact on astrophysical and cosmological observations. In particular, we use the bounds derived from possible modifications of the supernovae cooling rate and the neutrino emission from SN1987A [491] and BBN constraints on late-time energy injections from decaying BSM species [480].

Important bounds are also associated with the metastable relic abundance of the long-lived dark vector  $A'$ . We implement them in accordance with [492] for the BBN constraints and [102] for the CMB bounds derived from the combined data from the *Planck* [18] and *COBE/FIRAS* [64] satellite experiments where we follow [102, 493, 494].

The DS richness of our model also offers very good prospects for discoveries of various BSM species in future searches. These include next-generation experiments

targeting light dark Higgs boson in a manner similar to that described in the previous paragraph, the upcoming intensity frontier searches for LLPs and the future CMB observations constraining the very long-lived  $A'$ .

### 7.6.2 Intensity frontier searches for light dark Higgs boson

Rare meson decays yield tight bounds on light, sub-GeV, dark Higgs bosons from various accelerator-based experiments run in the past. Similar future searches are expected to further constrain the available model parameter space. In particular, light dark Higgs bosons with mass range below the di-muon threshold,  $m_{h_D} < 2m_\mu$ , will be constrained by rare kaon decays in the KLEVER [234, 495] and KOTO step-2 [496] detectors, and in the next run of the NA62 experiment as discussed in [497]. Further limits for both light and slightly heavier scalars - but lying below the kaon threshold for the  $h_D$  production,  $m_{h_D} < m_K - m_\pi$  - can be obtained by Fermilab Short-Baseline Neutrino Program. We present the expected limits from the NuMI-ICARUS and BNB-SBND detectors following [489].

For the heavier dark Higgs boson, in mass range of the order of a few GeV, the most stringent future constraints should come from the displaced visible decays of  $h_{DS}$  produced in either beam-dump or collider experiments. Below we show future sensitivity reach contours for the proposed SHiP experiment at CERN SPS [258], as well as the LHC searches at Codex-b ( $300 \text{ fb}^{-1}$ ) [498, 499], FASER 2 [280, 284], and MATHUSLA [287, 288]. In addition, we also show the expected sensitivity resulting from searches for dark scalars in rare  $B$  meson decays in the Belle-II experiment [277, 278].

### 7.6.3 Dark matter detection

The parameters of our model can also be tested in experiments dedicated to DM searches. This is especially the case for ID searches for signatures induced by the dominant heavy DM component  $\chi$ . In this case, the discovery prospects depend on the DM annihilation rates. These, in turn, can depend on only the unsuppressed couplings present in the secluded dark sector and, therefore, they remain large. Instead, future DD searches are much less promising as they explicitly depend on the tiny interaction strength between the  $\chi$  and the SM particles which occur only via intermediate  $\phi$  and  $\eta$  species. The same is true for the lighter DM species  $\eta$  which has negligible relic abundance and suppressed couplings to light quarks. Below, we then focus on ID searches for the signatures induced by  $\chi$  DM. In particular, we discuss the relevant detection prospects in the future  $\gamma$ -ray observations that can lead to distinct phenomenological effects, as discussed above.

**Indirect detection of DM** In the model under study, ID signatures do not appear at the leading order, as the dominant  $2 \rightarrow 2$  annihilation channel,  $\chi\chi \rightarrow \eta\eta$ , produces invisible stable dark species  $\eta$ . Instead, it comes from the  $\chi$  annihilations at the next-to-leading order as a result of the  $2 \rightarrow 3$  process  $\chi\chi \rightarrow \eta\eta A'$  shown in Fig. 7.4. This is particularly important for the increasing value of the dark coupling constant  $g_D$  because larger values of  $g_D$  increases the chance of the final-

state  $A'$ -strahlung off the  $\eta$  leg, see Eq. (E.1.13) and Eq. (E.1.14). As we described above, cosmological and collider constraints also prefer such large values of  $g_D$ .

In our discussion, we focus on novel ID effects characteristic for our scenario. We enumerate three distinct features that distinguish it from the simplest secluded DM models: (i) it relies on the  $2 \rightarrow 3$  annihilation process which results in a continuous energy spectrum of the meta-stable  $A'$ , (ii) it uses multi-step cascade decays ultimately resulting in the photon flux, i.e., it relies on the decay  $A' \rightarrow h_D A''$ , followed by indirect production of  $\gamma$ -rays via the dark Higgs boson decays,  $h_D \rightarrow 4e, 4\mu, \text{hadrons} \rightarrow \gamma$ , see, *e.g.*, [473, 500] for a similar discussion; (iii) it leads to non-local DM ID effects occurring for the very long-lived  $A'$ . The first two features result in smearing of the spectrum (spectrum is softer) of the final state SM particles. This can be further affected by the non-local effects. In result, our model effectively avoids bounds from the searches for peaked spectral features in the positron data [218, 501]. Instead, the searches for a diffuse DM-induced  $\gamma$ -ray flux are a particularly promising way to study such a scenario. In our analysis, we employ the Einasto DM profile, already introduced in Eq. (6.4.1). The relevant photon flux is given by Eq. (7.3.2) in which the photon spectrum from  $2 \rightarrow 3$  annihilations of  $\chi$  and subsequent three-body and cascade decays of  $A'$  is denoted by  $(dN_\gamma/dE_\gamma)_\chi$ , cf. Appendix E.2 for further discussion of the technical details.

#### 7.6.4 Future Cosmic Microwave Background surveys

As mentioned in Section 7.6.1, CMB observations provide another complementary way to study our BSM scenario. In particular, future surveys are projected to significantly improve the bounds on CMB spectral distortions and essentially rule out BSM scenarios predicting mediator lifetimes between  $\tau_{A'} \sim 10^5$  s and  $10^{12}$  s. In result, the relict abundances of unstable, very long-lived species should be no greater than a small fraction of the total DM relict density,  $\Omega_{A'} \lesssim 10^{-6} \Omega_{\text{DM}}$ , but, depending on  $\tau_{A'}$ , even much more stringent limits,  $\Omega_{A'} \lesssim 10^{-12} \Omega_{\text{DM}}$ , can be derived. In contrast, for the CMB anisotropy data, the expected improvement over the current constraints is less spectacular, but will also result in tighter bounds by about a factor of a few in  $\Omega_{A'}$ , relevant for the large lifetime regime,  $\tau_{A'} > 10^{12}$  s. We emphasize that while the CMB data remain complementary to DM ID searches for intermediate mediator lifetimes  $\tau_{A'} \gtrsim 10^5$  s, they will be the best way to probe scenarios with extremely long-lived  $A'$ s that would predict significantly suppressed ID signals.

## 7.7 Results

Although the non-minimal content of our model results in 12 free parameters, cf. Section 7.4, the thermal history and the ID signal rates depend crucially on only a few of them. We therefore limit our discussion to only slices of this multidimensional parameter space, presenting the results of our analysis in the most convenient two-dimensional  $(m_{A'}, g_D)$  plane.

We show the results for three values of the dark Higgs boson mass:  $m_{h_D} = 20, 250, \text{ and } 500 \text{ MeV}$  which correspond to different dominant decays of  $h_D$ , into



value of the thermal relic density,  $\Omega_\chi h^2 \simeq 0.12$ , while  $\Omega_\eta h^2$  is negligible.

The values of the dark coupling constant  $g_D$  are a priori only constrained by the perturbativity bound which for simplicity we take to be  $g_D < 4\pi$ . On the other hand, the astrophysical, cosmological, and collider bounds discussed in Section 7.6.1 put limits on too low values of this coupling constant, effectively leading to the bound  $g_D \gtrsim 0.1$ . In particular, lower values of  $g_D$  would lead to an overabundance of  $A'$ , and its late-time decays would violate BBN and CMB limits. As we will see in the figures, collider bounds also affect the region of the parameter space with too low values of  $g_D$ . This is because for fixed  $m_{A'}$  and  $\lambda_{Hh_D}$  the mixing angle  $\theta_{h_D H}$  increases as  $g_D$  decreases,  $\theta_{h_D H} \simeq \lambda_{Hh_D} v_D v_{\text{SM}} / m_H^2 = \lambda_{Hh_D} m_{A'} v_{\text{SM}} / (m_H^2 g_D)$ , valid for  $m_{h_D} \ll m_H$ . Eventually, it reaches the level at which it has already been excluded in searches for the dark Higgs boson.

Finally, we also fix the dark coupling between the dark Higgs boson and the lighter scalar DM component  $\eta$ ,  $\lambda_{h_D \eta} = 4 \times 10^{-7}$ ,  $4 \times 10^{-6}$ , or  $4 \times 10^{-5}$ , in order that the lifetime of  $A'$  can be large enough to be of astrophysical relevance, cf. Eq. (7.4.8). We also fix the kinetic mixing parameter between the two dark vectors to the following small value:  $\tilde{\epsilon} = 10^{-6}$ . As we will discuss below, both of these choices do not violate current bounds, while allowing one to better illustrate non-standard aspects of the phenomenology of the model.

We show the results for the heaviest dark Higgs boson we consider,  $m_{h_D} = 500$  MeV, and for  $\lambda_{h_D \eta} = 4 \times 10^{-6}$  in the left panel of Fig. 7.6. The grayed areas are already excluded, and we denote the origin of the bounds by the appropriate labels. As can be seen, the allowed region of the model parameter space prefers the values of the dark coupling constant  $g_D$  exactly in the ballpark for future searches in the proposed Codex-b, FASER 2, MATHUSLA, and SHiP detectors, as well as in the range of the Belle-II experiment. For this mass of the dark Higgs boson, it decays dominantly into light quarks that hadronize into pion pairs, including neutral pions that decay into two photons. This leads to a sizable ID signal in  $\gamma$ -ray searches. In gray we highlight the upper bounds obtained from null searches for DM signals in dwarf galaxies performed by Fermi-LAT following [214, 502]. Importantly, this limit places a constraint on excessively large values of the dark coupling constant  $g_D$ , which correspond to a too strong predicted ID signal rate. Note that for lower values of the dark photon mass,  $m_{A'} \lesssim 10$  GeV, ID bounds quickly decrease with the increasing dark vector lifetime - which is one of the effects of non-local ID effects discussed in Section 7.6.3. However, this region of the parameter space is constrained in part by the past CMB surveys, as indicated by the appropriate limits. This corresponds to a very large lifetime regime of the dark vector.

For smaller values of the dark vector lifetime, additional bounds can be obtained in future DM ID searches with CTA. We show the corresponding sensitivity curve with a purple dotted contour that bounds the region of the parameter space above the line. This corresponds to photon flux coming from the region around the GC with  $0.3^\circ < |b| < 1^\circ$  and  $|l| < 1^\circ$ . In this case the projected CTA sensitivity also becomes weaker in the limit of increasing  $\tau_{A'}$ . It is worth noting that in the large lifetime regime, complementary probes of the model will be available thanks to future CMB surveys. These may cover parts of the allowed region of the parameter space of the model below the dotted red and

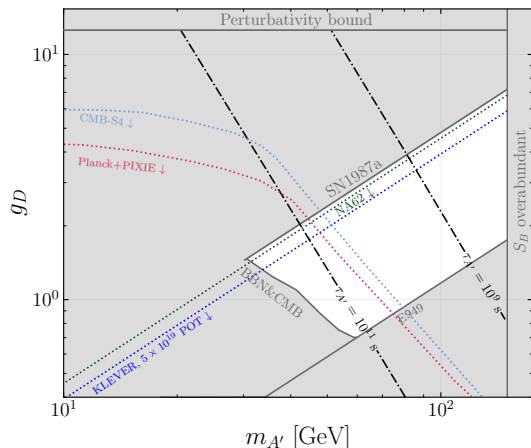


Figure 7.7: Same as the left panel of Fig. 7.6 but for different values of the fixed parameters:  $m_{h_D} = 20$  MeV,  $\lambda_{h_D\eta} = 4 \times 10^{-7}$  (left) and  $m_{h_D} = 250$  MeV,  $\lambda_{h_D\eta} = 4 \times 10^{-5}$  (right).

light blue lines corresponding to future data from *Planck* and PIXIE, respectively, as well as to the combined data from CMB-S4, LittleBIRD, and *PRISM* (labeled CMB-S4 in the figure), cf. Section 7.6.4.

In the right panel of Fig. 7.6, we compare the CTA bounds obtained when considering the non-local DM ID regime for large  $\bar{d}_{A'}$  with the one which does not properly take this effect into account. The latter sensitivity reach line is labeled “Standard” in the figure. As can be seen, the presence of non-local effects significantly weakens the impact of CTA on the model parameter space. This could be improved in studies focusing on larger RoIs, as schematically illustrated in the figure for the RoI characterized by  $|b|, |l| < 12^\circ$ . Although we expect the sensitivity reach lines obtained for the larger RoI to be shifted relative to those obtained for the smaller region around the GC, in the figure, for illustration, we have artificially rescaled the reach for  $|b|, |l| < 12^\circ$ . This is to match the standard sensitivity reach lines in the small lifetime regime of  $A'$  and to better highlight the relative difference in the non-local effect in the two cases that appear for increasing  $\tau_{A'}$ . For the larger RoI the weakening of the bounds is only seen for much smaller values of  $m_{A'}$  that lead to larger values of  $\bar{d}_{A'}$ . Instead, for smaller decay lengths, the dark vector typically does not escape the larger RoI before decaying and its signal remains unsuppressed. Interestingly, the anisotropy effects discussed in Section 7.6.3 lead to a mild improvement in the expected CTA sensitivity near  $m_{A'} \simeq (3 - 4)$  GeV.

In Fig. 7.7 we present similar bounds for  $m_{h_D} = 20$  and 250 MeV in the left and right panels, respectively. We also fix the value of the coupling constant in the Higgs sector,  $\lambda_{h_D\eta} = 4 \times 10^{-7}$  and  $4 \times 10^{-5}$  in the left and right panel, respectively. As expected from Eq. (7.4.8), a larger  $\lambda_{h_D\eta}$  implies a smaller  $A'$  lifetime. As a result, for increased  $\lambda_{h_D\eta}$  the cosmological limits constrain smaller fractions of the available parameter space, and the corresponding bounds are shifted towards smaller values of the dark vector mass. This can be observed by comparing the size of the currently excluded gray-shaded regions in both panels. In both cases, CTA will not probe the allowed region of the model parameter space. This is due to a relatively softer  $\gamma$ -ray spectrum produced after the dark Higgs boson decay into

the leptonic final states,  $e^+e^-$  and  $\mu^+\mu^-$  for  $m_{h_D} = 20$  and 250 MeV, respectively. Instead, collider searches and CMB surveys will provide complementary coverage of such scenarios.

In the left panel of Fig. 7.7 where  $m_{h_D} = 20$  MeV, the currently allowed region of the parameter space of the model is bounded by supernova SN198a and NA62 bounds on the dark Higgs boson, and by the BBN and CMB constraints on long-lived  $A'$ . In this case,  $h_D$  decays mainly into electrons and has a large lifetime, beyond the reach of high intensity frontier experiments targeting displaced LLP decays. However, one can search for it in rare kaon decays. In particular, we project the future bounds from the KLEVER and NA62 detectors to cover almost the whole allowed parameter space. In turn, the future CMB bounds only cover the regions below the dotted red and light blue lines which corresponds to  $m_{A'} \lesssim$  a few GeV.

The heavier dark Higgs boson with  $m_{h_D} = 250$  MeV (the right panel of Fig. 7.7) decays dominantly into a pair of muons and therefore has a much smaller lifetime, determined by its couplings to the SM fermions similar to the Yukawa couplings. Consequently, in this case, much of the parameter space can be explored by the future intensity frontier, neutrino experiments, and at collider detectors. The complementarity of these searches with future CMB surveys will thus lead to the exploration of a large region in the  $(m_{A'}, g_D)$  plane over a wide range of  $A'$  lifetimes.

## 7.8 Conclusions

Most studies of light sub-GeV portal to date have focused on simplified frameworks with only a limited number of new species added to extend the SM. Although this approach allows for easy comparison of multiple experimental proposals, new effects can be observed in more elaborate, and more realistic, models with a larger number of BSM species, perhaps with an extended mass hierarchy. We studied such a rich DS model containing both light, sub-GeV species and particles with masses up to 10 TeV or so. In particular, we invoke a heavy scalar DM with the mass above the TeV scale and a potentially very long-lived dark vector mediator that is secluded from the SM.

This scenario remains beyond the reach of current and near-future DD searches. However, in this chapter we have shown that perhaps the best way of probing this type of model, in addition to the intensity frontier searches for LLPs, is to employ DM-induced signatures in both future ID and CMB experiments. We illustrated this for the very long-lived dark vector  $A'$  which can decay at kpc-size distance from its production point. This can lead to interesting non-local effects in the DM ID searches. In particular, one can expect a larger than typical discrepancy between the prospects for DM detection in ID observations employing small regions in the Galaxy and beyond, e.g. in dwarf galaxies, and such searches in extensive RoIs. When compared to traditional WIMP DM searches, in certain regions of the parameter space of the model that we studied, one can observe an increased intensity of the DM signal from the GC and a simultaneous suppression of the corresponding rates expected from dwarf galaxies. Similarly, the DM-induced  $\gamma$ -ray flux may in this case be characterized by a distinct morphology that does not

necessarily follow the true DM density distribution.

While the models predicting the existence of heavy WIMP DM candidates and scenarios with light, sub-GeV degrees of freedom have been extensively studied in the literature in recent years, the phenomenological consequences of their simultaneous presence in BSM models is much less explored. Careful tests of such scenarios will require a multi-messenger approach employing both accelerator-based searches and astrophysical observations. Further surprising effects might also be revealed in DM ID studies. In particular, the traditional approach to DM ID might have to be modified to better explain the data, *e.g.*, observations of both small and large RoIs around the GC may lead to significant differences in expected photon fluxes. If such differences were to be observed, it could mean the simple WIMP-like scenarios studied so far would need to be extended to incorporate additional light and very long-lived BSM particles that can play the role of the mediators between the SM and DS.



# Chapter 8

## Self-interacting dark matter and the Hubble tension

### 8.1 Introduction

In this chapter, we continue to explore rich dark sector models that contain particles spanning several orders of magnitude in their mass. Specifically, we consider a dark sector comprised of self-interacting DM and a light vector mediator - which provides the sufficiently strong DM self-interactions - connected to the SM through a dark Higgs portal. We focus on the cosmological impact of such a scenario - which could be related to several recently uncovered observational anomalies - therefore, we concentrate on constraints from indirect searches for new physics, including CMB and other astrophysical and cosmological data.

The  $\Lambda$ CDM model assumes that DM behaves as a cold, non-interacting, pressureless fluid. As discussed in Chapter 2, this simple approach leads to remarkably successful description of the Universe at large scales. At smaller scales, however, serious discrepancies have been observed between theoretical predictions based on such assumptions and observations [77]. Some of the most significant problems are listed and discussed in Section 2.3.2.

Moreover, recent advances in observational cosmology allowed to identify other tensions within the  $\Lambda$ CDM scenario, see [19, 503, 504] for recent reviews of these problems, most notably the discrepancy between different measured values of the Hubble rate parameter,  $H_0$  [19, 20, 24, 505], and, to a lesser extent, of the “clumpiness” parameter,  $S_8 = \sigma_8 (\Omega_{\text{matter}}/0.3)^{0.5}$ , where  $\sigma_8$  is the power spectrum amplitude on the scale of  $8h^{-1}$  Mpc [25, 506, 507], which is the scale of galaxy clusters.

It is therefore interesting to consider *modification of only the DM component of the Universe as a solution to both small and large-scale problems of  $\Lambda$ CDM*. In light of this, we study a new mechanism for SIDM production via decays of heavy messenger state into SIDM and, to a lesser extent, also into dark radiation (*e.g.*, through higher-order processes that are phase-space or loop suppressed) that occur after the recombination. The model that we discuss provides

---

The contents of this chapter is based on: A. Hryczuk and K. Jodlowski, *Self-interacting dark matter from late decays and the  $H_0$  tension*, *Phys. Rev. D* **102** (2020) 043024, [2006.16139].

another illustration of the interplay between light and heavy new physics with potentially fundamental phenomenological consequences for ongoing observations and experimental searches.

## 8.2 Hubble tension and other selected problems in the $\Lambda$ CDM model and astroparticle physics

Before we present the details of our BSM scenario, we first introduce the most relevant observational and experimental anomalies for our study. As we described in Section 2.3.2,  $\Lambda$ CDM model has long-standing small-scale structure problems. A popular solution of them invokes sufficiently strong DM self-interactions, which we will discuss in more detail in the next section.

We begin by discussing other recent problems and anomalies that may also point to the need of modifying the  $\Lambda$ CDM model or to the existence of some other BSM physics. While the list of such potential anomalies identified in recent years can be quite extensive, cf. recent reviews [26, 508, 509], we will focus on the ones that are directly related to our discussion in the remaining part of this chapter.

**Hubble tension** The current expansion rate of the Universe,  $H_0$ , is accurately determined from direct observations of the local Universe based on the cosmic distance ladder constructed from BAO and Supernovae (SNe) data. As shown in Fig. 8.1, such model-independent observations yield  $H_0 \cong 74 \pm 1$  km/s/Mpc, which is much larger than  $H_0 \cong 67 \pm 0.5$  km/s/Mpc, the value obtained from indirect measurements, *e.g.*, those employing CMB anisotropy and BAO data, and assuming the validity of  $\Lambda$ CDM to extrapolate the expansion rate from the early period to the present.

The systematic errors are believed not to be the source of the tension, as: (i) the largest uncertainty is associated with the local measurements using the distance ladder, and not *Planck* observations, however, recent study which used the data collected by the SH0ES collaboration, [510], showed the robustness of the distance ladder method; (ii) the explanation of the  $H_0$  tension without invoking new physics would require several uncorrelated errors to be present in the current analysis [511].

As a result, the BSM explanations have been proposed to address the tension. In particular, it has been shown, *e.g.*, [513–515] that converting a small fraction of DM energy into radiation at late times significantly increases the present-day Hubble rate, the  $H_0$  constant; see also the updated analyses collected in recent reviews of Hubble tension solutions [396, 511]. Such processes *reduce the matter density at late times* and thus increase the present-day Hubble rate,  $H_0$ , with respect to the  $\Lambda$ CDM predictions. This can be easily seen by considering the angular size of the last scattering surface [503],

$$\theta_s = \frac{r_s}{D_A}, \tag{8.2.1}$$

## 8.2. HUBBLE TENSION AND OTHER SELECTED PROBLEMS IN THE $\Lambda$ CDM MODEL AND ASTROPARTICLE PHYSICS

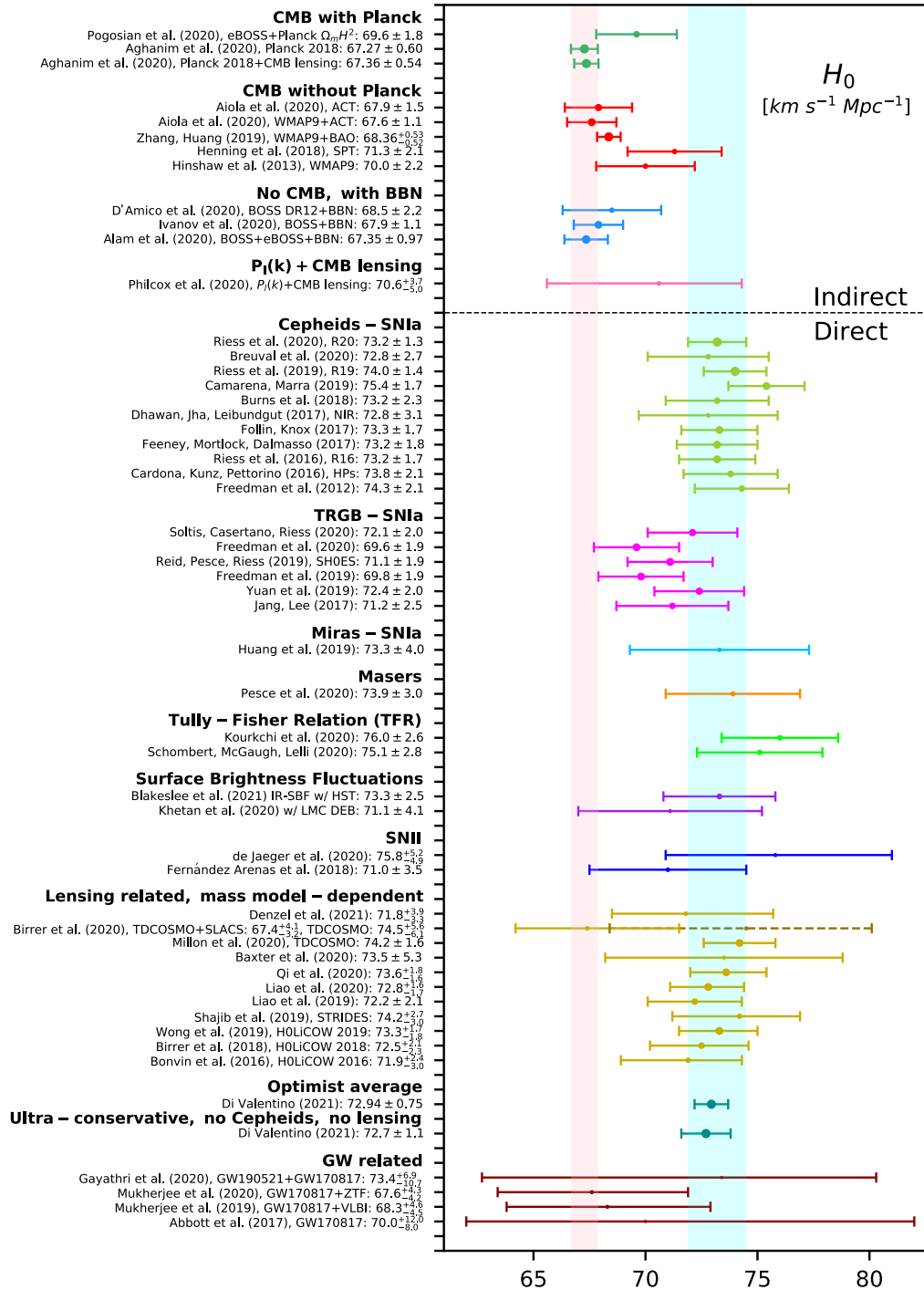


Figure 8.1: Combined results of experiments determining  $H_0$ . Note the significant discrepancy between the values obtained by the late-Universe observations (e.g., SH0ES [512]) indicated by cyan vertical band and the early-Universe (pre-recombination) observations (e.g., Planck [18]) indicated by the light pink vertical band. All values were determined under the assumption of the  $\Lambda$ CDM model. Taken from [511], where one can find an extensive discussion and a list of the relevant references.

where

$$r_s = \int_0^{t_{\text{recomb}}} \frac{c_s(t) dt}{a(t)} \cong \frac{1}{H_{\text{recomb}}} \int_0^{t_{\text{recomb}}} \frac{c_s(t) dt / t_{\text{recomb}}}{[\rho(t) / \rho(t_{\text{recomb}})]^{1/2}} \quad (8.2.2)$$

is the size of the baryon-photon sound horizon, and

$$D_A = \int_{t_{\text{recomb}}}^{t_{\text{present}}} \frac{cdt}{a(t)} \cong \frac{c}{H_0} \int_{t_{\text{recomb}}}^{t_{\text{present}}} \frac{cdt / t_{\text{present}}}{[\rho(t) / \rho_0]^{1/2}} \quad (8.2.3)$$

is the angular diameter distance to the last scattering surface. From these equations we obtain the following expression:

$$H_0 = H_{\text{recomb}} \frac{\int_{t_{\text{recomb}}}^{t_{\text{present}}} \frac{cdt / t_{\text{present}}}{[\rho(t) / \rho_0]^{1/2}}}{\int_0^{t_{\text{recomb}}} \frac{c_s(t) dt / t_{\text{recomb}}}{[\rho(t) / \rho(t_{\text{recomb}})]^{1/2}}}, \quad (8.2.4)$$

where  $\rho(t)$  is the total energy density of the Universe at time  $t$  and  $\rho_0 = \rho(t_{\text{present}})$ , while  $c_s$  is the speed of the sound wave. Clearly,  $H_0$  will increase if one:

- decreases energy (*e.g.*, matter) density at late times (late-time solutions) or
- decreases the sound speed in the early Universe (early-time solutions).

This observation has been used by many proposed mechanisms, see [396, 511] for up-to-date catalog of solutions. However, there is currently no consensus on the preferred solution. On the other hand, it has been understood that late-time solutions seem to be disfavored by the data [503, 516, 517] due to stringent BAO, CMB, and SNe observations.

For example, as it was understood after our initial study had been published [3] a decaying dark matter (DCDM) solution similar to the one described below, would not only decrease the sound horizon of the last scattering - which increases  $H_0$  (as desired) - but the amount needed to fully resolve these tensions would also severely decrease the photon diffusion damping scale, leading to an unacceptably worse fit to large  $l$  part of the CMB spectrum. In order for the scenario discussed below to fully address the Hubble tension, one should then also allow for an additional mechanism to improve the CMB fit which, however, goes beyond the scope of our analysis.

**$S_8$  tension** A similar deviation from the  $\Lambda$ CDM comes from the determination of the matter energy density  $\Omega_m$  and the amplitude of the power spectrum on the scale of  $8h^{-1}$  Mpc,  $\sigma_8$ . Combining those parameters together, one obtains the parameter  $S_8 = \sigma_8 (\Omega_{\text{matter}}/0.3)^{0.5}$ , which is constrained by the *Planck* data [506], redshift surveys [518, 519], and weak lensing measurements [507, 520]. The discrepancy takes place between the results obtained by the *Planck* collaboration, which points towards a smaller value of  $S_8$  (and thus less structure in the Universe at the  $8h^{-1}$  Mpc scale), and the other aforementioned observations that prefer a larger value of  $S_8$ . The  $S_8$  discrepancy is less statistically significant ( $\sim 2\sigma$ ) than the Hubble tension ( $\sim 4\sigma$ ), as it is potentially susceptible to various less understood systematic errors - see Fig.9 in [521] and discussion therein. One of the natural solutions of the  $S_8$  tension is again DCDM [522], as it obviously reduces the matter density at late times - see also recent review [523] for other proposals and extensive discussion.

**Supermassive black hole formation puzzle** Observation of very old,  $z \gtrsim 7$ , and very massive,  $M_{\text{SMBH}} > 10^9 M_{\text{Sun}}$ , SMBHs [524–526], poses a challenge to the standard theory of black hole formation. In the standard picture, a massive black hole originates as a much smaller compact object, called progenitor, which has a mass of  $M_{\text{SMBH}} > 10 M_{\text{Sun}}$  and grows by accretion of the rotating baryonic matter surrounding it and by merging with other black holes [527, 528]. However, due to the Eddington limit, which is a bound on the rate of accretion derived from the balance between gravitational pull and radiative pressure, there would not be enough time for black holes to form as large as observed by  $z \gtrsim 7$  [529], see also recent review [530] for extensive discussion of the problem and the possible solutions.

One of them is based on the gravothermal collapse of a small halo of ultra SIDM  $\chi$  [531, 532], which can occur much faster than accretion, and forms an initial seed for accelerating the growth of SMBHs.<sup>1</sup> The ultra SIDM regime is defined as  $\sigma_{\text{tr}}/m_\chi \gtrsim 10^3 \text{cm}^2/g^2$  of much stronger self-interactions than allowed by the bound given in Eq. (3.2.2). Therefore, to evade this bound, one needs to consider multi-component DM model in which the abundance of ultra SIDM can be only a fraction, of the order  $\lesssim 10\%$ , of total DM energy density. For discussion of this problem within our model, see Section 8.6.3.

**XENON1T and horizontal branch stars cooling anomalies** Recently, the XENON1T experiment [534] reported an unaccounted excess of events over the background in electronic recoils around 1–7 keV with  $\sim 3\sigma$  significance. The collaboration studied various hypotheses for the origin of the anomaly, like unaccounted  $\beta$  decays of tritium (without invoking new physics), as well as solar axion and neutrino magnetic moment, which are BSM scenarios. Another promising explanation of this excess invokes [535] a light,  $\sim 1$  keV, dark photon coupled to the SM via the kinetic mixing term  $-\frac{\kappa}{2} F_{\mu\nu} F'^{\mu\nu}$ .<sup>3</sup> The result of that paper is that both the XENON1T excess and observations of cooling anomalies in horizontal branch stars [536–538] could be explained by such light dark photon with the kinetic mixing parameter  $\kappa \sim 10^{-15}$ . Such mixing makes the dark photon unstable, however, its lifetime is much greater than the age of the Universe, evading the BBN and CMB bounds, see. Section 7.6.4. It turns out, that our model, described by Eq. (8.4.2), can easily accommodate for such dark photon, including the case where one can simultaneously explain small-scale problems of  $\Lambda$ CDM,  $H_0$  tension, the XENON1T anomaly, and observations of cooling anomalies in horizontal branch stars.

---

<sup>1</sup>In fact, this mechanism was inspired by the ordinary gravothermal collapse, which is believed to be responsible for the formation of globular clusters [533].

<sup>2</sup>See Eq. (3.2.1) for the definition of  $\sigma_{\text{tr}}$ .

<sup>3</sup>We used  $\kappa$  as a kinetic mixing parameter because  $\epsilon$  in this chapter is used as a  $Z_2$  symmetry breaking parameter, cf. Eq. (8.4.2).

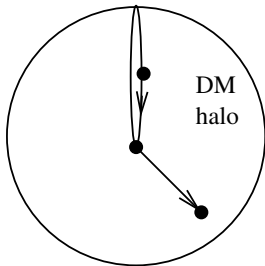


Figure 8.2: A DM particle in the central region of the DM halo is ejected from it due to the scattering with an energetic outer DM particle. Such dark matter self-interactions result in a core-like DM density profile near the center of the halo, as favored by observations (“cusp vs. core” problem). Taken from [541].

### 8.3 Dark matter self-interactions

Dark matter self-interactions are known to give better fits to galactic-scale data than the  $\Lambda$ CDM model, see Section 2.3.2, as shown in N-body simulations [539, 540], due to *efficient energy transfer between SIDM particles* ( $\chi$ 's), which does not occur for cold DM. We illustrate this mechanism schematically in Fig. 8.2. For further discussion of the astrophysical and cosmological impact of the SIDM model, see a recent review [189].

One can estimate the strength of self-interactions required to influence the macroscopic properties of DM halos by comparing the scattering rate with the Hubble rate [541], which corresponds to the condition that at least one DM interaction per particle took place in the lifetime of the Universe,

$$\Gamma = n\sigma_{\text{tr}}v = \frac{\rho}{m_\chi}\sigma_{\text{tr}}v \sim H, \quad (8.3.1)$$

where  $n$  is the SIDM number density,  $\sigma_{\text{tr}}$  is the transfer cross section (see Eq. (3.2.1)), and  $m_\chi$  is the SIDM mass. The preferred value of the transfer cross section is [38]

$$\frac{\sigma_{\text{tr}}}{m_\chi} \sim (0.1-1) \frac{\text{cm}^2}{\text{g}} \left( \frac{0.1-1 \text{ GeV/cm}^3}{\rho} \right) \left( \frac{10 \text{ km/s}}{v} \right), \quad (8.3.2)$$

which is compatible with cluster scales observations, such as the Bullet Cluster [251] - see Section 3.2.

The required strength of DM self interactions translates into a sizable cross section of the order of  $\sigma_{\text{tr}}/m_\chi \sim 1\text{cm}^2/\text{g} \approx 2 \text{ barn}/\text{GeV}$ . For illustration, in the case of a  $m_\chi \sim 100 \text{ GeV}$  neutralino (an outstanding WIMP DM candidate discussed in Chapter 6), self-interactions arise due to a  $Z$  boson exchange and lead to the value of the cross section suppressed by many orders of magnitude with respect to the SIDM benchmark,  $\sigma_{\text{tr}}/m_\chi \sim (g^4 m_\chi)/m_Z^4 \sim 10^{-14}\text{cm}^2/\text{g}$  strength. Therefore, to obtain sizable DM self-interaction cross sections, one typically postulates the existence of a *new light mediator* particle with distinct phenomenological consequences.

The DM self-interaction cross section used in N-body SIDM simulations is the transfer cross section,  $\sigma_{\text{tr}}$ , defined by Eq. (3.2.1). Assuming the differential cross

section,  $d\sigma/d\Omega$ , can be expressed by the partial waves expansion,

$$\frac{d\sigma}{d\Omega} = \frac{1}{k^2} \left| \sum_{\ell=0}^{\ell_{max}} (2\ell + 1) e^{i\delta_\ell} P_\ell(\cos\theta) \sin\delta_\ell \right|^2, \quad (8.3.3)$$

where  $\delta_\ell$  is the phase shift of the partial wave  $\ell$ , the  $\sigma_{tr}$  can be easily calculated:<sup>4</sup>

$$\begin{aligned} \sigma_{tr} &= \int d\Omega (1 - \cos\theta) \frac{d\sigma}{d\Omega} \\ &= \frac{4\pi}{k^2} \sum_{\ell=0}^{\ell_{max}} [(2\ell + 1) \sin^2 \delta_\ell - 2(\ell + 1) \sin\delta_\ell \times \\ &\quad \times \sin\delta_{\ell+1} \cos(\delta_{\ell+1} - \delta_\ell)]. \end{aligned} \quad (8.3.4)$$

To determine  $\sigma_{tr}$ , one therefore needs to determine the phase shifts,  $\delta_\ell$ , which requires solving the Schrödinger equation (in one dimension) for the radial wave function  $R_\ell(r)$  of the reduced  $\chi$ - $\chi$  system,

$$\frac{1}{r^2} \frac{d}{dr} \left( r^2 \frac{dR_\ell}{dr} \right) + \left( k^2 - \frac{\ell(\ell+1)}{r^2} - 2\mu V(r) \right) R_\ell = 0, \quad (8.3.5)$$

where  $v$  is the relative velocity of the system,  $\mu = m_\chi/2$  is the reduced mass, and  $k$  is the total momentum,  $k = \mu v$ . In the following, we will assume that the potential,  $V(r)$ , arises from gauge interactions of the light mediator,  $A^\mu$ , coupled to  $\chi$  with a coupling strength  $\alpha_\chi = g^2/(4\pi)$ , cf. Eq. (8.4.2). The result is a Yukawa-type potential

$$V(r) = \pm \frac{\alpha_\chi}{r} e^{-m_A r}. \quad (8.3.6)$$

We consider a vector mediator, so the interactions between the two DM particles are attractive for the  $\chi\bar{\chi}$  scattering, i.e., they correspond to the minus sign in front in Eq. (8.3.6) ( $-$ ). Instead, they are repulsive ( $+$ ) for the  $\chi\chi$  or  $\bar{\chi}\bar{\chi}$  scatterings. Following [543], we take the total interaction cross section to be the average of the attractive and repulsive interactions.

Far from the range of the Yukawa potential, Eq. (8.3.5) has a well-known solution in terms of the spherical Bessel functions  $j_\ell(r)$  and  $n_\ell(r)$  (for definitions and properties of the spherical Bessel functions see, *e.g.*, sec. 10.47 in [169])

$$\lim_{r \rightarrow \infty} R_\ell(r) \propto \cos\delta_\ell j_\ell(kr) - \sin\delta_\ell n_\ell(kr) \quad (8.3.7)$$

Eq. (8.3.5) should be solved numerically for  $a \leq r \leq b$ , where  $a$  is a positive number close to 0 and  $b$  is a positive number which is large enough that the Yukawa potential can be neglected for  $r \sim b$ . We also require that the numerical solution matches the analytical solution at  $r = b$  which uniquely determines the phase shift  $\delta_\ell$ .

In our study, we have obtained the numerical solution to the Schrödinger equation with the use of the Numerov's method [544, 545] which is a fourth-order

---

<sup>4</sup>In estimating the force acting between two DM particles due to the elastic scatterings at present-day velocities,  $v \sim 10^{-3}$ , we use the standard numerical procedure for solving the Schrödinger equation described in [542, 543].

linear method with a fixed step size  $h = (b - a)/n$ , where  $n$  is the number of points in the grid. The boundary points,  $a$  and  $b$ , are determined by requiring that at a Eq. (8.3.5) is dominated by the centrifugal term, which means that  $a \ll \frac{1}{m_A}, \frac{\ell+1}{\mu v}$ . The upper bound,  $b$ , is determined by requiring that the potential term is much smaller than the kinetic term:  $\frac{\alpha_\chi}{b} e^{-m_A b} \ll \frac{\mu v^2}{2}$ . The phase shift is determined by the matching which leads to the following expression [546]:

$$\tan(\delta_\ell) = \frac{j_\ell(k(b-h))R_\ell(b) - j_\ell(kb)R_\ell(b-h)}{n_\ell(k(b-h))R_\ell(b) - n_\ell(kb)R_\ell(b-h)}, \quad (8.3.8)$$

where  $R_\ell$  is the numerically obtained wave function and  $j_\ell, n_\ell$  are spherical Bessel functions.

We calculate the resulting phase shifts until  $\sigma_{\text{tr}}$  determined by Eq. (8.3.4) converges. This is obtained if the consecutive values of  $\sigma_{\text{tr}}$  obtained for  $\ell_{\text{max}}$  and  $\ell_{\text{max}} \rightarrow \ell_{\text{max}} + 1$  differ by less than 0.1%.

We note that obtaining the *numerical solution is absolutely necessary only in the resonant regime*, which occurs when  $\frac{\alpha_\chi m_\chi}{m_A} \gtrsim 1$ . In other regions of the parameter space analytical formulas can be used to speed up the numerical scan. These can be obtained either from the perturbative expansion in  $\alpha_\chi$  - the so-called Born regime [547] which applies when  $\frac{\alpha_\chi m_\chi}{m_A} \ll 1$  - or from classical charged particle calculations. The other, so-called classical regime [547–550] applies when  $\frac{vm_\chi}{m_A} \gg 1$ .

The analytical solution to the Schrödinger equation in the Born regime does not depend on the sign of the potential, and the following formula holds for both attractive and repelling potentials:

$$\sigma_{\text{tr}}^{\text{Born}} = \frac{8\pi\alpha_\chi^2}{m_\chi^2 v^4} \left( \log(1 + m_\chi^2 v^2 / m_A^2) - \frac{m_\chi^2 v^2}{m_A^2 + m_\chi^2 v^2} \right). \quad (8.3.9)$$

The same is not true in the classical regime. For the attractive potential, the relevant cross section is

$$\sigma_{\text{tr}}^{\text{clas}} = \begin{cases} \frac{4\pi}{m_A^2} \beta^2 \ln(1 + \beta^{-1}) & \beta \lesssim 10^{-1} \\ \frac{8\pi}{m_A^2} \beta^2 / (1 + 1.5\beta^{1.65}) & 10^{-1} \lesssim \beta \lesssim 10^3 \\ \frac{\pi}{m_A^2} (\ln \beta + 1 - \frac{1}{2} \ln^{-1} \beta)^2 & \beta \gtrsim 10^3, \end{cases} \quad (8.3.10)$$

while for the repulsive potential the following equation holds:

$$\sigma_{\text{tr}}^{\text{clas}} = \begin{cases} \frac{2\pi}{m_j^2} \beta^2 \ln(1 + \beta^{-2}) & \beta \lesssim 1 \\ \frac{\pi}{m_j^2} (\ln 2\beta - \ln \ln 2\beta)^2 & \beta \geq 1, \end{cases} \quad (8.3.11)$$

where  $\beta \equiv 2\alpha_\chi m_A / (m_\chi v^2)$ . We find a good agreement between numerical results and analytic formulas, where they apply.

**Dark matter self-interaction regimes** The above procedure leads to the determination of the strength of DM self interactions which can span many orders of magnitude in the predicted cross section. In the simplest description, this is determined by two free parameters - the coupling  $g$  between the DM species,

which defines the parameter  $\alpha_\chi = g^2/4\pi$ , and the light mediator mass  $m_A$ . In the classical regime the relevant cross section can be obtained with Eqs. (8.3.10) and (8.3.11), in the perturbative regime we follow Eq. (8.3.9), while the resonant regime requires using numerical methods. Of particular phenomenological interest are the two regions we will focus on:

- The first occurs for  $\sigma_{\text{tr}}/m_\chi \in (10^{-1}, 10^1) \text{ cm}^2/g$ , which leads to momentum transfer rates in the preferred range required by small-scale structure problems of  $\Lambda\text{CDM}$ .
- The second is the so-called ultra SIDM regime with  $\sigma_{\text{tr}}/m_\chi \gtrsim 10^3 \text{ cm}^2/g$  which could solve the SMBHs formation puzzle in a two-component DM scenario with a subdominant ultra SIDM component, cf. Section 8.2.

Having introduced the main observational and experimental anomalies of our interest and a general framework of SIDM scenarios, we will now discuss an illustration of the proposed mechanism to ease the aforementioned tensions in the data in a concrete model based on the Higgs portal between the SM and dark sector particles.

## 8.4 The mechanism

The proposed mechanism for SIDM production is based on late decays of a scalar particle  $S$ , which freezes out from thermal plasma like ordinary WIMP DM, but is not absolutely stable due to broken symmetry (which in our case is the  $Z_2$  symmetry acting as  $S \rightarrow -S$ ). Late-time  $S$  decays populate the Universe with stable DM species  $\chi$  that are coupled with each other via a light vector mediator particle  $A'$ . Below, we discuss the benchmark of  $m_S = 1 \text{ GeV}$ , and  $\delta = 10^{-4}$ , where

$$\delta \equiv 1 - \frac{2m_\chi}{m_S} \quad (8.4.1)$$

is the dimensionless mass difference between the decaying  $S$  and its products.

An important part of this mechanism is that the dark sector species other than  $S$  never reach chemical equilibrium with the visible sector. As a result, the light, stable mediator is effectively absent from the plasma, evading the constraints imposed by CMB and indirect detection observations. Another view of the mechanism is that it is an extension of the Higgs portal freeze-in [551] or superWIMP [552] scenarios which employs even weaker couplings in the dark sector than assumed by these mechanisms.

The aforementioned symmetry breaking can be parametrized by a small parameter  $\epsilon$ . Its value is primarily responsible for the lifetime of  $S$ , see Eq. (8.5.1) below. Depending on the value of this lifetime, we can distinguish four different regimes in the model parameter space:

- 0)  $10^{-8} \lesssim \epsilon$  ( $S$  decays before BBN): a thermal self-interacting model which is subject to strong constraints due to the presence of the chemical equilibrium between the DS and the SM,

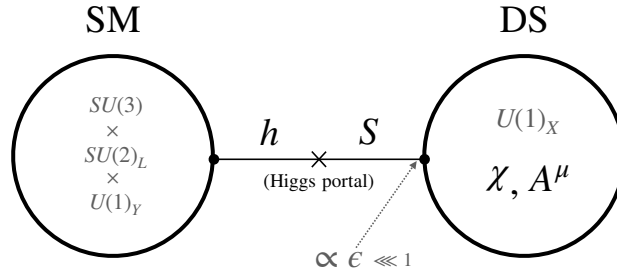


Figure 8.3: A simplified illustration of the model in which the proposed mechanism is implemented. The SM is connected to the DS via a Higgs portal mediator field  $S$ . We also introduce a Dirac fermion field  $\chi$  charged under spontaneously broken  $U(1)_{\text{dark}}$  (this symmetry breaking may, but does not have to be associated with the  $Z_2$  breaking), resulting in a massive vector  $A^\mu$ .

- A)  $10^{-13} \lesssim \epsilon \lesssim 10^{-8}$  ( $S$  decays after BBN but before recombination): viable self-interacting DM model,
- B) ultra weak  $10^{-17} \lesssim \epsilon \lesssim 10^{-13}$  ( $S$  decays after recombination but before  $\sim 1$  Gyr): viable self-interacting DM also affecting the  $H_0$  tension,
- C)  $\epsilon \lesssim 10^{-17}$  ( $S$  decays after  $\sim 1$  Gyr<sup>5</sup>): two-component DM (dominant pseudo-WIMP  $S$  with a small component of ultra-strong SIDM that can affect the formation of SMBHs through gravothermal collapse, see Section 8.2, with an impact on the  $H_0$  tension by very late decays.

Regimes 0 and A indicate that the symmetry breaking takes place at a relatively low energy scale, close to the DM mass. Smaller values of  $\epsilon$ , which lead to regimes B and C, occur naturally when the breaking occurs at a very high scale, such as the GUT or even Planck scale.

As mentioned above, we concentrate on the Higgs portal scenario which is illustrated in Fig. 8.3 and described by the following Lagrangian:

$$\begin{aligned} \mathcal{L}^{\text{DS}} = & \quad \bar{\chi}(i\gamma_\mu\partial^\mu - m_\chi)\chi + \frac{1}{2}m_A^2 A_\mu A^\mu \\ & + igA^\mu \bar{\chi}\gamma_\mu\chi + \epsilon S\bar{\chi}\chi, \end{aligned} \quad (8.4.2)$$

where  $\chi$  is the SIDM,  $S$  is the decaying pseudo-WIMP, and  $A^\mu$  is the light vector mediator. The connection with the visible sector is given by the mixing with the SM Higgs boson doublet  $H$

$$\begin{aligned} \mathcal{L}^{\text{portal}} = & \quad \frac{1}{2}(\partial^\mu S)(\partial_\mu S) + \frac{\mu_S^2}{2} S^2 + \frac{\lambda_3}{3!} S^3 + \frac{\lambda_4}{4!} S^4 \\ & + \epsilon \mu_{HS} S H^\dagger H + \lambda_{HS} S^2 H^\dagger H. \end{aligned} \quad (8.4.3)$$

Here, we have explicitly taken out the  $\epsilon$  factor in the trilinear term to emphasize that this term is allowed only as a result of the  $Z_2$  breaking. This guarantees that  $S$  decays mainly into DS states as long as  $\mu_{HS}$  is small enough or  $S$  is light enough that decays into SM particles are kinematically suppressed.

<sup>5</sup>The typical lifetime of  $S$  in this case is of the order of 5 Gyr.

## 8.5 Phenomenology

After introducing the theoretical framework in which we will aim to address the Hubble and small-scale tensions in the  $\Lambda$ CDM model, we describe the main phenomenological properties of our scenario.

### 8.5.1 Thermal history

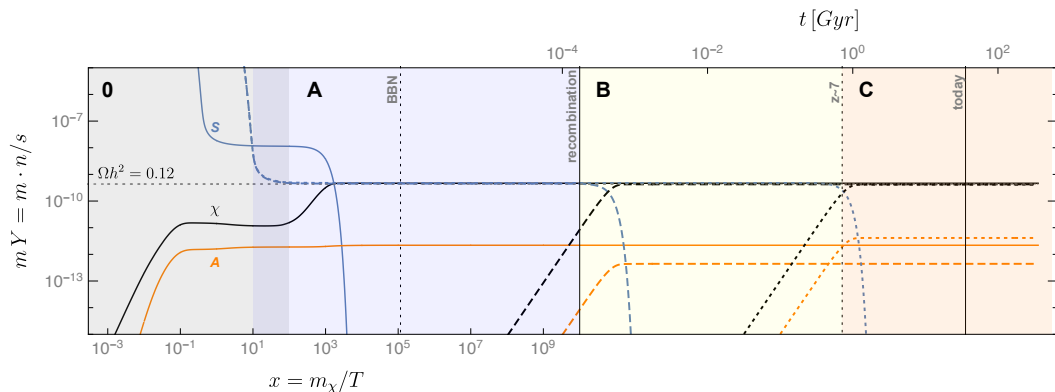


Figure 8.4: Thermal history of the model: evolution of the energy densities of  $S$  (blue),  $\chi$  (black) and  $A^\mu$  (orange) as a function of  $x = m_\chi/T$ . Representative parameters were chosen, which lead to early (regime A, solid lines), late (regime B, dashed) and very late (regime C, dotted) decays of  $S$ .

The basic assumption concerning the thermal history of our implementation of the SIDM scenario is that only the SM sector is populated during the reheating process, while the number and energy densities of the DS species at the beginning of the radiation dominated epoch are negligible - similar to the freeze-in DM production mechanism [187]. The connector scalar field  $S$  introduced in the previous section undergoes cosmological evolution similar to WIMPs, i.e., it thermalizes early on with the SM plasma due to the mixing with the SM Higgs boson and the quartic coupling  $\lambda_{HS}$ . When its annihilation rate drops below the Hubble rate it undergoes the freeze-out process. At a later time, perhaps even after recombination, it decays via  $S \rightarrow \bar{\chi}\chi$  and subdominantly to the SM species.

Fig. 8.4 shows example evolution of the mass densities of  $S$ ,  $\chi$  and  $A^\mu$  for all the regimes of the model parameter space discussed above. It is obtained by numerically solving the relevant Boltzmann equations describing the temperature evolution of the yield of each species. As one can see, the pseudo-WIMP  $S$  freezes out in the early Universe to the thermal relic density thanks to the mixing with the SM. At this time,  $\chi$  and  $A^\mu$  undergo inefficient freeze-in production until the onset of  $S$  decays that transfer the energy density of  $S$  to them. The decays can occur in various epochs of the Universe which we indicatively grouped into the regimes described previously.<sup>6</sup> In the regimes 0, A, and B the whole abundance of  $S$  is transferred into (mainly) SIDM  $\chi$  and (partly) dark radiation  $A^\mu$  which leads

<sup>6</sup>The separation of the epochs and the time variable at the top of the plot are not-to-scale and are shown for illustrative purposes.

to both modification of the cosmological history and production of SIDM (which can influence the small-scale problems of the  $\Lambda$ CDM). On the other hand, in the regime C only a (typically small) fraction of  $S$  decays up to present, therefore we obtain a two-component DM model.

It should be noted that the transitions between these regimes are only approximate and not sharply defined. In particular, the chosen redshift of  $z \sim 7$  line separating cases B and C corresponds to the times of the oldest observed quasars with SMBHs [525, 526, 553]. The decays of  $S$  at that time can affect the formation rate of SMBHs, see sec. 8.6.3. The  $S$  decays can also occur later, even up to and beyond the present day, which means that all the regimes combined cover a very wide range of possible lifetimes of  $S$ . In the A case (viable SIDM scenario),  $S$  typically needs to be chemically decoupled at a number density higher than it would be dictated by the DM thermal abundance. This is because during the decay process some of its energy is transferred to the kinetic energy of  $\chi$ , which later becomes redshifted. Let us also note that the annihilation process  $\chi\bar{\chi} \rightarrow AA$  can have some effect on the final  $\chi$  DM abundance even if the relevant number densities do not reach equilibrium values. This can be seen in the plot as a slight decrease in the  $\chi$  yield at early times, *e.g.*,  $10^{-1} \lesssim x \lesssim 10^1$  for the regime A. For larger  $S$  lifetimes, taking place in the B and C regimes, the  $\chi$  particles must be produced with very low kinetic energy. Otherwise they will negatively affect structure formation, as will be discussed in sec. 8.5.3.2.

### 8.5.2 Late time decays

Under the assumptions described in Section 8.4, the dominant decay channel of  $S$  is into two DM particles,  $S \rightarrow \bar{\chi}\chi$ . The relevant decay width is given by

$$\Gamma_{S \rightarrow \bar{\chi}\chi} = \frac{\epsilon^2 (m_S^2 - 4m_\chi^2)^{3/2}}{8\pi m_S^2} \approx 5.3 \times 10^4 \left( \frac{m_S}{1\text{GeV}} \right) \left( \frac{\epsilon}{10^{-16}} \right)^2 \left( \frac{\delta}{10^{-4}} \right)^{3/2} \text{ km/s/Mpc}, \quad (8.5.1)$$

where we introduced benchmark parameter values that lead to late decays.

At higher order, the three-body decay  $S \rightarrow \bar{\chi}\chi A$  and the loop-induced decay  $S \rightarrow AA$  are also present. By dimensional analysis it follows that  $\Gamma_{S \rightarrow \bar{\chi}\chi A} / \Gamma_{S \rightarrow \bar{\chi}\chi} \sim g^2$  and  $\Gamma_{S \rightarrow AA} / \Gamma_{S \rightarrow \bar{\chi}\chi} \sim g^4$ . From these relations, one can see that the decay of  $S$  naturally results in the transfer of a small fraction of energy to radiation ( $A$ , which is stable or extremely long-lived) taking place after the recombination, which is known to alleviate the  $H_0$  tension, cf. Section 8.2. In addition, thanks to the presence of such ultra-light mediator  $A$ , a viable SIDM model can be obtained for the  $\chi$  particles.

The final products of the  $S$  decays are non-relativistic in the case of the dominant decay channel  $S \rightarrow \bar{\chi}\chi$  and act as DM, while they remain relativistic for the loop decays  $S \rightarrow AA$ . In the latter case the  $A$  species act as dark radiation. The decay products of the three-body decay  $S \rightarrow \bar{\chi}\chi A$  are both relativistic ( $A$ ) and non-relativistic ( $\chi$ ). In the last case we adopt the prescription that  $\chi$  will always behave as matter (an excellent approximation as long as  $\delta$  is small, as we assume), while  $A^\mu$  will be considered as matter if its kinetic energy satisfies the condition  $E_{k,A} < m_A$ . Otherwise, we treat it as radiation.

The differential rate of the three-body decay is given by

$$\frac{d^2\Gamma_{S\rightarrow\bar{\chi}\chi A}}{dE_{k,A}dE_\chi} = \frac{|\mathcal{M}_{S\rightarrow\bar{\chi}\chi A}|^2}{64\pi^3 m_S}, \quad (8.5.2)$$

where the amplitude  $\mathcal{M}_{S\rightarrow\bar{\chi}\chi A}$  reads

$$\mathcal{M}_{S\rightarrow\bar{\chi}\chi A} = \epsilon g \epsilon_r^{\mu*}(p_1) \bar{\chi}(p_3, m_\chi) \left( \frac{1}{\not{p}_1 + \not{p}_3 - m_\chi} - \frac{1}{\not{p}_1 + \not{p}_2 + m_\chi} \right) \chi(p_2, m_\chi), \quad (8.5.3)$$

where  $p_1$  is the momentum of  $A$  and  $p_2, p_3$  are, respectively, the momenta of  $\bar{\chi}$  and  $\chi$  in the rest frame of  $S$ , while  $\epsilon_r^*(p_1)$  is the polarization vector of the external  $A^\mu$  field.

To obtain the total decay width  $\Gamma_{S\rightarrow\bar{\chi}\chi A}$ , we integrate the differential rate over the entire kinematically allowed region in the phase space. On the other hand, to obtain the fraction of energy transferred to radiation,  $F$ , we need to restrict the region to the part, where  $A^\mu$  is relativistic at decay

$$F = \frac{\Gamma_{S\rightarrow AA} + \Delta \times \Gamma_{S\rightarrow\bar{\chi}\chi A}}{\Gamma_{S\rightarrow\bar{\chi}\chi} + \Gamma_{S\rightarrow AA} + \Gamma_{S\rightarrow\chi\chi A}}, \quad (8.5.4)$$

where

$$\Delta = \frac{1}{\Gamma_{S\rightarrow\bar{\chi}\chi A}} \int_{2m_A}^{E_{k,A}^{max}} \int_{E_\chi^{min}}^{E_\chi^{max}} \frac{d^2\Gamma_{S\rightarrow\bar{\chi}\chi A}}{dE_\chi dE_{k,A}} dE_\chi dE_{k,A} \quad (8.5.5)$$

is the fraction of the decay width resulting in  $A^\mu$  having the kinetic energy equal to or greater than its mass.

The one loop decay  $S \rightarrow AA$  is of higher order in perturbation theory, but it is not phase-space suppressed and transfers all the energy of  $S$  to radiation. When analyzing the impact of this decay channel, we used the `Mathematica` packages `FeynCalc` [554–556] and `Package-X` [557] to calculate the amplitudes symbolically.

The amplitude  $\mathcal{M}_{S\rightarrow AA}$  is given by

$$\begin{aligned} \mathcal{M}_{S\rightarrow AA} = & -12m_\chi [-2B_0(m_S^2; m_\chi, m_\chi) \\ & + 8C_{00}(m_A^2, m_S^2, m_A^2; m_\chi, m_\chi, m_\chi) \\ & + (2m_A^2 - m_S^2)C_0(m_A^2, m_S^2, m_A^2; m_\chi, m_\chi, m_\chi)], \end{aligned} \quad (8.5.6)$$

where  $B_0$  and  $C_0$  are the two and three-points Passarino–Veltman [558] scalar functions, respectively, while  $C_{00}$  is the coefficient of the three-point tensor function proportional to the metric tensor. We follow the conventions of [557], where the  $1/(16\pi^2)$  is factored-out in the definition of the  $C_{00}$  function, hence it reappears in Eq. (8.5.7). Note that  $B_0$  and  $C_{00}$  are UV divergent, but their divergent parts cancel out in Eq. (8.5.7), making the whole expression finite.

The resulting expressions is computed numerically in a dedicated Python code used to obtain the total decay width

$$\Gamma_{S\rightarrow AA} = \frac{|\mathcal{M}_{S\rightarrow AA}|^2 g^4 \epsilon^2 \sqrt{m_S^2 - 4m_A^2}}{(16\pi^2)^2 16\pi m_S^2}. \quad (8.5.7)$$

### 8.5.3 Impact of late decays on the $H_0$ tension and structure formation

As already discussed in Chapter 2, and illustrated in Fig. 2.2, cosmological observations are becoming increasingly precise, further limiting the alternatives to the standard cosmological model. On the other hand, the determination of the Hubble parameter  $H_0$  is one of the persistent tensions, which actually became more severe with more data. An important aspect of this tension is that there is a general disagreement within the early and late Universe observations [19].

#### 8.5.3.1 Cosmological scan

One possibility to address this outstanding issue is to employ DCDM [396], where a dark matter particle decays partially into dark radiation; see also Section 8.2 for more details. As radiation redshifts faster than dark matter, its late-time production results in the reduced expansion rate as compared to the early periods in the evolution of the Universe. The scenario that we consider in this chapter has a similar impact on cosmology as the DCDM model, and therefore we expect that it will provide a better fit to the cosmological data than the  $\Lambda$ CDM model. In the following, we will refer to our scenario as DCDM for simplicity.

To analyze the impact of our model on cosmological predictions, we modified publicly available Boltzmann solver code CLASS [559] in combination with a Markov Chain Monte Carlo (MCMC) tool MontePython [560, 561]. We used the following datasets, coming from both early and late Universe observations, to constrain our model:

- *Planck* 2018 measurements of the CMB spectrum [562] (we used full TTTEEE high- $\ell$ , TT, EE low- $\ell$ , and lensing likelihoods),
- BAO data from the BOSS survey [563–565],
- the galaxy cluster survey from the *Planck* catalog (PC) [566],
- the local measurement from the Hubble Telescope  $H_0 = 74.03 \pm 1.42$  km/s/Mpc [24].

We performed a numerical scan over a multi-dimensional parameter space which consists of 6 standard cosmological parameters (discussed in Section 2.2), i.e.,  $\{\omega_b = \Omega_b h^2, \omega_{cdm}, \ln 10^{10} A_s, n_s, 100\theta_s, \tau_{reio}\}$ , and two additional ones:  $\Gamma$  and  $F$ . They denote the total decay width and the fraction of DCDM that decays into dark radiation, respectively. In the context of our model, the latter parameter has already been introduced in eq. Eq. (8.5.4), while  $\Gamma$  is the total decay width of  $S$  given by Eq. (8.5.1). We then used the resulting cosmological limits on  $\Gamma$  and  $F$  to find regions of our model’s parameter space that is preferred from the cosmological point of view.

In particular, we ran three separate scans, using the same likelihood functions in each case: (i) the  $\Lambda$ CDM model without DCDM, (ii) the DCDM model with a log prior favoring low  $S$  lifetimes (in the following, we refer to this scenario as *short*  $\tau_{\text{DCDM}}$ ), and (iii) the DCDM model with a prior favoring late decay times

of  $S$ , comparable to the current age of the Universe (*long*  $\tau_{\text{DCDM}}$ ). The last scan is motivated by [514], which found that the DCDM model with the lifetime of the decaying species of the order of  $\sim 20$  Gyr can alleviate the Hubble tension. Following that work, in the *long*  $\tau_{\text{DCDM}}$  scan we fixed the reionization time, initial amplitude of scalar perturbations  $A_s$ , and its spectral index  $n_s$  to the  $\Lambda$ CDM best fit values following [18].

When varying 6  $\Lambda$ CDM parameters we used flat priors with the following ranges:  $\omega_b = \Omega_b h^2 \in (0.01, 0.1)$ ,  $\omega_{\text{cdm}} \in (0.05, 0.3)$ ,  $100\theta_s \in (0.8, 1.2)$ ,  $\tau \in (0.01, 0.2)$ ,  $\ln(10^{10} A_s) \in (2, 4)$ ,  $n_s \in (0.9, 1.1)$ . For the two additional parameters, we used a flat prior on the amount of dark radiation coming from the decay:  $\log_{10} F \in (-4, -0.4)$ , while we used two different priors on the DCDM lifetime corresponding to *short* and *long*  $\tau_{\text{DCDM}}$  regimes:  $\log_{10} \Gamma \in (2, 7)$  [km/s/Mpc] and  $\log_{10} \Gamma \in (0, 3)$  [km/s/Mpc], respectively. We generated multiple MCMC chains until convergence, determined by the Gelman-Rubin criterion, see [560] for extensive discussion. The results of the scans are presented in Fig. 8.5.

We found two disjoint regions in the  $(F, \Gamma)$  plane that improve the fit by mildly increasing  $H_0$  relative to the best fit value of the  $\Lambda$ CDM model. These correspond, respectively, to early  $S$  decays ( $\tau_{\text{DCDM}} \sim 4$  Myr) with  $F \sim 1\%$ , and late decays ( $\tau_{\text{DCDM}} \sim 5$  Gyr) with  $F \sim 10\%$ . Such an anticorrelation between  $\Gamma$  and  $F$  has been previously noted, *e.g.*, in [567, 568]. The first case corresponds to the regime in which the whole but 1% of the  $S$  abundance is changed into  $\chi$ s before structure formation begins, therefore  $\chi$ 's self-interactions can improve the small scale structure problems of  $\Lambda$ CDM. The situation is different in the second case, where only a small fraction of the  $S$  abundance transforms into SIDM at early times, which is not sufficient to influence structure formation. On the other hand, in this *long*  $\tau_{\text{DCDM}}$  regime, DM self-interactions can be much stronger than 0.1–10  $\text{cm}^2/\text{g}$  for a subdominant DM component, so even a tiny fraction of ultra-SIDM can serve as SMBHs seeds [531, 532].

A comparison between the results obtained for the DCDM and  $\Lambda$ CDM models in the  $H_0$ – $\sigma_8$  plane is shown on the left in Fig. 8.5 while table 8.1 contains the respective mean values of the cosmological parameters. The DCDM models in both regimes result in a mild reduction of the tension between the early and late Universe determinations of  $H_0$  and  $\sigma_8$ .

### 8.5.3.2 Structure formation limits on decaying dark matter

As discussed above, late decays of the scalar  $S$  can affect not only the Hubble parameter but also the formation of large-scale structures in the Universe, since the decay products can acquire enough kinetic energy to free-stream out of gravity wells and suppress structure growth.

We impose the relevant limits derived from the halo mass concentration, the galaxy-cluster mass function, and the Lyman- $\alpha$  power spectrum [569–573] as an upper bound on the mass splitting  $\delta$ , which we defined in Eq. (8.4.1). We can estimate the free-streaming length of the decay product particle as follows [573]:

$$\lambda_{\text{fs}} = \int_{\tau_d}^{\tau_0} d\tau v(\tau) \sim \frac{3v_{\text{kick}}\Gamma^{-1}}{a_d}, \quad (8.5.8)$$

where  $\tau$  is conformal time and  $v_{\text{kick}}$  are the velocities of the decay products. The

	short	long	$\Lambda$ CDM
$100\omega_b$	$2.26^{+0.017}_{-0.015}$	$2.26^{+0.013}_{-0.014}$	$2.254^{+0.014}_{-0.014}$
$\omega_{cdm}$	$0.116^{+0.0011}_{-0.00084}$	$0.107^{+0.0032}_{-0.0043}$	$0.118^{+0.001}_{-0.001}$
$n_s$	$0.972^{+0.0043}_{-0.0040}$	0.9654	$0.9705^{+0.0038}_{-0.0039}$
$10^9 A_s$	$2.05^{+0.032}_{-0.030}$	2.106	$2.107^{+0.036}_{-0.037}$
$100\theta_s$	$1.04^{+0.00029}_{-0.00029}$	$1.04^{+0.00036}_{-0.00047}$	$1.042^{+0.00029}_{-0.00029}$
$\tau_{reio}$	$0.0475^{+0.0080}_{-0.0070}$	0.0557	$0.0578^{+0.0077}_{-0.0085}$
$\log_{10} F$	$-2.41^{+0.96}_{-0.48}$	$-1.1^{+0.25}_{-0.081}$	-
$\log_{10} \Gamma$	$4.36^{+1.38}_{-1.49}$	$2.33^{+0.13}_{-0.33}$	-
$H_0$	$69.4^{+0.43}_{-0.60}$	$69.7^{+0.33}_{-0.44}$	$68.28^{+0.45}_{-0.45}$
$\sigma_8$	$0.791^{+0.0062}_{-0.0051}$	$0.80^{+0.0030}_{-0.0031}$	$0.8065^{+0.0073}_{-0.0077}$

Table 8.1: Results of the Monte Carlo Markov Chain scan - we show the constraints on cosmological parameters. The uncertainties on the mean values are given at the  $1\sigma$  (68%) level. The values of  $\Gamma$  and  $H_0$  are given in units of km/s/Mpc.

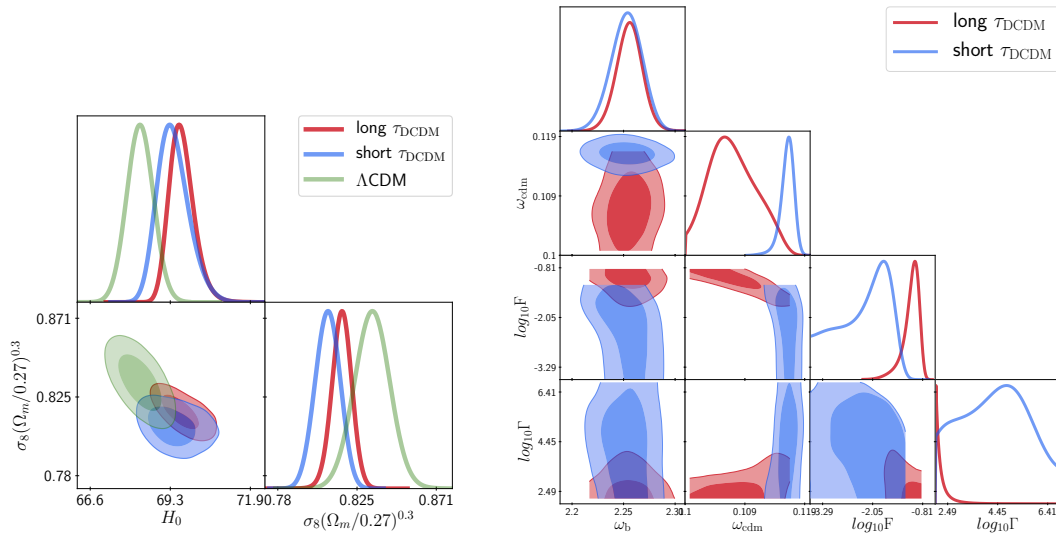


Figure 8.5: Constraints on the cosmological parameters for the B (blue) and C (red) regimes of DCDM and  $\Lambda$ CDM. Both DCDM regimes lead to slightly better values of  $H_0$  and  $\sigma_8 (\Omega_{\text{matter}}/0.27)^{0.3}$  than  $\Lambda$ CDM.

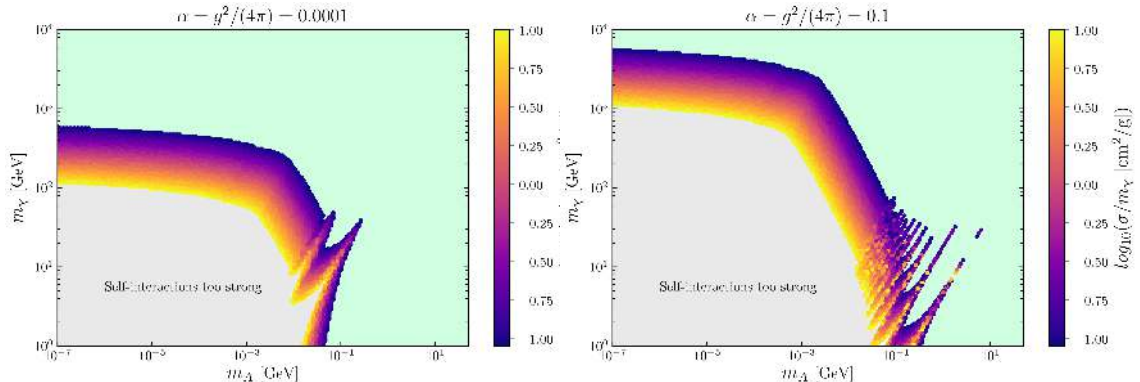


Figure 8.6: Results of the analysis relevant for the SIDM regime (A) in the  $m_A$ - $m_\chi$  plane. We show with the colorful shading the region in the parameter space of the model for which the self-interaction cross section  $\sigma_{\text{tr}}/m_\chi$  is in the range preferred by the small-scale problems of the  $\Lambda$ CDM model, i.e., between 0.1 and 10  $\text{cm}^2/\text{g}$ . The green-shaded and gray-shaded areas indicate too weak and too strong DM self-interactions, respectively. The results are presented for two representative values of the coupling constant  $\alpha_\chi = 0.0001$  (left) and  $\alpha_\chi = 0.1$  (right).

integration over  $\tau$  is performed between the conformal time of the decay,  $\tau_d$ , and present  $\tau_0$ . In the second step we use the  $S$  decay width  $\Gamma$ , and the scale factor evaluated at the time of decay,  $a_d$ .

The lifetimes considered in our analysis correspond to  $\Gamma^{-1} \lesssim 10$  Gyr, for which the mass splitting was found [571–573] to be constrained such as  $\delta \lesssim 10^{-2}$  in the short DCDM lifetime regime, and  $\delta \lesssim 10^{-3.5}$  in the long lifetime regime (cf. Fig. 11 in [573]). The quoted constraints were derived assuming a WIMP DM, whereas in the case of significant self-interactions, the elastic scatterings between DM particles would further suppress free-streaming. Therefore, applying the quoted limits can be considered as a conservative approach, which we follow.

## 8.6 Results

Finally, we present and discuss results of our analysis for the three decay lifetime regimes - A, B, and C - that result in the SIDM production (note that regime 0 results in thermal SIDM which is strongly constrained by CMB and ID observations [461]).

### 8.6.1 The SIDM regime (A)

In the regime A, where  $\epsilon$  is small enough that the DS species do not thermalize with the SM, but also large enough for essentially all the  $S$  particles to decay before recombination, the SIDM production in  $S$  decays is possible, although it does not affect the value of the Hubble parameter,  $H_0$ . In Fig. 8.6 we show the slice of the parameter space of our model in the  $m_A - m_\chi$  plane for two values of the dark gauge coupling  $\alpha_\chi = 0.0001$  (left) and  $\alpha_\chi = 0.1$  (right). Both of them lead to the self-interaction cross section strength required to solve the

small-scale problems of the  $\Lambda$ CDM model. We mark this region in the parameter space with a colorful gradient shading which corresponds to the range of values of  $0.1 \lesssim \sigma_{\text{tr}}/m_\chi \lesssim 10 \text{ cm}^2/\text{g}$ . Instead, the gray-shaded area is excluded due to too strong self-interactions [51, 52, 574], while the light-green-shaded area leads to too weak self-interactions. Note that the values of  $(m_A, m_\chi)$  shown on both sides of Fig. 8.6 correspond to the classical (smaller  $m_A$ ) and resonant (larger  $m_A$ ) regimes of self-interactions. The former is described by Eq. (8.3.10), from which it follows that for fixed  $m_\chi$  stronger self-interactions are obtained for smaller  $m_A$  and vice versa. The latter requires numerical procedure described in Section 8.3, and can lead to the well-known resonance behavior (the lower right part of the plot) which becomes more pronounced as  $\alpha_\chi$  increases.

It is important to point out important differences between the proposed SIDM production mechanism and the usual thermal production mechanism. They differ in two main ways: (i) in our case, the strength of self-interactions is governed by a different coupling that the one responsible for obtaining the correct relic abundance which opens a much wider parameter space with both cosmological and astrophysical constraints satisfied and (ii) the light mediator in our analysis can be absolutely stable which allows the model to evade the CMB and ID limits derived from annihilations of the light mediator into SM species [461].

### 8.6.2 The SIDM from late decays regime (B)

Further decreasing  $\epsilon$  suppresses early  $S$  decays which then happen typically after recombination. This modifies the evolution of background and perturbation quantities with respect to the  $\Lambda$ CDM model, while producing SIDM. The resulting dark matter phenomenology is still governed by the  $m_\chi$ ,  $m_A$ , and  $\alpha_\chi$  parameters, but, in this regime, varying  $m_S$  and the precise value of  $\epsilon$  also have important observational consequences, affecting decay kinematics and the  $S$  lifetime, respectively.

The main results of our analysis in this case are shown in Fig. 8.7. It shows the results of the numerical scan relevant for the *short*  $\tau_{\text{DCDM}}$  regime discussed above projected onto the  $m_A$ – $m_\chi$  plane. In the plot, we fixed the value of the DM self-interaction cross section at  $\sigma_{\text{tr}}/m_\chi \sim (1 \pm 0.1) \text{ cm}^2/\text{g}$ . The colored bar represents the coupling strength  $g$ , cf. Eq. (8.3.6). Moreover, with dark green we show the region relaxing the Hubble tension, while the light green line denotes the best fit parameters. The latter corresponds to  $H_0 \simeq 70$  and  $\sigma_8 \simeq 0.795$ . The fit cannot be further improved because it would require an even larger transition of DM energy into dark radiation, which would significantly worsen the fit to the large  $l$  part of the CMB spectrum.

In order to obtain the results, the numerical scan over the particle physics parameters was performed, sampling  $m_S$ ,  $m_A$ ,  $m_\chi$  and  $g$  - the four parameters that uniquely determine the fraction  $F$  - with the condition that the mass splitting is small,  $\delta \in [10^{-6}, 10^{-1}]$ . The remaining cosmologically relevant parameter is the decay width  $\Gamma$ , which is brought to the value of  $\tau_S = 1/\Gamma \simeq 0.37 \text{ Myr} - 1 \text{ Gyr}$  by appropriate rescaling of the symmetry breaking parameter  $\epsilon$ .

The  $1\sigma$  region shown in Fig. 8.7 is bounded from above by the condition on  $F$  derived from the cosmological scan, see Table 8.1. The points in the parameter

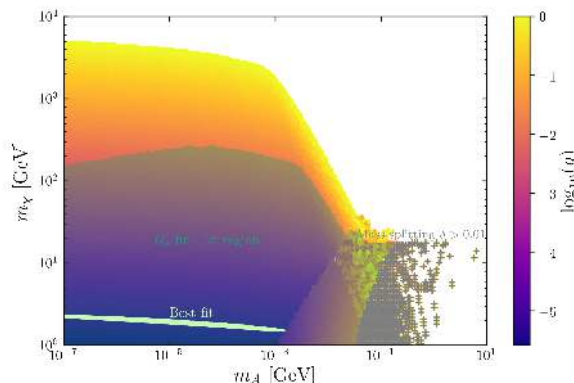


Figure 8.7: Results of the numerical scans performed for the regime B - the SIDM regime in which late  $S$  decays take place. Color coding indicates the value of the coupling  $g$  leading to  $\sigma_{\text{tr}}/m_\chi \sim (1 \pm 10\%) \text{ cm}^2/\text{g}$ . In addition, the dark green shading marks the region at  $1\sigma$  level around the mean values of DCDM parameters that relax the  $H_0$  tension.

space of the model that lie above this boundary give an over-efficient conversion of the  $S$  abundance into radiation. The lower right region in the figure represents the resonant regime similar to the one discussed in Sec. 8.6.1. A lower density of points is seen here compared to the Born and classical regimes, and larger values of  $g$  are allowed. For the largest  $m_A$ , the points are very sparse. It is due to an irregular arrangement of consecutive resonance peaks which have a very small width for a large value of  $\alpha_\chi$ . About half of the resonance parameter space is also marked with gray plus signs that indicate that these points are characterized by large  $\delta$  which is in tension with the structure formation constraints. Differentiating by the dominant decay channel, the resonant and  $\alpha_\chi \sim 1$  regimes in Fig. 8.7 are dominated by the loop-induced decay of  $S$  into two  $A$ s, while the rest of the parameter space is dominated by the three-body decays of  $S$ .

### 8.6.3 The ultra SIDM regime (C)

Finally, for the largest lifetimes of  $S$  confirmed (even comparable to the age of the Universe) we enter the regime of two-component DM, where  $\chi$  can be much more strongly interacting while contributing subdominantly to the total DM relic density. We show the corresponding results in Fig. 8.8 in the  $F' - \sigma_{\text{tr}}/m_\chi$  plane, where  $F'$  denotes the fraction of uSIDM that existed up to  $z = 7$ .

In light blue, we show the region at  $2\sigma$  (95%) level around the mean values of the DCDM parameters that relax the Hubble tension in the long lifetime scenario. In turn, the light green area denotes the parameter space in which  $S$  decays occur too late to significantly affect the  $H_0$  tension, while the gray area corresponds to earlier decays, which do not lie in the regime C. In this region, however,  $\sigma_{\text{tr}}/m_\chi$  and  $F'$  are sufficiently large to be important for accelerating the formation of SMBHs. The red lines denote the results of numerical simulations performed in [532] (cf. Fig. 5 therein, Model A for elastic scatterings) and correspond to the redshift  $z = 7$  (solid) and  $z = 15$  (dashed).

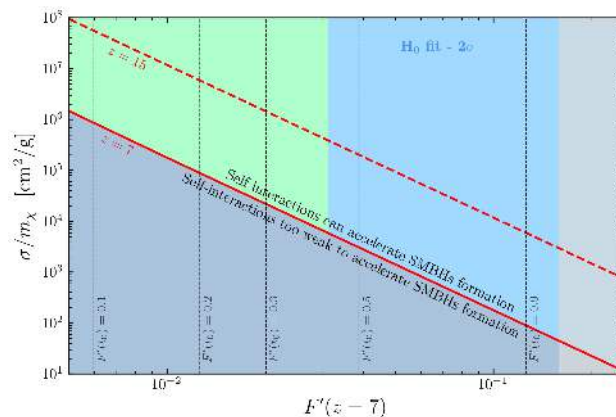


Figure 8.8: Results of regime C, where the Hubble tension is mildly relaxed (light blue region) and self-interactions are strong enough to accelerate SMBHs formation rates (green and light blue regions).

In summary, we find that the uSIDM production by late  $S$  decays is strongly constrained if we limit the decay time to be  $\lesssim 40$  Gyr, which simultaneously relaxes the Hubble tension. Difficulties arise in the very early time of the SMBH formation, since  $z \sim 7$  corresponds to the age of the Universe  $\sim 0.77$  Gyr, while the decay times relevant to the Hubble tension correspond to either earlier ( $\sim 4$  Myr) or later ( $\sim 5$  Gyr) times. However, if the decay occurred even later than 40 Gyr, this may be a viable mechanism for accelerating the formation of early SMBHs.

## 8.7 Conclusions

In summary, we have studied the cosmological implications of a SIDM production mechanism based on decays of WIMP-like state  $S$  occurring at late times. The dominant decay mode of  $S$  leads to the SIDM production, which occurs via a tree-level process, while higher order processes transfer a small fraction of the decaying state energy to dark radiation. Such higher order processes naturally lead to the transfer of only a small fraction of the DM energy to the radiation, which is necessary due to the stringent CMB constraints. Overall, we observe an improved fit to the  $H_0$  and  $S_8$  parameters in the scenario that can simultaneously address some of the small-scale problems of the  $\Lambda$ CDM model.

Finally, we note that the light dark photon introduced by us to, *e.g.*, mediate sufficiently strong DM self-interactions, can also be related to the XENON1T electron recoil anomaly and the stellar cooling anomalies described in Section 8.2. Interestingly, the  $m_A \sim 1$  keV,  $\kappa \sim 10^{-15}$  region of the parameter space invoked to explain these anomalies [535], can naturally be included in any of the A, B or C regimes of our scenario.<sup>7</sup> In particular, regime B could simultaneously explain these anomalies and small-scale problems of the  $\Lambda$ CDM, and also partly relieve the  $H_0$  and  $S_8$  tensions, which further motivates the scenario considered by us.

<sup>7</sup>With appropriate values of other parameters adjusted in each regime as discussed in Section 8.6.

# Chapter 9

## Conclusions

Extensive searches for a WIMP-like DM have so far yielded null results, placing strong constraints on the candidate. Moreover, the lack of discoveries at the LHC - beyond measuring the mass of the Higgs boson - further reiterate the need to explore alternative scenarios of new physics, and thus also to probe various observables arising from such models.

One of the emerging new frontiers - called intensity frontier - is devoted to the study of new light, sub-GeV particles that interact with the SM even more weakly than WIMPs. Possible consequences of the existence of these postulated light long-lived particles have been thoroughly studied in the literature in recent years and a plethora of new experiments have been proposed to target them. In some cases, they can also be invoked as a solution to various anomalies in collider physics and cosmology, *e.g.*, the  $(g - 2)_\mu$  anomaly.

However, while the simplest models of this type have been investigated in detail, they should generically emerge from more elaborate dark sectors that can contain multiple light degrees of freedom or comprise of both light and heavy new species. In this thesis, we have focused on phenomenological consequences of some of such scenarios that could go beyond what is expected in both the simplified LLP models and in generic models predicting the existence of heavy WIMP DM.

The work described in this thesis covers both standard scenarios, such as WIMPs, and the ones related to intensity frontier searches, like new LLPs and sub-GeV particles, as well as it discusses a possible interplay between them based on example BSM models. In particular, we discussed:

- The role of secondary LLP production which occurs by coherent upscattering of lighter LLP on the material just in front ( $\sim 1-10$  m) of the detector. This process extends the sensitivity of the detectors toward shorter lifetimes, which is the regime often linked to the DM problem as well as to various experimental anomalies. We studied this mechanism within scenarios extending the standard renormalizable portals:
  - scalar and vector portal (Chapter 4) and
  - models with extended neutrino sector or non-standard neutrino interactions (Chapter 5).

In all the cases, we showed excellent prospects for this kind of searches, and one of our results was featured in an important community workshop report [236] (Fig. 14 therein).

- Prospects for the detection of a prominent supersymmetric DM candidate - the lightest neutralino - in next-generation ID detectors like CTA (Chapter 6). We significantly improved over previous studies of this kind by, *e.g.*,
  - including full implementation of SE effect which is crucial for reliable sensitivity predictions of heavy ( $\gtrsim 1$  TeV) DM prospects and following the methodology used by the CTA collaboration.
  - Showing a key complementarity between ID and DD searches for covering  $\sim 1$  TeV higgsino, which is one of the most interesting candidates in the MSSM.
- Complementarity of searches for new physics in a rich dark sector model with a LLP, light and heavy DM particles (Chapter 7).
  - Usually LLPs are constrained by intensity frontier searches, while light DM species can be probed in DD searches depending on the benchmark scenario. Instead, a complementarity of such searches with ID and CMB observations in rich dark sector models has remained largely unexplored. We illustrated the resulting synergy of searches within an example rich DS model characterized by a wide range of mass scales. In particular, it contained a secluded heavy DM particle with the mass of the order of 1 TeV connected to the SM species through the sub-GeV dark Higgs boson mediator.
  - We showed that the resulting non-local ID effects can be very pronounced and can lead to signatures that are distinctly different from the ones taking place for ID of WIMPs, while stringent cosmological bounds can be evaded in such models.
- A novel mechanism for SIDM production that occurs via late decays of pseudo-WIMP  $S$  state taking place after the recombination (Chapter 8).
  - We showed that such a scenario may partially relieve the  $H_0$  and  $S_8$  tensions present in the  $\Lambda$ CDM model, while simultaneously providing the solution to the small-scale problems of generic cold DM scenarios (in case of not-too-late,  $\tau_S \lesssim 10$  Myr, decays) or other problems like formation of SMBHs (in case of very late,  $\tau_S \gtrsim 1$  Gyr, decays).
  - The model we studied naturally accommodates the parameter space shown [535] to fit recent anomaly in electronic recoils in the XENON1T experiment [534] and observations of cooling anomalies in horizontal branch stars [536–538].

In conclusion, the nature of DM is one of the most important puzzles of modern physics, on both theoretical and experimental front. The lack of detection of the

---

most explored DM candidates like WIMPs or axions motivates the exploration of other, less explored possibilities, which was the main goal of my thesis.

The research described here has been largely motivated by near-future experiments, *e.g.*, those related to the Forward Physics Facility [6], and represents my modest contribution to this promising research direction. I expect to build on the experience gained during my PhD studies and conduct further research in this area.



# Appendix A

## Frequently used cosmology and particle physics formulae

### A.1 Units

In this thesis we consistently work in the natural units, where by definition:  $\hbar = c = \epsilon_0 = k_b = 1$ . Therefore, dimensionful quantities will be expressed in powers of mass

$$[E] = [p] = [m] = 1, \text{ while } [x] = [t] = -1. \quad (\text{A.1.1})$$

To convert quantities expressed in the natural units into the SI units, it is convenient to use web calculator [575] which additionally uses the convention that the electric charge  $e = \sqrt{\alpha_{\text{EM}}} \simeq 0.0854$ , instead of the usual  $e = \sqrt{\alpha_{\text{EM}} 4\pi} \simeq 0.303$ . We checked independently that the results of this calculator are reliable.

### A.2 Phase space

Lorentz invariant phase space for  $N$  final state particles is:

$$dQ_N \equiv \frac{1}{n!} \frac{1}{(2\pi)^{3N-4}} \prod_{l=1}^N \frac{d^3 p_l}{2E_l} \delta^{(4)}(\mathcal{P}_i - \mathcal{P}_f), \quad (\text{A.2.1})$$

where  $n$  is the number of identical particles in the final state and  $\mathcal{P}_i, \mathcal{P}_f$  are the sums of the initial and final four-momentums, respectively.

Let us quote, cf. [576], the results for the first few  $N$ , all evaluated in the CoM frame:

$$dQ_1 = 2\pi \delta(s - m_1^2) = \frac{\pi}{s} \delta\left(1 - \frac{m_1}{\sqrt{s}}\right), \quad (\text{A.2.2})$$

$$dQ_2 = \frac{\bar{\beta}}{8\pi} \frac{d \cos \theta}{2} \frac{d\phi}{2\pi}, \quad (\text{A.2.3})$$

where

$$\bar{\beta} = \sqrt{1 - \frac{2(m_1^2 + m_2^2)}{s} + \frac{(m_1^2 - m_2^2)^2}{s^2}} \quad (\text{A.2.4})$$

and  $\theta$  is the polar angle, while  $\phi$  is the azimuthal angle.

$$dQ_3 = \frac{1}{128\pi^3 s} ds_{23} ds_{13} \quad (\text{A.2.5})$$

The integration limits are:

$$s_{13}^{\min} = (m_1 + m_3)^2, \quad s_{13}^{\max} = (\sqrt{s} - m_2)^2,$$

and

$$\begin{aligned} s_{23}^{\min} &= \frac{1}{4s_{13}} \left\{ (s - m_1^2 - m_2^2 + m_3^2)^2 \right. \\ &\quad \left. - [\lambda^{1/2}(s, s_{13}, m_2^2) + \lambda^{1/2}(s_{13}, m_1^2, m_3^2)]^2 \right\}, \\ s_{23}^{\max} &= \frac{1}{4s_{13}} \left\{ (s - m_1^2 - m_2^2 + m_3^2)^2 \right. \\ &\quad \left. - [\lambda^{1/2}(s, s_{13}, m_2^2) - \lambda^{1/2}(s_{13}, m_1^2, m_3^2)]^2 \right\}, \end{aligned}$$

where we used the triangle (Kallen) function:

$$\lambda(x, y, z) = (x - y - z)^2 - 4yz. \quad (\text{A.2.6})$$

### A.3 Decay width and cross section definitions

The decay width in the rest frame of the decaying particle  $a$  is

$$\Gamma(a \rightarrow 1+2+\dots+N) = \frac{1}{2m_a} \frac{1}{(2j_a + 1)} \sum_{\lambda_a, \lambda_1, \dots, \lambda_N} \int dQ_N |\mathcal{M}(a \rightarrow 1+2+\dots+N)|^2, \quad (\text{A.3.1})$$

The Lorentz-invariant cross section for scattering of particles  $a$  and  $b$  is

$$\begin{aligned} \sigma(a+b \rightarrow 1+\dots+N) & \quad (\text{A.3.2}) \\ &= \frac{1}{2\lambda^{1/2}(s, m_a^2, m_b^2)} \frac{1}{(2j_a + 1)(2j_b + 1)} \sum_{\lambda_a, \lambda_b, \lambda_1, \dots, \lambda_N} \int dQ_N |\mathcal{M}(a+b \rightarrow 1+\dots+N)|^2, \end{aligned}$$

where  $\lambda_i$  denotes the polarization of species with index  $i$ .

### A.4 Bremsstrahlung

We frequently encounter  $2 \rightarrow 3$  processes, similar to the bremsstrahlung process  $e^-e^+ \rightarrow e^-e^+\gamma$ . Below we provide a general expression for the total cross section valid for five different masses, expanding and correcting the expressions from [577],

$$\begin{aligned} \sigma &= \frac{1}{64\pi^4 \sqrt{\lambda(s, m_1^2, m_2^2)}} \int_{E_3^{\min}}^{E_3^{\max}} dE_3 \sqrt{E_3^2 - m_3^2} \int_0^\pi d\theta \sin\theta \int_0^\pi d\theta^* \sin\theta^* \\ &\quad \int_0^{2\pi} d\varphi^* \frac{1}{8} \frac{\sqrt{((m_{45} + m_4)^2 - m_5^2)((m_{45} - m_4)^2 - m_5^2)}}{m_{45}^2 + m_5^2 - m_4^2} |\overline{M}|^2. \end{aligned} \quad (\text{A.4.1})$$

We have already performed a trivial integral over the azimuth angle  $\phi$  which gives a factor of  $2\pi$ . The incoming particles have momenta  $p_1, p_2$  and the outgoing particles have momenta  $p_3, p_4, p_5$ . The angles written without the asterisk are evaluated in the CoM frame of a pair of particles with momenta  $p_1$  and  $p_2$ . In turn, quantities with the asterisk (\*) are evaluated in the CoM frame of pair of particles with momenta  $p_4$  and  $p_5$ . For example,  $\theta$  is the scattering angle between the particle with momentum  $p_3$  and the collision axis of the particles with momenta  $p_1$  and  $p_2$  in their CoM frame, while  $\theta^*$  and  $\phi^*$  denote the angles of the particle with momentum  $p_3$  in the frame where  $\vec{p}_4 + \vec{p}_5 = 0$

$$\begin{aligned} E_3^{\min} &= m_3, \\ E_3^{\max} &= \frac{s + m_3^2 - (m_4 + m_5)^2}{2\sqrt{s}}. \end{aligned} \quad (\text{A.4.2})$$

In order to obtain the quantities with the asterisk, one needs to use the following boost factor:

$$\gamma = \frac{E_{45}}{m_{45}}, \quad \beta = \sqrt{1 - \frac{1}{\gamma^2}}. \quad (\text{A.4.3})$$

The invariant mass  $m_{45}$  and the energy of the pair  $E_{45}$  are given by

$$\begin{aligned} m_{45} &= \sqrt{(p_4 + p_5)^2} = \sqrt{s - 2\sqrt{s}E_3 + m_3^2}, \\ E_{45} &= \frac{s + m_{45}^2 - m_3^2}{2\sqrt{s}}. \end{aligned} \quad (\text{A.4.4})$$

We also write down the expressions for all components of  $p_4$  and  $p_5$

$$\left\{ \begin{array}{l} p_4^{*0} = \frac{m_{45}^2 + m_4^2 - m_5^2}{2m_{45}} \\ p_4^{*1} = p_{45}^{\text{CM}} \sin \theta^* \cos \varphi^* \\ p_4^{*2} = p_{45}^{\text{CM}} \sin \theta^* \sin \varphi^* \\ p_4^{*3} = p_{45}^{\text{CM}} \cos \theta^* \end{array} \right\}, \quad \left\{ \begin{array}{l} p_5^{*0} = \frac{m_{45}^2 + m_5^2 - m_4^2}{2m_{45}} \\ p_5^{*1} = -p_{45}^{\text{CM}} \sin \theta^* \cos \varphi^* \\ p_5^{*2} = -p_{45}^{\text{CM}} \sin \theta^* \sin \varphi^* \\ p_5^{*3} = -p_{45}^{\text{CM}} \cos \theta^* \end{array} \right\}, \quad (\text{A.4.5})$$

where

$$p_{45}^{\text{CM}} = \sqrt{(p_4^{*0})^2 - m_4^2}. \quad (\text{A.4.6})$$

Finally, we can express  $p_4$  and  $p_5$  in the CoM frame as a function of  $(E_3, \theta, \theta^*, \phi^*)$  by applying the following boost and rotation transformations

$$p_{4,5} = \text{Rot}_{\mathbf{y}}(\theta + \pi) \cdot \mathbf{Boost}_{\mathbf{z}}(\beta) \cdot p_{4,5}^*, \quad (\text{A.4.7})$$

where the usual boost and rotation matrices are given by

$$\mathbf{Boost}_{\mathbf{z}}(\beta) = \begin{bmatrix} \gamma & 0 & 0 & \gamma\beta \\ 0 & 1 & 0 & 0 \\ 0 & 0 & 1 & 0 \\ \gamma\beta & 0 & 0 & \gamma \end{bmatrix}, \quad \mathbf{Rot}_{\mathbf{y}}(\theta) = \begin{bmatrix} 1 & 0 & 0 & 0 \\ 0 & \cos \theta & 0 & \sin \theta \\ 0 & 0 & 1 & 0 \\ 0 & -\sin \theta & 0 & \cos \theta \end{bmatrix}. \quad (\text{A.4.8})$$

## A.5 Non-relativistic thermally averaged cross section

In this section we present the results for the non-relativistic limit of the thermally averaged cross section, using [168, 266].

It is shown there that

$$\langle \sigma v \rangle = \frac{2x^{3/2}}{\sqrt{\pi}} \int_0^\infty \sigma v_{\text{lab}} \epsilon^{1/2} \exp(-x\epsilon) d\epsilon, \quad (\text{A.5.1})$$

where  $x \equiv m_{\text{DM}}/T$ ,  $\epsilon \equiv \frac{s-4m_{\text{DM}}^2}{4m_{\text{DM}}^2}$ ,  $v_{\text{lab}} = \sqrt{s(s-4m_{\text{DM}}^2)}/(s-2m_{\text{DM}}^2) = (2\epsilon^{1/2}(1+\epsilon)^{1/2})/(1+2\epsilon)$  ( $v_{\text{lab}}$  is the relative velocity in rest frame of one of the DM particles) and  $\sigma v_{\text{lab}}$  is defined as the following integral calculated in the center of mass frame

$$\begin{aligned} \sigma v_{\text{lab}}(m_{\text{DM}} + m_{\text{DM}} \rightarrow m_3 + m_4) &= \frac{1}{64\pi^2 s} \frac{p_3^*}{p_1^*} \int d\Omega |M|^2 \frac{\sqrt{\lambda(s, m_{\text{DM}}^2, m_{\text{DM}}^2)}}{s-2m_{\text{DM}}^2} \\ &= \frac{1}{64\pi^2 s} \frac{\sqrt{\lambda(s, m_3^2, m_4^2)}}{\sqrt{\lambda(s, m_{\text{DM}}^2, m_{\text{DM}}^2)}} \int d\Omega |M|^2 \frac{\sqrt{\lambda(s, m_{\text{DM}}^2, m_{\text{DM}}^2)}}{s-2m_{\text{DM}}^2} \\ &= \frac{1}{64\pi^2 s} \frac{\sqrt{\lambda(s, m_3^2, m_4^2)}}{s-2m_{\text{DM}}^2} \int d\Omega |M|^2. \end{aligned}$$

After expanding this expression as a series in even powers of the velocity<sup>1</sup> (or equivalently as powers of  $\epsilon$ ), and keeping only the first two terms,  $(\sigma v)_{\text{lab}} \simeq a + 4b\epsilon$ , one can use the following analytical results:

$$\begin{aligned} \frac{2x^{3/2}}{\sqrt{\pi}} \int_0^\infty \epsilon^{1/2} \exp(-x\epsilon) d\epsilon &= 1, \\ \frac{2x^{3/2}}{\sqrt{\pi}} \int_0^\infty \epsilon^{3/2} \exp(-x\epsilon) d\epsilon &= \frac{3}{2x} \simeq \frac{1}{8} v_{\text{lab}}^2. \end{aligned} \quad (\text{A.5.2})$$

Therefore,

$$\langle \sigma v \rangle \simeq a + \frac{1}{2} b v_{\text{lab}}^2 \simeq a + \frac{6}{x} b, \quad (\text{A.5.3})$$

and the relic density is

$$\Omega_{\text{DM}} h^2 \approx \frac{1.07 \times 10^9 (\text{GeV})^{-1} x_f}{g_*^{1/2} M_{\text{Planck}} (a + 3b/x_f)}, \quad (\text{A.5.4})$$

where  $x_f = m_{\text{DM}}/T_f$  corresponds to the freeze out temperature  $T_f$ .

<sup>1</sup>This expansion is often called the partial wave expansion because it is equivalent to the expansion into angular-momentum eigenstates.

# Appendix B

## Appendix for Chapter 4

### B.1 Decay branching ratios, $(g - 2)_\mu$ and all that

Here we include the results concerning the dark sector described in Chapter 4 which lie outside of the main discussion.

#### B.1.1 $(g - 2)_\mu$ contribution from $A'$

The 1-loop contribution of the dark photon into the anomalous magnetic moment of the muon reads [325]

$$a_\mu = \frac{\alpha\epsilon^2}{2\pi} \int_0^1 dz \frac{2m_\mu^2 z(1-z)^2}{m_\mu^2(1-z)^2 + m_{A'}^2 z}, \quad (\text{B.1.1})$$

however, vanilla dark photon portal where  $A'$  decays visibly, *e.g.*, into a pair of  $e^+e^-$ , is already excluded. However, recent work [578] has shown that in models where  $A'$  decays invisibly - such as iDM - such explanation is still a viable solution to the  $(g - 2)_\mu$  puzzle. In particular, in Fig. 4.4, the green bands indicate the region preferred by this puzzle.

#### B.1.2 Primary production of LLPs

**Dark Photon Production** Light dark photon is mainly produced through pseudoscalar meson decays,  $P = \pi^0, \eta, \eta'$ . The corresponding branching fraction is:

$$B_{P \rightarrow \gamma A'} = 2\epsilon^2 B_{P \rightarrow \gamma\gamma} \lambda^{\frac{3}{2}}(m_P^2, m_{A'}^2, 0) / \lambda^{\frac{3}{2}}(m_P^2, 0, 0) = 2\epsilon^2 B_{P \rightarrow \gamma\gamma} \left(1 - m_{A'}^2/m_P^2\right)^3, \quad (\text{B.1.2})$$

where  $m_P$  is the mass of the pseudoscalar meson and  $B_{P \rightarrow \gamma\gamma}$  is the corresponding branching fraction. We also used the Källén function which is defined as follows:

$$\lambda(a, b, c) = (a - b - c)^2 - 4bc, \quad (\text{B.1.3})$$

In addition, dark photon can be produced by vector meson  $V = \rho, \omega$  decaying into a pseudoscalar meson  $P$  and a dark photon (*e.g.*,  $\omega \rightarrow \pi^0 A'$ ), and

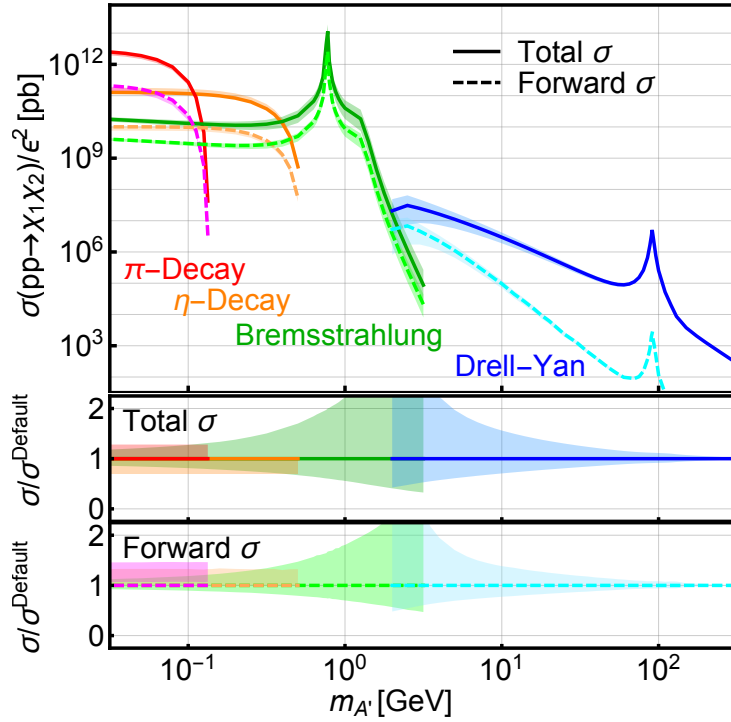


Figure B.1: Main channels of dark photon primary production as a function of its mass. Taken from [311].

by the pseudoscalar meson  $P$  decaying into a vector meson  $V$  and a dark photon (*e.g.*,  $\eta' \rightarrow \rho^0 A'$ ). We give the corresponding branching fractions, following [309]:

$$B_{V \rightarrow P A'} = \epsilon^2 B_{V \rightarrow P \gamma} \lambda^{\frac{3}{2}}(m_V^2, m_P^2, m_{A'}^2) / \lambda^{\frac{3}{2}}(m_V^2, m_P^2, 0) \quad \text{and} \quad (\text{B.1.4})$$

$$B_{P \rightarrow V A'} = \epsilon^2 B_{P \rightarrow V \gamma} \lambda^{\frac{3}{2}}(m_P^2, m_V^2, m_{A'}^2) / \lambda^{\frac{3}{2}}(m_P^2, m_V^2, 0). \quad (\text{B.1.5})$$

**Fermionic Dark Matter** If the dark fermions are heavy,  $m_1 + m_2 > m_{A'}$ , the pseudoscalar meson differential branching ratio of the  $P$  decay into  $\gamma \chi_1 \chi_2$  is [294, 296]:

$$\begin{aligned} \frac{d^2 B_{P \rightarrow \gamma \chi_1 \chi_2}}{ds d\theta} &= \mathcal{S} \epsilon^2 \alpha_D B_{P \rightarrow \gamma \gamma} \times \frac{\sin \theta \lambda^{\frac{1}{2}}(s, m_1^2, m_2^2)}{4\pi s^2} \times \\ &\times \frac{-\lambda(s, m_1^2, m_2^2) \sin^2 \theta + 2s[s - (m_1 - m_2)^2]}{(s - m_{A'}^2)^2 + m_{A'}^2 \Gamma_{A'}^2} \times \left[ 1 - \frac{s}{m_P^2} \right]^3, \end{aligned} \quad (\text{B.1.6})$$

where  $s$  is the square of the  $A'^*$  four-momentum, while  $\theta$  is the angle of the momentum of  $\chi_1$  in the rest frame of  $A'^*$ . The factor  $\mathcal{S}$  is equal to 1/2 for a single dark fermion, and 1 for different dark fermions.

In turn, if dark fermions are light,  $m_1 + m_2 < m_{A'}$ , the dominant  $\chi_1 \chi_2$  production mode is rapid decay of on-shell dark photon,  $A' \rightarrow \chi_1 \chi_2$ , with the corresponding branching ratio which is  $B(A' \rightarrow \chi_1 \chi_2) \simeq 1$  for  $\alpha_D \gg \alpha \epsilon^2$  which we assume.

**Secluded dark Higgs boson** Pseudoscalar meson decay  $P \rightarrow \gamma A'^* \rightarrow \gamma S A'$  occurs with the following branching fraction [308]:

$$\frac{d^2 B_{P \rightarrow \gamma S A'}}{ds d\theta} = \epsilon^2 \alpha_D B_{P \rightarrow \gamma \gamma} \times \frac{\sin \theta \lambda^{\frac{1}{2}}(s, m_{A'}^2, m_S^2)}{8\pi s^2} \times \frac{8m_{A'}^2 s + \lambda(s, m_{A'}^2, m_S^2) \sin^2 \theta}{(s - m_{A'}^2)^2 + m_{A'}^2 \Gamma_{A'}^2} \times \left[ 1 - \frac{s}{m_P^2} \right]^3, \quad (\text{B.1.7})$$

where  $s$  and  $\theta$  are defined analogous to Eq. (B.1.6), with  $\chi \rightarrow S$  replacement. Moreover, the branching ratio of a given vector meson, *e.g.*,  $\rho$  decays into a dark Higgs boson and a dark photon,  $\rho \rightarrow S A'$ , is [297, 308]:

$$B_{\rho \rightarrow S A'} = \epsilon^2 q_S^2 \alpha_D B_{\rho \rightarrow e^+ e^-} \times \frac{\lambda^{\frac{1}{2}}(m_\rho^2, m_{A'}^2, m_S^2)}{\alpha_{em} m_\rho^2} \times \frac{12 M_{A'}^2 m_\rho^2 + \lambda(m_\rho^2, m_{A'}^2, m_S^2)}{(m_\rho^2 - m_{A'}^2)^2 + m_{A'}^2 \Gamma_{A'}^2}. \quad (\text{B.1.8})$$

### B.1.3 LLPs decays

**Dark Photon decays** Dark photon decays into SM particles are characterized by the following decay width:

$$\Gamma_{A'} = \frac{\Gamma_{A' \rightarrow e^+ e^-}}{B_e(m_{A'})}, \quad \text{where} \quad \Gamma_{A' \rightarrow e^+ e^-} = \frac{\epsilon^2 e^2 m_{A'}}{12\pi} \times \left[ 1 - \frac{4m_e^2}{m_{A'}^2} \right]^{\frac{1}{2}} \times \left[ 1 + \frac{2m_e^2}{m_{A'}^2} \right], \quad (\text{B.1.9})$$

where  $m_e$  is the mass of the electron, and  $B_e = B(A' \rightarrow e^+ e^-)$  is the branching fraction corresponding to the decay into an electron-positron pair. In our analysis  $m_{A'}$  typically lies below the di-muon threshold where  $B_e = 1$ . For heavier dark photons, another decay channels open up:  $\mu^+ \mu^-$ , and also hadronic final states are possible [579].

**Decay of  $\chi_2$  in iDM models** For the differential branching ratio for three-body decay into an electron-positron pair,  $\chi_2 \rightarrow \chi_1 e^+ e^-$ , we use the formula from [302]. For heavier dark fermions and a larger mass splitting between them, decays to other SM particles become kinematically allowed. We take this into account by considering the branching ratio of an off-shell dark photon decaying into an electron-positron pair,  $B_e(m_{A'^*} = m_{ee})$ , evaluated at the invariant mass of the electron pair  $m_{ee}$ . The decay width is then given by

$$\Gamma_2 = \frac{g_{12}^2 \epsilon^2 \alpha}{64\pi^2 m_{\chi_2}^3} \times \int_{s_2^-}^{s_2^+} ds_2 \int_{s_1^-}^{s_1^+} ds_1 \frac{4|A|^2}{(m_1^2 + m_2^2 + 2m_e^2 - s_1 - s_2 - m_{A'}^2)^2 + m_{A'}^2 \Gamma_{A'}^2} \times \frac{1}{B_e(m_{A'^*} = m_{ee})}, \quad (\text{B.1.10})$$

where  $\Gamma_{A'}$  is given in Eq. (B.1.9) and

$$|A|^2 = (s_1 + s_2 - 2m_1 m_2 - 2m_e^2) [(m_1 + m_2)^2 + 4m_e^2] + 2(m_e^2 + m_1 m_2)^2 - s_1^2 - s_2^2, \quad (\text{B.1.11})$$

and integration limits are

$$s_1^\pm = m_1^2 + m_e^2 + \frac{1}{2s_2} \left[ (m_2^2 - m_e^2 - s_2)(m_1^2 - m_e^2 + s_2) \pm \lambda^{\frac{1}{2}}(s_2, m_2^2, m_e^2) \lambda^{\frac{1}{2}}(s_2, m_1^2, m_e^2) \right], \quad (\text{B.1.12})$$

$$s_2^+ = (m_2 - m_e)^2, \text{ and } s_2^- = (m_1 + m_e)^2. \quad (\text{B.1.13})$$

## B.2 Scattering cross sections for secondary LLP production

We give formulae for the scattering cross sections leading to secondary LLP production,  $\text{LLP}_1 + T \rightarrow \text{LLP}_2 + T$  where an electron or a nucleus can be the target,  $T = e, N$ . Specifically, in the models discussed by us in Sections 4.2.1 to 4.2.3,  $\text{LLP}_1 = \chi, \chi_1$  or  $S$ , while  $\text{LLP}_2 = A', \chi_2$  or  $A'$ , respectively. It is worth noting that all models have slightly different kinematics in both the secondary production and the subsequent decay of  $\text{LLP}_2$ :

- $2 \rightarrow 3$  scattering followed by a 2-body decay (dark bremsstrahlung; cf Section 4.2.1),
- $2 \rightarrow 2$  scattering followed by a 3-body decay (iDM; cf Section 4.2.2),
- $2 \rightarrow 2$  scattering followed by a 2-body decay (secluded dark Higgs boson; cf Section 4.2.3).

### B.2.1 $2 \rightarrow 2$ scatterings

For models with iDM and secluded dark Higgs boson,  $2 \rightarrow 2$  scattering processes lead to secondary LLP production. The differential cross section in the lab frame is

$$\frac{d\sigma}{dE_T} = \frac{m_T}{8\pi\lambda(s, m_T^2, m_1^2)} \overline{|\mathcal{M}|^2}, \quad (\text{B.2.1})$$

where  $E_T$  and  $m_T$  is the energy and mass of the recoiling target, and  $m_1 \equiv m_{\text{LLP}_1}$  is the mass of the initial state scattered LLP. The limits of integration are

$$E_T^\pm = \frac{s + m_T^2 - m_2^2}{2s} \times (E_1 + m_T) \pm \frac{\lambda^{\frac{1}{2}}(s, m_T^2, m_2^2)}{2s} \times p_1, \quad (\text{B.2.2})$$

where  $E_1$  and  $E_2$  are the initial and final state LLP energies, and  $m_2 \equiv m_{\text{LLP}_2}$ .

#### B.2.1.1 Scatterings with electrons

**iDM** The squared matrix element for upscattering  $\chi_1 e \rightarrow \chi_2 e$  is given by [306]:

$$\overline{|\mathcal{M}|^2} = \frac{8(\epsilon e g_{12})^2 m_e}{(2m_e(E_{\chi_2} - E_{\chi_1}) - m_{A'}^2)^2} \times \mathcal{M}_0, \quad (\text{B.2.3})$$

where the amplitude is:

$$\begin{aligned} \mathcal{M}_0 = & m_e (E_{\chi_1}^2 + E_{\chi_2}^2) - (\delta m_\chi)^2 (E_{\chi_2} - E_{\chi_1} + m_e) / 2 + m_e^2 (E_{\chi_2} - E_{\chi_1}) \\ & + m_{\chi_1}^2 E_{\chi_2} - m_{\chi_2}^2 E_{\chi_1}, \text{ with } \delta m_\chi = m_{\chi_2} - m_{\chi_1}. \end{aligned} \quad (\text{B.2.4})$$

**Secluded dark Higgs boson** The squared matrix element for the process  $Se \rightarrow A'e$  is [580]:

$$|\overline{\mathcal{M}}|^2 = \frac{4(\epsilon e g_{12})^2 m_e}{\{2m_e(E_2 - E_1) - m_{A'}^2\}^2} [E_1(2E_2 m_e + m_{A'}^2) + E_2(m_S^2 - 2m_{A'}^2) - 2m_{A'}^2 m_e], \quad (\text{B.2.5})$$

where  $E_1 = E_S$  and  $E_2 = E_{A'}$ .

### B.2.1.2 Scatterings with nuclei

The coupling between dark photon and protons depends on nuclear form factors in the following way:  $\mathcal{J}_\mu = \bar{u}(p_4) [F_1 \gamma_\mu - (\sigma_{\mu\nu} q^\nu / 2m_p)] u(p_2)$  which is the nucleon electromagnetic current.  $F_1(q^2)$  and  $F_2(q^2)$  are the Dirac and Pauli form factors, respectively, and  $q^2 = -Q^2 < 0$  is the momentum transfer squared. We use the following commonly used Sachs form factors:  $G_E = F_1 - \tau F_2$  and  $G_M = F_1 + F_2$  where we defined  $\tau = Q^2 / (4m_p^2) > 0$ . We will also use the dipole approximation, applicable for  $Q^2 \lesssim 1$  GeV which is the regime of low momentum exchange relevant for our analysis

$$G_E = (1 + Q^2 / 0.71 \text{ GeV}^2)^{-2} = G_M / \mu_p, \quad (\text{B.2.6})$$

where  $\mu_p = 2.79$  is the magnetic moment of the proton, and in the last step we used the usual approximation that a simple scaling  $G_M \simeq \mu_p G_E$  holds for small values of  $Q^2$ . The most convenient parametrization of the form factors is as follows:

$$G_1 = \tau G_M^2 = \tau \mu_p^2 G_E^2 \quad \text{and} \quad G_2 = \frac{G_E^2 + \tau G_M^2}{1 + \tau} \stackrel{\tau_1}{\simeq} G_E^2 [1 + \tau (\mu_p^2 - 1)]. \quad (\text{B.2.7})$$

One sees that from Eq. (B.2.7) that for a small momentum transfer,  $\tau \ll 1$ ,  $G_2 \gg G_1$  so any term proportional to  $G_1$  in the cross section can be neglected. Moreover, whenever the momentum transfer is small, the scattering occurs with the nuclei coherently and we implement the relevant nuclear form factors following [581–583]

$$G_{2,\text{tot}}(t) = G_{2,\text{el}}(t) + G_{2,\text{inel}}(t), \quad (\text{B.2.8})$$

where  $G_{2,\text{el}}$  and  $G_{2,\text{inel}}$  are the coherent and incoherent scattering form factors given by

$$G_{2,\text{el}}(t) = Z^2 \left[ \frac{a^2 t}{1 + a^2 t} \right]^2 \left[ \frac{1}{1 + td} \right]^2 \quad \text{and} \quad G_{2,\text{inel}}(t) = Z \left[ \frac{a'^2 t}{1 + a'^2 t} \right]^2 \left[ \frac{G_E^2 + \tau G_M^2}{1 + \tau} \right] \simeq Z \left[ \frac{a'^2 t}{1 + a'^2 t} \right]^2 \left[ \frac{1 + (t/4m_p^2)(\mu_p^2 - 1)}{(1 + t/0.71 \text{ GeV}^2)^4} \right]. \quad (\text{B.2.9})$$

The atomic coherent and incoherent form factors are parametrized by:  $a = 111 Z^{-1/3} / m_e$ , and  $a' = 773 Z^{-2/3} / m_e$ , respectively, while the coherent nucleus form factor is parametrized by:  $d = 0.164 \text{ GeV}^2 A^{-2/3}$  where  $Z$  ( $A$ ) is the atomic (mass) number of the nucleus.

**Inelastic DM** The squared matrix element for process  $\chi_1 N \rightarrow \chi_2 N$  is:

$$|\overline{\mathcal{M}}|^2 = \frac{8(\epsilon e g_{12})^2 m_p}{(2m_p(E_{\chi_2} - E_{\chi_1}) - m_{A'}^2)^2} \times \left[ \frac{1}{2} \mathcal{M}_1 G_2 + \frac{G_1}{\tau} (\mathcal{M}_0 - \frac{1}{2} \mathcal{M}_1) \right], \quad (\text{B.2.10})$$

where  $\mathcal{M}_0$  is given by Eq. (B.2.4) and  $\mathcal{M}_1$  is:

$$\begin{aligned} \mathcal{M}_1 = m_T & \left( [E_{\chi_1} + E_{\chi_2} - (m_{\chi_2}^2 - m_{\chi_1}^2)/(2m_T)]^2 \right. \\ & \left. + (E_{\chi_1} - E_{\chi_2} + 2m_T)[(E_{\chi_2} - E_{\chi_1}) - \delta_m^2/(2m_T)] \right). \end{aligned} \quad (\text{B.2.11})$$

**Secluded dark Higgs Boson** The squared matrix element for the process  $SN \rightarrow A'N$  is:

$$\begin{aligned} |\overline{\mathcal{M}}|^2 = & \frac{2(\epsilon e g_{12})^2}{\{2m_p(E_{\chi_2} - E_{\chi_1}) - m_{A'}^2\}^2} \left[ \right. \\ & - \left( m_S^2 Q^2 + \frac{1}{4} (Q^2 - m_S^2 + m_{A'}^2)^2 + 3m_{A'}^2 Q^2 \right) \frac{G_1}{\tau} \\ & \left. + \left\{ \left( 2E_1 m_T - \frac{1}{2} (Q^2 - m_S^2 + m_{A'}^2) \right)^2 - m_{A'}^2 (Q^2 + 4m_T^2) \right\} \right. \\ & \left. \left[ G_2 - G_1 \frac{2(\mu_p - 1)}{\mu_p^2} \right] \right]. \end{aligned} \quad (\text{B.2.12})$$

The above scattering cross sections are dominated by the contributions proportional to  $G_2 = G_{2,\text{tot}}$ , as mentioned previously.

# Appendix C

## Appendix for Chapter 5

### C.1 HNL production in neutrino interactions

Here we report the results needed to obtain the HNL spectrum due to the secondary production, which we described in Chapter 5.

#### C.1.1 Coherent scatterings with nuclei

The coherent scatterings between the SM neutrinos and nuclei provide the dominant secondary production channel for the HNLs due to the  $Z^2$  and  $(A - Z)^2$  enhancement factors [191] and to the typically low momentum transfer associated with such scattering. This avoids the activation of veto layers in secondary production processes occurring upstream of the detector. In our analysis, we follow [2] regarding the cuts used in the analysis. In addition, we require an additional momentum transfer suppression,  $|Q^2| < (100 \text{ MeV})^2$ , for the scattering events generating high-energy ( $E_\gamma > 1 \text{ TeV}$  or  $3 \text{ TeV}$ ) single photons in the ECC detector. This allows the identification of single photon vertices without additional hadronic activity in the emulsion. The formulae for coherent production cross sections are:

- for the neutrino dipole portal model to HNLs, cf. Section 5.3.1,

$$\begin{aligned} \frac{d\sigma(\nu + X_Z^A \rightarrow N + X_Z^A)}{dt} &= \frac{-\alpha\mu_N^2 F_1^2(\sqrt{-t})}{t^2(m_T^2 - m_N(2E_\nu + m_N))^2} \times \\ &\times \left( m_N t (8E_\nu^2 m_N + 4E_\nu(m_N^2 + t) + m_N(m_N^2 + t)) \right. \\ &\quad \left. + 2m_T^2(-2m_N t(2E_\nu + m_N) + m_N^4 - t^2) + 2m_T^4 t \right) \\ &+ \frac{\alpha\mu_N^2 F_2^2(\sqrt{-t})}{2tm_T^2(m_T^2 - m_N(2E_\nu + m_N))^2} \times \\ &\times \left( 4t(m_T^2 - 2E_\nu m_N)(m_T^2 - m_N(2E_\nu + m_N)) \right. \\ &\quad \left. + m_N t^2(8E_\nu + 3m_N) - 4m_T^2 m_N^4 + t^3 \right), \end{aligned} \tag{C.1.1}$$

- for the model with the dark gauge boson,

$$\begin{aligned} \frac{d\sigma(\nu + X_Z^A \rightarrow N + X_Z^A)}{dt} &= \frac{\alpha F_1^2(\sqrt{-t}) |U_{D4}|^2 (1 - |U_{D4}|^2)}{32s_W^4 c_W^4 E_\nu^2 m_T^2 (m_Z^2 - t)^2 (m_{Z_D}^2 - t)^2} \times \quad (\text{C.1.2}) \\ &\times \left( 8E_\nu^2 m_T^2 + 4E_\nu m_T (t - m_N^2) - (2m_T^2 + t)(m_N^2 - t) \right) \times \\ &\times \left( \pi\alpha (m_{Z_D}^2 - t)^2 \frac{(A + 4s_W^2 Z - 2Z)^2}{Z^2} + 32c_W^4 \epsilon^2 g_D^2 s_W^4 (m_Z^2 - t)^2 \right), \end{aligned}$$

where the masses of the target nucleus and the HNL are  $m_T$  and  $m_N$ , respectively,  $A$  ( $Z$ ) is the atomic mass (number) of the nucleus, while  $s_W$  and  $c_W$  are the sine and cosine of the Weinberg angle.

In the above expressions, we take the electric form factor  $F_1$  which we parametrize with the Helm form factor  $F$  [584]

$$F_1^2(\sqrt{-t}) = Z^2 F^2(\sqrt{-t}), \quad (\text{C.1.3})$$

where

$$F = F_{\text{Helm}}(Q) = 3 \exp\left(\frac{-Q^2 s^2}{2}\right) \frac{\sin(Qr) - Qr \cos(Qr)}{(Qr)^3}, \quad (\text{C.1.4})$$

and  $Q = \sqrt{-q^2} = \sqrt{-t}$  is the square root of the momentum transfer. We assume  $s = 1$  fm,  $r = \sqrt{R^2 - 5s^2}$ , and  $R = 1.2A^{1/3}$  fm.

We also included the effect of electron screening of the nucleus which can occur in the coherent regime. This is achieved by multiplying Appendix C.1.1 by the atomic form factor [581, 582]

$$G_{at}(Q) = \frac{a^2 Q^2}{1 + a^2 Q^2}, \quad (\text{C.1.5})$$

where  $a = 111Z^{-1/3}/m_e$ . We verified that this effect has a negligible impact on the results, therefore, we do not include it in the formulae for the cross sections above.

The magnetic form factor is not known analytically in the coherent regime, but in it there is no enhancement by factor of  $Z^2$ , so the corresponding contribution to the cross section is negligible relative to the contribution proportional to  $F_1$ .

### C.1.2 Elastic incoherent scatterings off individual nucleons

Neutrino upscattering to HNLs can also occur incoherently, by scatterings with individual protons or neutrons. In such a case, the expression for the scattering cross section is also given by Eqs. (C.1.1) and (C.1.2), but with the following replacements. The target mass is replaced by  $m_T = m_p$  or  $m_n$ , and one needs to use the following form factors:

$$\begin{aligned} F_1^{p,n} &= \frac{G_E^{p,n} + G_M^{p,n} \frac{Q^2}{4m_p^2}}{1 + \frac{Q^2}{4ma_p^2}}, \\ F_2^{p,n} &= \frac{G_M^{p,n} - G_E^{p,n}}{1 + \frac{Q^2}{4m_p^2}}. \end{aligned} \quad (\text{C.1.6})$$

We express the electric ( $F_1^{p,n}$ ) and magnetic ( $F_2^{p,n}$ ) form factors through the Sachs electric and magnetic form factors  $G_E^{p,n}$  and  $G_M^{p,n}$ , respectively. We employ the dipole approximation to evaluate them which is standard practice, provided the momentum transfer is small,  $Q^2 \sim 10 \text{ GeV}^2$  [585] which is indeed satisfied in our analysis. This leads to the following formulae used by us:

$$G_D = \left(1 + \frac{Q^2}{0.71 \text{ GeV}^2}\right)^{-2}, \quad (\text{C.1.7})$$

where

$$\begin{aligned} G_E^{\{p,n\}} &= \{G_D, 0\}, \\ G_M^{\{p,n\}} &= \mu_{\{p,n\}} G_D, \\ \mu_{p,n} &= \{2.793, -1.913\}. \end{aligned} \quad (\text{C.1.8})$$

It is worth pointing out that in the incoherent regime, the total cross section scales only linearly with the number of nucleons,  $\sigma_{\text{total, incoh.}} = Z \times \sigma_p + (A - Z) \times \sigma_n$  which explains why the coherent scatterings dominate.

### C.1.3 Scattering off electrons

HNLs are also produced by neutrino upscattering on electrons. The corresponding cross section formulae are of the form

- for the neutrino dipole portal,

$$\begin{aligned} \frac{d\sigma(\nu + e^- \rightarrow N + e^-)}{dt} &= \frac{-\alpha\mu_N^2}{2m_e^2 E_\nu^2 t^2} (2m_e^2(4E_\nu^2 t + m_N^4 - m_N^2 t) \\ &\quad + 4E_\nu m_e t(t - m_N^2) + m_N^2 t(m_N^2 - t)), \end{aligned} \quad (\text{C.1.9})$$

- for the dark gauge boson portal,

$$\begin{aligned} \frac{d\sigma(\nu + e^- \rightarrow N + e^-)}{dt} &= \alpha\epsilon^2 g_D^2 U_{4\tau}^2 (1 - U_{4\tau}^2) \times \\ &\quad \frac{(8E_1^2 m_e^2 - 2m_N^2(4E_1 m_e + m_e^2 + t) + 2m_e t(2E_1 + m_e) + 2m_N^4 + t^2)}{2E_1^2 m_e^2 (m_{Z_D}^2 - t)^2}. \end{aligned} \quad (\text{C.1.10})$$

We also consider elastic scattering of HNLs on electrons with the corresponding cross section given by

$$\frac{d\sigma(N + e^- \rightarrow N + e^-)}{dt} = \alpha\epsilon^2 g_D^2 \frac{(8E_1^2 m_e^2 + 2t(m_e(2E_1 + m_e) + m_N^2) + t^2)}{2m_e^2 (E_1^2 - m_N^2) (m_{Z_D}^2 - t)^2}. \quad (\text{C.1.11})$$

## C.2 Decays widths

For completeness, we also report the corresponding decay widths used in our study.

**Neutrino dipole portal to HNLs** In the dipole portal scenario, the dominant width of the two-body decay of the HNL into a SM neutrino and a photon is given by [356]

$$\Gamma = \frac{\mu_N^2 m_N^3}{4\pi}. \quad (\text{C.2.1})$$

HNL can also decay into a three-body final state. The corresponding decay width into a pair of leptons and a photon,  $N \rightarrow \gamma \ell \ell$ , is

$$\Gamma_{N \rightarrow \gamma \ell \ell} = \frac{1}{512\pi^3 m_N^3} \int_{4m_\ell^2}^{m_N^2} ds_2 \int_{s_1^{\min}}^{s_1^{\max}} ds_1 |M|^2, \quad (\text{C.2.2})$$

where

$$|M|^2 = \frac{8\mu_N^2 e^2}{s_2^2} \left( 2m_\ell^4 s_2 + 2m_\ell^2 (m_N^4 - s_2(2s_1 + s_2)) + s_2 (m_N^4 - m_N^2(2s_1 + s_2) + 2s_1(s_1 + s_2)) \right). \quad (\text{C.2.3})$$

The differential cross section is

$$\frac{d\Gamma_{N \rightarrow \gamma \ell \ell}}{ds_2} = \frac{\mu_N^2 e^2 \sqrt{1 - \frac{4m_\ell^2}{s_2}} (2m_\ell^2 + s_2) (m_N^2 - s_2)^2 (2m_N^2 + s_2)}{192\pi^3 s_2^2 m_N^3}. \quad (\text{C.2.4})$$

The total cross section is

$$\begin{aligned} \Gamma_{N \rightarrow \gamma \ell \ell} = & \frac{e^2 \mu_N^2}{96\pi^3 m_N^3} \left( \left( 8m_\ell^6 - 2m_N^6 \right) \log \left( \frac{2m_\ell}{\sqrt{m_N^2 - 4m_\ell^2} + m_N} \right) + \right. \\ & \left. + m_N \sqrt{m_N^2 - 4m_\ell^2} \left( -2m_\ell^4 + 5m_\ell^2 m_N^2 - 3m_N^4 \right) \right) \end{aligned} \quad (\text{C.2.5})$$

To apply a 100 GeV threshold for the visible energy in the detector, the integration in Eq. (C.2.4) must be performed with the appropriate conditions enforced. We call the result an ‘‘effective’’ branching fraction when, *e.g.*, discussing the right panel of Fig. 5.2 in Section 5.4.

**Model with the dark gauge boson** In the case where  $m_N > m_{Z_D}$ , in which the decay  $N \rightarrow Z_D \nu$  is possible, we use the result from [332]

$$\Gamma_{N_D \rightarrow Z_D \nu} = \frac{\alpha_D}{2} |U_{D4}|^2 (1 - |U_{D4}|^2) \frac{m_{N_D}^3}{m_{Z_D}^2} \left( 1 - \frac{m_{Z_D}^2}{m_{N_D}^2} \right) \left( 1 + \frac{m_{Z_D}^2}{m_{N_D}^2} - 2 \frac{m_{Z_D}^4}{m_{N_D}^4} \right). \quad (\text{C.2.6})$$

In this case, the dark gauge boson can subsequently decay into an  $e^+e^-$  or  $\nu\bar{\nu}$  pair with the corresponding decay widths given, respectively, by

$$\Gamma_{Z_D \rightarrow e^+e^-} \approx \frac{\alpha \epsilon^2}{3} m_{Z_D}, \quad (\text{C.2.7})$$

and

$$\Gamma_{Z_D \rightarrow \nu\nu} = \frac{\alpha_D}{3} (1 - |U_{D4}|^2)^2 m_{Z_D}, \quad (\text{C.2.8})$$

where  $\alpha_D = g_D^2/(4\pi)$ . We considered the benchmark scenarios where  $\alpha \epsilon^2 \gg \alpha_D (1 - |U_{D4}|^2)^2$  where  $Z_D$  decays mainly into the  $e^+e^-$  final state.

For the case of  $m_N < m_{Z_D}$ , we use the result from [383, 586]

$$\Gamma_{N \rightarrow \nu_\tau e^- e^+} = \frac{G_D^2 \epsilon^2}{48\pi^3} |U_{\tau 4}|^2 m_N^5 \left[ I_2 \left( 0, \frac{m_e}{m_N}, \frac{m_e}{m_N} \right) + 2I_1 \left( 0, \frac{m_e}{m_N}, \frac{m_e}{m_N} \right) \right], \quad (\text{C.2.9})$$

where  $G_D = g_D^2 / (4\sqrt{2}m_{Z_D}^2)$  and the definitions of the functions  $I_1, I_2$  are

$$I_1(x, y, z) = 12 \int_{(x+y)^2}^{(1-z)^2} \frac{ds}{s} (s - x^2 - y^2) (1 + z^2 - s) \lambda^{1/2}(s, x^2, y^2) \lambda^{1/2}(1, s, z^2), \quad (\text{C.2.10})$$

$$I_2(x, y, z) = 24yz \int_{(y+z)^2}^{(1-x)^2} \frac{ds}{s} (1 + x^2 - s) \lambda^{1/2}(s, y^2, z^2) \lambda^{1/2}(1, s, x^2), \quad (\text{C.2.11})$$

where we used Eq. (B.1.3).



# Appendix D

## Appendix for Chapter 6

Below, we briefly discuss formal aspects of supersymmetry which are relevant to our discussion in Chapter 6.

### D.1 Superalgebra and superspace

Another motivations for SUSY was circumvention of the Coleman-Mandula theorem [587] which states that assuming commutation relations form a Lie algebra represented by bosonic generator, the most general symmetries of a relativistic quantum field theory are Poincare invariance and gauge symmetries. SUSY is defined by a graded Lie superalgebra which introduces both commuting, and anticommuting generators. Moreover, such extension was shown to be unique by Haag, Lopuszanski and Sohnius [588], generalizing the Coleman-Mandula theorem. We will introduce SUSY from this angle in this section, while in the next one, we will discuss the physical content of the simplest phenomenologically viable supersymmetric theory - the MSSM.

The superalgebra with  $\mathcal{N} = 1^1$  fermion generator  $Q_\alpha$  is defined by relations (the generators of  $SU(3) \times SU(2) \times U(1)$  which commute with the generators for the Poincare group - translations  $P^\mu$  and Lorentz transformations  $M^{\mu\nu}$  - are not shown):

$$\begin{aligned} [P^\mu, P^\nu] &= 0, \\ [M^{\mu\nu}, P^\lambda] &= i(g^{\nu\lambda}P^\mu - g^{\mu\lambda}P^\nu), \\ [M^{\mu\nu}, M^{\rho\sigma}] &= i(g^{\nu\rho}M^{\mu\sigma} + g^{\mu\sigma}M^{\nu\rho} - g^{\mu\rho}M^{\nu\sigma} - g^{\nu\sigma}M^{\mu\rho}), \\ [P^\mu, Q_\alpha] &= 0 = [P^\mu, Q_{\dot{\alpha}}], \\ [M^{\mu\nu}, Q_\alpha] &= -i(\sigma^{\mu\nu})_\alpha{}^\beta Q_\beta, \\ [M^{\mu\nu}, Q_{\dot{\alpha}}] &= -i(\bar{\sigma}^{\mu\nu})^{\dot{\alpha}}{}_{\dot{\beta}} Q^{\dot{\beta}}, \\ \{Q_\alpha, Q_\beta\} &= 0 = \{Q_{\dot{\alpha}}, Q_{\dot{\beta}}\}, \\ \{Q_\alpha, Q_{\dot{\beta}}\} &= 2\sigma_{\alpha\dot{\beta}}^\mu P_\mu. \end{aligned} \tag{D.1.1}$$

---

<sup>1</sup>We limit further discussion to this case which, nonetheless, leads to a rich phenomenology, since this is the only case that incorporates chiral fermions which are a peculiar and rather constraining feature of the SM.

Formally, from the above superalgebra, one can construct a Poincare supergroup where any of its element has the following form:

$$g = \exp i(\omega^{\mu\nu} M_{\mu\nu} + a^\mu P_\mu + \theta^\alpha Q_\alpha + \bar{\theta}_{\dot{\alpha}} \bar{Q}^{\dot{\alpha}}). \quad (\text{D.1.2})$$

The first two terms under the exponent correspond to Lorentz transformations and translations, while the last two - to transformations in fermionic dimension. In fact,  $\theta^\alpha$  and  $\bar{\theta}_{\dot{\alpha}}$  are Weyl spinors, whose components are Grassmann variables.

To guarantee the stability of the lightest SUSY particle - and also to prohibit proton decay - a discrete symmetry, called  $R$  parity is introduced

$$P_R = (-1)^{3B+L+2s}, \quad (\text{D.1.3})$$

where  $B$  is the baryon number,  $L$  is the lepton number, and  $s$  is the spin.

In result, the SM and Higgs particles are R-even, while their supersymmetric counterparts are R-odd.

**Superfields** are objects living in a superspace that transform appropriately with respect to the superalgebra Eq. (D.1.1).

The formal definition of a superspace is that of a quotient space

$$\text{Superspace} = \text{Superalgebra Poincare/Lorentz algebra} = \{\omega^{\mu\nu}, x^\mu, \theta^\alpha, \bar{\theta}_{\dot{\alpha}}\} / \{\omega^{\mu\nu}\}, \quad (\text{D.1.4})$$

and superfield is a function  $\Phi(x, \theta, \bar{\theta})$ . Due to the anticommutation of  $\theta_\alpha$ , a superfield can be a polynomial of at most second degree in  $(\theta, \bar{\theta})$ .

On the one hand,  $\Phi(x, \theta, \bar{\theta})$  is a field operator, while on the other hand, it is an element of the state space (representation of superalgebra) which is a Hilbert space.

Thus, by performing the infinitesimal transformation in both ways and comparing, we obtain the form of the operators in Hilbert space and the infinitesimal transformation of the superspace ( $\epsilon, \bar{\epsilon}$  to infinitezimalne parametry) [589]

$$\begin{aligned} (x^\mu, \theta, \bar{\theta}) &\mapsto (x^\mu + i\theta\sigma^\mu\bar{\epsilon} - i\epsilon\sigma^\mu\bar{\theta}, \theta + \epsilon, \bar{\theta} + \bar{\epsilon}), \\ \mathcal{P}_\mu &= -i\partial_\mu, \\ \mathcal{Q}_\alpha &= -i\frac{\partial}{\partial\theta^\alpha} - (\sigma^\mu)_{\alpha\dot{\beta}}\bar{\theta}^{\dot{\beta}}\frac{\partial}{\partial x^\mu}, \\ \bar{\mathcal{Q}}_{\dot{\alpha}} &= i\frac{\partial}{\partial\bar{\theta}^{\dot{\alpha}}} + \theta^\beta(\sigma^\mu)_{\beta\dot{\alpha}}\frac{\partial}{\partial x^\mu}. \end{aligned} \quad (\text{D.1.5})$$

Due to the chiral structure of the SM (weak interactions only select the left-handed components), also in supersymmetric models one should use chiral superfields that retain the given chirality upon supertransformations.

To realize this bound, supercovariant derivatives are introduced

$$D_\alpha = \frac{\partial}{\partial\theta^\alpha} + i(\sigma^\mu)_{\alpha\dot{\beta}}\bar{\theta}^{\dot{\beta}}\frac{\partial}{\partial x^\mu}, \quad \bar{D}_{\dot{\alpha}} = -\frac{\partial}{\partial\bar{\theta}^{\dot{\alpha}}} - i\theta^\beta(\sigma^\mu)_{\beta\dot{\alpha}}\frac{\partial}{\partial x^\mu}. \quad (\text{D.1.6})$$

They fulfill the following anticommutation relations:

$$\{D_\alpha, \mathcal{Q}_\beta\} = \{D_\alpha, \bar{\mathcal{Q}}_{\dot{\beta}}\} = \{\bar{D}_{\dot{\alpha}}, \mathcal{Q}_\beta\} = \{\bar{D}_{\dot{\alpha}}, \bar{\mathcal{Q}}_{\dot{\beta}}\} = 0, \quad (\text{D.1.7})$$

and

$$\{D_\alpha, \bar{D}_{\dot{\beta}}\} = 2\sigma_{\alpha\dot{\beta}}^\mu P_\mu, \quad \{D_\alpha, D_\beta\} = \{\bar{D}_{\dot{\alpha}}, \bar{D}_{\dot{\beta}}\} = 0. \quad (\text{D.1.8})$$

With supercovariant derivatives, one can define irreducible superfields

- chiral:  $\bar{D}_{\dot{\alpha}}\Phi = 0$
- anti-chiral:  $D_\alpha\bar{\Phi} = 0$
- vector:  $V^\dagger = V$ .

As one can directly check,

$$\bar{D}_{\dot{\alpha}}(x^\mu + i\theta\sigma^\mu\bar{\theta}) = 0, \quad (\text{D.1.9})$$

therefore, any function of the variable  $y^\mu = x^\mu + i\theta\sigma^\mu\bar{\theta}$  is a chiral superfield.

## D.2 Constructing SUSY Lagrangian

The superfield formalism is introduced, among other things, in order to be able to write down the supersymmetric theory in a relatively simple way, as we show below.

We write down the chiral superfield explicitly

$$\Phi(y, \theta) = \phi(y) + \sqrt{2}\theta\psi(y) + \theta\theta F(y), \quad (\text{D.2.1})$$

where  $\phi$  is a complex scalar,  $\psi$  is a Weyl fermion, and  $F$  is a bosonic field of dimension 2.

One can show that under supersymmetry transformation the components change as follows [590]:

$$\begin{aligned} \delta_\epsilon\phi(x) &= \sqrt{2}\epsilon\psi(x), \\ \delta_\epsilon\psi(x) &= i\sqrt{2}\sigma^\mu\bar{\epsilon}\partial_\mu\phi(x) + \sqrt{2}\epsilon F(x), \\ \delta_\epsilon F(x) &= i\sqrt{2}\bar{\epsilon}\bar{\sigma}^\mu\partial_\mu\psi(x). \end{aligned} \quad (\text{D.2.2})$$

The last equation states that  $\delta_\epsilon F(x)$  is a total derivative, hence  $|F|^2$  term can appear in SUSY Lagrangian.

Moreover, the product of chiral superfields is also chiral, thus,  $F$  terms arising from linear combinations of products of other chiral fields will also form a supersymmetric Lagrangian. Such terms, provided they are also gauge invariant, form the superpotential  $W$ .

We showed that

$$L_{SUSY} \supseteq \int d^2\theta W(\Phi) + h.c., \quad (\text{D.2.3})$$

where demanding renormalizability, we obtained  $[\mathcal{L}] \leq 4$ , and because  $[d^2\theta] = 1$ ,  $[W] \leq 3$  follows.

Using Taylor expansion in Grassmann variables, we obtain a part of SUSY Lagrangian density

$$\mathcal{L}_{SUSY} \supset \left| \frac{\partial W(\phi)}{\partial \Phi} \right|^2 - \frac{1}{2} \left( \frac{\partial^2 W(\phi)}{\partial \Phi \partial \Phi} \psi\psi + h.c. \right), \quad (\text{D.2.4})$$

where the first term is a Mexican-hat type potential, while the second term gives the Yukawa interactions.

To introduce interactions with the gauge bosons, we introduce a vector superfield which in the Wess-Zumino gauge has the following form:

$$V(x, \theta, \bar{\theta}) = \theta\sigma\bar{\theta}V_\mu(x) + i\theta\theta\bar{\theta}\bar{\lambda}(x) + \frac{1}{2}\theta\theta\bar{\theta}\bar{\theta}D(x), \quad (\text{D.2.5})$$

where  $V_\mu$  is a real vector field,  $\lambda$  is a Majorana fermion<sup>2</sup> (called gaugino), and  $D$  is a bosonic field of dimension 2.

Similarly to Eq. (D.2.2) one can show that the components of the vector superfield transform appropriately under the supersymmetry transformation, and that in particular the  $D$  term transforms as a total derivative. It is used to construct another term in the SUSY Lagrangian, the so-called, Kähler potential

$$\mathcal{L}_{SUSY} \supset K(\Phi, \Phi^\dagger)|_D, \quad (\text{D.2.6})$$

where  $K$  is at most dimension 2, gauge invariant, real function of  $\Phi$  and  $\Phi^\dagger$ , while  $|_D$  indicates that one only takes the term proportional to  $D$ . Thus, thanks to transformation properties of  $D$  and  $F$ , we obtained the kinetic term and potential terms in the Lagrangian, respectively.

After introducing the basics of SUSY, one can easily construct realistic phenomenological models of (softly-broken) supersymmetry, see. Section 6.2 for a brief description of MSSM, the simplest realistic model of this type.

---

<sup>2</sup>Such fermion is its own antiparticle.

# Appendix E

## Appendix for Chapter 7

### E.1 Particle physics formulae

Below, we give expressions for the decay widths and scattering cross sections relevant to our analysis described in Chapter 7.

#### E.1.1 Decay widths

**Decay width of  $h_D$**  The partial decay width of the dark Higgs boson decay into a pair of leptons,  $h_D \rightarrow l^+l^-$ , is [267]

$$\Gamma(h_D \rightarrow l^+l^-) = \frac{\theta_{Hh_D}^2 m_l^2 m_{h_D}}{8\pi v_{SM}^2} \left(1 - \frac{4m_l^2}{m_{h_D}^2}\right)^{3/2}, \quad (\text{E.1.1})$$

where  $v_{SM} = 246$  GeV, and  $\theta_{Hh_D}$  is the mixing angle between the dark and the SM Higgs bosons. It is given by  $\theta_{Hh_D} \simeq \lambda_{Hh_D} v_D v_h / m_H^2 = \lambda_{Hh_D} m_{A'} v_h / (m_H^2 g_D)$ , valid for  $m_{h_D} \ll m_H$ . The total decay width of  $h_D$  is given by the relation  $\Gamma_{h_D} = \Gamma(h_D \rightarrow l^+l^-) / \mathcal{B}(h_D \rightarrow l^+l^-)$  where the  $\mathcal{B}(h_D \rightarrow l^+l^-)$  can be found in [591].

**Decay width of  $A'$**

$$\Gamma_{A' \rightarrow A'' h_D} = \frac{|\mathcal{M}_{A' \rightarrow A'' h_D}|^2 \sqrt{m_{A'}^2 - 4m_{h_D}^2}}{(16\pi^2)^2 48\pi m_{A'}^2}, \quad (\text{E.1.2})$$

where  $\mu_{\eta h_D} = \lambda_{h_D \eta} m_{A'} / g_D$ . The amplitude  $\mathcal{M}_{A' \rightarrow A'' h_D}$  is given by the formula

$$M_{A' \rightarrow A'' h_D} = \epsilon(p)_r^\mu \epsilon(p_1)_s^\nu (q_{A''} g_D^2 \mu_{\eta h_D}) (4p_\nu p_{1\mu} C_{12}(m_{A'}^2, m_{h_D}^2, 0, m_\eta, m_\eta, m_\eta) + 4g_{\mu\nu} C_{00}(m_{A'}^2, m_{h_D}^2, 0, m_\eta, m_\eta, m_\eta)), \quad (\text{E.1.3})$$

where  $p$  is the incoming momentum of  $A'$  and  $r$  denotes its polarization, while  $p_1$  is the outgoing momentum of  $A''$  and  $s$  denotes its polarization. To obtain the loop functions  $C_{00}$  (UV divergent) and  $C_{12}$  (UV finite), we used the **X-package** [557]. We follow the conventions of this software where, *e.g.*, a constant factor  $1/(16\pi)^2$  is factored out from the definition of loop functions and therefore reappears

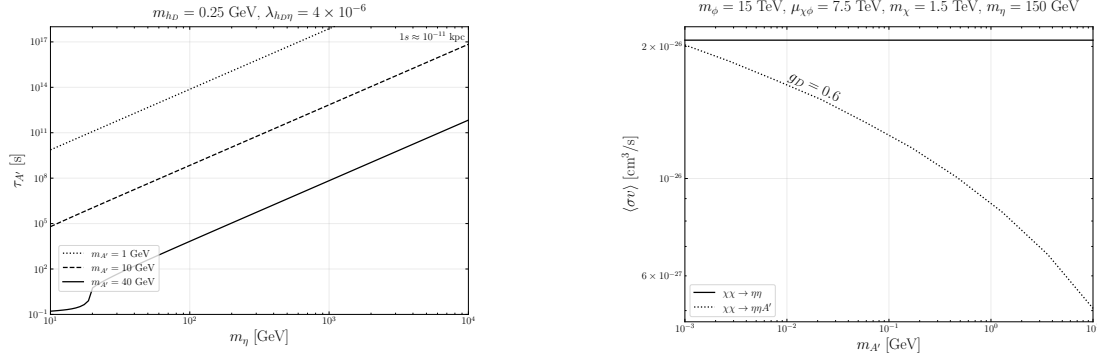


Figure E.1: Left: The lifetime of  $A'$  decaying into  $h_D$  and  $A''$  as a function of  $m_\eta$  (particle flowing in the loop). Right: Dotted black line denotes the  $\langle\sigma v\rangle$  for  $\chi\bar{\chi} \rightarrow \eta\bar{\eta}A'$  which is relevant for  $\chi$  ID, as a function of  $m_{A'}$ , while the solid black line corresponds to the  $\langle\sigma v\rangle$  yielding  $\Omega_\chi h^2 \sim 0.1$ .

in Eq. (E.1.2). In order to render the amplitude  $\mathcal{M}_{A' \rightarrow A'' h_D}$  finite, we add a suitable counterterm to our Lagrangian. We use dimensional regularization to and determine the counterterms in the  $\overline{MS}$  renormalization scheme.

In the mass regime defined by Eq. (7.4.7), the loop functions simplify are greatly simplified and the amplitude squared is given by the following compact expression:

$$|M_{A' \rightarrow A'' h_D}|^2 = \frac{g_{A''}^2 g_D^4 \mu_\eta^2 (m_{A'}^2 - m_{h_D}^2)^2}{72 m_\eta^4}. \quad (\text{E.1.4})$$

The resulting lifetime can be very large, as shown in the left panel of Fig. E.1. There we fix the dark Higgs boson mass,  $m_{h_D} = 250$  MeV, the coupling constant,  $\lambda_{h_D \eta} = 4 \times 10^{-6}$ , and the kinetic mixing angle,  $\tilde{\epsilon} = 10^{-6}$ . The same values also correspond to the right panel of Fig. 7.7.

**Decay width of  $\phi$**  Although not essential to our study, for completeness we also provide the decay width of the heavy auxiliary scalar  $\phi$  which can decay into both the  $\chi\bar{\chi}$  and  $\eta\bar{\eta}$  pairs

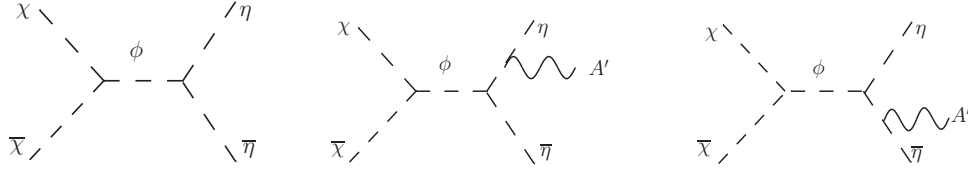
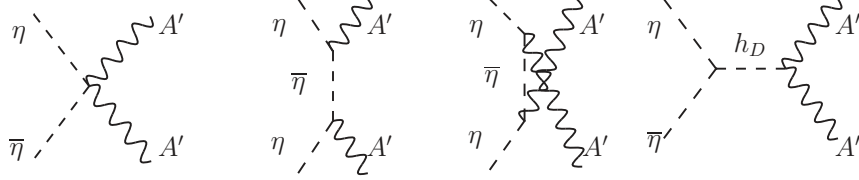
$$\Gamma_\phi = \Gamma_{\phi \rightarrow \chi\bar{\chi}} + \Gamma_{\phi \rightarrow \eta\bar{\eta}} = \frac{\mu_\chi^2 \sqrt{m_\phi^2 - 4m_\chi^2}}{16\pi m_\phi^2} + \frac{\mu_\eta^2 \sqrt{m_\phi^2 - 4m_\eta^2}}{16\pi m_\phi^2}. \quad (\text{E.1.5})$$

For the assumed mass scheme, Eq. (7.4.7), and for  $\mu_\chi = \mu_\eta$ ,  $\mu_\chi/m_\phi \sim 0.1$ , we see that  $\phi$  decays promptly, and therefore does not have any impact on our analysis

$$\tau_\phi \sim \frac{8\pi m_\phi}{\mu_\chi^2} \sim 10^{-25} \text{ s} \left( \frac{1 \text{ TeV}}{\mu_\chi} \right)^2 \frac{m_\phi}{10 \text{ TeV}}. \quad (\text{E.1.6})$$

## E.1.2 Annihilation cross sections

**$\chi\chi \rightarrow \eta\eta$**  The  $\chi\chi$  annihilations, illustrated on the left panel in Fig. E.2, are responsible for the  $\chi$  thermal freeze-out. The relevant cross section is given by the


 Figure E.2: Heavy DM annihilation processes contributing to the  $\chi$  relic density.

 Figure E.3: Feynman diagrams for the  $\eta$  annihilation processes into a pair of dark vectors.

formula

$$\langle\sigma v\rangle_{\chi\bar{\chi}\rightarrow\eta\bar{\eta}} = \frac{\mu_{\chi'}^2 \mu_{\eta}^2 \sqrt{m_{\chi}^2 - m_{\eta}^2}}{32\pi m_{\chi}^3 [(m_{\phi}^2 - 4m_{\chi}^2)^2 + \Gamma_{\phi}^2 m_{\phi}^2]} \sim 10^{-9} \text{ GeV}^{-2} \left(\frac{\mu}{0.1}\right)^4 \left(\frac{30 \text{ GeV}}{m_{\chi}}\right)^2. \quad (\text{E.1.7})$$

$\eta\eta \rightarrow A'A'$  The relic density of  $\eta$  is obtained by its annihilations into light mediators,  $A'$  and  $h_D$ , as shown in Figs. E.3 and E.4. Assuming a hierarchy of masses defined by Eq. (7.4.7), the dominant mode of annihilation is into a pair of dark vectors where the cross section is

$$\begin{aligned} \langle\sigma v\rangle_{\eta\eta\rightarrow A'A'} &= \frac{\sqrt{m_{\eta}^2 - m_{A'}^2}}{16\pi m_{\eta}^3} \left( \frac{g_D^4 (3m_{A'}^8 - 24m_{A'}^6 m_{\eta}^2 + 88m_{A'}^4 m_{\eta}^4 - 128m_{A'}^2 m_{\eta}^6 + 64m_{\eta}^8)}{m_{A'}^4 (m_{A'}^2 - 2m_{\eta}^2)^2} \right. \\ &\quad \left. + \frac{2g_D^2 \lambda_{h_D\eta} (3m_{A'}^4 - 8m_{A'}^2 m_{\eta}^2 + 8m_{\eta}^4)}{m_{A'}^2 (m_H^2 - 4m_{\eta}^2)} + \frac{\lambda_{h_D\eta}^2 (3m_{A'}^4 - 4m_{A'}^2 m_{\eta}^2 + 4m_{\eta}^4)}{(m_H^2 - 4m_{\eta}^2)^2} \right). \end{aligned} \quad (\text{E.1.8})$$

The above expression simplifies to

$$\langle\sigma v\rangle_{\eta\eta\rightarrow A'A'} \simeq \frac{g_D^4 m_{\eta}^2}{\pi m_{A'}^4}. \quad (\text{E.1.9})$$

in the limit of  $m_{\eta} \gg m_{A'} \gg m_{h_D}$ .

We also provide the expression for the  $\eta\bar{\eta} \rightarrow h_D h_D$  cross section contributing subdominantly to the total annihilation rate.

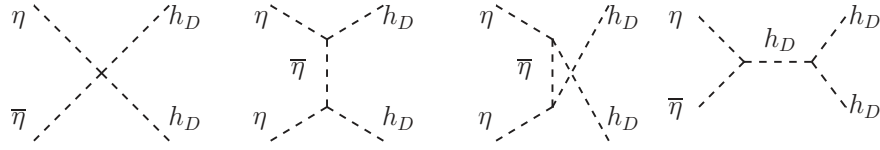


Figure E.4: Feynman diagrams for the  $\eta$  annihilation processes into a pair of dark Higgs bosons.

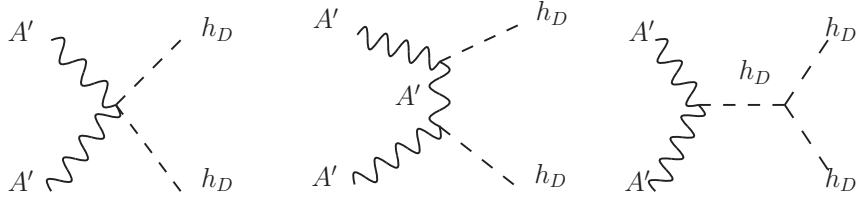


Figure E.5: Feynman diagrams for the dark vector annihilations into light dark Higgs bosons.

**$\eta\eta \rightarrow h_D h_D$**  The cross section for  $\eta$  annihilations into light dark Higgs bosons is

$$\begin{aligned} \langle\sigma v\rangle_{\eta\eta\rightarrow h_D h_D} &= \frac{\lambda_{h_D\eta}^2 \sqrt{m_\eta^2 - m_{h_D}^2}}{64\pi g_D^4 m_\eta^3 (m_{h_D}^4 - 6m_{h_D}^2 m_\eta^2 + 8m_\eta^4)^2} \times \\ &\times (g_D^2 (5m_{h_D}^4 - 18m_{h_D}^2 m_\eta^2 + 16m_\eta^4) - 2\lambda_{h_D\eta} m_{A'}^2 (m_{h_D}^2 - 4m_\eta^2))^2, \end{aligned} \quad (\text{E.1.10})$$

which, in the limit of  $m_\eta \gg m_{h_D}$ , simplifies to

$$\langle\sigma v\rangle_{\eta\eta\rightarrow h_D h_D} = \frac{\lambda_{h_D\eta}^2}{16\pi m_\eta^2}. \quad (\text{E.1.11})$$

For values of  $\lambda_{h_D\eta}$  that are relevant for our analysis, this cross section remains much smaller than the one given by Eq. (E.1.9).

**$A'A' \rightarrow h_D h_D$**  The metastable relic density of the dark vector is obtained by its annihilations into  $h_D h_D$  pairs, as shown in Fig. E.5. The corresponding expression is

$$\langle\sigma v\rangle_{A'A'\rightarrow h_D h_D} = \frac{g_D^4 \sqrt{1-r} (r^2 - 2r - 2)^2}{3\pi m_{A'}^2 (8 - 6r + r^2)^2} \sim 0.01 \frac{g_D^4}{m_{A'}^2}, \quad (\text{E.1.12})$$

where  $r = m_{h_D}^2/m_{A'}^2 \ll 1$ . Note that both Eq. (E.1.12) and Eq. (E.1.8) depend on the dark gauge coupling  $g_D$  as  $\sim g_D^4$  which due to stringent BBN bounds on metastable relic density of  $A'$ , implies that  $\Omega_\eta \sim \Omega_{A'}$ . In fact, Eq. (E.1.8) leads to a cross section proportional to  $m_\eta^2/(\pi m_{A'}^4)$  which can be compared to the factor  $0.01/m_{A'}^2$  present in Eq. (E.1.12). Given the assumed mass scheme, Eq. (7.4.7), this leads to  $\Omega_\eta \lesssim \Omega_{A'}$ .

**$\chi\chi \rightarrow \eta\eta A'$**  For large values of the dark gauge coupling  $g_D$ , the dark bremsstrahlung process becomes important, cf. the right panel of Fig. E.1. The

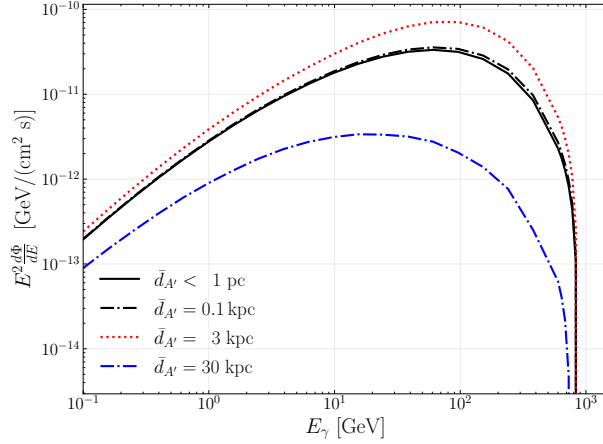


Figure E.6: Differential flux of photons produced in the DM cascade, shown as a function of the photon energy. The result for the standard scenario is indicated by the black solid line. The black dash-dotted, red dotted, and blue dashed lines correspond to the long-lived regime where the relevant typical decay length of boosted  $A'$ 's equal to 0.1, 3, and 30 kpc, respectively.

amplitude of this process depends, among other things, on the momenta of all the particles involved and the total energy in the CoM frame  $\sqrt{s} = \sqrt{(p_1 + p_2)^2}$

$$M_{\chi\chi \rightarrow \eta A'} = \frac{g_D \mu_\chi \mu_\eta}{s - m_\phi^2} \left( \frac{(p_3 + 2p_4)^\mu}{(p_3 + p_4)^2 - m_4^2} + \frac{(-p_3 - 2p_5)^\mu}{(p_3 + p_5)^2 - m_4^2} \right) \epsilon_\mu(p_3, m_3), \quad (\text{E.1.13})$$

where the incoming particles  $\chi$  have momenta  $p_1, p_2$ , the outgoing particles  $\eta$  have momenta  $p_4, p_5$ , and the outgoing dark vector  $A'$  has momentum  $p_3$ . The total cross section is obtained from the general formula, Eq. (A.4.1), described in Appendix A.4

$$\sigma_{\chi\chi \rightarrow \eta A'} = \frac{1}{64\pi^4 \sqrt{\lambda(s, m_1^2, m_2^2)}} \int_{E_3^{\min}}^{E_3^{\max}} dE_3 \sqrt{E_3^2 - m_3^2} \int_0^\pi d\theta \sin\theta \int_0^\pi d\theta^* \sin\theta^* \int_0^{2\pi} d\varphi^* \frac{1}{8} \frac{\sqrt{((m_{45} + m_4)^2 - m_5^2)((m_{45} - m_4)^2 - m_5^2)}}{m_{45}^2 + m_5^2 - m_4^2} |M_{\chi\chi \rightarrow \eta A'}|^2, \quad (\text{E.1.14})$$

We set

$$\begin{aligned} m_1 &= m_2 = m_\chi, \\ m_3 &= m_{A'}, \quad m_4 = m_5 = m_\eta. \end{aligned} \quad (\text{E.1.15})$$

## E.2 Spectrum of gamma rays induced by DM cascade

For the primary  $\gamma$  rays spectra we rely on the PPPC package [420], cf. also [592] for useful discussion. We denote such spectrum obtained in the rest frame of the final decaying light mediator - the dark Higgs boson - by  $(dN_\gamma/dE_\gamma^{h_D})_{h_D}$ . To obtain

the flux of photons in the Galactic frame, we first boost this spectrum to the rest frame of  $A'$  [500],

$$\left(\frac{dN_\gamma}{dE'_\gamma}\right)_{A'} \simeq \frac{m_{h_D}}{m_{A'}} \int_{E'_\gamma}^{m_{A'}} \frac{dE_\gamma^{h_D}}{E_\gamma^{h_D}} \left(\frac{dN_\gamma}{dE_\gamma^{h_D}}\right)_{h_D}, \quad (\text{E.2.1})$$

where  $E'_\gamma$  denotes the energy of the photon in the rest frame of  $A'$ . In the above expression, we assumed that  $m_{A'} \gg m_{h_D}$  which in our analysis is the typical case. Then, we boost the spectrum into the  $\chi$  rest frame. For a fixed energy of the dark vector,  $E_{A'}$ , we obtain the corresponding photon spectrum from the  $\chi\chi \rightarrow \eta\eta A'$  process as

$$\left(\frac{dN_\gamma}{dE_\gamma}\right)_\chi \Big|_{E_{A'}} \simeq \frac{m_{A'}}{2E_{A'}} \int_{E_\gamma}^{E_{A'}} \frac{dE'_\gamma}{E'_\gamma} \left(\frac{dN_\gamma}{dE'_\gamma}\right)_{A'}, \quad (\text{E.2.2})$$

where  $E_\gamma$  is the energy of the photon in the rest frame of  $\chi$  which in practice is the Galactic frame for DM  $\chi$ . To obtain the final  $\gamma$ -ray spectrum  $(dN_\gamma/dE_\gamma)_\chi$ , we then convolute this quantity with the continuous  $A'$  spectrum from  $2 \rightarrow 3$  annihilations,  $\chi\chi \rightarrow \eta\eta A'$  (cf. Eq. (E.1.14) for the corresponding differential cross section). To simplify our analysis, we compute it as a discretized weighted average

$$\left(\frac{dN_\gamma}{dE_\gamma}\right)_\chi = \sum_{\text{bins } E_{A'}} \frac{\langle\sigma v\rangle_{E_{A'}}}{\langle\sigma v\rangle} \left(\frac{dN_\gamma}{dE_\gamma}\right)_\chi \Big|_{E_{A'}}, \quad (\text{E.2.3})$$

where  $\langle\sigma v\rangle_{E_{A'}}$  corresponds to the  $2 \rightarrow 3$  cross section integrated over a limited range of the outgoing  $A'$  energies (within the energy bin centered around  $E_{A'}$ ), while  $\langle\sigma v\rangle$  is the total cross section. We used 20 uniformly distributed bins in  $x_{A'} = E_{A'}/E_\chi$  on a logarithmic scale which is numerically sufficiently accurate treatment.

An example of a gamma-ray spectrum obtained in this way is shown by the black solid line in Fig. E.6. There we fixed the masses of the DS species  $m_\chi = 1.5$  TeV,  $m_\eta = 150$  GeV,  $m_{A'} = 10$  or 3 GeV, and  $m_{h_D} = 500$  MeV, as well as for the dark coupling constant set to  $g_D = 0.01$ . While the assumed mass of  $\chi$  is above 1 TeV, the resulting spectrum is much softer, with a peak near  $E_\gamma \sim$  tens of GeV. We show the photon fluxes for the  $|b|, |l| < 12^\circ$  region around the GC. As discussed in Section 7.6.3, for  $\bar{d}_{A'} \ll d_{\text{RoI}} \simeq 2.3$  kpc the impact of non-local effects on the observed spectrum is very small and the photon spectrum resembles that obtained in the short lifetime regime which we indicated with the black dash-dotted line. For larger values of the decay length,  $\bar{d}_{A'} \sim d_{\text{RoI}}$ , we see a relative increase in the photon flux coming from this RoI due to the anisotropy effects, indicated by the red dotted line. Finally, for very large decay lengths,  $\bar{d}_{A'} \gg d_{\text{RoI}}$ , the flux becomes suppressed due to finite support of the DM density distribution which is illustrated by the blue dash-dotted line. The suppression is even more pronounced for highly energetic photons which originate from more boosted dark vectors that can more easily escape the RoI before decaying. As a result, the observed photon spectrum is even more shifted towards lower energies.

# Bibliography

- [1] A. Hryczuk, K. Jodłowski, E. Moulin, L. Rinchuso, L. Roszkowski, E. M. Sessolo et al., *Testing dark matter with Cherenkov light - prospects of H.E.S.S. and CTA for exploring minimal supersymmetry*, *JHEP* **10** (2019) 043, [[1905.00315](#)]. Cited on the pages 79, 80, and 83.
- [2] K. Jodłowski, F. Kling, L. Roszkowski and S. Trojanowski, *Extending the reach of FASER, MATHUSLA, and SHiP towards smaller lifetimes using secondary particle production*, *Phys. Rev. D* **101** (2020) 095020, [[1911.11346](#)]. Cited on the pages 40, 47, and 145.
- [3] A. Hryczuk and K. Jodłowski, *Self-interacting dark matter from late decays and the  $H_0$  tension*, *Phys. Rev. D* **102** (2020) 043024, [[2006.16139](#)]. Cited on page 114.
- [4] K. Jodłowski and S. Trojanowski, *Neutrino beam-dump experiment with FASER at the LHC*, *JHEP* **05** (2021) 191, [[2011.04751](#)]. Cited on page 55.
- [5] K. Jodłowski, L. Roszkowski and S. Trojanowski, *Indirect detection of long-lived particles in a rich dark sector with a dark Higgs boson portal*, [[2112.11993](#)].
- [6] L. A. Anchordoqui et al., *The Forward Physics Facility: Sites, Experiments, and Physics Potential*, [[2109.10905](#)]. Cited on the pages 38, 50, 57, and 133.
- [7] K. Jodłowski, *Self-interacting dark matter from late decays and the  $H_0$  tension*, [[2110.11622](#)].
- [8] E. Kolb and M. Turner, *The Early Universe*. Frontiers in physics. Avalon Publishing, 1994. Cited on the pages 5 and 22.
- [9] S. Dodelson and F. Schmidt, *Modern Cosmology*. Elsevier Inc, 2 ed., 2020. Cited on the pages 5, 12, and 13.
- [10] A. Friedmann, *Über die Krümmung des Raumes*, *Zeitschrift für Physik* **10** (Jan., 1922) 377–386. Cited on the pages 5 and 6.
- [11] A. G. Lemaître, *A Homogeneous Universe of Constant Mass and Increasing Radius accounting for the Radial Velocity of Extra-galactic Nebulae*, *Monthly Notices of the Royal Astronomical Society* **91** (03, 1931) 483–490. Cited on page 5.

- [12] H. P. Robertson, *Kinematics and World-Structure III.*, *ApJ* **83** (May, 1936) 257. Cited on page 5.
- [13] G. Hinshaw, D. Larson, E. Komatsu, D. N. Spergel, C. L. Bennett, J. Dunkley et al., *Nine-year wilkinson microwave anisotropy probe (wmap) observations: Cosmological parameter results*, *The Astrophysical Journal Supplement Series* **208** (Sep, 2013) 19. Cited on the pages 5 and 15.
- [14] D. Chowdhury, J. Martin, C. Ringeval and V. Vennin, *Assessing the scientific status of inflation after Planck*, *Phys. Rev. D* **100** (2019) 083537, [[1902.03951](#)]. Cited on page 6.
- [15] J. Hartle, *Gravity: An Introduction to Einstein's General Relativity*. Addison-Wesley, 2003. Cited on page 6.
- [16] P. Brax, *What makes the Universe accelerate? A review on what dark energy could be and how to test it*, *Rept. Prog. Phys.* **81** (2018) 016902. Cited on page 6.
- [17] M. Joyce, *Electroweak Baryogenesis and the Expansion Rate of the Universe*, *Phys. Rev. D* **55** (1997) 1875–1878, [[hep-ph/9606223](#)]. Cited on page 7.
- [18] PLANCK collaboration, N. Aghanim et al., *Planck 2018 results. VI. Cosmological parameters*, *Astron. Astrophys.* **641** (2020) A6, [[1807.06209](#)]. Cited on the pages xxiv, 7, 99, 102, 113, and 125.
- [19] L. Verde, T. Treu and A. G. Riess, *Tensions between the Early and the Late Universe*, [1907.10625](#). Cited on the pages 7, 111, and 124.
- [20] PLANCK collaboration, N. Aghanim et al., *Planck 2018 results. VI. Cosmological parameters*, *Astron. Astrophys.* **641** (2020) A6, [[1807.06209](#)]. Cited on the pages xix, 8, 13, 82, and 111.
- [21] N. Suzuki, D. Rubin, C. Lidman, G. Aldering, R. Amanullah, K. Barbary et al., *Thehubble space telescopecluster supernova survey. v. improving the dark-energy constraints above  $z > 1$  and building an early-type-hosted supernova sample*, *The Astrophysical Journal* **746** (Jan, 2012) 85. Cited on the pages xix and 9.
- [22] S. Nadathur, W. J. Percival, F. Beutler and H. Winther, *Testing Low-Redshift Cosmic Acceleration with Large-Scale Structure*, *Phys. Rev. Lett.* **124** (2020) 221301, [[2001.11044](#)]. Cited on the pages xix and 9.
- [23] M. S. Turner,  *$\Lambda$  CDM: Much More Than We Expected, but Now Less Than What We Want*, *Found. Phys.* **48** (2018) 1261–1278, [[2109.01760](#)]. Cited on the pages 7 and 8.
- [24] A. G. Riess, S. Casertano, W. Yuan, L. M. Macri and D. Scolnic, *Large Magellanic Cloud Cepheid Standards Provide a 1% Foundation for the Determination of the Hubble Constant and Stronger Evidence for Physics*

- beyond  $\Lambda$ CDM*, *Astrophys. J.* **876** (2019) 85, [1903.07603].  
Cited on the pages 7, 111, and 124.
- [25] C. Heymans et al., *KiDS-1000 Cosmology: Multi-probe weak gravitational lensing and spectroscopic galaxy clustering constraints*, *Astron. Astrophys.* **646** (2021) A140, [2007.15632]. Cited on the pages 7 and 111.
- [26] L. Perivolaropoulos and F. Skara, *Challenges for  $\Lambda$ CDM: An update*, **2105.05208**. Cited on the pages 7 and 112.
- [27] J. Einasto, *Dark Matter*, *arXiv e-prints* (Jan., 2009) arXiv:0901.0632, [0901.0632]. Cited on page 9.
- [28] S. van den Bergh, *The Early history of dark matter*, *Publ. Astron. Soc. Pac.* **111** (1999) 657, [astro-ph/9904251]. Cited on page 9.
- [29] L. Bergström, *Nonbaryonic dark matter: Observational evidence and detection methods*, *Rept. Prog. Phys.* **63** (2000) 793, [hep-ph/0002126].  
Cited on page 9.
- [30] G. Bertone and D. Hooper, *A History of Dark Matter*, *Rev. Mod. Phys.* **90** (2018) 045002, [1605.04909]. Cited on the pages xix, 9, and 14.
- [31] J. H. Jeans, *The Motions of Stars in a Kapteyn Universe*, *mnras* **82** (Jan., 1922) 122–132. Cited on page 9.
- [32] F. Zwicky, *Die Rotverschiebung von extragalaktischen Nebeln*, *Helvetica Physica Acta* **6** (Jan., 1933) 110–127. Cited on page 9.
- [33] V. C. Rubin, J. Ford, W. K. and N. Thonnard, *Extended rotation curves of high-luminosity spiral galaxies. IV. Systematic dynamical properties, Sa -> Sc.*, *ApJ* **225** (Nov., 1978) L107–L111. Cited on page 10.
- [34] V. C. Rubin, J. Ford, W. K. and N. Thonnard, *Rotational properties of 21 SC galaxies with a large range of luminosities and radii, from NGC 4605 ( $R=4kpc$ ) to UGC 2885 ( $R=122kpc$ ).*, *ApJ* **238** (June, 1980) 471–487.  
Cited on page 10.
- [35] E. Corbelli and P. Salucci, *The Extended Rotation Curve and the Dark Matter Halo of M33*, *Mon. Not. Roy. Astron. Soc.* **311** (2000) 441–447, [astro-ph/9909252]. Cited on the pages xix and 10.
- [36] P. Fischer and J. A. Tyson, *The Mass distribution of the most luminous X-ray cluster RXJ1347.5-1145 from gravitational lensing*, *Astron. J.* **114** (1997) 14, [astro-ph/9703189]. Cited on the pages xix, 11, and 12.
- [37] V. Springel, C. S. Frenk and S. D. M. White, *The large-scale structure of the Universe*, *Nature* **440** (2006) 1137, [astro-ph/0604561].  
Cited on the pages xix and 14.
- [38] S. Profumo, *An Introduction to Particle Dark Matter*. World Scientific,

- 2017, [10.1142/q0001](https://arxiv.org/abs/10.1142/q0001). Cited on the pages 10, 14, 18, and 116.
- [39] C. S. Frenk, A. E. Evrard, S. D. M. White and F. J. Summers, *Galaxy dynamics in clusters*, *Astrophys. J.* **472** (1996) 460, [[astro-ph/9504020](https://arxiv.org/abs/astro-ph/9504020)]. Cited on page 10.
- [40] J. Silk et al., *Particle Dark Matter: Observations, Models and Searches*. Cambridge Univ. Press, Cambridge, 2010, [10.1017/CBO9780511770739](https://arxiv.org/abs/10.1017/CBO9780511770739). Cited on page 10.
- [41] F. W. Dyson, A. S. Eddington and C. Davidson, *A Determination of the Deflection of Light by the Sun's Gravitational Field, from Observations Made at the Total Eclipse of May 29, 1919*, *Philosophical Transactions of the Royal Society of London Series A* **220** (Jan., 1920) 291–333. Cited on page 11.
- [42] F. Zwicky, *Nebulae as gravitational lenses*, *Phys. Rev.* **51** (Feb, 1937) 290–290. Cited on page 11.
- [43] D. Walsh, R. F. Carswell and R. J. Weymann, *0957+561 A, B: twin quasistellar objects or gravitational lens?*, *Nature* **279** (May, 1979) 381–384. Cited on page 11.
- [44] R. Massey, T. Kitching and J. Richard, *The dark matter of gravitational lensing*, *Rept. Prog. Phys.* **73** (2010) 086901, [[1001.1739](https://arxiv.org/abs/1001.1739)]. Cited on page 11.
- [45] D. M. Wittman, J. A. Tyson, D. Kirkman, I. Dell'Antonio and G. Bernstein, *Detection of weak gravitational lensing distortions of distant galaxies by cosmic dark matter at large scales*, *Nature* **405** (2000) 143–149, [[astro-ph/0003014](https://arxiv.org/abs/astro-ph/0003014)]. Cited on page 11.
- [46] A. Refregier, *Weak gravitational lensing by large scale structure*, *Ann. Rev. Astron. Astrophys.* **41** (2003) 645–668, [[astro-ph/0307212](https://arxiv.org/abs/astro-ph/0307212)]. Cited on page 11.
- [47] D. Kraljic and S. Sarkar, *How rare is the Bullet Cluster (in a  $\Lambda$ CDM universe)?*, *JCAP* **04** (2015) 050, [[1412.7719](https://arxiv.org/abs/1412.7719)]. Cited on page 11.
- [48] C. Lage and G. R. Farrar, *The bullet cluster is not a cosmological anomaly*, *JCAP* **2015** (Feb., 2015) 038, [[1406.6703](https://arxiv.org/abs/1406.6703)]. Cited on page 11.
- [49] R. Thompson, R. Davé and K. Nagamine, *The rise and fall of a challenger: the Bullet Cluster in  $\Lambda$  cold dark matter simulations*, *Mon. Not. Roy. Astron. Soc.* **452** (2015) 3030–3037, [[1410.7438](https://arxiv.org/abs/1410.7438)]. Cited on page 11.
- [50] D. Clowe, A. Gonzalez and M. Markevitch, *Weak lensing mass reconstruction of the interacting cluster 1E0657-558: Direct evidence for the existence of dark matter*, *Astrophys. J.* **604** (2004) 596–603, [[astro-ph/0312273](https://arxiv.org/abs/astro-ph/0312273)]. Cited on page 11.
- [51] M. Markevitch, A. Gonzalez, D. Clowe, A. Vikhlinin, L. David, W. Forman

- et al., *Direct constraints on the dark matter self-interaction cross-section from the merging galaxy cluster 1E0657-56*, *Astrophys. J.* **606** (2004) 819–824, [[astro-ph/0309303](#)]. Cited on the pages 11 and 128.
- [52] D. Clowe, M. Bradac, A. H. Gonzalez, M. Markevitch, S. W. Randall, C. Jones et al., *A direct empirical proof of the existence of dark matter*, *Astrophys. J. Lett.* **648** (2006) L109–L113, [[astro-ph/0608407](#)]. Cited on the pages 11 and 128.
- [53] D. Harvey, R. Massey, T. Kitching, A. Taylor and E. Tittley, *The non-gravitational interactions of dark matter in colliding galaxy clusters*, *Science* **347** (2015) 1462–1465, [[1503.07675](#)]. Cited on the pages 12 and 32.
- [54] M. Milgrom, *MOND: A pedagogical review*, *Acta Phys. Polon. B* **32** (2001) 3613, [[astro-ph/0112069](#)]. Cited on page 12.
- [55] R. Durrer, *The Cosmic Microwave Background*. Cambridge University Press, 12, 2020, [10.1017/9781316471524](#). Cited on page 12.
- [56] R. Durrer, *The cosmic microwave background: the history of its experimental investigation and its significance for cosmology*, *Class. Quant. Grav.* **32** (2015) 124007, [[1506.01907](#)]. Cited on page 12.
- [57] T. Rindler-Daller, *Understanding CMB physics through the exploration of exotic cosmological models: a classroom study using CLASS*, *Eur. J. Phys.* **41** (2020) 035602, [[1908.05042](#)]. Cited on page 12.
- [58] A. A. Penzias and R. W. Wilson, *A Measurement of Excess Antenna Temperature at 4080 Mc/s.*, *ApJ* **142** (July, 1965) 419–421. Cited on page 12.
- [59] R. H. Dicke, P. J. E. Peebles, P. G. Roll and D. T. Wilkinson, *Cosmic Black-Body Radiation.*, *ApJ* **142** (July, 1965) 414–419. Cited on page 12.
- [60] A. Sacharow *Zh. Eksp. Teoret. Fiz.*, **49**, 345 (1965) . Cited on page 13.
- [61] P. J. E. Peebles, *Recombination of the Primeval Plasma*, *ApJ* **153** (July, 1968) 1. Cited on page 13.
- [62] Y. B. Zel’dovich, V. G. Kurt and R. A. Syunyaev, *Recombination of Hydrogen in the Hot Model of the Universe*, *Soviet Journal of Experimental and Theoretical Physics* **28** (Jan., 1969) 146. Cited on page 13.
- [63] J. Silk, *Cosmic Black-Body Radiation and Galaxy Formation*, *ApJ* **151** (Feb., 1968) 459. Cited on page 13.
- [64] D. J. Fixsen, E. S. Cheng, J. M. Gales, J. C. Mather, R. A. Shafer and E. L. Wright, *The Cosmic Microwave Background spectrum from the full COBE FIRAS data set*, *Astrophys. J.* **473** (1996) 576, [[astro-ph/9605054](#)]. Cited on the pages 13 and 102.

- [65] P. J. E. Peebles, *Large-scale background temperature and mass fluctuations due to scale-invariant primeval perturbations*, *ApJ* **263** (Dec., 1982) L1–L5. Cited on page 13.
- [66] J. Lesgourgues and S. Pastor, *Massive neutrinos and cosmology*, *Phys. Rept.* **429** (2006) 307–379, [[astro-ph/0603494](#)]. Cited on page 14.
- [67] D. J. Eisenstein, H.-j. Seo, E. Sirko and D. Spergel, *Improving Cosmological Distance Measurements by Reconstruction of the Baryon Acoustic Peak*, *Astrophys. J.* **664** (2007) 675–679, [[astro-ph/0604362](#)]. Cited on page 14.
- [68] C. Blake, E. A. Kazin, F. Beutler, T. M. Davis, D. Parkinson, S. Brough et al., *The wigglez dark energy survey: mapping the distance-redshift relation with baryon acoustic oscillations*, *Monthly Notices of the Royal Astronomical Society* **418** (Oct, 2011) 1707–1724. Cited on page 14.
- [69] N. Padmanabhan, X. Xu, D. J. Eisenstein, R. Scalzo, A. J. Cuesta, K. T. Mehta et al., *A 2 per cent distance to  $z=0.35$  by reconstructing baryon acoustic oscillations – i. methods and application to the sloan digital sky survey*, *Monthly Notices of the Royal Astronomical Society* **427** (Nov, 2012) 2132–2145. Cited on page 14.
- [70] BOSS collaboration, S. Alam et al., *The clustering of galaxies in the completed SDSS-III Baryon Oscillation Spectroscopic Survey: cosmological analysis of the DR12 galaxy sample*, *Mon. Not. Roy. Astron. Soc.* **470** (2017) 2617–2652, [[1607.03155](#)]. Cited on page 14.
- [71] S. Dodelson, *The Real Problem with MOND*, *Int. J. Mod. Phys. D* **20** (2011) 2749–2753, [[1112.1320](#)]. Cited on page 14.
- [72] S. D. M. White, *Simulations of sinking satellites*, *ApJ* **274** (Nov., 1983) 53–61. Cited on page 15.
- [73] M. Davis, G. Efstathiou, C. S. Frenk and S. D. M. White, *The evolution of large-scale structure in a universe dominated by cold dark matter*, *ApJ* **292** (May, 1985) 371–394. Cited on page 15.
- [74] V. Springel, S. D. M. White, A. Jenkins, C. S. Frenk, N. Yoshida, L. Gao et al., *Simulations of the formation, evolution and clustering of galaxies and quasars*, *Nature* **435** (June, 2005) 629–636, [[astro-ph/0504097](#)]. Cited on page 15.
- [75] 2DFGRS collaboration, M. Colless et al., *The 2dF Galaxy Redshift Survey: Spectra and redshifts*, *Mon. Not. Roy. Astron. Soc.* **328** (2001) 1039, [[astro-ph/0106498](#)]. Cited on page 15.
- [76] SDSS collaboration, M. Tegmark et al., *The 3-D power spectrum of galaxies from the SDSS*, *Astrophys. J.* **606** (2004) 702–740, [[astro-ph/0310725](#)]. Cited on page 15.
- [77] J. S. Bullock and M. Boylan-Kolchin, *Small-Scale Challenges to the*

- ΛCDM Paradigm*, *Annu. Rev. Astron. Astrophys.* **55** (2017) 343–387, [1707.04256]. Cited on the pages 15 and 111.
- [78] A. A. Klypin, A. V. Kravtsov, O. Valenzuela and F. Prada, *Where are the missing Galactic satellites?*, *Astrophys. J.* **522** (1999) 82–92, [astro-ph/9901240]. Cited on page 15.
- [79] M. Boylan-Kolchin, J. S. Bullock and M. Kaplinghat, *Too big to fail? the puzzling darkness of massive milky way subhaloes*, *Monthly Notices of the Royal Astronomical Society: Letters* **415** (Jun, 2011) L40–L44. Cited on page 15.
- [80] B. Moore, *Evidence against dissipation-less dark matter from observations of galaxy haloes*, *Nature* **370** (Aug., 1994) 629–631. Cited on page 15.
- [81] J. F. Navarro, V. R. Eke and C. S. Frenk, *The cores of dwarf galaxy halos*, *Mon. Not. Roy. Astron. Soc.* **283** (1996) L72–L78, [astro-ph/9610187]. Cited on page 15.
- [82] K. A. Oman et al., *The unexpected diversity of dwarf galaxy rotation curves*, *Mon. Not. Roy. Astron. Soc.* **452** (2015) 3650–3665, [1504.01437]. Cited on page 15.
- [83] A. Pontzen and F. Governato, *How supernova feedback turns dark matter cusps into cores*, *MNRAS* **421** (Apr., 2012) 3464–3471, [1106.0499]. Cited on page 15.
- [84] F. Governato, A. Zolotov, A. Pontzen, C. Christensen, S. H. Oh, A. M. Brooks et al., *Cuspy no more: how outflows affect the central dark matter and baryon distribution in Λ cold dark matter galaxies*, *MNRAS* **422** (May, 2012) 1231–1240, [1202.0554]. Cited on page 15.
- [85] M. Vogelsberger, S. Genel, V. Springel, P. Torrey, D. Sijacki, D. Xu et al., *Introducing the Illustris Project: Simulating the coevolution of dark and visible matter in the Universe*, *Mon. Not. Roy. Astron. Soc.* **444** (2014) 1518–1547, [1405.2921]. Cited on page 15.
- [86] P. F. Hopkins, D. Keres, J. Onorbe, C.-A. Faucher-Giguere, E. Quataert, N. Murray et al., *Galaxies on FIRE (Feedback In Realistic Environments): Stellar Feedback Explains Cosmologically Inefficient Star Formation*, *Mon. Not. Roy. Astron. Soc.* **445** (2014) 581–603, [1311.2073]. Cited on page 15.
- [87] e. a. Billard, Julien, *Direct Detection of Dark Matter – APPEC Committee Report*, 2104.07634. Cited on the pages xx, 16, 28, 29, and 90.
- [88] D. J. Hegyi and K. A. Olive, *A Case against Baryons in Galactic Halos*, *ApJ* **303** (Apr., 1986) 56. Cited on page 15.
- [89] A. Dar, *Baryonic Dark Matter and Big Bang Nucleosynthesis*, *ApJ* **449** (Aug., 1995) 550, [astro-ph/9504082]. Cited on page 15.

- [90] MACHO collaboration, C. Alcock et al., *The MACHO project: Microlensing results from 5.7 years of LMC observations*, *Astrophys. J.* **542** (2000) 281–307, [[astro-ph/0001272](#)]. Cited on page 15.
- [91] EROS collaboration, T. Lasserre, *Not enough stellar mass machos in the galactic halo*, *Astron. Astrophys.* **355** (2000) L39–L42, [[astro-ph/0002253](#)]. Cited on page 15.
- [92] EROS-2 collaboration, P. Tisserand et al., *Limits on the Macho Content of the Galactic Halo from the EROS-2 Survey of the Magellanic Clouds*, *Astron. Astrophys.* **469** (2007) 387–404, [[astro-ph/0607207](#)]. Cited on page 15.
- [93] B. Paczynski, *Gravitational Microlensing by the Galactic Halo*, *ApJ* **304** (May, 1986) 1. Cited on page 15.
- [94] B. J. Carr and S. W. Hawking, *Black holes in the early Universe*, *MNRAS* **168** (Aug., 1974) 399–416. Cited on page 15.
- [95] LIGO SCIENTIFIC, VIRGO collaboration, B. P. Abbott et al., *Observation of Gravitational Waves from a Binary Black Hole Merger*, *Phys. Rev. Lett.* **116** (2016) 061102, [[1602.03837](#)]. Cited on page 17.
- [96] A. M. Green and B. J. Kavanagh, *Primordial Black Holes as a dark matter candidate*, *J. Phys. G* **48** (2021) 043001, [[2007.10722](#)]. Cited on page 17.
- [97] B. C. Lacki and J. F. Beacom, *Primordial Black Holes as Dark Matter: Almost All or Almost Nothing*, *Astrophys. J. Lett.* **720** (2010) L67–L71, [[1003.3466](#)]. Cited on page 17.
- [98] Y. N. Eroshenko, *Dark matter density spikes around primordial black holes*, *Astron. Lett.* **42** (2016) 347–356, [[1607.00612](#)]. Cited on page 17.
- [99] J. Adamek, C. T. Byrnes, M. Gosenca and S. Hotchkiss, *WIMPs and stellar-mass primordial black holes are incompatible*, *Phys. Rev. D* **100** (2019) 023506, [[1901.08528](#)]. Cited on page 17.
- [100] G. Bertone, A. M. Coogan, D. Gaggero, B. J. Kavanagh and C. Weniger, *Primordial Black Holes as Silver Bullets for New Physics at the Weak Scale*, *Phys. Rev. D* **100** (2019) 123013, [[1905.01238](#)]. Cited on page 17.
- [101] M. Taoso, G. Bertone and A. Masiero, *Dark Matter Candidates: A Ten-Point Test*, *JCAP* **03** (2008) 022, [[0711.4996](#)]. Cited on page 17.
- [102] M. Lucca, N. Schöneberg, D. C. Hooper, J. Lesgourgues and J. Chluba, *The synergy between CMB spectral distortions and anisotropies*, *JCAP* **02** (2020) 026, [[1910.04619](#)]. Cited on the pages 17 and 102.
- [103] J. M. Cline, Z. Liu and W. Xue, *Millicharged Atomic Dark Matter*, *Phys. Rev. D* **85** (2012) 101302, [[1201.4858](#)]. Cited on page 17.

- [104] A. Doroshkevich, Y. Zeldovich and R. Sunyaev, *Formation and evolution of Galaxies and Stars*, Nauka (1976) . Cited on page 17.
- [105] S. Hannestad, A. Mirizzi, G. G. Raffelt and Y. Y. Y. Wong, *Neutrino and axion hot dark matter bounds after WMAP-7*, *JCAP* **08** (2010) 001, [1004.0695]. Cited on page 17.
- [106] PARTICLE DATA GROUP collaboration, M. Tanabashi et al., *Review of Particle Physics*, *Phys. Rev.* **D98** (2018) 030001. Cited on the pages 17, 25, and 36.
- [107] M. Viel, G. D. Becker, J. S. Bolton and M. G. Haehnelt, *Warm dark matter as a solution to the small scale crisis: New constraints from high redshift Lyman- $\alpha$  forest data*, *Phys. Rev. D* **88** (2013) 043502, [1306.2314]. Cited on page 17.
- [108] R. D. Peccei and H. R. Quinn, *CP Conservation in the Presence of Instantons*, *Phys. Rev. Lett.* **38** (1977) 1440–1443. Cited on page 18.
- [109] R. D. Peccei and H. R. Quinn, *Constraints Imposed by CP Conservation in the Presence of Instantons*, *Phys. Rev. D* **16** (1977) 1791–1797. Cited on page 18.
- [110] S. Weinberg, *A New Light Boson?*, *Phys. Rev. Lett.* **40** (1978) 223–226. Cited on page 18.
- [111] F. Wilczek, *Problem of Strong P and T Invariance in the Presence of Instantons*, *Phys. Rev. Lett.* **40** (1978) 279–282. Cited on page 18.
- [112] J. Preskill, M. B. Wise and F. Wilczek, *Cosmology of the Invisible Axion*, *Phys. Lett. B* **120** (1983) 127–132. Cited on the pages 18 and 27.
- [113] P. W. Graham, I. G. Irastorza, S. K. Lamoreaux, A. Lindner and K. A. van Bibber, *Experimental Searches for the Axion and Axion-Like Particles*, *Ann. Rev. Nucl. Part. Sci.* **65** (2015) 485–514, [1602.00039]. Cited on page 18.
- [114] GAIA collaboration, A. G. A. Brown et al., *Gaia Data Release 2: Summary of the contents and survey properties*, *Astron. Astrophys.* **616** (2018) A1, [1804.09365]. Cited on the pages 18 and 32.
- [115] W. Hu, R. Barkana and A. Gruzinov, *Cold and fuzzy dark matter*, *Phys. Rev. Lett.* **85** (2000) 1158–1161, [astro-ph/0003365]. Cited on page 18.
- [116] J.-W. Lee, *Brief History of Ultra-light Scalar Dark Matter Models*, *EPJ Web Conf.* **168** (2018) 06005, [1704.05057]. Cited on page 18.
- [117] L. Hui, *Wave Dark Matter*, *Ann. Rev. Astron. Astrophys.* **59** (2021) 247–289, [2101.11735]. Cited on page 18.
- [118] E. G. M. Ferreira, *Ultra-light dark matter*, *Astron. Astrophys. Rev.* **29**

- (2021) 7, [2005.03254]. Cited on page 18.
- [119] B. Pontecorvo, *Mesonium and Antimesonium*, *Soviet Journal of Experimental and Theoretical Physics* **6** (Jan., 1958) 429. Cited on page 18.
- [120] R. Davis, D. S. Harmer and K. C. Hoffman, *Search for Neutrinos from the Sun*, *PRL* **20** (May, 1968) 1205–1209. Cited on page 18.
- [121] P. Minkowski,  $\mu \rightarrow e\gamma$  at a Rate of One Out of  $10^9$  Muon Decays?, *Phys. Lett. B* **67** (1977) 421–428. Cited on the pages 18 and 55.
- [122] S. Dodelson and L. M. Widrow, *Sterile-neutrinos as dark matter*, *Phys. Rev. Lett.* **72** (1994) 17–20, [hep-ph/9303287]. Cited on the pages 18 and 27.
- [123] X.-D. Shi and G. M. Fuller, *A New dark matter candidate: Nonthermal sterile neutrinos*, *Phys. Rev. Lett.* **82** (1999) 2832–2835, [astro-ph/9810076]. Cited on page 18.
- [124] A. Kusenko, *Sterile neutrinos: The Dark side of the light fermions*, *Phys. Rept.* **481** (2009) 1–28, [0906.2968]. Cited on page 19.
- [125] E. Bulbul, M. Markevitch, A. Foster, R. K. Smith, M. Loewenstein and S. W. Randall, *Detection of An Unidentified Emission Line in the Stacked X-ray spectrum of Galaxy Clusters*, *Astrophys. J.* **789** (2014) 13, [1402.2301]. Cited on page 19.
- [126] A. Boyarsky, O. Ruchayskiy, D. Iakubovskiy and J. Franse, *Unidentified Line in X-Ray Spectra of the Andromeda Galaxy and Perseus Galaxy Cluster*, *Phys. Rev. Lett.* **113** (2014) 251301, [1402.4119]. Cited on page 19.
- [127] K. Abazajian, *Linear cosmological structure limits on warm dark matter*, *Phys. Rev. D* **73** (2006) 063513, [astro-ph/0512631]. Cited on page 19.
- [128] A. Boyarsky, M. Drewes, T. Lasserre, S. Mertens and O. Ruchayskiy, *Sterile neutrino Dark Matter*, *Prog. Part. Nucl. Phys.* **104** (2019) 1–45, [1807.07938]. Cited on the pages 19, 37, and 60.
- [129] K. Abazajian, G. M. Fuller and M. Patel, *Sterile neutrino hot, warm, and cold dark matter*, *Phys. Rev. D* **64** (2001) 023501, [astro-ph/0101524]. Cited on page 19.
- [130] K. N. Abazajian, *Sterile neutrinos in cosmology*, *Phys. Rept.* **711-712** (2017) 1–28, [1705.01837]. Cited on page 19.
- [131] B. W. Lee and S. Weinberg, *Cosmological Lower Bound on Heavy Neutrino Masses*, *Phys. Rev. Lett.* **39** (1977) 165–168. Cited on page 19.
- [132] P. Hut, *Limits on Masses and Number of Neutral Weakly Interacting Particles*, *Phys. Lett. B* **69** (1977) 85. Cited on page 19.
- [133] M. I. Vysotsky, A. D. Dolgov and Y. B. Zeldovich, *Cosmological Restriction*

- on Neutral Lepton Masses*, *JETP Lett.* **26** (1977) 188–190. Cited on page 19.
- [134] J. Ruderman, *Dark Matter Production without Prejudice*, in *Les Houches summer school on Dark Matter*. Cited on the pages 19 and 27.
- [135] L. Roszkowski, E. M. Sessolo and S. Trojanowski, *WIMP dark matter candidates and searches—current status and future prospects*, *Rept. Prog. Phys.* **81** (2018) 066201, [[1707.06277](#)]. Cited on the pages 20, 35, and 71.
- [136] G. Arcadi, M. Dutra, P. Ghosh, M. Lindner, Y. Mambrini, M. Pierre et al., *The waning of the WIMP? A review of models, searches, and constraints*, *Eur. Phys. J. C* **78** (2018) 203, [[1703.07364](#)]. Cited on page 20.
- [137] Y. A. Golfand and E. P. Likhtman, *Extension of the Algebra of Poincare Group Generators and Violation of  $p$  Invariance*, *JETP Lett.* **13** (1971) 323–326. Cited on page 20.
- [138] J. Wess and B. Zumino, *Supergauge Transformations in Four-Dimensions*, *Nucl. Phys. B* **70** (1974) 39–50. Cited on page 20.
- [139] H. Georgi, H. R. Quinn and S. Weinberg, *Hierarchy of interactions in unified gauge theories*, *Phys. Rev. Lett.* **33** (Aug, 1974) 451–454.  
Cited on page 20.
- [140] S. Dimopoulos, S. Raby and F. Wilczek, *Supersymmetry and the scale of unification*, *Phys. Rev. D* **24** (Sep, 1981) 1681–1683. Cited on page 20.
- [141] W. J. Marciano and G. Senjanović, *Predictions of supersymmetric grand unified theories*, *Phys. Rev. D* **25** (Jun, 1982) 3092–3095. Cited on page 20.
- [142] P. Nath and R. Arnowitt, *Generalized super-gauge symmetry as a new framework for unified gauge theories*, *Physics Letters B* **56** (1975) 177–180.  
Cited on page 20.
- [143] D. Z. Freedman, P. van Nieuwenhuizen and S. Ferrara, *Progress toward a theory of supergravity*, *Phys. Rev. D* **13** (Jun, 1976) 3214–3218.  
Cited on page 20.
- [144] S. Deser, *A brief history (and geography) of Supergravity: the first 3 weeks... and after*, *Eur. Phys. J. H* **43** (2018) 281–291, [[1704.05886](#)].  
Cited on page 20.
- [145] H. Pagels and J. R. Primack, *Supersymmetry, cosmology, and new physics at teraelectronvolt energies*, *Phys. Rev. Lett.* **48** (Jan, 1982) 223–226.  
Cited on page 20.
- [146] M. Bolz, A. Brandenburg and W. Buchmuller, *Thermal production of gravitinos*, *Nucl. Phys. B* **606** (2001) 518–544, [[hep-ph/0012052](#)].  
Cited on page 20.
- [147] H. Baer, K.-Y. Choi, J. E. Kim and L. Roszkowski, *Dark matter production*

- in the early Universe: beyond the thermal WIMP paradigm*, *Phys. Rept.* **555** (2015) 1–60, [[1407.0017](#)]. Cited on the pages 20 and 27.
- [148] K. Rajagopal, M. S. Turner and F. Wilczek, *Cosmological implications of axinos*, *Nucl. Phys. B* **358** (1991) 447–470. Cited on page 20.
- [149] L. Roszkowski, *Axino: New candidate for cold dark matter*, in *4th International Conference on Particle Physics and the Early Universe*, pp. 71–84, 2, 2001, [hep-ph/0102325](#). Cited on page 20.
- [150] K.-Y. Choi, L. Covi, J. E. Kim and L. Roszkowski, *Axino Cold Dark Matter Revisited*, *JHEP* **04** (2012) 106, [[1108.2282](#)]. Cited on page 20.
- [151] H. E. Haber and G. L. Kane, *The Search for Supersymmetry: Probing Physics Beyond the Standard Model*, *Phys. Rept.* **117** (1985) 75–263. Cited on page 20.
- [152] S. P. Martin, *A Supersymmetry primer*, *Adv. Ser. Direct. High Energy Phys.* **18** (1998) 1–98, [[hep-ph/9709356](#)]. Cited on page 20.
- [153] G. Jungman, M. Kamionkowski and K. Griest, *Supersymmetric dark matter*, *Phys. Rept.* **267** (1996) 195–373, [[hep-ph/9506380](#)]. Cited on page 20.
- [154] H. Goldberg, *Constraint on the Photino Mass from Cosmology*, *Phys. Rev. Lett.* **50** (1983) 1419. Cited on page 20.
- [155] J. R. Ellis, J. S. Hagelin, D. V. Nanopoulos, K. A. Olive and M. Srednicki, *Supersymmetric Relics from the Big Bang*, *Nucl. Phys. B* **238** (1984) 453–476. Cited on the pages 20 and 71.
- [156] G. F. Giudice, E. W. Kolb and A. Riotto, *Largest temperature of the radiation era and its cosmological implications*, *Phys. Rev. D* **64** (2001) 023508, [[hep-ph/0005123](#)]. Cited on page 21.
- [157] G. B. Gelmini and P. Gondolo, *Neutralino with the right cold dark matter abundance in (almost) any supersymmetric model*, *Phys. Rev. D* **74** (2006) 023510, [[hep-ph/0602230](#)]. Cited on page 21.
- [158] L. Roszkowski, S. Trojanowski and K. Turzyński, *Neutralino and gravitino dark matter with low reheating temperature*, *JHEP* **11** (2014) 146, [[1406.0012](#)]. Cited on page 21.
- [159] P. Salati, *Quintessence and the Relic Density of Neutralinos*, *Physics Letters B* **571** (2003) 121–131, [[astro-ph/0207396](#)]. Cited on page 21.
- [160] G. Steigman, B. Dasgupta and J. F. Beacom, *Precise Relic WIMP Abundance and its Impact on Searches for Dark Matter Annihilation*, *Phys. Rev. D* **86** (2012) 023506, [[1204.3622](#)]. Cited on page 22.
- [161] C. M. Bender and S. Sarkar, *Asymptotic Analysis of the Boltzmann*

- Equation for Dark Matter Relics*, *J. Math. Phys.* **53** (2012) 103509, [1203.1822]. Cited on the pages 22 and 23.
- [162] T. Binder, T. Bringmann, M. Gustafsson and A. Hryczuk, *DRAKE: Dark matter Relic Abundance beyond Kinetic Equilibrium*, *Eur. Phys. J. C* **81** (2021) 577, [2103.01944]. Cited on page 22.
- [163] T. Binder, T. Bringmann, M. Gustafsson and A. Hryczuk, *Early kinetic decoupling of dark matter: When the standard way of calculating the thermal relic density fails*, *Phys. Rev. D* **96** (2017) 115010, [1706.07433]. Cited on page 22.
- [164] G. Belanger, F. Boudjema, A. Pukhov and A. Semenov, *micrOMEGAs: A Tool for dark matter studies*, *Nuovo Cim. C* **033N2** (2010) 111–116, [1005.4133]. Cited on page 23.
- [165] G. Bélanger, F. Boudjema, A. Goudelis, A. Pukhov and B. Zaldivar, *micrOMEGAs5.0 : Freeze-in*, *Comput. Phys. Commun.* **231** (2018) 173–186, [1801.03509]. Cited on page 23.
- [166] P. Gondolo, J. Edsjo, P. Ullio, L. Bergstrom, M. Schelke and E. A. Baltz, *DarkSUSY: Computing supersymmetric dark matter properties numerically*, *JCAP* **07** (2004) 008, [astro-ph/0406204]. Cited on page 23.
- [167] T. Bringmann, J. Edsjö, P. Gondolo, P. Ullio and L. Bergström, *DarkSUSY 6 : An Advanced Tool to Compute Dark Matter Properties Numerically*, *JCAP* **07** (2018) 033, [1802.03399]. Cited on page 23.
- [168] P. Gondolo and G. Gelmini, *Cosmic abundances of stable particles: Improved analysis*, *Nuclear Physics B* **360** (1991) 145–179. Cited on the pages 23 and 138.
- [169] F. W. Olver, D. W. Lozier, R. F. Boisvert and C. W. Clark, *NIST Handbook of Mathematical Functions*. Cambridge University Press, USA, 1st ed., 2010. Cited on the pages 23 and 117.
- [170] S. Profumo, L. Giani and O. F. Piattella, *An Introduction to Particle Dark Matter*, 1910.05610. Cited on page 24.
- [171] K. Griest and D. Seckel, *Three exceptions in the calculation of relic abundances*, *Phys. Rev. D* **43** (1991) 3191–3203. Cited on the pages 25 and 26.
- [172] J. Hisano, S. Matsumoto, M. Nagai, O. Saito and M. Senami, *Non-perturbative effect on thermal relic abundance of dark matter*, *Phys. Lett.* **B646** (2007) 34–38, [hep-ph/0610249]. Cited on the pages 26 and 83.
- [173] S. Cassel, *Sommerfeld factor for arbitrary partial wave processes*, *J. Phys. G: Nucl. Part. Phys.* **37** (2010) 105009, [0903.5307]. Cited on page 26.
- [174] R. Iengo, *Sommerfeld enhancement: General results from field theory diagrams*, *JHEP* **05** (2009) 024, [0902.0688]. Cited on page 26.

- [175] T. R. Slatyer, *The Sommerfeld enhancement for dark matter with an excited state*, *JCAP* **1002** (2010) 028, [[0910.5713](#)]. Cited on page 26.
- [176] T. Binder, L. Covi and K. Mukaida, *Dark Matter Sommerfeld-enhanced annihilation and Bound-state decay at finite temperature*, *Phys. Rev. D* **98** (2018) 115023, [[1808.06472](#)]. Cited on page 26.
- [177] T. R. Slatyer, *Indirect Detection of Dark Matter*, [1710.05137](#). Cited on the pages xx and 26.
- [178] D. Tucker-Smith and N. Weiner, *Inelastic dark matter*, *Phys. Rev. D* **64** (2001) 043502, [[hep-ph/0101138](#)]. Cited on page 26.
- [179] R. T. D’Agnolo and J. T. Ruderman, *Light Dark Matter from Forbidden Channels*, *Phys. Rev. Lett.* **115** (2015) 061301, [[1505.07107](#)]. Cited on page 26.
- [180] R. T. D’Agnolo, D. Liu, J. T. Ruderman and P.-J. Wang, *Forbidden Dark Matter Annihilations into Standard Model Particles*, *JHEP* **21** (2020) 103, [[2012.11766](#)]. Cited on page 27.
- [181] J. L. Feng and J. Kumar, *The WIMPless Miracle: Dark-Matter Particles without Weak-Scale Masses or Weak Interactions*, *Phys. Rev. Lett.* **101** (2008) 231301, [[0803.4196](#)]. Cited on the pages 27, 42, and 90.
- [182] G. F. Giudice and R. Rattazzi, *Theories with gauge mediated supersymmetry breaking*, *Phys. Rept.* **322** (1999) 419–499, [[hep-ph/9801271](#)]. Cited on page 27.
- [183] C. F. Kolda, *Gauge mediated supersymmetry breaking: Introduction, review and update*, *Nucl. Phys. B Proc. Suppl.* **62** (1998) 266–275, [[hep-ph/9707450](#)]. Cited on page 27.
- [184] C. Boehm and P. Fayet, *Scalar dark matter candidates*, *Nucl. Phys. B* **683** (2004) 219–263, [[hep-ph/0305261](#)]. Cited on the pages 27, 42, and 90.
- [185] M. Pospelov, A. Ritz and M. B. Voloshin, *Secluded WIMP Dark Matter*, *Phys. Lett. B* **662** (2008) 53–61, [[0711.4866](#)]. Cited on the pages 27, 37, 42, and 90.
- [186] D. E. Kaplan, M. A. Luty and K. M. Zurek, *Asymmetric Dark Matter*, *Phys. Rev. D* **79** (2009) 115016, [[0901.4117](#)]. Cited on page 27.
- [187] L. J. Hall, K. Jedamzik, J. March-Russell and S. M. West, *Freeze-In Production of FIMP Dark Matter*, *J. High Energ. Phys.* **2010** (2010) 80, [[0911.1120](#)]. Cited on the pages 27 and 121.
- [188] E. Morgante, *Aspects of WIMP Dark Matter searches at colliders and other probes*, Ph.D. thesis, Geneva U., Dept. Theor. Phys., 9, 2016. 10.1007/978-3-319-67606-7. Cited on the pages xx and 28.

- 
- [189] S. Tulin and H.-B. Yu, *Dark Matter Self-interactions and Small Scale Structure*, *Phys. Rept.* **730** (2018) 1–57, [[1705.02358](#)].  
Cited on the pages 28, 32, and 116.
- [190] A. Drukier and L. Stodolsky, *Principles and Applications of a Neutral Current Detector for Neutrino Physics and Astronomy*, *Phys. Rev. D* **30** (1984) 2295. Cited on page 28.
- [191] D. Z. Freedman, *Coherent Neutrino Nucleus Scattering as a Probe of the Weak Neutral Current*, *Phys. Rev. D* **9** (1974) 1389–1392.  
Cited on the pages 28 and 145.
- [192] M. W. Goodman and E. Witten, *Detectability of certain dark-matter candidates*, *Phys. Rev. D* **31** (Jun, 1985) 3059–3063. Cited on page 28.
- [193] A. K. Drukier, K. Freese and D. N. Spergel, *Detecting cold dark-matter candidates*, *Phys. Rev. D* **33** (Jun, 1986) 3495–3508. Cited on page 28.
- [194] COHERENT collaboration, D. Akimov et al., *Observation of Coherent Elastic Neutrino-Nucleus Scattering*, *Science* **357** (2017) 1123–1126, [[1708.01294](#)]. Cited on page 28.
- [195] DAMA collaboration, R. Bernabei et al., *First results from DAMA/LIBRA and the combined results with DAMA/NaI*, *Eur. Phys. J. C* **56** (2008) 333–355, [[0804.2741](#)]. Cited on page 28.
- [196] G. Adhikari et al., *An experiment to search for dark-matter interactions using sodium iodide detectors*, *Nature* **564** (2018) 83–86, [[1906.01791](#)].  
Cited on page 28.
- [197] J. Billard, L. Strigari and E. Figueroa-Feliciano, *Implication of neutrino backgrounds on the reach of next generation dark matter direct detection experiments*, *Phys. Rev. D* **89** (2014) 023524, [[1307.5458](#)]. Cited on page 29.
- [198] C. A. J. O’Hare, *New Definition of the Neutrino Floor for Direct Dark Matter Searches*, *Phys. Rev. Lett.* **127** (2021) 251802, [[2109.03116](#)].  
Cited on page 29.
- [199] R. Essig, J. Mardon and T. Volansky, *Direct Detection of Sub-GeV Dark Matter*, *Phys. Rev. D* **85** (2012) 076007, [[1108.5383](#)]. Cited on page 29.
- [200] M. Ibe, W. Nakano, Y. Shoji and K. Suzuki, *Migdal effect in dark matter direct detection experiments*, *J. High Energ. Phys.* **2018** (2018) 194.  
Cited on page 29.
- [201] C. Kouvaris and J. Pradler, *Probing sub-GeV Dark Matter with conventional detectors*, *Phys. Rev. Lett.* **118** (2017) 031803, [[1607.01789](#)].  
Cited on page 29.
- [202] S. Knapen, T. Lin, M. Pyle and K. M. Zurek, *Detection of Light Dark Matter With Optical Phonons in Polar Materials*, *Phys. Lett. B* **785** (2018)

- 386–390, [[1712.06598](#)]. Cited on page 29.
- [203] P. Salati, *Indirect and direct dark matter detection*, *PoS cargese* (2009) 009. Cited on the pages 29 and 77.
- [204] T. Lin, *Dark matter models and direct detection*, *PoS* **333** (2019) 009, [[1904.07915](#)]. Cited on page 29.
- [205] Y. Hochberg, Y. Kahn, M. Lisanti, K. M. Zurek, A. G. Grushin, R. Ilan et al., *Detection of sub-MeV Dark Matter with Three-Dimensional Dirac Materials*, *Phys. Rev. D* **97** (2018) 015004, [[1708.08929](#)]. Cited on page 29.
- [206] Y. Hochberg, T. Lin and K. M. Zurek, *Absorption of light dark matter in semiconductors*, *Phys. Rev. D* **95** (2017) 023013, [[1608.01994](#)]. Cited on page 29.
- [207] K. Schutz and K. M. Zurek, *Detectability of Light Dark Matter with Superfluid Helium*, *Phys. Rev. Lett.* **117** (2016) 121302, [[1604.08206](#)]. Cited on page 29.
- [208] D. Hooper, *TASI Lectures on Indirect Searches For Dark Matter*, *PoS TASI2018* (2019) 010, [[1812.02029](#)]. Cited on the pages 29, 30, and 77.
- [209] R. K. Leane, *Indirect Detection of Dark Matter in the Galaxy*, [2006.00513](#). Cited on page 29.
- [210] T. R. Slatyer, *Les Houches Lectures on Indirect Detection of Dark Matter*, in *Les Houches summer school on Dark Matter*, 9, 2021, [2109.02696](#). Cited on the pages 29, 30, and 77.
- [211] M. Cirelli, *Status of Indirect (and Direct) Dark Matter searches*, *PoS ICRC2015* (2016) 014, [[1511.02031](#)]. Cited on the pages xx and 30.
- [212] H.E.S.S. collaboration, H. Abdallah et al., *Search for dark matter annihilations towards the inner Galactic halo from 10 years of observations with H.E.S.S.*, *Phys. Rev. Lett.* **117** (2016) 111301, [[1607.08142](#)]. Cited on page 30.
- [213] K. N. Abazajian, S. Horiuchi, M. Kaplinghat, R. E. Keeley and O. Macias, *Strong constraints on thermal relic dark matter from Fermi-LAT observations of the Galactic Center*, *Phys. Rev. D* **102** (2020) 043012, [[2003.10416](#)]. Cited on the pages 30 and 87.
- [214] FERMI-LAT collaboration, M. Ackermann et al., *Searching for Dark Matter Annihilation from Milky Way Dwarf Spheroidal Galaxies with Six Years of Fermi Large Area Telescope Data*, *Phys. Rev. Lett.* **115** (2015) 231301, [[1503.02641](#)]. Cited on the pages 30, 95, and 106.
- [215] S. Hoof, A. Geringer-Sameth and R. Trotta, *A Global Analysis of Dark Matter Signals from 27 Dwarf Spheroidal Galaxies using 11 Years of Fermi-LAT Observations*, *JCAP* **02** (2020) 012, [[1812.06986](#)].

Cited on page 30.

- [216] AMS collaboration, M. Aguilar et al., *Antiproton Flux, Antiproton-to-Proton Flux Ratio, and Properties of Elementary Particle Fluxes in Primary Cosmic Rays Measured with the Alpha Magnetic Spectrometer on the International Space Station*, *Phys. Rev. Lett.* **117** (2016) 091103. Cited on page 30.
- [217] A. Cuoco, M. Krämer and M. Korsmeier, *Novel Dark Matter Constraints from Antiprotons in Light of AMS-02*, *Phys. Rev. Lett.* **118** (2017) 191102, [1610.03071]. Cited on page 30.
- [218] I. John and T. Linden, *Cosmic-ray positrons strongly constrain leptophilic dark matter*, *JCAP* **12** (2021) 007, [2107.10261].  
Cited on the pages 30 and 104.
- [219] M. Danninger, *Review of indirect detection of dark matter with neutrinos*, in *Journal of Physics Conference Series*, vol. 888 of *Journal of Physics Conference Series*, p. 012039, Sept., 2017, DOI. Cited on page 30.
- [220] R. Essig, E. Kuffik, S. D. McDermott, T. Volansky and K. M. Zurek, *Constraining light dark matter with diffuse X-ray and gamma-ray observations*, *J. High Energ. Phys.* **2013** (2013) 193. Cited on page 30.
- [221] T. E. Jeltema and S. Profumo, *Dark Matter Detection with Hard X-ray Telescopes*, *Mon. Not. Roy. Astron. Soc.* **421** (2012) 1215, [1108.1407].  
Cited on page 30.
- [222] C. Evoli, A. Mesinger and A. Ferrara, *Unveiling the nature of dark matter with high redshift 21 cm line experiments*, *JCAP* **11** (2014) 024, [1408.1109]. Cited on page 30.
- [223] L. Goodenough and D. Hooper, *Possible Evidence For Dark Matter Annihilation In The Inner Milky Way From The Fermi Gamma Ray Space Telescope*, 0910.2998. Cited on page 30.
- [224] S. Murgia, *The Fermi–LAT Galactic Center Excess: Evidence of Annihilating Dark Matter?*, *Ann. Rev. Nucl. Part. Sci.* **70** (2020) 455–483.  
Cited on page 30.
- [225] FERMI-LAT, DES collaboration, A. Albert et al., *Searching for Dark Matter Annihilation in Recently Discovered Milky Way Satellites with Fermi-LAT*, *Astrophys. J.* **834** (2017) 110, [1611.03184].  
Cited on the pages 30 and 87.
- [226] AMS collaboration, L. Accardo et al., *High Statistics Measurement of the Positron Fraction in Primary Cosmic Rays of 0.5–500 GeV with the Alpha Magnetic Spectrometer on the International Space Station*, *Phys. Rev. Lett.* **113** (2014) 121101. Cited on page 30.
- [227] J. Goodman, M. Ibe, A. Rajaraman, W. Shepherd, T. M. P. Tait and H.-B.

- Yu, *Constraints on Dark Matter from Colliders*, *Phys. Rev. D* **82** (2010) 116010, [1008.1783]. Cited on the pages xx and 31.
- [228] G. Sciolla et al., *The DMTPC project*, *J. Phys. Conf. Ser.* **179** (2009) 012009, [0903.3895]. Cited on page 31.
- [229] KIMS collaboration, H. S. Lee et al., *Limits on WIMP-nucleon cross section with CsI(Tl) crystal detectors*, *Phys. Rev. Lett.* **99** (2007) 091301, [0704.0423]. Cited on page 31.
- [230] S. Archambault et al., *Dark Matter Spin-Dependent Limits for WIMP Interactions on F-19 by PICASSO*, *Phys. Lett. B* **682** (2009) 185–192, [0907.0307]. Cited on page 31.
- [231] E. Aprile, K. Arisaka, F. Arneodo, A. Askin, L. Baudis, A. Behrens et al., *First Dark Matter Results from the XENON100 Experiment*, *Phys. Rev. Lett.* **105** (Sept., 2010) 131302, [1005.0380]. Cited on page 31.
- [232] F. Kahlhoefer, *Review of LHC Dark Matter Searches*, *Int. J. Mod. Phys. A* **32** (2017) 1730006, [1702.02430]. Cited on page 31.
- [233] A. Boveia and C. Doglioni, *Dark Matter Searches at Colliders*, *Annu. Rev. Nucl. Part. Sci.* **68** (2018) 429–459, [1810.12238]. Cited on page 31.
- [234] J. Beacham et al., *Physics Beyond Colliders at CERN: Beyond the Standard Model Working Group Report*, *J. Phys. G* **47** (2020) 010501, [1901.09966]. Cited on the pages 32, 35, 37, 38, 41, 42, 44, 49, 62, 90, 102, and 103.
- [235] J. Alimena et al., *Searching for long-lived particles beyond the Standard Model at the Large Hadron Collider*, *J. Phys. G* **47** (2020) 090501, [1903.04497]. Cited on the pages 32, 35, 37, 38, 41, and 90.
- [236] P. Agrawal et al., *Feebly-interacting particles: FIPs 2020 workshop report*, *Eur. Phys. J. C* **81** (2021) 1015, [2102.12143]. Cited on the pages 32, 37, 38, 41, 90, and 132.
- [237] BABAR collaboration, J. P. Lees et al., *Search for Invisible Decays of a Dark Photon Produced in  $e^+e^-$  Collisions at BaBar*, *Phys. Rev. Lett.* **119** (2017) 131804, [1702.03327]. Cited on page 32.
- [238] BABAR collaboration, B. Aubert et al., *A Search for Invisible Decays of the Upsilon(1S)*, *Phys. Rev. Lett.* **103** (2009) 251801, [0908.2840]. Cited on page 32.
- [239] BELLE-II collaboration, T. Abe et al., *Belle II Technical Design Report*, 1011.0352. Cited on page 32.
- [240] LDMX collaboration, T. Åkesson et al., *Light Dark Matter eXperiment (LDMX)*, 1808.05219. Cited on page 32.
- [241] Y. Kahn, G. Krnjaic, N. Tran and A. Whitbeck,  $M^3$ : a new muon missing

- momentum experiment to probe  $(g - 2)_\mu$  and dark matter at Fermilab*, *JHEP* **09** (2018) 153, [[1804.03144](#)]. Cited on page 32.
- [242] D. Banerjee et al., *Dark matter search in missing energy events with NA64*, *Phys. Rev. Lett.* **123** (2019) 121801, [[1906.00176](#)]. Cited on page 32.
- [243] MINIBOONE DM collaboration, A. A. Aguilar-Arevalo et al., *Dark Matter Search in Nucleon, Pion, and Electron Channels from a Proton Beam Dump with MiniBooNE*, *Phys. Rev. D* **98** (2018) 112004, [[1807.06137](#)]. Cited on page 32.
- [244] M. Battaglieri et al., *US Cosmic Visions: New Ideas in Dark Matter 2017: Community Report*, in *U.S. Cosmic Visions: New Ideas in Dark Matter*, 7, 2017, [1707.04591](#). Cited on the pages 32, 35, 37, 38, 42, and 90.
- [245] B. Batell, J. L. Feng and S. Trojanowski, *Detecting Dark Matter with Far-Forward Emulsion and Liquid Argon Detectors at the LHC*, *Phys. Rev. D* **103** (2021) 075023, [[2101.10338](#)]. Cited on the pages 32, 42, 57, 59, 60, 68, and 69.
- [246] SHiP Collaboration, C. Ahdida, A. Akmete, R. Albanese, A. Alexandrov, M. Andreini et al., *SND @LHC*, *arXiv e-prints* (Feb., 2020) arXiv:2002.08722, [[2002.08722](#)]. Cited on page 32.
- [247] SHiP Collaboration, *Sensitivity of the SHiP experiment to light dark matter*, *arXiv e-prints* (Oct., 2020) arXiv:2010.11057, [[2010.11057](#)]. Cited on page 32.
- [248] L. Marsicano, M. Battaglieri, M. Bondí, C. D. R. Carvajal, A. Celentano, M. De Napoli et al., *Novel Way to Search for Light Dark Matter in Lepton Beam-Dump Experiments*, *Phys. Rev. Lett.* **121** (2018) 041802, [[1807.05884](#)]. Cited on page 32.
- [249] L. Buonocore, P. deNiverville and C. Frugiuele, *The hunt for sub-GeV dark matter at neutrino facilities: A survey of past and present experiments*, [1912.09346](#). Cited on page 32.
- [250] M. R. Buckley and A. H. G. Peter, *Gravitational probes of dark matter physics*, *Physics Reports* **761** (2018) 1–60, [[1712.06615](#)]. Cited on page 32.
- [251] S. W. Randall, M. Markevitch, D. Clowe, A. H. Gonzalez and M. Bradac, *Constraints on the Self-Interaction Cross-Section of Dark Matter from Numerical Simulations of the Merging Galaxy Cluster 1E 0657-56*, *Astrophys. J.* **679** (2008) 1173–1180, [[0704.0261](#)]. Cited on the pages 32 and 116.
- [252] K. E. Andrade, J. Fuson, S. Gad-Nasr, D. Kong, Q. Minor, M. G. Roberts et al., *A Stringent Upper Limit on Dark Matter Self-Interaction Cross Section from Cluster Strong Lensing*, [2012.06611](#). Cited on page 32.
- [253] K. Bondarenko, A. Boyarsky, T. Bringmann and A. Sokolenko,

- Constraining self-interacting dark matter with scaling laws of observed halo surface densities*, *JCAP* **04** (2018) 049, [[1712.06602](#)]. Cited on page 32.
- [254] J. Zavala, M. R. Lovell, M. Vogelsberger and J. D. Burger, *Diverse dark matter density at sub-kiloparsec scales in Milky Way satellites: Implications for the nature of dark matter*, *Phys. Rev. D* **100** (2019) 063007, [[1904.09998](#)]. Cited on page 32.
- [255] T. Hambye and L. Vanderheyden, *Minimal self-interacting dark matter models with light mediator*, [1912.11708](#). Cited on page 32.
- [256] R. K. Leane, T. R. Slatyer, J. F. Beacom and K. C. Y. Ng, *GeV-scale thermal WIMPs: Not even slightly ruled out*, *Phys. Rev. D* **98** (2018) 023016, [[1805.10305](#)]. Cited on page 33.
- [257] M. J. Strassler and K. M. Zurek, *Echoes of a hidden valley at hadron colliders*, *Phys. Lett. B* **651** (2007) 374–379, [[hep-ph/0604261](#)].  
Cited on the pages 35 and 90.
- [258] S. Alekhin et al., *A facility to Search for Hidden Particles at the CERN SPS: the SHiP physics case*, *Rept. Prog. Phys.* **79** (2016) 124201, [[1504.04855](#)]. Cited on the pages xx, 35, 36, 38, 40, 44, 59, and 103.
- [259] A. De Simone and T. Jacques, *Simplified models vs. effective field theory approaches in dark matter searches*, *Eur. Phys. J. C* **76** (2016) 367, [[1603.08002](#)]. Cited on page 35.
- [260] M. Fabbrichesi, E. Gabrielli and G. Lanfranchi, *The Dark Photon*, [2005.01515](#). Cited on the pages 36, 90, and 99.
- [261] M. Bauer, P. Foldenauer and J. Jaeckel, *Hunting All the Hidden Photons*, *JHEP* **07** (2018) 094, [[1803.05466](#)]. Cited on the pages 36, 62, and 97.
- [262] A. Filippi and M. De Napoli, *Searching in the dark: the hunt for the dark photon*, *Rev. Phys.* **5** (2020) 100042, [[2006.04640](#)].  
Cited on the pages 36 and 90.
- [263] L. B. Okun, *Limits of electrodynamics: paraphotons?*, *Sov. Phys. JETP* **56** (1982) 502. Cited on the pages 36 and 99.
- [264] B. Holdom, *Two U(1)'s and Epsilon Charge Shifts*, *Phys. Lett.* **166B** (1986) 196–198. Cited on the pages 36 and 99.
- [265] T. Gherghetta, J. Kersten, K. Olive and M. Pospelov, *Evaluating the price of tiny kinetic mixing*, *Phys. Rev. D* **100** (2019) 095001, [[1909.00696](#)].  
Cited on the pages 36 and 99.
- [266] G. Arcadi, A. Djouadi and M. Raidal, *Dark Matter through the Higgs portal*, *Phys. Rept.* **842** (2020) 1–180, [[1903.03616](#)].  
Cited on the pages 36 and 138.

- [267] O. Lebedev, *The Higgs portal to cosmology*, *Prog. Part. Nucl. Phys.* **120** (2021) 103881, [[2104.03342](#)]. Cited on the pages 36 and 155.
- [268] K. Bondarenko, A. Boyarsky, D. Gorbunov and O. Ruchayskiy, *Phenomenology of GeV-scale Heavy Neutral Leptons*, *JHEP* **11** (2018) 032, [[1805.08567](#)]. Cited on the pages 37 and 60.
- [269] PLANCK collaboration, P. A. R. Ade et al., *Planck 2015 results. XIII. Cosmological parameters*, *Astron. Astrophys.* **594** (2016) A13, [[1502.01589](#)]. Cited on page 37.
- [270] T. R. Slatyer, N. Padmanabhan and D. P. Finkbeiner, *CMB Constraints on WIMP Annihilation: Energy Absorption During the Recombination Epoch*, *Phys. Rev. D* **80** (2009) 043526, [[0906.1197](#)]. Cited on page 37.
- [271] B. Batell, M. Pospelov and A. Ritz, *Probing a Secluded  $U(1)$  at  $B$ -factories*, *Phys. Rev. D* **79** (2009) 115008, [[0903.0363](#)]. Cited on the pages 37, 42, 44, and 90.
- [272] A. Berlin, N. Blinov, G. Krnjaic, P. Schuster and N. Toro, *Dark Matter, Millicharges, Axion and Scalar Particles, Gauge Bosons, and Other New Physics with LDMX*, *Phys. Rev.* **D99** (2019) 075001, [[1807.01730](#)]. Cited on the pages 37 and 43.
- [273] J. Alexander et al., *Dark Sectors 2016 Workshop: Community Report*, [1608.08632](#). Cited on the pages 37 and 38.
- [274] FASER collaboration, H. Abreu et al., *Detecting and Studying High-Energy Collider Neutrinos with FASER at the LHC*, *Eur. Phys. J. C* **80** (2020) 61, [[1908.02310](#)]. Cited on the pages xx, 38, and 56.
- [275] MATHUSLA collaboration, E. Torr o Pastor, *Searches for ultra long-lived particles with MATHUSLA*, *PoS EPS-HEP2019* (2020) 572. Cited on the pages xx and 38.
- [276] P. Candia, G. Cottin, A. M endez and V. Mu oz, *Searching for light long-lived neutralinos at Super-Kamiokande*, *Phys. Rev. D* **104** (2021) 055024, [[2107.02804](#)]. Cited on page 38.
- [277] A. Filimonova, R. Sch afer and S. Westhoff, *Probing dark sectors with long-lived particles at BELLE II*, *Phys. Rev. D* **101** (2020) 095006, [[1911.03490](#)]. Cited on the pages 38 and 103.
- [278] A. Kachanovich, U. Nierste and I. Nišandžić, *Higgs portal to dark matter and  $B \rightarrow K^{(*)}$  decays*, *Eur. Phys. J. C* **80** (2020) 669, [[2003.01788](#)]. Cited on the pages 38 and 103.
- [279] BABAR collaboration, J. P. Lees et al., *Search for Long-Lived Particles in  $e^+e^-$  Collisions*, *Phys. Rev. Lett.* **114** (2015) 171801, [[1502.02580](#)]. Cited on page 38.

- [280] J. L. Feng, I. Galon, F. Kling and S. Trojanowski, *ForwArd Search ExpeRiment at the LHC*, *Phys. Rev. D* **97** (2018) 035001, [[1708.09389](#)]. Cited on the pages 38, 46, 58, and 103.
- [281] J. L. Feng, I. Galon, F. Kling and S. Trojanowski, *Dark Higgs bosons at the ForwArd Search ExpeRiment*, *Phys. Rev. D* **97** (2018) 055034, [[1710.09387](#)]. Cited on the pages 38 and 44.
- [282] F. Kling and S. Trojanowski, *Heavy Neutral Leptons at FASER*, *Phys. Rev. D* **97** (2018) 095016, [[1801.08947](#)]. Cited on page 38.
- [283] J. L. Feng, I. Galon, F. Kling and S. Trojanowski, *Axionlike particles at FASER: The LHC as a photon beam dump*, *Phys. Rev. D* **98** (2018) 055021, [[1806.02348](#)]. Cited on page 38.
- [284] FASER collaboration, A. Ariga et al., *FASER's physics reach for long-lived particles*, *Phys. Rev. D* **99** (2019) 095011, [[1811.12522](#)]. Cited on the pages 38, 57, and 103.
- [285] FASER collaboration, H. Abreu et al., *Detecting and Studying High-Energy Collider Neutrinos with FASER at the LHC*, *Eur. Phys. J. C* **80** (2020) 61, [[1908.02310](#)]. Cited on the pages 39, 55, 56, and 57.
- [286] FASER COLLABORATION collaboration, H. Abreu, Y. Afik, C. Antel, J. Arakawa, A. Ariga, T. Ariga et al., *First neutrino interaction candidates at the lhc*, *Phys. Rev. D* **104** (Nov, 2021) L091101. Cited on page 39.
- [287] J. P. Chou, D. Curtin and H. J. Lubatti, *New Detectors to Explore the Lifetime Frontier*, *Phys. Lett. B* **767** (2017) 29–36, [[1606.06298](#)]. Cited on the pages 40 and 103.
- [288] D. Curtin et al., *Long-Lived Particles at the Energy Frontier: The MATHUSLA Physics Case*, *Rept. Prog. Phys.* **82** (2019) 116201, [[1806.07396](#)]. Cited on the pages 40 and 103.
- [289] MATHUSLA collaboration, C. Alpigiani et al., *A Letter of Intent for MATHUSLA: A Dedicated Displaced Vertex Detector above ATLAS or CMS.*, [1811.00927](#). Cited on page 40.
- [290] M. Anelli et al., *A facility to Search for Hidden Particles (SHiP) at the CERN SPS*, . Cited on the pages 40 and 59.
- [291] SHiP collaboration, C. Ahdida et al., *SHiP Experiment - Progress Report*, Tech. Rep. CERN-SPSC-2019-010. SPSC-SR-248, CERN, Geneva, Jan, 2019. Cited on the pages 40, 47, and 52.
- [292] K. S. Babu, C. F. Kolda and J. March-Russell, *Implications of generalized  $Z - Z'$  mixing*, *Phys. Rev. D* **57** (1998) 6788–6792, [[hep-ph/9710441](#)]. Cited on page 42.
- [293] E. Izaguirre, G. Krnjaic, P. Schuster and N. Toro, *Analyzing the Discovery*

- Potential for Light Dark Matter*, *Phys. Rev. Lett.* **115** (2015) 251301, [1505.00011]. Cited on page 42.
- [294] Y. Kahn, G. Krnjaic, J. Thaler and M. Toups, *DAEδALUS and dark matter detection*, *Phys. Rev.* **D91** (2015) 055006, [1411.1055]. Cited on the pages 42 and 140.
- [295] A. de Gouvêa, P. J. Fox, R. Harnik, K. J. Kelly and Y. Zhang, *Dark Tridents at Off-Axis Liquid Argon Neutrino Detectors*, *JHEP* **01** (2019) 001, [1809.06388]. Cited on page 42.
- [296] V. De Romeri, K. J. Kelly and P. A. N. Machado, *DUNE-PRISM Sensitivity to Light Dark Matter*, *Phys. Rev. D* **100** (2019) 095010, [1903.10505]. Cited on the pages 42, 46, and 140.
- [297] B. Batell, M. Pospelov and A. Ritz, *Exploring Portals to a Hidden Sector Through Fixed Targets*, *Phys. Rev.* **D80** (2009) 095024, [0906.5614]. Cited on the pages 42, 44, and 141.
- [298] B. Batell, R. Essig and Z. Surujon, *Strong Constraints on Sub-GeV Dark Sectors from SLAC Beam Dump E137*, *Phys. Rev. Lett.* **113** (2014) 171802, [1406.2698]. Cited on page 42.
- [299] P. deNiverville, C.-Y. Chen, M. Pospelov and A. Ritz, *Light dark matter in neutrino beams: production modelling and scattering signatures at MiniBooNE, T2K and SHiP*, *Phys. Rev. D* **95** (2017) 035006, [1609.01770]. Cited on the pages 42, 46, and 58.
- [300] BDX collaboration, M. Battaglieri et al., *Dark Matter Search in a Beam-Dump eXperiment (BDX) at Jefferson Lab*, 1607.01390. Cited on page 42.
- [301] L. Buonocore, C. Frugiuele, F. Maltoni, O. Mattelaer and F. Tramontano, *Event generation for beam dump experiments*, *JHEP* **05** (2019) 028, [1812.06771]. Cited on the pages 42 and 52.
- [302] G. F. Giudice, D. Kim, J.-C. Park and S. Shin, *Inelastic Boosted Dark Matter at Direct Detection Experiments*, *Phys. Lett.* **B780** (2018) 543–552, [1712.07126]. Cited on the pages 42 and 141.
- [303] L. Darmé, S. Rao and L. Roszkowski, *Signatures of dark Higgs boson in light fermionic dark matter scenarios*, *JHEP* **12** (2018) 014, [1807.10314]. Cited on the pages 42, 50, and 95.
- [304] D. Tucker-Smith and N. Weiner, *Inelastic dark matter*, *Phys. Rev.* **D64** (2001) 043502, [hep-ph/0101138]. Cited on page 43.
- [305] E. Izaguirre, G. Krnjaic and B. Shuve, *Discovering Inelastic Thermal-Relic Dark Matter at Colliders*, *Phys. Rev.* **D93** (2016) 063523, [1508.03050]. Cited on the pages 43 and 50.

- [306] D. Kim, J.-C. Park and S. Shin, *Dark Matter “Collider” from Inelastic Boosted Dark Matter*, *Phys. Rev. Lett.* **119** (2017) 161801, [[1612.06867](#)].  
Cited on the pages 43 and 142.
- [307] E. Izaguirre, Y. Kahn, G. Krnjaic and M. Moschella, *Testing Light Dark Matter Coannihilation With Fixed-Target Experiments*, *Phys. Rev.* **D96** (2017) 055007, [[1703.06881](#)]. Cited on page 43.
- [308] L. Darmé, S. Rao and L. Roszkowski, *Light dark Higgs boson in minimal sub-GeV dark matter scenarios*, *JHEP* **03** (2018) 084, [[1710.08430](#)].  
Cited on the pages 43, 95, and 141.
- [309] A. Berlin, S. Gori, P. Schuster and N. Toro, *Dark Sectors at the Fermilab SeaQuest Experiment*, *Phys. Rev.* **D98** (2018) 035011, [[1804.00661](#)].  
Cited on the pages 43 and 140.
- [310] J. R. Jordan, Y. Kahn, G. Krnjaic, M. Moschella and J. Spitz, *Signatures of Pseudo-Dirac Dark Matter at High-Intensity Neutrino Experiments*, *Phys. Rev.* **D98** (2018) 075020, [[1806.05185](#)]. Cited on page 43.
- [311] A. Berlin and F. Kling, *Inelastic Dark Matter at the LHC Lifetime Frontier: ATLAS, CMS, LHCb, CODEX-b, FASER, and MATHUSLA*, *Phys. Rev. D* **99** (2019) 015021, [[1810.01879](#)].  
Cited on the pages xxv, 43, 50, and 140.
- [312] L. Heurtier, D. Kim, J.-C. Park and S. Shin, *Explaining the ANITA Anomaly with Inelastic Boosted Dark Matter*, *Phys. Rev.* **D100** (2019) 055004, [[1905.13223](#)]. Cited on page 43.
- [313] J. D. Clarke, R. Foot and R. R. Volkas, *Phenomenology of a very light scalar ( $100 \text{ MeV} < m_h < 10 \text{ GeV}$ ) mixing with the SM Higgs*, *JHEP* **02** (2014) 123, [[1310.8042](#)]. Cited on page 44.
- [314] J. A. Evans, *Detecting Hidden Particles with MATHUSLA*, *Phys. Rev.* **D97** (2018) 055046, [[1708.08503](#)]. Cited on page 44.
- [315] T. Pierog, I. Karpenko, J. M. Katzy, E. Yatsenko and K. Werner, *EPOS LHC: Test of collective hadronization with data measured at the CERN Large Hadron Collider*, *Phys. Rev.* **C92** (2015) 034906, [[1306.0121](#)].  
Cited on the pages 45 and 58.
- [316] C. Baus, T. Pierog and R. Ulrich, *Cosmic Ray Monte Carlo (CRMC)*, .  
Cited on the pages 45 and 58.
- [317] A. Faessler, M. I. Krivoruchenko and B. V. Martemyanov, *Once more on electromagnetic form factors of nucleons in extended vector meson dominance model*, *Phys. Rev.* **C82** (2010) 038201, [[0910.5589](#)].  
Cited on page 46.
- [318] J. Blümlein and J. Brunner, *New Exclusion Limits on Dark Gauge Forces from Proton Bremsstrahlung in Beam-Dump Data*, *Phys. Lett. B* **731**

- (2014) 320–326, [1311.3870]. Cited on the pages 46 and 58.
- [319] A. Ariga et al., *Letter of Intent for FASER: ForwArd Search ExpeRiment at the LHC*, . Cited on page 47.
- [320] A. Ariga et al., *Technical Proposal for FASER: ForwArd Search ExpeRiment at the LHC*, . Cited on page 47.
- [321] SHiP collaboration, M. Anelli et al., *A facility to Search for Hidden Particles (SHiP) at the CERN SPS*, 1504.04956.  
Cited on the pages 47 and 52.
- [322] G. Lanfranchi, M. Pospelov and P. Schuster, *The Search for Feebly Interacting Particles*, *Ann. Rev. Nucl. Part. Sci.* **71** (2021) 279–313, [2011.02157]. Cited on the pages 49 and 102.
- [323] FASER collaboration, H. Abreu et al., *Technical Proposal: FASERnu*, 2001.03073. Cited on page 50.
- [324] MUON G-2 collaboration, G. W. Bennett et al., *Final Report of the Muon E821 Anomalous Magnetic Moment Measurement at BNL*, *Phys. Rev.* **D73** (2006) 072003, [hep-ex/0602035]. Cited on page 50.
- [325] M. Pospelov, *Secluded  $U(1)$  below the weak scale*, *Phys. Rev. D* **80** (2009) 095002, [0811.1030]. Cited on the pages 50 and 139.
- [326] MUON G-2 collaboration, B. Abi et al., *Measurement of the Positive Muon Anomalous Magnetic Moment to 0.46 ppm*, *Phys. Rev. Lett.* **126** (2021) 141801, [2104.03281]. Cited on page 50.
- [327] M. Gell-Mann, P. Ramond and R. Slansky, *Complex Spinors and Unified Theories*, *Conf. Proc.* **C790927** (1979) 315–321, [1306.4669].  
Cited on page 55.
- [328] R. N. Mohapatra and G. Senjanovic, *Neutrino Mass and Spontaneous Parity Violation*, *Phys. Rev. Lett.* **44** (1980) 912. Cited on page 55.
- [329] T. Yanagida, *Horizontal Symmetry and Masses of Neutrinos*, *Prog. Theor. Phys.* **64** (1980) 1103. Cited on page 55.
- [330] J. Schechter and J. W. F. Valle, *Neutrino Masses in  $SU(2) \times U(1)$  Theories*, *Phys. Rev.* **D22** (1980) 2227. Cited on page 55.
- [331] S. Gninenko, *The MiniBooNE anomaly and heavy neutrino decay*, *Phys. Rev. Lett.* **103** (2009) 241802, [0902.3802]. Cited on the pages 55 and 62.
- [332] E. Bertuzzo, S. Jana, P. A. Machado and R. Zukanovich Funchal, *Dark Neutrino Portal to Explain MiniBooNE excess*, *Phys. Rev. Lett.* **121** (2018) 241801, [1807.09877]. Cited on the pages 55, 62, 63, 66, and 148.
- [333] V. Brdar, A. Greljo, J. Kopp and T. Opferkuch, *The Neutrino Magnetic*

- Moment Portal: Cosmology, Astrophysics, and Direct Detection*, *JCAP* **01** (2021) 039, [[2007.15563](#)]. Cited on the pages 55, 61, 64, and 68.
- [334] SUPER-KAMIOKANDE collaboration, Y. Fukuda et al., *Evidence for oscillation of atmospheric neutrinos*, *Phys. Rev. Lett.* **81** (1998) 1562–1567, [[hep-ex/9807003](#)]. Cited on page 55.
- [335] SNO collaboration, Q. Ahmad et al., *Measurement of the rate of  $\nu_e + d \rightarrow p + p + e^-$  interactions produced by  $^8\text{B}$  solar neutrinos at the Sudbury Neutrino Observatory*, *Phys. Rev. Lett.* **87** (2001) 071301, [[nucl-ex/0106015](#)]. Cited on page 55.
- [336] SNO collaboration, Q. Ahmad et al., *Direct evidence for neutrino flavor transformation from neutral current interactions in the Sudbury Neutrino Observatory*, *Phys. Rev. Lett.* **89** (2002) 011301, [[nucl-ex/0204008](#)]. Cited on page 55.
- [337] DUNE collaboration, B. Abi et al., *Deep Underground Neutrino Experiment (DUNE), Far Detector Technical Design Report, Volume I Introduction to DUNE*, *JINST* **15** (2020) T08008, [[2002.02967](#)]. Cited on page 55.
- [338] HYPER-KAMIOKANDE collaboration, K. Abe et al., *Hyper-Kamiokande Design Report*, [1805.04163](#). Cited on page 55.
- [339] *Neutrino Non-Standard Interactions: A Status Report*, vol. 2, 2019. [10.21468/SciPostPhysProc.2.001](#). Cited on page 55.
- [340] A. Branca, G. Brunetti, A. Longhin, M. Martini, F. Pupilli and F. Terranova, *A New Generation of Neutrino Cross Section Experiments: Challenges and Opportunities*, *Symmetry* **13** (2021) 1625, [[2108.12212](#)]. Cited on page 55.
- [341] ICECUBE, FERMI-LAT, MAGIC, AGILE, ASAS-SN, HAWC, H.E.S.S., INTEGRAL, KANATA, KISO, KAPTEYN, LIVERPOOL TELESCOPE, SUBARU, SWIFT NUSTAR, VERITAS, VLA/17B-403 collaboration, M. Aartsen et al., *Multimessenger observations of a flaring blazar coincident with high-energy neutrino IceCube-170922A*, *Science* **361** (2018) eaat1378, [[1807.08816](#)]. Cited on page 55.
- [342] ICECUBE collaboration, M. G. Aartsen et al., *IceCube-Gen2: A Vision for the Future of Neutrino Astronomy in Antarctica*, [1412.5106](#). Cited on page 55.
- [343] ICECUBE collaboration, M. Aartsen et al., *Evidence for High-Energy Extraterrestrial Neutrinos at the IceCube Detector*, *Science* **342** (2013) 1242856, [[1311.5238](#)]. Cited on page 55.
- [344] ICECUBE collaboration, M. Aartsen et al., *Measurement of the multi-TeV neutrino cross section with IceCube using Earth absorption*, *Nature* **551**

- (2017) 596–600, [1711.08119]. Cited on page 55.
- [345] M. Bustamante and A. Connolly, *Extracting the Energy-Dependent Neutrino-Nucleon Cross Section above 10 TeV Using IceCube Showers*, *Phys. Rev. Lett.* **122** (2019) 041101, [1711.11043]. Cited on page 55.
- [346] FASER collaboration, H. Abreu et al., *Technical Proposal: FASERnu*, 2001.03073. Cited on the pages 55 and 57.
- [347] SHiP collaboration, C. Ahdida et al., *SND @LHC*, 2002.08722. Cited on page 56.
- [348] W. Bai, M. Diwan, M. V. Garzelli, Y. S. Jeong and M. H. Reno, *Far-forward neutrinos at the Large Hadron Collider*, *JHEP* **06** (2020) 032, [2002.03012]. Cited on page 56.
- [349] F. Kling, *Forward Neutrino Fluxes at the LHC*, 2105.08270. Cited on page 56.
- [350] PARTICLE DATA GROUP collaboration, P. Zyla et al., *Review of Particle Physics*, *PTEP* **2020** (2020) 083C01. Cited on page 56.
- [351] M. Lindner, F. S. Queiroz, W. Rodejohann and X.-J. Xu, *Neutrino-electron scattering: general constraints on  $Z'$  and dark photon models*, *JHEP* **05** (2018) 098, [1803.00060]. Cited on page 57.
- [352] M. Lindner, W. Rodejohann and X.-J. Xu, *Coherent Neutrino-Nucleus Scattering and new Neutrino Interactions*, *JHEP* **03** (2017) 097, [1612.04150]. Cited on page 57.
- [353] FASER collaboration, A. Ariga et al., *Technical Proposal for FASER: ForwArd Search ExpeRiment at the LHC*, 1812.09139. Cited on the pages 57 and 58.
- [354] N. Beni et al., *Further studies on the physics potential of an experiment using LHC neutrinos*, *J. Phys. G* **47** (2020) 125004, [2004.07828]. Cited on page 57.
- [355] FASER collaboration, A. Ariga et al., *Letter of Intent for FASER: ForwArd Search ExpeRiment at the LHC*, 1811.10243. Cited on page 58.
- [356] G. Magill, R. Plestid, M. Pospelov and Y.-D. Tsai, *Dipole Portal to Heavy Neutral Leptons*, *Phys. Rev. D* **98** (2018) 115015, [1803.03262]. Cited on the pages 59, 61, 62, 64, and 148.
- [357] SHiP collaboration, C. Ahdida et al., *The magnet of the scattering and neutrino detector for the SHiP experiment at CERN*, *JINST* **15** (2020) P01027, [1910.02952]. Cited on page 59.
- [358] A. Ferrari, P. R. Sala, A. Fasso and J. Ranft, *FLUKA: A multi-particle transport code (Program version 2005)*, . Cited on page 59.

- [359] G. Battistoni et al., *Overview of the FLUKA code*, *Annals Nucl. Energy* **82** (2015) 10–18. Cited on page 59.
- [360] C. Andreopoulos et al., *The GENIE Neutrino Monte Carlo Generator*, *Nucl. Instrum. Meth. A* **614** (2010) 87–104, [0905.2517]. Cited on page 59.
- [361] C. Andreopoulos, C. Barry, S. Dytman, H. Gallagher, T. Golan, R. Hatcher et al., *The GENIE Neutrino Monte Carlo Generator: Physics and User Manual*, 1510.05494. Cited on page 59.
- [362] T. Asaka and M. Shaposhnikov, *The  $\nu$ MSM, dark matter and baryon asymmetry of the universe*, *Phys. Lett. B* **620** (2005) 17–26, [hep-ph/0505013]. Cited on page 60.
- [363] Y. Farzan, M. Lindner, W. Rodejohann and X.-J. Xu, *Probing neutrino coupling to a light scalar with coherent neutrino scattering*, *JHEP* **05** (2018) 066, [1802.05171]. Cited on page 61.
- [364] S. Petcov, *The Processes  $\mu \rightarrow e \gamma$ ,  $\mu \rightarrow e e \text{ anti-}e$ , Neutrino  $\rightarrow$  Neutrino gamma in the Weinberg-Salam Model with Neutrino Mixing*, *Sov. J. Nucl. Phys.* **25** (1977) 340. Cited on page 61.
- [365] K. Fujikawa and R. Shrock, *The Magnetic Moment of a Massive Neutrino and Neutrino Spin Rotation*, *Phys. Rev. Lett.* **45** (1980) 963. Cited on page 61.
- [366] P. B. Pal and L. Wolfenstein, *Radiative Decays of Massive Neutrinos*, *Phys. Rev. D* **25** (1982) 766. Cited on page 61.
- [367] R. E. Shrock, *Electromagnetic Properties and Decays of Dirac and Majorana Neutrinos in a General Class of Gauge Theories*, *Nucl. Phys. B* **206** (1982) 359–379. Cited on page 61.
- [368] M. Dvornikov and A. Studenikin, *Electric charge and magnetic moment of massive neutrino*, *Phys. Rev. D* **69** (2004) 073001, [hep-ph/0305206]. Cited on page 61.
- [369] C. Giunti and A. Studenikin, *Neutrino electromagnetic interactions: a window to new physics*, *Rev. Mod. Phys.* **87** (2015) 531, [1403.6344]. Cited on page 61.
- [370] M. Lindner, B. Radovčić and J. Welter, *Revisiting Large Neutrino Magnetic Moments*, *JHEP* **07** (2017) 139, [1706.02555]. Cited on page 61.
- [371] K. S. Babu, S. Jana and M. Lindner, *Large Neutrino Magnetic Moments in the Light of Recent Experiments*, *JHEP* **10** (2020) 040, [2007.04291]. Cited on page 61.
- [372] P. Coloma, P. A. Machado, I. Martinez-Soler and I. M. Shoemaker, *Double-Cascade Events from New Physics in Icecube*, *Phys. Rev. Lett.* **119** (2017) 201804, [1707.08573]. Cited on the pages 61 and 64.

- [373] I. M. Shoemaker and J. Wyenberg, *Direct Detection Experiments at the Neutrino Dipole Portal Frontier*, *Phys. Rev. D* **99** (2019) 075010, [1811.12435]. Cited on the pages 61 and 64.
- [374] I. M. Shoemaker, Y.-D. Tsai and J. Wyenberg, *Active-to-sterile neutrino dipole portal and the XENON1T excess*, *Phys. Rev. D* **104** (2021) 115026, [2007.05513]. Cited on page 61.
- [375] S. N. Gninenko, *A resolution of puzzles from the LSND, KARMEN, and MiniBooNE experiments*, *Phys. Rev. D* **83** (2011) 015015, [1009.5536]. Cited on page 62.
- [376] MINIBOONE collaboration, A. Aguilar-Arevalo et al., *A Search for Electron Neutrino Appearance at the  $\Delta m^2 \sim 1\text{eV}^2$  Scale*, *Phys. Rev. Lett.* **98** (2007) 231801, [0704.1500]. Cited on the pages 62, 64, and 70.
- [377] LSND collaboration, C. Athanassopoulos et al., *Evidence for anti-muon-neutrino  $\rightarrow$  anti-electron-neutrino oscillations from the LSND experiment at LAMPF*, *Phys. Rev. Lett.* **77** (1996) 3082–3085, [nucl-ex/9605003]. Cited on page 62.
- [378] MINIBOONE collaboration, A. Aguilar-Arevalo et al., *Updated MiniBooNE Neutrino Oscillation Results with Increased Data and New Background Studies*, 2006.16883. Cited on the pages 62 and 70.
- [379] V. Brdar, O. Fischer and A. Y. Smirnov, *Model-independent bounds on the nonoscillatory explanations of the MiniBooNE excess*, *Phys. Rev. D* **103** (2021) 075008, [2007.14411]. Cited on the pages 62 and 63.
- [380] MINERvA collaboration, J. Park et al., *Measurement of Neutrino Flux from Neutrino-Electron Elastic Scattering*, *Phys. Rev. D* **93** (2016) 112007, [1512.07699]. Cited on the pages 62, 63, and 66.
- [381] F. Kling, *Probing light gauge bosons in tau neutrino experiments*, *Phys. Rev. D* **102** (2020) 015007, [2005.03594]. Cited on page 62.
- [382] P. Ballett, S. Pascoli and M. Ross-Lonergan,  *$U(1)'$  mediated decays of heavy sterile neutrinos in MiniBooNE*, *Phys. Rev. D* **99** (2019) 071701, [1808.02915]. Cited on the pages 62 and 63.
- [383] Y. Jho, J. Kim, P. Ko and S. C. Park, *Search for sterile neutrino with light gauge interactions: recasting collider, beam-dump, and neutrino telescope searches*, 2008.12598. Cited on the pages 63, 68, and 149.
- [384] J. Orloff, A. N. Rozanov and C. Santoni, *Limits on the mixing of tau neutrino to heavy neutrinos*, *Phys. Lett. B* **550** (2002) 8–15, [hep-ph/0208075]. Cited on the pages 63 and 68.
- [385] CHARM-II collaboration, P. Vilain et al., *Precision measurement of electroweak parameters from the scattering of muon-neutrinos on electrons*, *Phys. Lett. B* **335** (1994) 246–252. Cited on the pages 63 and 66.

- [386] C. A. Argüelles, M. Hostert and Y.-D. Tsai, *Testing New Physics Explanations of the MiniBooNE Anomaly at Neutrino Scattering Experiments*, *Phys. Rev. Lett.* **123** (2019) 261801, [[1812.08768](#)].  
Cited on the pages 63, 66, and 69.
- [387] CHARM-II collaboration, D. Geiregat et al., *A New Determination of the Electroweak Mixing Angle From  $\nu_\mu$  Electron Scattering*, *Phys. Lett. B* **232** (1989) 539. Cited on page 64.
- [388] NOMAD collaboration, J. Altegoer et al., *The NOMAD experiment at the CERN SPS*, *Nucl. Instrum. Meth. A* **404** (1998) 96–128. Cited on page 64.
- [389] DELPHI collaboration, P. Abreu et al., *Search for new phenomena using single photon events in the DELPHI detector at LEP*, *Z. Phys. C* **74** (1997) 577–586. Cited on page 64.
- [390] D. E. Groom, N. V. Mokhov and S. I. Striganov, *Muon stopping power and range tables 10-MeV to 100-TeV*, *Atom. Data Nucl. Data Tabl.* **78** (2001) 183–356. Cited on page 65.
- [391] A. Atre, T. Han, S. Pascoli and B. Zhang, *The Search for Heavy Majorana Neutrinos*, *JHEP* **05** (2009) 030, [[0901.3589](#)]. Cited on page 66.
- [392] A. de Gouvêa and A. Kobach, *Global Constraints on a Heavy Neutrino*, *Phys. Rev. D* **93** (2016) 033005, [[1511.00683](#)]. Cited on page 66.
- [393] P. D. Bolton, F. F. Deppisch and P. Bhupal Dev, *Neutrinoless double beta decay versus other probes of heavy sterile neutrinos*, *JHEP* **03** (2020) 170, [[1912.03058](#)]. Cited on page 66.
- [394] P. Ballett, M. Hostert and S. Pascoli, *Dark Neutrinos and a Three Portal Connection to the Standard Model*, *Phys. Rev. D* **101** (2020) 115025, [[1903.07589](#)]. Cited on page 67.
- [395] J. L. Bernal, L. Verde and A. G. Riess, *The trouble with  $H_0$* , *JCAP* **10** (2016) 019, [[1607.05617](#)]. Cited on page 68.
- [396] N. Schöneberg, G. Franco Abellán, A. Pérez Sánchez, S. J. Witte, V. Poulin and J. Lesgourgues, *The  $H_0$  Olympics: A fair ranking of proposed models*, [2107.10291](#). Cited on the pages 68, 112, 114, and 124.
- [397] A. Kobach and S. Dobbs, *Heavy Neutrinos and the Kinematics of Tau Decays*, *Phys. Rev. D* **91** (2015) 053006, [[1412.4785](#)]. Cited on page 68.
- [398] DELPHI collaboration, P. Abreu et al., *Search for neutral heavy leptons produced in Z decays*, *Z. Phys. C* **74** (1997) 57–71. Cited on page 68.
- [399] NOMAD collaboration, P. Astier et al., *Search for heavy neutrinos mixing with tau neutrinos*, *Phys. Lett. B* **506** (2001) 27–38, [[hep-ex/0101041](#)].  
Cited on page 68.

- [400] CHARM-II collaboration, D. Geiregat et al., *An Improved determination of the electroweak mixing angle from muon-neutrino electron scattering*, *Phys. Lett. B* **259** (1991) 499–507. Cited on page 69.
- [401] CHARM-II collaboration, P. Vilain et al., *Neutral current coupling constants from neutrino and anti-neutrino - electron scattering*, *Phys. Lett. B* **281** (1992) 159–166. Cited on page 69.
- [402] A. Abdullahi, M. Hostert and S. Pascoli, *A dark seesaw solution to low energy anomalies: MiniBooNE, the muon ( $g - 2$ ), and BaBar*, *Phys. Lett. B* **820** (2021) 136531, [2007.11813]. Cited on page 70.
- [403] A. Datta, S. Kamali and D. Marfatia, *Dark sector origin of the KOTO and MiniBooNE anomalies*, *Phys. Lett. B* **807** (2020) 135579, [2005.08920]. Cited on page 70.
- [404] B. Dutta, S. Ghosh and T. Li, *Explaining  $(g - 2)_{\mu,e}$ , the KOTO anomaly and the MiniBooNE excess in an extended Higgs model with sterile neutrinos*, *Phys. Rev. D* **102** (2020) 055017, [2006.01319]. Cited on page 70.
- [405] W. Abdallah, R. Gandhi and S. Roy, *Understanding the MiniBooNE and the muon and electron  $g - 2$  anomalies with a light  $Z$  and a second Higgs doublet*, *JHEP* **12** (2020) 188, [2006.01948]. Cited on page 70.
- [406] K. Griest, *Cross-Sections, Relic Abundance and Detection Rates for Neutralino Dark Matter*, *Phys. Rev. D* **38** (1988) 2357. Cited on page 71.
- [407] R. Barbieri, M. Frigeni and G. F. Giudice, *Dark Matter Neutralinos in Supergravity Theories*, *Nucl. Phys. B* **313** (1989) 725–735. Cited on page 71.
- [408] L. Roszkowski, *Light neutralino as dark matter*, *Phys. Lett. B* **262** (1991) 59–67. Cited on page 71.
- [409] K. Kowalska and E. M. Sessolo, *The discreet charm of higgsino dark matter - a pocket review*, *Adv. High Energy Phys.* **2018** (2018) 6828560, [1802.04097]. Cited on the pages xxii, 71, and 75.
- [410] S. Pokorski, *Gauge Field Theories*. Cambridge Monographs on Mathematical Physics. Cambridge University Press, 2000. Cited on page 71.
- [411] C. Csáki and P. Tanedo, *Beyond the Standard Model*, in *2013 European School of High-Energy Physics*, pp. 169–268, 2015, 1602.04228, DOI. Cited on page 71.
- [412] M. T. Grisaru, W. Siegel and M. Roček, *Improved methods for supergraphs*, *Nuclear Physics B* **159** (Nov., 1979) 429–450. Cited on page 72.
- [413] J. Rosiek, *Complete set of Feynman rules for the MSSM: Erratum*, [hep-ph/9511250](https://arxiv.org/abs/hep-ph/9511250). Cited on the pages 73 and 81.
- [414] C. Arina and N. Fornengo, *Sneutrino cold dark matter, a new analysis:*

- Relic abundance and detection rates*, *JHEP* **11** (2007) 029, [0709.4477].  
Cited on page 73.
- [415] N. Arkani-Hamed, A. Delgado and G. F. Giudice, *The Well-tempered neutralino*, *Nucl. Phys. B* **741** (2006) 108–130, [hep-ph/0601041].  
Cited on page 74.
- [416] M. Bauer and T. Plehn, *Yet Another Introduction to Dark Matter*, **1705.01987**. Cited on the pages xxii and 75.
- [417] J. A. Hinton and W. Hofmann, *Teraelectronvolt Astronomy*, *araa* **47** (Sept., 2009) 523–565, [1006.5210]. Cited on the pages xxii and 76.
- [418] G. Bertone, D. Hooper and J. Silk, *Particle Dark Matter: Evidence, Candidates and Constraints*, *Physics Reports* **405** (2005) 279–390, [hep-ph/0404175]. Cited on the pages xxii and 77.
- [419] M. Cirelli, “Dark matter phenomenology.”  
<http://www.marcocirelli.net/talks/lecturenotesIPhT.pdf>.  
Cited on the pages xxii and 77.
- [420] M. Cirelli, G. Corcella, A. Hektor, G. Hutsi, M. Kadastik, P. Panci et al., *PPPC 4 DM ID: A Poor Particle Physicist Cookbook for Dark Matter Indirect Detection*, *JCAP* **03** (2011) 051, [1012.4515].  
Cited on the pages xxii, 77, 78, and 159.
- [421] Y. Mambrini, “Histories of particles in the dark universe.”  
[http://www.ymambrini.com/My\\_World/Physics\\_files/Universe.pdf](http://www.ymambrini.com/My_World/Physics_files/Universe.pdf).  
Cited on the pages xxii and 79.
- [422] Gaia Collaboration, A. G. A. Brown, A. Vallenari, T. Prusti, J. H. J. de Bruijne, C. Babusiaux et al., *Gaia Data Release 2. Summary of the contents and survey properties*, *A&A* **616** (Aug., 2018) A1, [1804.09365].  
Cited on page 76.
- [423] L. Posti and A. Helmi, *Mass and shape of the Milky Way’s dark matter halo with globular clusters from Gaia and Hubble*, *A&A* **621** (Jan., 2019) A56, [1805.01408]. Cited on page 76.
- [424] J. Einasto, *On the Construction of a Composite Model for the Galaxy and on the Determination of the System of Galactic Parameters*, *Trudy Astrofizicheskogo Instituta Alma-Ata* **5** (1965) 87–100. Cited on page 76.
- [425] J. F. Navarro, C. S. Frenk and S. D. M. White, *A Universal density profile from hierarchical clustering*, *Astrophys. J.* **490** (1997) 493–508, [astro-ph/9611107]. Cited on page 76.
- [426] R. Catena and P. Ullio, *A novel determination of the local dark matter density*, *J. Cosmol. Astropart. Phys.* **2010** (2010) , [0907.0018].  
Cited on page 76.

- [427] B. Moore, S. Ghigna, F. Governato, G. Lake, T. R. Quinn, J. Stadel et al., *Dark matter substructure within galactic halos*, *Astrophys. J. Lett.* **524** (1999) L19–L22, [[astro-ph/9907411](#)]. Cited on page 76.
- [428] J. M. Gaskins, *A review of indirect searches for particle dark matter*, *Contemp. Phys.* **57** (2016) 496–525, [[1604.00014](#)]. Cited on page 77.
- [429] C. van Eldik, *Gamma rays from the Galactic Centre region: a review*, *Astropart. Phys.* **71** (2015) 45–70, [[1505.06055](#)]. Cited on page 78.
- [430] H.E.S.S. collaboration, H. Abdallah et al., *Search for dark matter annihilations towards the inner Galactic halo from 10 years of observations with H.E.S.S.*, *Phys. Rev. Lett.* **117** (2016) 111301, [[1607.08142](#)]. Cited on page 78.
- [431] HESS collaboration, H. Abdallah et al., *Search for  $\gamma$ -Ray Line Signals from Dark Matter Annihilations in the Inner Galactic Halo from 10 Years of Observations with H.E.S.S.*, *Phys. Rev. Lett.* **120** (2018) 201101, [[1805.05741](#)]. Cited on the pages xxii, 78, and 80.
- [432] T. C. T. A. Consortium, B. S. Acharya, I. Agudo, I. A. Samarai, R. Alfaro, J. Alfaro et al., *Science with the Cherenkov Telescope Array*, [1709.07997](#). Cited on page 78.
- [433] E. Moulin, J. Carr, J. Gaskins, M. Doro, C. Farnier, M. Wood et al., *Dark Matter Programme*, pp. 45–81. 2019. 10.1142/9789813270091\_0004. Cited on the pages 78 and 79.
- [434] H.E.S.S. collaboration, F. Aharonian et al., *Very high energy gamma rays from the composite SNR G0.9+0.1*, *Astron. Astrophys.* **432** (2005) L25–L29, [[astro-ph/0501265](#)]. Cited on page 78.
- [435] H.E.S.S. collaboration, F. Aharonian et al., *Discovery of very-high-energy gamma-rays from the galactic centre ridge*, *Nature* **439** (2006) 695–698, [[astro-ph/0603021](#)]. Cited on page 78.
- [436] H.E.S.S. collaboration, A. Abramowski et al., *Acceleration of petaelectronvolt protons in the Galactic Centre*, *Nature* **531** (2016) 476, [[1603.07730](#)]. Cited on page 78.
- [437] A. Djouadi, S. Rosier-Lees, M. Bezouh, M. A. Bizouard, C. Boehm, F. Borzumati et al., *The Minimal Supersymmetric Standard Model: Group Summary Report*, [hep-ph/9901246](#). Cited on page 81.
- [438] M. Cahill-Rowley, J. L. Hewett, A. Ismail and T. G. Rizzo, *Lessons and prospects from the pMSSM after LHC Run I*, *Phys. Rev.* **D91** (2015) 055002, [[1407.4130](#)]. Cited on the pages 81 and 83.
- [439] F. Feroz and M. P. Hobson, *Multimodal nested sampling: an efficient and robust alternative to MCMC methods for astronomical data analysis*, *Mon. Not. Roy. Astron. Soc.* **384** (2008) 449, [[0704.3704](#)]. Cited on page 81.

- [440] F. Feroz, M. P. Hobson and M. Bridges, *MultiNest: an efficient and robust Bayesian inference tool for cosmology and particle physics*, *Mon. Not. Roy. Astron. Soc.* **398** (2009) 1601–1614, [[0809.3437](#)]. Cited on page 81.
- [441] W. Porod, *SPheno, a program for calculating supersymmetric spectra, SUSY particle decays and SUSY particle production at  $e^+ e^-$  colliders*, *Comput. Phys. Commun.* **153** (2003) 275–315, [[hep-ph/0301101](#)]. Cited on page 81.
- [442] W. Porod and F. Staub, *SPheno 3.1: Extensions including flavour, CP-phases and models beyond the MSSM*, *Comput. Phys. Commun.* **183** (2012) 2458–2469, [[1104.1573](#)]. Cited on page 81.
- [443] J. R. Ellis, A. Ferstl and K. A. Olive, *Reevaluation of the elastic scattering of supersymmetric dark matter*, *Phys. Lett.* **B481** (2000) 304–314, [[hep-ph/0001005](#)]. Cited on page 81.
- [444] C. Cheung, L. J. Hall, D. Pinner and J. T. Ruderman, *Prospects and Blind Spots for Neutralino Dark Matter*, *JHEP* **05** (2013) 100, [[1211.4873](#)]. Cited on page 81.
- [445] ATLAS, CDF, CMS, D0 collaboration, *First combination of Tevatron and LHC measurements of the top-quark mass*, [1403.4427](#). Cited on page 82.
- [446] G. Belanger, F. Boudjema, A. Pukhov and A. Semenov, *MicrOMEGAs: A Program for calculating the relic density in the MSSM*, *Comput. Phys. Commun.* **149** (2002) 103–120, [[hep-ph/0112278](#)]. Cited on page 82.
- [447] G. Belanger, F. Boudjema, A. Pukhov and A. Semenov, *micrOMEGAs: Version 1.3*, *Comput. Phys. Commun.* **174** (2006) 577–604, [[hep-ph/0405253](#)]. Cited on page 82.
- [448] A. Hryczuk, *The Sommerfeld enhancement for scalar particles and application to sfermion co-annihilation regions*, *Phys. Lett.* **B699** (2011) 271–275, [[1102.4295](#)]. Cited on page 82.
- [449] M. Cirelli, A. Strumia and M. Tamburini, *Cosmology and Astrophysics of Minimal Dark Matter*, *Nucl. Phys.* **B787** (2007) 152–175, [[0706.4071](#)]. Cited on page 83.
- [450] A. Hryczuk, R. Iengo and P. Ullio, *Relic densities including Sommerfeld enhancements in the MSSM*, *JHEP* **03** (2011) 069, [[1010.2172](#)]. Cited on page 83.
- [451] A. Fowlie, K. Kowalska, L. Roszkowski, E. M. Sessolo and Y.-L. S. Tsai, *Dark matter and collider signatures of the MSSM*, *Phys. Rev.* **D88** (2013) 055012, [[1306.1567](#)]. Cited on page 83.
- [452] L. Roszkowski, E. M. Sessolo and A. J. Williams, *Prospects for dark matter searches in the  $p$ MSSM*, *JHEP* **02** (2015) 014, [[1411.5214](#)]. Cited on the pages 83 and 85.

- [453] M. E. C. Catalan, S. Ando, C. Weniger and F. Zandanel, *Indirect and direct detection prospect for TeV dark matter in the MSSM-9*, *Phys. Rev. D* **92** (2015) 035018, [[1503.00599](#)]. Cited on the pages 83 and 85.
- [454] ATLAS collaboration, G. Aad et al., *Summary of the ATLAS experiment's sensitivity to supersymmetry after LHC Run 1 — interpreted in the phenomenological MSSM*, *JHEP* **10** (2015) 134, [[1508.06608](#)].  
Cited on page 83.
- [455] M. Beneke, A. Bharucha, A. Hryczuk, S. Recksiegel and P. Ruiz-Femenia, *The last refuge of mixed wino-Higgsino dark matter*, *JHEP* **01** (2017) 002, [[1611.00804](#)]. Cited on page 83.
- [456] A. Arbey, M. Boudaud, F. Mahmoudi and G. Robbins, *Robustness of dark matter constraints and interplay with collider searches for New Physics*, *JHEP* **11** (2017) 132, [[1707.00426](#)]. Cited on page 83.
- [457] GAMBIT collaboration, P. Athron et al., *A global fit of the MSSM with GAMBIT*, *Eur. Phys. J. C* **77** (2017) 879, [[1705.07917](#)]. Cited on page 83.
- [458] S. Abel, D. G. Cerdeño and S. Robles, *The Power of Genetic Algorithms: what remains of the pMSSM?*, [1805.03615](#). Cited on page 83.
- [459] XENON collaboration, E. Aprile et al., *Dark Matter Search Results from a One Ton-Year Exposure of XENON1T*, *Phys. Rev. Lett.* **121** (2018) 111302, [[1805.12562](#)]. Cited on page 85.
- [460] G. Arcadi, A. Djouadi and M. Kado, *The Higgs-portal for dark matter: effective field theories versus concrete realizations*, *Eur. Phys. J. C* **81** (2021) 653, [[2101.02507](#)]. Cited on page 90.
- [461] T. Bringmann, F. Kahlhoefer, K. Schmidt-Hoberg and P. Walia, *Strong constraints on self-interacting dark matter with light mediators*, *Phys. Rev. Lett.* **118** (2017) 141802, [[1612.00845](#)]. Cited on the pages 90, 127, and 128.
- [462] Z. Chacko, H.-S. Goh and R. Harnik, *The Twin Higgs: Natural electroweak breaking from mirror symmetry*, *Phys. Rev. Lett.* **96** (2006) 231802, [[hep-ph/0506256](#)]. Cited on page 90.
- [463] R. M. Schabinger and J. D. Wells, *A Minimal spontaneously broken hidden sector and its impact on Higgs boson physics at the large hadron collider*, *Phys. Rev. D* **72** (2005) 093007, [[hep-ph/0509209](#)]. Cited on page 90.
- [464] B. Patt and F. Wilczek, *Higgs-field portal into hidden sectors*, [hep-ph/0605188](#). Cited on page 90.
- [465] G. C. Branco, P. M. Ferreira, L. Lavoura, M. N. Rebelo, M. Sher and J. P. Silva, *Theory and phenomenology of two-Higgs-doublet models*, *Phys. Rept.* **516** (2012) 1–102, [[1106.0034](#)]. Cited on page 90.
- [466] N. Craig, A. Katz, M. Strassler and R. Sundrum, *Naturalness in the Dark*

- at the LHC, *JHEP* **07** (2015) 105, [[1501.05310](#)]. Cited on page 90.
- [467] I. Z. Rothstein, T. Schwetz and J. Zupan, *Phenomenology of Dark Matter annihilation into a long-lived intermediate state*, *JCAP* **07** (2009) 018, [[0903.3116](#)]. Cited on page 91.
- [468] D. Kim, J.-C. Park and S. Shin, *Dark Matter "Transporting" Mechanism Explaining Positron Excesses*, *J. High Energ. Phys.* **2018** (2018) 93, [[1702.02944](#)]. Cited on page 91.
- [469] X. Chu, S. Kulkarni and P. Salati, *Dark matter indirect signals with long-lived mediators*, *JCAP* **11** (2017) 023, [[1706.08543](#)]. Cited on the pages 91 and 94.
- [470] S. Gori, S. Profumo and B. Shakya, *Wobbly Dark Matter Signals at Cherenkov Telescopes from Long Lived Mediator Decays*, *Phys. Rev. Lett.* **122** (2019) 191103, [[1812.08694](#)]. Cited on page 91.
- [471] K. Agashe, S. J. Clark, B. Dutta and Y. Tsai, *Nonlocal effects from boosted dark matter in indirect detection*, *Phys. Rev. D* **103** (2021) 083006, [[2007.04971](#)]. Cited on page 91.
- [472] T. Bringmann and C. Weniger, *Gamma Ray Signals from Dark Matter: Concepts, Status and Prospects*, *Physics of the Dark Universe* **1** (2012) 194–217, [[1208.5481](#)]. Cited on page 91.
- [473] G. Elor, N. L. Rodd and T. R. Slatyer, *Multistep cascade annihilations of dark matter and the Galactic Center excess*, *Phys. Rev. D* **91** (2015) 103531, [[1503.01773](#)]. Cited on the pages 91 and 104.
- [474] C. Siqueira, *Secluded Dark Matter in light of the Cherenkov Telescope Array (CTA)*, *Phys. Lett. B* **797** (2019) 134840, [[1901.11055](#)]. Cited on the pages xxiii and 94.
- [475] C. Siqueira, G. N. Fortes, F. S. Queiroz and A. Viana, *Indirect Searches for Secluded Dark Matter*, [2107.04053](#). Cited on page 95.
- [476] M. Duerr, T. Ferber, C. Hearty, F. Kahlhoefer, K. Schmidt-Hoberg and P. Tunney, *Invisible and displaced dark matter signatures at Belle II*, *JHEP* **02** (2020) 039, [[1911.03176](#)]. Cited on page 95.
- [477] E. Ma, *Inception of Self-Interacting Dark Matter with Dark Charge Conjugation Symmetry*, *Phys. Lett. B* **772** (2017) 442–445, [[1704.04666](#)]. Cited on page 97.
- [478] M. Duerr, K. Schmidt-Hoberg and S. Wild, *Self-interacting dark matter with a stable vector mediator*, *JCAP* **09** (2018) 033, [[1804.10385](#)]. Cited on page 97.
- [479] M. E. Peskin and D. V. Schroeder, *An Introduction to quantum field theory*. Addison-Wesley, Reading, USA, 1995. Cited on page 98.

- [480] J. Berger, K. Jedamzik and D. G. E. Walker, *Cosmological Constraints on Decoupled Dark Photons and Dark Higgs*, *JCAP* **11** (2016) 032, [[1605.07195](#)]. Cited on the pages 99 and 102.
- [481] G. Belanger and J.-C. Park, *Assisted freeze-out*, *JCAP* **03** (2012) 038, [[1112.4491](#)]. Cited on page 100.
- [482] E949 collaboration, A. V. Artamonov et al., *New measurement of the  $K^+ \rightarrow \pi^+ \nu \bar{\nu}$  branching ratio*, *Phys. Rev. Lett.* **101** (2008) 191802, [[0808.2459](#)]. Cited on page 102.
- [483] LHCb collaboration, R. Aaij et al., *Search for hidden-sector bosons in  $B^0 \rightarrow K^{*0} \mu^+ \mu^-$  decays*, *Phys. Rev. Lett.* **115** (2015) 161802, [[1508.04094](#)]. Cited on page 102.
- [484] LHCb collaboration, R. Aaij et al., *Search for long-lived scalar particles in  $B^+ \rightarrow K^+ \chi(\mu^+ \mu^-)$  decays*, *Phys. Rev. D* **95** (2017) 071101, [[1612.07818](#)]. Cited on page 102.
- [485] CHARM collaboration, F. Bergsma et al., *Search for Axion Like Particle Production in 400-GeV Proton - Copper Interactions*, *Phys. Lett. B* **157** (1985) 458–462. Cited on page 102.
- [486] MICROBOONE collaboration, P. Abratenko et al., *Search for a Higgs Portal Scalar Decaying to Electron-Positron Pairs in the MicroBooNE Detector*, *Phys. Rev. Lett.* **127** (2021) 151803, [[2106.00568](#)]. Cited on page 102.
- [487] NA62 collaboration, E. Cortina Gil et al., *Measurement of the very rare  $K^+ \rightarrow \pi^+ \nu \bar{\nu}$  decay*, *JHEP* **06** (2021) 093, [[2103.15389](#)]. Cited on page 102.
- [488] M. W. Winkler, *Decay and detection of a light scalar boson mixing with the Higgs boson*, *Phys. Rev. D* **99** (2019) 015018, [[1809.01876](#)]. Cited on page 102.
- [489] B. Batell, J. Berger and A. Ismail, *Probing the Higgs Portal at the Fermilab Short-Baseline Neutrino Experiments*, *Phys. Rev. D* **100** (2019) 115039, [[1909.11670](#)]. Cited on the pages 102 and 103.
- [490] B. Batell, J. A. Evans, S. Gori and M. Rai, *Dark Scalars and Heavy Neutral Leptons at DarkQuest*, *JHEP* **05** (2021) 049, [[2008.08108](#)]. Cited on page 102.
- [491] J. H. Chang, R. Essig and S. D. McDermott, *Supernova 1987A Constraints on Sub-GeV Dark Sectors, Millicharged Particles, the QCD Axion, and an Axion-like Particle*, *JHEP* **09** (2018) 051, [[1803.00993](#)]. Cited on page 102.
- [492] V. Poulin, J. Lesgourgues and P. D. Serpico, *Cosmological constraints on exotic injection of electromagnetic energy*, *J. Cosmol. Astropart. Phys.* **03** (2017) , [[1610.10051](#)]. Cited on page 102.

- [493] T. R. Slatyer, *Indirect dark matter signatures in the cosmic dark ages. I. Generalizing the bound on s-wave dark matter annihilation from Planck results*, *Phys. Rev.* **D93** (2016) 023527, [1506.03811]. Cited on page 102.
- [494] T. R. Slatyer, *Indirect Dark Matter Signatures in the Cosmic Dark Ages II. Ionization, Heating and Photon Production from Arbitrary Energy Injections*, *Phys. Rev. D* **93** (2016) 023521, [1506.03812]. Cited on page 102.
- [495] KLEVER PROJECT collaboration, F. Ambrosino et al., *KLEVER: An experiment to measure  $BR(K_L \rightarrow \pi^0 \nu \bar{\nu})$  at the CERN SPS*, 1901.03099. Cited on page 103.
- [496] T. Nomura, *A future  $K_L^0 \rightarrow \pi^0 \nu \bar{\nu}$  experiment at J-PARC*, *J. Phys. Conf. Ser.* **1526** (2020) 012027. Cited on page 103.
- [497] K. Bondarenko, A. Boyarsky, T. Bringmann, M. Hufnagel, K. Schmidt-Hoberg and A. Sokolenko, *Direct detection and complementary constraints for sub-GeV dark matter*, *JHEP* **03** (2020) 118, [1909.08632]. Cited on page 103.
- [498] V. V. Gligorov, S. Knapen, M. Papucci and D. J. Robinson, *Searching for Long-lived Particles: A Compact Detector for Exotics at LHCb*, *Phys. Rev. D* **97** (2018) 015023, [1708.09395]. Cited on page 103.
- [499] G. Aielli et al., *Expression of interest for the CODEX-b detector*, *Eur. Phys. J. C* **80** (2020) 1177, [1911.00481]. Cited on page 103.
- [500] J. Mardon, Y. Nomura, D. Stolarski and J. Thaler, *Dark Matter Signals from Cascade Annihilations*, *JCAP* **05** (2009) 016, [0901.2926]. Cited on the pages 104 and 160.
- [501] L. Bergstrom, T. Bringmann, I. Cholis, D. Hooper and C. Weniger, *New Limits on Dark Matter Annihilation from AMS Cosmic Ray Positron Data*, *Phys. Rev. Lett.* **111** (2013) 171101, [1306.3983]. Cited on page 104.
- [502] S. Profumo, F. S. Queiroz, J. Silk and C. Siqueira, *Searching for Secluded Dark Matter with H.E.S.S., Fermi-LAT, and Planck*, *JCAP* **03** (2018) 010, [1711.03133]. Cited on page 106.
- [503] L. Knox and M. Millea, *Hubble constant hunter’s guide*, *Phys. Rev. D* **101** (2020) 043533, [1908.03663]. Cited on the pages 111, 112, and 114.
- [504] A. G. Riess, *The expansion of the Universe is faster than expected*, *Nat Rev Phys* **2** (2020) 10–12. Cited on page 111.
- [505] A. G. Riess et al., *A 2.4% Determination of the Local Value of the Hubble Constant*, *Astrophys. J.* **826** (2016) 56, [1604.01424]. Cited on page 111.
- [506] PLANCK collaboration, P. A. R. Ade et al., *Planck 2013 results. XX. Cosmology from Sunyaev–Zeldovich cluster counts*, *Astron. Astrophys.* **571** (2014) A20, [1303.5080]. Cited on the pages 111 and 114.

- [507] DES collaboration, T. M. C. Abbott et al., *Dark Energy Survey year 1 results: Cosmological constraints from galaxy clustering and weak lensing*, *Phys. Rev. D* **98** (2018) 043526, [[1708.01530](#)].  
Cited on the pages 111 and 114.
- [508] E. Di Valentino et al., *Snowmass2021 - Letter of interest cosmology intertwined II: The Hubble constant tension*, *Astropart. Phys.* **131** (2021) 102605, [[2008.11284](#)]. Cited on page 112.
- [509] E. Di Valentino et al., *Snowmass2021 - Letter of interest cosmology intertwined IV: The age of the universe and its curvature*, *Astropart. Phys.* **131** (2021) 102607, [[2008.11286](#)]. Cited on page 112.
- [510] A. G. Riess, W. Yuan, S. Casertano, L. M. Macri and D. Scolnic, *The Accuracy of the Hubble Constant Measurement Verified through Cepheid Amplitudes*, *Astrophys. J. Lett.* **896** (2020) L43, [[2005.02445](#)].  
Cited on page 112.
- [511] E. Di Valentino, O. Mena, S. Pan, L. Visinelli, W. Yang, A. Melchiorri et al., *In the realm of the Hubble tension - a review of solutions*, *Class. Quant. Grav.* **38** (2021) 153001, [[2103.01183](#)].  
Cited on the pages xxiv, 112, 113, and 114.
- [512] A. G. Riess, S. Casertano, W. Yuan, J. B. Bowers, L. Macri, J. C. Zinn et al., *Cosmic Distances Calibrated to 1% Precision with Gaia EDR3 Parallaxes and Hubble Space Telescope Photometry of 75 Milky Way Cepheids Confirm Tension with  $\Lambda$ CDM*, *Astrophys. J. Lett.* **908** (2021) L6, [[2012.08534](#)]. Cited on the pages xxiv and 113.
- [513] G. Blackadder and S. M. Koushiappas, *Cosmological constraints to dark matter with two- and many-body decays*, *Phys. Rev. D* **93** (2016) 023510, [[1510.06026](#)]. Cited on page 112.
- [514] K. Vattis, S. M. Koushiappas and A. Loeb, *Dark matter decaying in the late Universe can relieve the  $H_0$  tension*, *Phys. Rev. D* **99** (2019) 121302, [[1903.06220](#)]. Cited on the pages 112 and 125.
- [515] Y. Gu, M. Khlopov, L. Wu, J. M. Yang and B. Zhu, *Light gravitino dark matter: LHC searches and the Hubble tension*, *Phys. Rev. D* **102** (2020) 115005, [[2006.09906](#)]. Cited on page 112.
- [516] P. Lemos, E. Lee, G. Efstathiou and S. Gratton, *Model independent  $H(z)$  reconstruction using the cosmic inverse distance ladder*, *Mon. Not. Roy. Astron. Soc.* **483** (2019) 4803–4810, [[1806.06781](#)]. Cited on page 114.
- [517] F.-Y. Cyr-Racine, *Cosmic Expansion: A mini review of the Hubble-Lemaître tension*, [2105.09409](#). Cited on page 114.
- [518] Z. Li, Y. P. Jing, P. Zhang and D. Cheng, *Measurement of Redshift-Space Power Spectrum for BOSS galaxies and the Growth Rate at redshift 0.57*,

- Astrophys. J.* **833** (2016) 287, [1609.03697]. Cited on page 114.
- [519] H. Gil-Marín, W. J. Percival, L. Verde, J. R. Brownstein, C.-H. Chuang, F.-S. Kitaura et al., *The clustering of galaxies in the SDSS-III Baryon Oscillation Spectroscopic Survey: RSD measurement from the power spectrum and bispectrum of the DR12 BOSS galaxies*, *Mon. Not. Roy. Astron. Soc.* **465** (2017) 1757–1788, [1606.00439]. Cited on page 114.
- [520] K. Kuijken et al., *Gravitational Lensing Analysis of the Kilo Degree Survey*, *Mon. Not. Roy. Astron. Soc.* **454** (2015) 3500–3532, [1507.00738]. Cited on page 114.
- [521] S. S. Boruah, M. J. Hudson and G. Lavaux, *Cosmic flows in the nearby Universe: new peculiar velocities from SNe and cosmological constraints*, *Mon. Not. Roy. Astron. Soc.* **498** (2020) 2703–2718, [1912.09383]. Cited on page 114.
- [522] G. F. Abellan, R. Murgia, V. Poulin and J. Lavalle, *Hints for decaying dark matter from  $S_8$  measurements*, 2008.09615. Cited on page 114.
- [523] E. Di Valentino, L. A. Anchordoqui, Y. Ali-Haïmoud, L. Amendola, N. Arendse, M. Asgari et al., *Cosmology Intertwined III:  $\sigma_8$  and  $S_8$* , 2008.11285. Cited on page 114.
- [524] E. L. Turner, *Quasars and Galaxy Formation*, in *The Space Distribution of Quasars* (D. Crampton, ed.), vol. 21 of *Astronomical Society of the Pacific Conference Series*, p. 361, Jan., 1991. Cited on page 115.
- [525] D. J. Mortlock, S. J. Warren, B. P. Venemans, M. Patel, P. C. Hewett, R. G. McMahon et al., *A luminous quasar at a redshift of  $z = 7.085$* , *Nature* **474** (Jun, 2011) 616–619. Cited on the pages 115 and 122.
- [526] G. De Rosa et al., *Black hole mass estimates and emission-line properties of a sample of redshift  $z > 6.5$  quasars*, *Astrophys. J.* **790** (2014) 145, [1311.3260]. Cited on the pages 115 and 122.
- [527] A. Küller, J. P. Ostriker, P. Natarajan, C. N. Lackner and R. Cen, *Understanding black hole mass assembly via accretion and mergers at late times in cosmological simulations*, *Astrophys. J.* **799** (2015) 178, [1307.3684]. Cited on page 115.
- [528] F. Pacucci and A. Loeb, *Separating Accretion and Mergers in the Cosmic Growth of Black Holes with X-ray and Gravitational Wave Observations*, *Astrophys. J.* **895** (2020) 95, [2004.07246]. Cited on page 115.
- [529] E. E. Salpeter, *Accretion of Interstellar Matter by Massive Objects.*, *ApJ* **140** (Aug., 1964) 796–800. Cited on page 115.
- [530] K. Inayoshi, E. Visbal and Z. Haiman, *The Assembly of the First Massive Black Holes*, *Ann. Rev. Astron. Astrophys.* **58** (2020) 27–97, [1911.05791]. Cited on page 115.

- [531] J. Pollack, D. N. Spergel and P. J. Steinhardt, *Supermassive Black Holes from Ultra-Strongly Self-Interacting Dark Matter*, *Astrophys. J.* **804** (2015) 131, [[1501.00017](#)]. Cited on the pages 115 and 125.
- [532] J. Choquette, J. M. Cline and J. M. Cornell, *Early formation of supermassive black holes via dark matter self-interactions*, *JCAP* **07** (2019) 036, [[1812.05088](#)]. Cited on the pages 115, 125, and 129.
- [533] D. Lynden-Bell and R. Wood, *The gravo-thermal catastrophe in isothermal spheres and the onset of red-giant structure for stellar systems*, *MNRAS* **138** (Jan., 1968) 495. Cited on page 115.
- [534] XENON collaboration, E. Aprile et al., *Observation of Excess Electronic Recoil Events in XENON1T*, [2006.09721](#). Cited on the pages 115 and 132.
- [535] G. Alonso-Álvarez, F. Ertas, J. Jaeckel, F. Kahlhoefer and L. Thormaehlen, *Hidden Photon Dark Matter in the Light of XENON1T and Stellar Cooling*, [2006.11243](#). Cited on the pages 115, 130, and 132.
- [536] G. G. Raffelt and D. S. Dearborn, *Bounds on Hadronic Axions From Stellar Evolution*, *Phys. Rev. D* **36** (1987) 2211. Cited on the pages 115 and 132.
- [537] A. Ayala, I. Domínguez, M. Giannotti, A. Mirizzi and O. Straniero, *Revisiting the bound on axion-photon coupling from Globular Clusters*, *Phys. Rev. Lett.* **113** (2014) 191302, [[1406.6053](#)]. Cited on the pages 115 and 132.
- [538] M. Giannotti, I. Irastorza, J. Redondo and A. Ringwald, *Cool WISPs for stellar cooling excesses*, *JCAP* **05** (2016) 057, [[1512.08108](#)]. Cited on the pages 115 and 132.
- [539] M. Vogelsberger, J. Zavala and A. Loeb, *Subhaloes in self-interacting galactic dark matter haloes*, *Monthly Notices of the Royal Astronomical Society* **423** (May, 2012) 3740–3752. Cited on page 116.
- [540] M. Rocha, A. H. G. Peter, J. S. Bullock, M. Kaplinghat, S. Garrison-Kimmel, J. Onorbe et al., *Cosmological Simulations with Self-Interacting Dark Matter I: Constant Density Cores and Substructure*, *Mon. Not. Roy. Astron. Soc.* **430** (2013) 81–104, [[1208.3025](#)]. Cited on page 116.
- [541] J. M. Cline, *TASI Lectures on Early Universe Cosmology: Inflation, Baryogenesis and Dark Matter*, *PoS TASI2018* (2019) 001, [[1807.08749](#)]. Cited on the pages xxiv and 116.
- [542] M. R. Buckley and P. J. Fox, *Dark Matter Self-Interactions and Light Force Carriers*, *Phys. Rev. D* **81** (2010) 083522, [[0911.3898](#)]. Cited on page 117.
- [543] S. Tulin, H.-B. Yu and K. M. Zurek, *Beyond Collisionless Dark Matter: Particle Physics Dynamics for Dark Matter Halo Structure*, *Phys. Rev. D* **87** (2013) 115007, [[1302.3898](#)]. Cited on page 117.

- [544] B. Numerov, *A Method of Extrapolation of Perturbations*, *Monthly Notices of the Royal Astronomical Society* **84** (06, 1924) 592–602. Cited on page 117.
- [545] B. Numerov, *Note on the numerical integration of  $d^2x/dt^2=f(x,t)$* , *Astronomische Nachrichten* **230** (Aug., 1927) 359. Cited on page 117.
- [546] Schmid, Erich and Spitz, Gerhard and Lösch, Wolfgang, *Theoretical Physics on the Personal Computer*. Springer, Berlin, Heidelberg, 1990. Cited on page 118.
- [547] J. L. Feng, M. Kaplinghat and H.-B. Yu, *Halo Shape and Relic Density Exclusions of Sommerfeld-Enhanced Dark Matter Explanations of Cosmic Ray Excesses*, *Phys. Rev. Lett.* **104** (2010) 151301, [0911.0422]. Cited on page 118.
- [548] S. Khrapak, A. Ivlev, G. Morfill and S. Zhdanov, *Scattering in the Attractive Yukawa Potential in the Limit of Strong Interaction*, *Phys. Rev. Lett.* **90** (2003) 225002. Cited on page 118.
- [549] S. Khrapak, *Classical scattering in strongly attractive potentials*, *Phys. Rev. E* **89** (2014) 032145, [1403.6000]. Cited on page 118.
- [550] S. Tulin, H.-B. Yu and K. M. Zurek, *Resonant Dark Forces and Small Scale Structure*, *Phys. Rev. Lett.* **110** (2013) 111301, [1210.0900]. Cited on page 118.
- [551] O. Lebedev and T. Toma, *Relativistic Freeze-in*, *Phys. Lett. B* **798** (2019) 134961, [1908.05491]. Cited on page 119.
- [552] J. L. Feng, A. Rajaraman and F. Takayama, *Superweakly interacting massive particles*, *Phys. Rev. Lett.* **91** (2003) 011302, [hep-ph/0302215]. Cited on page 119.
- [553] E. Banados et al., *An 800-million-solar-mass black hole in a significantly neutral Universe at redshift 7.5*, *Nature* **553** (2018) 473–476, [1712.01860]. Cited on page 122.
- [554] R. Mertig, M. Bohm and A. Denner, *FEYN CALC: Computer algebraic calculation of Feynman amplitudes*, *Comput. Phys. Commun.* **64** (1991) 345–359. Cited on page 123.
- [555] V. Shtabovenko, R. Mertig and F. Orellana, *New Developments in FeynCalc 9.0*, *Comput. Phys. Commun.* **207** (2016) 432–444, [1601.01167]. Cited on page 123.
- [556] V. Shtabovenko, R. Mertig and F. Orellana, *FeynCalc 9.3: New features and improvements*, 2001.04407. Cited on page 123.
- [557] H. H. Patel, *Package-X 2.0: A Mathematica package for the analytic calculation of one-loop integrals*, *Comput. Phys. Commun.* **218** (2017) 66–70, [1612.00009]. Cited on the pages 123 and 155.

- [558] G. Passarino and M. Veltman, *One Loop Corrections for  $e^+ e^-$  Annihilation Into  $\mu^+ \mu^-$  in the Weinberg Model*, *Nucl. Phys. B* **160** (1979) 151–207. Cited on page 123.
- [559] D. Blas, J. Lesgourgues and T. Tram, *The cosmic linear anisotropy solving system (class). part ii: Approximation schemes*, *Journal of Cosmology and Astroparticle Physics* **2011** (Jul, 2011) 034–034. Cited on page 124.
- [560] T. Brinckmann and J. Lesgourgues, *MontePython 3: boosted MCMC sampler and other features*, *Phys. Dark Univ.* **24** (2019) 100260, [1804.07261]. Cited on the pages 124 and 125.
- [561] B. Audren, J. Lesgourgues, K. Benabed and S. Prunet, *Conservative Constraints on Early Cosmology: an illustration of the Monte Python cosmological parameter inference code*, *JCAP* **1302** (2013) 001, [1210.7183]. Cited on page 124.
- [562] PLANCK collaboration, N. Aghanim et al., *Planck 2018 results. V. CMB power spectra and likelihoods*, 1907.12875. Cited on page 124.
- [563] BOSS collaboration, S. Alam et al., *The clustering of galaxies in the completed SDSS-III Baryon Oscillation Spectroscopic Survey: cosmological analysis of the DR12 galaxy sample*, *Mon. Not. Roy. Astron. Soc.* **470** (2017) 2617–2652, [1607.03155]. Cited on page 124.
- [564] F. Beutler, C. Blake, M. Colless, D. H. Jones, L. Staveley-Smith, L. Campbell et al., *The 6df galaxy survey: baryon acoustic oscillations and the local hubble constant*, *Monthly Notices of the Royal Astronomical Society* **416** (Jul, 2011) 3017–3032. Cited on page 124.
- [565] A. J. Ross, L. Samushia, C. Howlett, W. J. Percival, A. Burden and M. Manera, *The clustering of the sdss dr7 main galaxy sample – i. a 4 per cent distance measure at  $z = 0.15$* , *Monthly Notices of the Royal Astronomical Society* **449** (Mar, 2015) 835–847. Cited on page 124.
- [566] PLANCK collaboration, P. Ade et al., *Planck 2015 results. XXIV. Cosmology from Sunyaev-Zeldovich cluster counts*, *Astron. Astrophys.* **594** (2016) A24, [1502.01597]. Cited on page 124.
- [567] V. Poulin, P. D. Serpico and J. Lesgourgues, *A fresh look at linear cosmological constraints on a decaying dark matter component*, *Journal of Cosmology and Astroparticle Physics* **2016** (Aug, 2016) 036–036. Cited on page 125.
- [568] A. Chudaykin, D. Gorbunov and I. Tkachev, *Dark matter component decaying after recombination: Sensitivity to baryon acoustic oscillation and redshift space distortion probes*, *Physical Review D* **97** (Apr, 2018) . Cited on page 125.
- [569] A. H. Peter, *Mapping the allowed parameter space for decaying dark matter*

- models*, *Phys. Rev. D* **81** (2010) 083511, [1001.3870]. Cited on page 125.
- [570] M.-Y. Wang, R. A. Croft, A. H. Peter, A. R. Zentner and C. W. Purcell, *Lyman- $\alpha$  forest constraints on decaying dark matter*, *Phys. Rev. D* **88** (2013) 123515, [1309.7354]. Cited on page 125.
- [571] M. Kaplinghat, *Dark matter from early decays*, *Phys. Rev. D* **72** (2005) 063510, [astro-ph/0507300]. Cited on the pages 125 and 127.
- [572] F. Borzumati, T. Bringmann and P. Ullio, *Dark matter from late decays and the small-scale structure problems*, *Phys. Rev. D* **77** (2008) 063514, [hep-ph/0701007]. Cited on the pages 125 and 127.
- [573] S. Aoyama, T. Sekiguchi, K. Ichiki and N. Sugiyama, *Evolution of perturbations and cosmological constraints in decaying dark matter models with arbitrary decay mass products*, *JCAP* **07** (2014) 021, [1402.2972]. Cited on the pages 125 and 127.
- [574] S. W. Randall, M. Markevitch, D. Clowe, A. H. Gonzalez and M. Bradac, *Constraints on the Self-Interaction Cross-Section of Dark Matter from Numerical Simulations of the Merging Galaxy Cluster 1E 0657-56*, *Astrophys. J.* **679** (2008) 1173–1180, [0704.0261]. Cited on page 128.
- [575] D. Levkov, P. Tinyakov and F. Bezrukov, “Calculator for dimensional quantities.” <http://ppc.inr.ac.ru/eng/uc.php>. Cited on page 135.
- [576] E. Byckling and K. Kajantie, *Particle Kinematics: (Chapters I-VI, X)*. University of Jyväskylä, Jyväskylä, Finland, 1971. Cited on page 135.
- [577] J. C. Romao, “Techniques for Calculations in Quantum Field Theory: W-strahlung in e colliders.” <https://porthos.tecnico.ulisboa.pt/CTQFT/files/Wstrahlung.pdf>. Cited on page 136.
- [578] G. Mohlabeng, *Revisiting the dark photon explanation of the muon anomalous magnetic moment*, *Phys. Rev.* **D99** (2019) 115001, [1902.05075]. Cited on page 139.
- [579] M. Buschmann, J. Kopp, J. Liu and P. A. N. Machado, *Lepton Jets from Radiating Dark Matter*, *JHEP* **07** (2015) 045, [1505.07459]. Cited on page 141.
- [580] D. E. Morrissey and A. P. Spray, *New Limits on Light Hidden Sectors from Fixed-Target Experiments*, *JHEP* **06** (2014) 083, [1402.4817]. Cited on page 143.
- [581] Y.-S. Tsai, *Pair Production and Bremsstrahlung of Charged Leptons*, *Rev. Mod. Phys.* **46** (1974) 815. Cited on the pages 143 and 146.
- [582] K. J. Kim and Y.-S. Tsai, *Improved Weizsacker-Williams method and its application to lepton and W boson pair production*, *Phys. Rev.* **D8** (1973)

3109. Cited on the pages 143 and 146.
- [583] J. D. Bjorken, R. Essig, P. Schuster and N. Toro, *New Fixed-Target Experiments to Search for Dark Gauge Forces*, *Phys. Rev. D* **80** (2009) 075018, [0906.0580]. Cited on page 143.
- [584] R. H. Helm, *Inelastic and Elastic Scattering of 187-Mev Electrons from Selected Even-Even Nuclei*, *Phys. Rev.* **104** (1956) 1466–1475.  
Cited on page 146.
- [585] I. Qattan et al., *Precision Rosenbluth measurement of the proton elastic form-factors*, *Phys. Rev. Lett.* **94** (2005) 142301, [nucl-ex/0410010].  
Cited on page 147.
- [586] J. C. Helo, S. Kovalenko and I. Schmidt, *Sterile neutrinos in lepton number and lepton flavor violating decays*, *Nucl. Phys. B* **853** (2011) 80–104, [1005.1607]. Cited on page 149.
- [587] S. Coleman and J. Mandula, *All possible symmetries of the  $s$  matrix*, *Phys. Rev.* **159** (Jul, 1967) 1251–1256. Cited on page 151.
- [588] R. Haag, J. T. Lopuszanski and M. Sohnius, *All Possible Generators of Supersymmetries of the  $s$  Matrix*, *Nucl. Phys. B* **88** (1975) 257.  
Cited on page 151.
- [589] I. J. R. Aitchison, *Supersymmetry in Particle Physics. An Elementary Introduction*. Cambridge University Press, Cambridge, 2007, 10.1017/CBO9780511619250. Cited on page 152.
- [590] F. Quevedo, S. Krippendorff and O. Schlotterer, *Cambridge Lectures on Supersymmetry and Extra Dimensions*, 1011.1491. Cited on page 153.
- [591] F. Bezrukov and D. Gorbunov, *Light inflaton Hunter’s Guide*, *J. High Energ. Phys.* **2010** (2010) 10, [0912.0390]. Cited on page 155.
- [592] J.-F. Fortin, J. Shelton, S. Thomas and Y. Zhao, *Gamma Ray Spectra from Dark Matter Annihilation and Decay*, 0908.2258. Cited on page 159.